

Spin-dependent X-ray Absorption Spectroscopy of *3d* Transition Metals: Systematics and Applications

Inaugural-Dissertation
zur Erlangung der Doktorwürde
am Fachbereich Physik
der Freien Universität Berlin

vorgelegt von
Andreas Scherz
aus Berlin

Oktober 2003

Scherz, Andreas:

Spin-dependent X-ray Absorption Spectroscopy of 3d Transition Metals :
Systematics and Applications / Andreas Scherz. – Als Ms. gedr. –

Berlin : dissertation.de – Verlag im Internet GmbH, 2004

Zugl.: Berlin, Freie Univ., Diss., 2003

ISBN 3-89825-779-7

1. Gutachter: Prof. Dr. K. Baberschke

2. Gutachter: Prof. Dr. F. Forstmann

Tag der Disputation: 10. Dezember 2003

Bibliografische Information Der Deutschen Bibliothek

Die Deutsche Bibliothek verzeichnet diese Publikation in der Deutschen Nationalbibliografie; detaillierte bibliografische Daten sind im Internet über <http://dnb.ddb.de> abrufbar.

Copyright dissertation.de – Verlag im Internet GmbH 2004

Alle Rechte, auch das des auszugsweisen Nachdruckes, der auszugsweisen oder vollständigen Wiedergabe, der Speicherung in Datenverarbeitungsanlagen, auf Datenträgern oder im Internet und der Übersetzung, vorbehalten.

Es wird ausschließlich chlorfrei gebleichtes
Papier (TCF) nach DIN-ISO 9706 verwendet.
Printed in Germany.

dissertation.de - Verlag im Internet GmbH
Pestalozzistraße 9
10 625 Berlin

URL: <http://www.dissertation.de>

Dedicated to my parents

Abstract

In this thesis, the magnetic and structural properties of the interfaces in Fe/V superlattices and prototype Fe/V/Fe trilayers are investigated by means of the x-ray magnetic circular dichroism (XMCD) at $L_{2,3}$ absorption edges. Properties such as the magnetic anisotropy and the magnetic transport properties are considered to be substantially influenced by the induced magnetism. The XMCD technique provides a site-specific insight to the induced magnetism at interfaces due to its element-specificity. In contrast to experiments, which probe the total magnetic response of the system as for instance the sample magnetization by VSM and the spectroscopic splitting g -factor by FMR, both the Fe moments and the induced V moments at the common interface can be determined. The frequently reported discrepancies between theory and experiments on the magnetic properties of interfaces are resolved by investigating the role of interdiffusion and roughness in prototype Fe/V/Fe trilayers which are grown with a certain growth recipe tuning the structural and magnetic properties at the interface.

The induced circular dichroism of the early $3d$ transition metals (TM's) is a very small difference between the absorption intensities for left and right circularly polarized light. However, the unique XMCD spectra for the early $3d$ TM's V, Ti, and Cr presented in this thesis were obtained using a gap-scan technique which drives both the undulator and monochromator on the beamline station simultaneously. In contrast to the XMCD spectra of the late $3d$ ferromagnets Fe, Co, and Ni, the XMCD spectra reveal a rich variety of spectral features in the absorption fine structure. It is demonstrated that the analysis of the XMCD spectra for the early $3d$ TM cannot be performed in straight-forward manner. By the systematic investigation of the XMCD spectra at the beginning of the $3d$ series, carried out in the framework of this thesis, it is shown that the application of the commonly used magneto-optical sum rules fails due to the presence of core hole correlation effects. Hence, an alternative approach for the determination of the spin and orbital moments is proposed by analyzing the spectral line-shape of the circular dichroism. For the interpretation of the XMCD spectra, the experimental data are compared to fully relativistic *ab initio* theory which provides both the magnetic moments and the corresponding spin-dependent absorption fine structure. Since a comprehensive theory to

describe the core hole correlation effects in the spin-dependent absorption spectra is not established up to now, a simple theoretical model is elaborated that allows to determine the correlation energies from the experimental spectra. The results can serve in the future as an input for theory to decide whether a theoretical model is suitable or not.

Finally, the spin-dependent absorption fine structure of dilute $3d$ impurities (Cr–Co) in noble metal hosts has been investigated for the first time revealing their intermediate character between a pure atomic configuration and the solid state. The importance of the hybridization effects with the host is discussed in view of the appearance or suppression of the orbital magnetism in dilute $3d$ impurities.

Kurzfassung

In der vorliegenden Arbeit wurden die magnetischen und strukturellen Eigenschaften der Grenzflächen in Fe/V-Vielfachschichten und Fe/V/Fe-Dreifachschichten untersucht. Es wird davon ausgegangen, dass der induzierte Magnetismus an der Grenzfläche unter anderem die magnetische Anisotropie und die magnetischen Transporteigenschaften erheblich beeinflusst. Die Elementspezifität des magnetischen Röntgenzirkulardichroismus (XMCD) ermöglicht hierbei den direkten Zugang zum induzierten Magnetismus. Im Gegensatz zu Experimenten, in denen nur die gesamte magnetische Antwort von dem System gemessen wird, wie z.B. bei Messungen der Probenmagnetisierung durch VSM und der Bestimmung des g -Faktors durch FMR, können sowohl die Fe-Momente als auch die induzierten V-Momente an der gemeinsamen Grenzfläche bestimmt werden. Die recht häufig in der Literatur diskutierten Diskrepanzen zwischen Theorie und Experiment über die magnetischen Grenzflächeneigenschaften konnten mit der Untersuchung von Interdiffusion und Rauheit in Fe/V/Fe-Dreifachschichten, in denen die magnetischen und strukturellen Eigenschaften der Grenzfläche angepasst werden können, aufgelöst werden.

Der induzierte Zirkulardichroismus der leichten $3d$ -Übergangsmetalle (TM's) ist eine sehr kleine Differenz zwischen den Absorptionsintensitäten für links- und rechtszirkular polarisiertes Röntgenlicht. Dennoch wurden einzigartige XMCD-Spektren der leichten $3d$ TM's V, Ti und Cr unter der Verwendung der "gap-scan"-Technik, die simultan den Undulator und den Monochromator des Strahlrohrs während der Messung fährt, erzielt. Die XMCD-Spektren weisen im Gegensatz zu den schweren $3d$ TM's eine Vielzahl von Absorptionsfeinstrukturen auf. Es wird gezeigt, dass die Analyse der XMCD-Spektren nicht auf einfache Weise durchgeführt werden kann. Anhand der systematischen Untersuchung der XMCD-Spektren zu Beginn der $3d$ -Serie stellt sich heraus, dass die gewohnte Anwendung der Summenregeln aufgrund von Korrelationseffekten mit dem Rumpfloch versagt. Eine alternative Herangehensweise zur Bestimmung von Spin- und Bahnmomenten, die die spektrale Linienform des Zirkulardichroismus analysiert, wird daher vorgeschlagen. Für die Interpretation der XMCD-Spektren werden die experimentellen Daten mit voll-relativistischen *ab initio* Rechnungen verglichen, welche sowohl die magnetischen Momente als auch die entsprechende Absorptionsfeinstruktur liefern. Da eine umfassende

Theorie zur Beschreibung der Rumpflocheffekte in den spinabhängigen Absorptionsspektren bis jetzt nicht besteht, wurde ein einfaches Modell erarbeitet, welches es ermöglicht, die Korrelationsenergien aus den experimentellen Spektren zu bestimmen. Diese können in Zukunft für die Entwicklung von Theoriemodellen genutzt werden.

In der vorliegenden Arbeit wurde auch erstmalig die spinabhängige Absorptionsfeinstruktur an verdünnten Legierungen von $3d$ -Atomen (Cr–Co) in Au untersucht. Die Bedeutung von Hybridisierungseffekten mit dem Wirt wird im Hinblick auf das Auftreten bzw. das Verschwinden des Bahnmagnetismus in den verdünnten $3d$ -Atomen in Au diskutiert.

Contents

Abstract	i
Kurzfassung	iii
Introduction	1
1 X-ray Magnetic Circular Dichroism	5
1.1 The x-ray absorption cross section	6
1.2 Theoretical models for XMCD	10
1.3 Analysis of experimental data	21
1.4 Electronic and magnetic properties of <i>3d</i> TM's	25
2 Experimental Details	29
2.1 Measurements at BESSY II: UE56/1-PGM	32
2.2 Measurements at ESRF: ID8 (Former ID12B)	34
3 Absorption Fine Structure of Early <i>3d</i> TM's	37
3.1 Electron core-hole interaction	39
3.2 Relation between XMCD and the magnetic ground-state for V	52
3.3 Limitations of magneto-optical sum rules for <i>3d</i> TM's	66
3.4 Multipole moment analysis versus SPR-KKR	71
4 Fe/V/Fe(110) Trilayers	75
4.1 Structural properties	78
4.2 Evidence of short-range spin-polarization	80
4.3 Influence of interdiffusion effects on V spin polarization	84
5 Interfacial Magnetic Properties of Fe/V(100) Superlattices	91
5.1 Structural properties	92

5.2	XMCD versus VSM: Interfacial Fe and induced V moments	94
5.3	XMCD versus FMR: Orbital magnetism in layered structures	99
5.4	Superparamagnetic behavior in ultrathin ferromagnetic layers	102
6	3d Impurities in Au-Host	107
6.1	Structural and magnetic properties	108
6.2	Absorption fine structure	109
6.3	Orbital magnetism	113
	Conclusion	119
A	XMCD Filemanager	123
B	SATEFF: Saturation Effects in XAS using TEY	125
C	Multipole Moment Analysis	129
	Bibliography	131
	List of Publications	145
	Curriculum Vitae	151
	Zusammenfassung	153
	Danksagung	157

Introduction

In the last decades, enormous progress has been made in composing magnetic nanostructures such as multilayers, thin films, and one-dimensional monatomic chains revealing novel electronic and magnetic properties which are relevant for technological applications as well as for fundamental research. At the same time, the continuous development of the synchrotron radiation facilities made it possible to extend magneto-optical effects to the soft and hard x-ray energy range. Since the first observation of the x-ray magnetic circular dichroism (XMCD) in 1987 [1], the technique has become a powerful tool for investigations of magnetic nanostructures in an element-specific manner and is nowadays widely used in the synchrotron community. Considering investigations of the $3d$ transition metals (TM's) the absorption process involves excitations of photoelectrons from the deep $2p$ core levels into the unoccupied $3d$ valence states according to the dipole selection rules. An imbalance of spin-up and spin-down electrons in the $3d$ shell leads to different absorption coefficients $\mu^\pm(E)$ of left and right circularly polarized light at the $L_{2,3}$ edge energy-range. The information on the electronic and magnetic properties are thus contained in the XMCD, which is defined as the difference of the absorption coefficients $\Delta\mu(E) = \mu^+(E) - \mu^-(E)$. The magneto-optical sum rules [2, 3] are most commonly applied to deduce spin and orbital moments from XMCD. Even though certain approximation limit the validity of the sum rules, their applicability has been theoretically and experimentally verified for the late $3d$ TM's [4–10]. Since most of the magnetic nanostructures are composed of the ferromagnets Fe, Co and Ni, the element-specific XMCD method had an enormous impact on the understanding of magnetism in these systems.

By miniaturizing magnetic multilayers consisting of ferromagnetic and non-magnetic layers with a periodicity on a nanometer-scale, the magnetic and structural properties of the interfaces are of increasing relevance. One topic is the layer-dependent distribution of the magnetic moments in the ferromagnetic layers and

the induced magnetic moment in the non-magnetic spacer layer. Hereby, properties such as the magnetic anisotropy and the magnetic transport properties are considered to be substantially influenced by the induced magnetism [11–15]. The direct access to the small contribution of induced magnetism is, however, difficult by for instance superconducting quantum interference device (SQUID) and vibrating sample magnetometries (VSM) as well as ferromagnetic resonance (FMR) probing the total magnetic response of the system. The XMCD technique supplies the need for an element-specific magnetometry with submonolayer-sensitivity.

In this thesis, we choose Fe/V layered structures as a model system for two reasons: (i) Vanadium acquires a sizable induced magnetic moment at the Fe/V interface and (ii) the Fe_n/V_m superlattices with a high structural and magnetic homogeneity have in the last years served as a prototype system to investigate the rich variety of multilayer magnetism such as the spin-dependent transport properties, interlayer exchange coupling and the magnetic anisotropies and orbital magnetism [16–21]. The following questions can be raised: How large is the magnitude and the range of the spin-polarization beyond the Fe/V interface? Do the conclusions drawn on the properties of the ferromagnetic constituent in the multilayers, as for example the orbital magnetism probed by FMR, change in view of the induced magnetism? A key point to answer these questions was, in the framework of this thesis, to compare the results from the Fe-XMCD and V-XMCD measurements with FMR and VSM and to resolve the quite frequently reported discrepancies between theory and experiment on the induced magnetic moment profiles in the multilayers [12, 22–30]. For this purpose we analyzed Fe/V/Fe trilayers, which serve as prototype samples for the Fe/V superlattices, for investigating the role of atomic exchange processes and roughness at the interfaces on the magnetic moment distribution. The preparation of the trilayers on a Cu(100) single crystal is based on a growth recipe developed in this thesis that reduces roughness and allows to control interdiffusion at the Fe/V interface.

The XMCD spectra at the $L_{2,3}$ edges of V are analyzed for deducing the induced magnetic moments in the Fe/V layered structures. In contrast to the ferromagnets Fe, Co, and Ni, which possess intrinsically magnetic moments, the circular dichroism of the early 3d elements is very small compared to the absorption intensities. In order to resolve the XMCD spectrum of thin V layers, the measurements were carried out on the undulator beamline UE56/1-PGM at BESSY II, the synchrotron facility in Berlin. On our initiative, the gap-scan technique was established which drives the

monochromator and the gap of the undulator simultaneously. It provides a high degree of photon flux and circular polarization over the required energy-range for near edge absorption measurements. Unlike previous studies, we thus measured the V-XMCD with a high signal-to-noise ratio by taking benefit of the gap-scan technique. The XMCD spectra reveal a detailed and complex fine structure $\Delta\mu(E)$. It is known that the absorption spectra of the early $3d$ elements suffer from core-hole correlation effects [31–34]. On the other hand, a comprehensive theory on its possible influence on the spin-dependent absorption fine structure is up to now not derived for the magnetic solid state. Therefore, the measurements of the spin-dependent absorption fine structure is systematically extended across the $3d$ series. The relation between the spectral distribution and the magnetic ground state and the influence of the core hole on the absorption spectra is addressed in this thesis. The experimental data are compared to fully relativistic *ab initio* calculations [9,35]. Finally, the approaches, such as the commonly used magneto-optical sum rules, to obtain magnetic ground-state properties from experimental absorption spectra are tested for their validity in view of the core-hole correlation effects.

For the first time, a systematic investigation of the absorption fine structure and orbital magnetism of dilute $3d$ impurities in noble metal hosts is performed. These systems attract great interest, since they can be considered as a bridge from the atomic to the solid state. While the $3d$ elements form large orbital and spin moments in free-atoms according to the Hund’s rules, they possess reduced moments in the magnetic solid state. In particular the orbital moment becomes quenched being typically a few percent of the spin moment only. The question thus arises, how crystal field and hybridization effects influence the orbital magnetism in case of dilute impurities.

The present work is organized as follows: In chapter 1 the basic principles and theoretical aspects of the x-ray magnetic circular dichroism are introduced. An overview of the experimental setup, sample preparation and the beamline stations at BESSY II and at ESRF is presented in chapter 2. In chapter 3, the systematics of the spin-dependent absorption fine structure of the early $3d$ elements are given. The induced magnetism and the role of interdiffusion at Fe/V interfaces in Fe/V/Fe trilayers as well as the orbital magnetism in Fe/V superlattices are discussed in chapter 4 and chapter 5, respectively. In chapter 6 the XMCD measurements on $3d$ impurities in Au are presented. The appendix summarizes the software packages for the data analysis that have been developed within this thesis.

Chapter 1

X-ray Magnetic Circular Dichroism

The x-ray magnetic circular dichroism (XMCD) technique is based on changes in the absorption cross section for circularly polarized light depending on the magnetic properties of the absorber. It can be classified to the *magneto-optical effects* that relate the spectroscopic and optical properties to the magnetic state of a given system. The discovery of magneto-optical effects goes back to Faraday in 1846 [36] who observed a rotation of the polarization vector upon transmission of linearly polarized light through matter in an applied magnetic field. Several years later Kerr found the same effect for the reflected beam [37]. One of today's conventional magnetometries is the magneto-optical Kerr effect (MOKE) using laser light. The photon energies are typically of the order of a few eV involving excitations of electrons from occupied to unoccupied valence states in an absorbing medium. The absorption in the exchange splitted valence states is different for the two circular components of the linear-polarized incident light due to the dipole selection rules. Hence, the reflected beam becomes elliptically polarized, and the Kerr-rotation is a measure of the sample magnetization. On the other hand, it is difficult to discriminate between different magnetic constituents by probing intra-band transitions and the technique is thus in general not element-specific.

Several attempts were made to extend magneto-optical effects to the x-ray regime with measurements of the x-ray absorption of a ferromagnetic Fe foil in the beginning of the last century [38, 39]. However, the first serious prediction of magneto-optical effects in x-ray absorption using circularly polarized light, i.e. the x-ray magnetic circular dichroism, at the $M_{2,3}$ edges of ferromagnetic Ni stems from Erskine and

Stern in 1975 [40]. It took several years for the first experimental proof of XMCD measured at the K edge of a Fe foil by Schütz *et al* [1] in 1987. This can be attributed to the development of synchrotron radiation sources providing a continuous spectrum of polarized x-rays with a high photon flux. Due to the characteristic energies of the excited core states this method is element-selective which is valuable for complex magnetic structures. Moreover, the core states are highly localized with defined quantum numbers that scans the density of final states according to Fermi's Golden rule. The measurements can be carried out at different edges (K , $L_{2,3}$ or $M_{4,5}$ edges) selecting the character of the final states (p -, d - and f -like states) with respect to the dipole selection rules. Hence, XMCD spectra at different edges contain intrinsically shell-selective information on the magnetic state of a system.

1.1 The x-ray absorption cross section

The absorption cross section σ_x is defined as the number of excited electrons per unit time divided by the photon flux I_{ph} ,

$$\sigma_x(E) = \frac{\Gamma_{i \rightarrow f}}{I_{ph}}. \quad (1.1)$$

It corresponds to the area that absorbs completely the incident photons of energy $E = \hbar\omega$. Hereby, the probability per unit time $\Gamma_{i \rightarrow f}$ to excite an electron from the initial state $|i\rangle$ to a final state $|f\rangle$ with the energy density $\rho(E_f)$ is given by Fermi's Golden rule

$$\Gamma_{i \rightarrow f} = \frac{2\pi}{\hbar} |\langle f | \mathcal{H}_{int} | i \rangle|^2 \rho(E_f) \delta(E_f - E_i - \hbar\omega), \quad (1.2)$$

where \mathcal{H}_{int} denotes the interaction operator reflecting a time-dependent perturbation of the Hamiltonian of the atom \mathcal{H}_0 . The electromagnetic field of the photons is expressed by the vector potential $\mathbf{A}(\mathbf{r}, t)$. Replacing $\frac{\hbar}{i}\nabla$ with $\frac{\hbar}{i}\nabla - \frac{e}{c}\mathbf{A}$ the Hamiltonian becomes

$$\begin{aligned} \mathcal{H} = \mathcal{H}_0 + \mathcal{H}_{int} &= \frac{1}{2m} \left(\frac{\hbar}{i}\nabla - \frac{e}{c}\mathbf{A} \right)^2 + \phi \\ &= \mathcal{H}_0 - \frac{e}{2mc}\mathbf{A} \cdot \frac{\hbar}{i}\nabla + \frac{e^2}{2mc^2}\mathbf{A}^2 \end{aligned} \quad (1.3)$$

where $\nabla \cdot \mathbf{A} = 0$ (Coulomb gauge). The vector potential can be expressed in terms of electromagnetic plane waves with the wave vector \mathbf{k} , frequency ω and

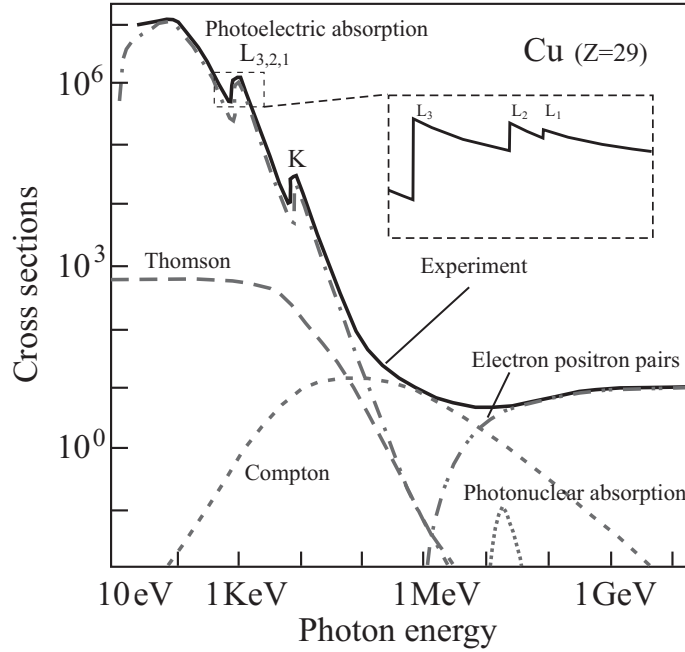


Figure 1.1: The total cross section of Cu ($Z=29$) and the comparison with its photoelectric absorption cross section and elastic as well as inelastic scattering processes [41].

polarization vector ϵ . Ignoring the last term in (1.3) which is related to two-photon annihilation/excitation processes, the interaction operator can be written as

$$\mathcal{H}_{int} = -\frac{e\hbar}{i2mc}A_0 \epsilon e^{i(\mathbf{kr}-\omega t)} \cdot \nabla. \quad (1.4)$$

The interaction between x-rays and matter is small compared to the electrostatic interactions in the atom. Hence, the absorption probability $\Gamma_{i \rightarrow f}$ is small and time-independent. Considering excitations in the soft x-ray regime, e.g. excitation of the L shell of Fe at $\hbar\omega \sim 700$ eV, the wavelength is $\lambda/2\pi \sim 2.8$ Å. Since $\mathbf{r} \ll 1$ Å is valid for excitations of core electrons, it is sufficient to develop the vector potential at $\mathbf{kr} \ll 1$, i.e.

$$A_0 \epsilon e^{i(\mathbf{kr}-\omega t)} = A_0 \epsilon e^{-i\omega t} \left\{ 1 - i\mathbf{kr} + \frac{1}{2}(i\mathbf{kr})^2 + \dots \right\}. \quad (1.5)$$

The terms on the right hand side describe the electric dipole (E1), magnetic dipole (M1), electric quadrupole transitions (E2) etc., respectively. The latter have to be taken into account in the hard x-ray range as for example at the $L_{2,3}$ edges of the rare earths [42]. Replacing the linear momentum operator

$$\frac{1}{m} \frac{\hbar}{i} \langle f | \epsilon \nabla | i \rangle = \frac{i}{\hbar} \langle f | \epsilon [\mathbf{r}, \mathcal{H}_0] | i \rangle = \frac{i}{\hbar} (E_f - E_i) \langle f | \epsilon \mathbf{r} | i \rangle$$

the transition probability (1.2) recasts to

$$\Gamma_{i \rightarrow f} = \frac{\pi e^2 A_0^2}{2\hbar^2 c^2} \hbar\omega |\langle f | \epsilon \mathbf{r} | i \rangle|^2 \rho(E_f) \delta(E_f - E_i - \hbar\omega) \quad (1.6)$$

within the dipole approximation (the zero order term of \mathbf{A}). Finally, according to (1.1) the photoelectron absorption cross section becomes

$$\sigma_x(\hbar\omega) = 4\pi^2 \alpha \hbar\omega |\langle f | \epsilon \mathbf{r} | i \rangle|^2 \rho(E_f) \delta(E_f - E_i - \hbar\omega) \quad (1.7)$$

using the fine structure constant $\alpha = e^2/(\hbar c)$ and the expression for the photon flux $I_{ph} = A_0^2 \omega / (8\pi \hbar c)$ which is the energy flux divided by the photon energy.

Apart from the photoelectron absorption cross section there are elastic and inelastic scattering processes up to 1 MeV. The sum over all different cross sections, i.e. the total cross section, is the quantity that can be measured in the experiment as illustrated in Figure 1.1 [41]. However, up to ~ 100 keV the dominant process of the interaction between x-rays and matter is the photoelectron absorption. Characteristic jumps in the absorption cross section indicate the successive excitations of the core shells, i.e. $K \hat{=} 1s$, $L_1 \hat{=} 2s$, $L_2 \hat{=} 2p_{1/2}$, $L_3 \hat{=} 2p_{3/2}$ etc. The absorption cross section in the vicinity of an edge jump can be roughly divided in the so called x-ray absorption near edge structure (XANES) which reflects excitations of the photoelectron into unoccupied valence states, and the so-called extended x-ray absorption fine structure (EXAFS) where the photoelectron is excited into the continuum and scatters with the environment of the absorber, for a review see [43]. The EXAFS is modelled by multi-scattering processes for low kinetic energies (< 40 eV) and single scattering processes for higher energies according to the universal curve for the mean-free-path of the electron.

Time scales of the absorption process

The time scales involved in absorption processes can be deconvoluted in a simplified model. The time scale of creating a core hole is of the order $\tau_e \approx 10^{-20}$ s while the rearrangement of the valence electrons in presence of the core hole (*screening*) is of the order $\tau_{screen} \approx 10^{-16} - 10^{-15}$ s. The lifetime of the core hole is determined by the sum over all relaxation processes and is about $\tau_c \approx 10^{-16} - 10^{-15}$ s. Because $\tau_{screen} \sim \tau_c$ screening effects are important for the XANES region while, depending on the kinetic energy of photoelectron, the sudden approximation (no rearrangement of the electrons in presence of the core hole) is valid in the EXAFS region. The time

scales of the decay channels restrict the core hole lifetime. For the lighter elements ($Z < 30$) the dominant process is the non-radiative Auger process and the larger Z the more the system relaxes by emission of fluorescence photons.

Evaluation of the matrix element

The absorption cross section can be evaluated from the matrix element of the transition probability. Therefore, an appropriate description of the initial and final states is needed. Due to their localization the initial core states have an atomic character with well defined quantum numbers jm . The main problem is the description of the final states. The excitation of an electron in an atom affects the other electrons which are perturbed by the core hole and correlations between the electrons. However, a rigorous description of the final states is difficult. Weakly correlated systems as for instance broad valence bands or continuum states may be treated within the independent particle scheme neglecting the screening effects and the core hole. This means accordingly that the final states are determined by the ground state of the system. The d valence band of $3d$ TM's is about 5 eV broad and even though the d electrons are delocalized the electron-electron correlation (~ 1 eV) cannot be treated as a small perturbation. The description of the absorption cross section for the $3d$ TM's is an intermediate case between the two extrema of strongly correlated atomic systems and weakly correlated itinerant systems. In chapter 6 the absorption fine structure of $3d$ TM's will be discussed with respect to atomic and band structure related features. In case of the early $3d$ TM's, one observes strong core-hole correlation effects that illustrate the need for a better description in particular of the near edge absorption spectra beyond the independent particle approximation for itinerant systems. Finally, one considers the dipole selection rules for linearly polarized light

$$\Delta j = 0, \pm 1 \quad \Delta s = 0 \quad \Delta l = \pm 1 \quad \Delta m = 0 \quad (1.8)$$

and for circularly polarized light

$$\Delta j = 0, \pm 1 \quad \Delta s = 0 \quad \Delta l = \pm 1 \quad \Delta m = \begin{cases} +1 & \text{left circular} \\ -1 & \text{right circular} \end{cases} \quad (1.9)$$

for the possible E1 transitions from an atomic-like core state of quantum numbers j, m, l and s according to the Wigner-Eckart theorem.

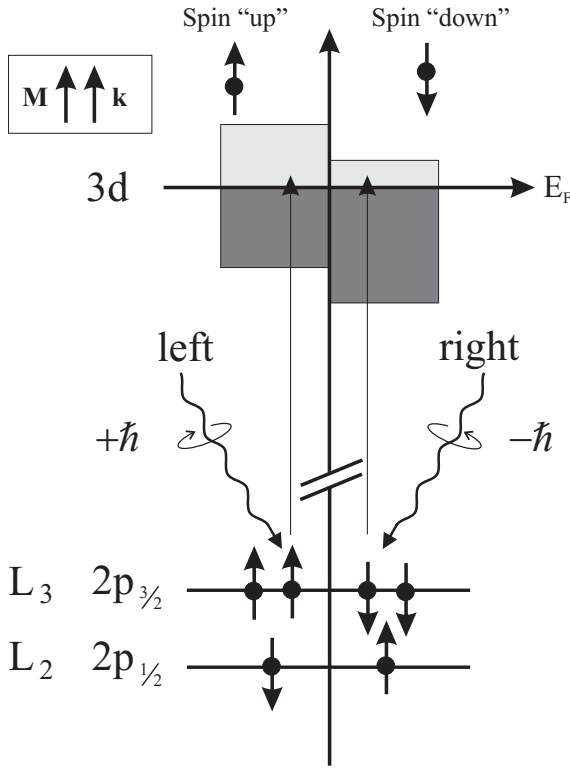


Figure 1.2: Schematic representation of the x-ray magnetic circular dichroism at the $L_{2,3}$ edges for $3d$ TM's. In the first step, the absorption of left (right) circularly polarized light leads to spin-up (spin-down) polarization of the photoelectrons at the L_3 edge via spin-orbit coupling ($j = l + s$) in the core level. In the second step, the d -valence band acts as a spin detector. Due to spin-conservation the left-circularly polarized light probes mainly the larger number of unoccupied spin-up d states with respect to direction of the magnetization \mathbf{M} . Hence, the absorption cross sections for the two helicities differ due to the imbalance of the spin-up and spin-down d valence band. The effect reverses at the L_2 edge due to the opposite spin-orbit coupling in the core level ($j = l - s$).

1.2 Theoretical models for XMCD

The two-step-model

The basic principle of the x-ray magnetic circular dichroism can be explained with a simple model as illustrated in Figure 1.2 for $3d$ TM's. The photoelectrons are excited from the initial states $L_3 : 2p_{3/2}$ and $L_2 : 2p_{1/2}$ that can be characterized by the quantum numbers j and m with $j = l + s$ and $j = l - s$, respectively. For evaluation of the matrix element it is useful to recast the dipole-operator in terms of spherical harmonics

$$\epsilon \mathbf{r} = \sqrt{\frac{4\pi}{3}} (\epsilon^0 Y_{10} + \epsilon^{+1} Y_{11} + \epsilon^{-1} Y_{1-1}) \cdot \mathbf{r} \quad (1.10)$$

where ϵ^0 corresponds to linearly polarized light. Following the definition in optics left (right) circularly polarized light corresponds to a $+\hbar$ ($-\hbar$) helicity with a polarization vector $\epsilon^{+1} = \frac{1}{\sqrt{2}} \{-\epsilon_x + i\epsilon_y\}$ ($\epsilon^{-1} = \frac{1}{\sqrt{2}} \{\epsilon_x + i\epsilon_y\}$).¹ The angular momentum

¹Thus, emission of left circularly polarized x-rays stems from electrons which rotate counter-clockwise (left) in a bending magnet with respect to the point of view of the sample.

Table 1.1: The angular part of the matrix elements for excitations from $2p$ core levels $|jm\rangle$ decomposed into $|l = 1, m_l, s = \frac{1}{2}, m_s\rangle$ and cataloged with respect to the spin and the circular polarization of the x-rays according to (1.11).

j, m	m_l, m_s	$I_{jm}^{+1}/\mathcal{R}^2$	$I_{jm}^{-1}/\mathcal{R}^2$
$\frac{3}{2}, +\frac{3}{2}$	$ +1 \uparrow\rangle$	$\left(\frac{2}{5}\right)_\uparrow$	$\left(\frac{1}{15}\right)_\uparrow$
$\frac{3}{2}, +\frac{1}{2}$	$\sqrt{\frac{1}{3}} +1 \downarrow\rangle + \sqrt{\frac{2}{3}} 0 \uparrow\rangle$	$\left(\frac{2}{15}\right)_\downarrow + \left(\frac{2}{15}\right)_\uparrow$	$\left(\frac{1}{45}\right)_\downarrow + \left(\frac{2}{15}\right)_\uparrow$
$\frac{3}{2}, -\frac{1}{2}$	$\sqrt{\frac{2}{3}} 0 \downarrow\rangle + \sqrt{\frac{1}{3}} -1 \uparrow\rangle$	$\left(\frac{2}{15}\right)_\downarrow + \left(\frac{1}{45}\right)_\uparrow$	$\left(\frac{2}{15}\right)_\downarrow + \left(\frac{2}{15}\right)_\uparrow$
$\frac{3}{2}, -\frac{3}{2}$	$ -1 \downarrow\rangle$	$\left(\frac{1}{15}\right)_\downarrow$	$\left(\frac{2}{5}\right)_\downarrow$
$\frac{1}{2}, +\frac{1}{2}$	$\sqrt{\frac{2}{3}} +1 \downarrow\rangle - \sqrt{\frac{1}{3}} 0 \uparrow\rangle$	$\left(\frac{4}{15}\right)_\downarrow + \left(\frac{1}{15}\right)_\uparrow$	$\left(\frac{2}{45}\right)_\downarrow + \left(\frac{1}{15}\right)_\uparrow$
$\frac{1}{2}, -\frac{1}{2}$	$\sqrt{\frac{1}{3}} 0 \downarrow\rangle - \sqrt{\frac{2}{3}} -1 \uparrow\rangle$	$\left(\frac{1}{15}\right)_\downarrow + \left(\frac{2}{45}\right)_\uparrow$	$\left(\frac{1}{15}\right)_\downarrow + \left(\frac{4}{15}\right)_\uparrow$

of the photon is sometimes called “photon spin” which is parallel (antiparallel) to the wave vector \mathbf{k} for $+\hbar$ ($-\hbar$).

Since the dipole-operator does not act on the spin-state the matrix element can be written with regard to l and m_l . According to the dipole selection rules the transitions occur from $2p$ states $|l, m_l\rangle$ into the $3d$ states with $|l + 1, m_l \pm 1\rangle$. Using the Wigner $3 - j$ symbols for the coupling of angular momenta the possible matrix elements are obtained from

$$\begin{aligned}
& \sqrt{\frac{4\pi}{3}} \langle l' = l + 1, m_l' = m_l \pm 1 | Y_{1\pm 1} | l, m_l \rangle \mathcal{R} \\
&= (-1)^{l-m_l} \sqrt{l+1} \begin{pmatrix} l+1 & 1 & l \\ -(m_l \pm 1) & \pm 1 & m_l \end{pmatrix} \mathcal{R} \\
&= -\sqrt{\frac{(l \pm m_l + 2)(l \pm m_l + 1)}{2(2l+3)(2l+1)}} \mathcal{R}
\end{aligned} \tag{1.11}$$

where the radial matrix element is given by

$$\mathcal{R} = \langle n', l + 1 | \epsilon^{\pm 1} \cdot r | n, l \rangle . \tag{1.12}$$

It is approximately constant for the considered transitions. The angular part of the

matrix elements

$$I_{jm}^{\pm 1}/\mathcal{R}^2 = \left| \sqrt{\frac{4\pi}{3}} \langle j', m' = m \pm 1 | Y_{1\pm 1} | j, m \rangle \right|^2 \quad (1.13)$$

is listed in Table 1.1 for the $|j, m\rangle$ sublevels with respect to the spin and the circular polarization of the x-rays. It shows that at the $2p_{3/2}$ ($j = l + s$) left circularly polarized light (photon-spin up) prefers excitations of spin-up photoelectrons whereas spin-down photoelectrons dominate the excitations with right circularly polarized light (photon-spin down). The resulting spin-polarization of the photoelectrons reverses for excitations from $2p_{1/2}$ states due to opposite spin-orbit coupling $j = l - s$. The creation of spin-polarized photoelectrons via the spin-orbit coupling in the initial states using circularly polarized light is the first step of the model, see Figure 1.2.

In the second step, the spin-polarization of the photoelectrons is revealed in case of an imbalance for the spin-up and spin-down electrons (equivalently holes) in the $3d$ valence band. In other words, the $3d$ valence band can be seen as a sensitive “spin-detector” of the spin-polarized photoelectrons. Setting the magnetization \mathbf{M} of the d band parallel to the direction of the wave vector \mathbf{k} , the occupation of the spin-down states is larger than the one of the spin-up states, or vice versa for the d -vacancies. Because of the spin-conservation, the photoelectrons excited from $2p_{3/2}$ ($2p_{1/2}$) by spin-up photons probe mostly the spin-up (spin-down) states above the Fermi-level. Hence, the absorption of left-circularly polarized x-rays will be enhanced at the L_3 edge and reduced at the L_2 edge with respect to the exchange-split $3d$ states. The opposite effect is expected for right circularly polarized light. This difference in the absorption is the x-ray magnetic circular dichroism. It is defined conventionally as

$$\Delta\mu(E) = \mu^+(E) - \mu^-(E), \quad (1.14)$$

i.e. the difference between the absorption of right and left circularly polarized x-rays with \mathbf{k} parallel to \mathbf{M} . Instead of changing the helicity of the x-rays one may also change the direction of the magnetization with respect to \mathbf{k} in order to obtain circular dichroism as it follows readily from abovementioned.

The resulting absorption spectra can be visualized using $I_{jm}^{\pm 1}$ of Table 1.1. In order to simulate the spectral shape of an XMCD spectrum an artificial exchange field H_{ex} is applied to the $2p$ core levels. H_{ex} lifts the degeneracy of the j, m sublevels representing some polarization of the core levels due to the exchange-split valence states and introduces an energy dispersion in the XMCD spectrum. It is useful to

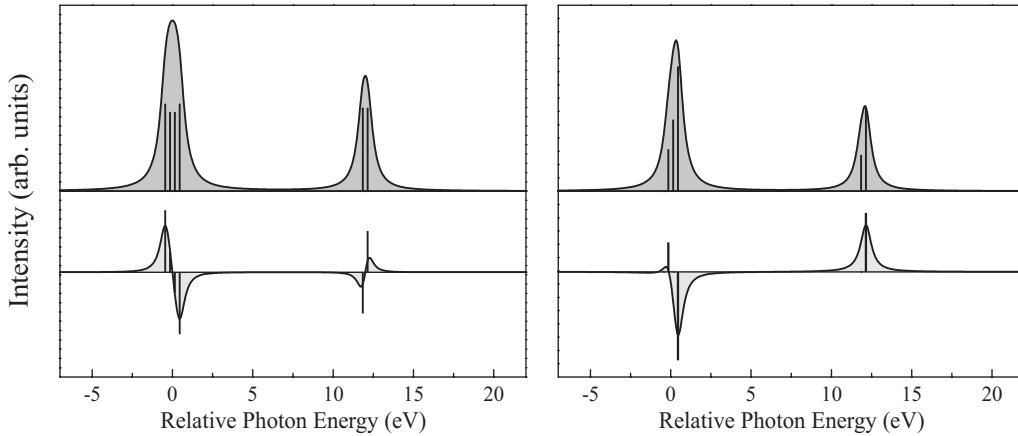


Figure 1.3: The isotropic absorption (above) and XMCD (below) is presented for two cases: (left) no exchange-splitting in the d valence states ($P_s^{3d} = 0$) leads to asymmetric line shapes of the circular dichroism while (right) symmetric peaks are obtained assuming the valence states 100% spin-polarized, i.e., the spin-up states are completely filled (Erskine-Stern model).

introduce the spin-polarization P_s^{3d} of the d band as

$$P_s^{3d} = \frac{n_h(\uparrow) - n_h(\downarrow)}{n_h(\uparrow) + n_h(\downarrow)} \quad (1.15)$$

where n_h denotes the number of d holes per atom. Two extreme cases are modeled and depicted in Figure 1.3: (i) The case of $P_s^{3d} = 0$ (non magnetized) results in fully asymmetric line shapes. The integral over each edge of the XMCD spectrum remains zero. Note that H_{ex} is actually also zero and therefore, in general no XMCD signal is revealed at all energies. The integrals over the average absorption spectrum are $\frac{8}{9}\mathcal{R}^2$ and $\frac{4}{9}\mathcal{R}^2$ for the $L_{2,3}$ edges, respectively. The L_3/L_2 ratio becomes then 2 : 1 corresponding to the manifold of the jm sublevels. The so-called *statistical branching ratio* refers to that value. (ii) In case of $P_s^{3d} = 1$ (only unoccupied spin-up d states are available, e.g. ferromagnetic Ni) the XMCD spectrum shows symmetric line shapes. In this case, the integral of $\Delta\mu$ for the L_3 and L_2 edge is $\frac{2}{9}\mathcal{R}^2$ and $-\frac{2}{9}\mathcal{R}^2$, respectively, and the L_3/L_2 ratio is for the XMCD spectrum -1:1. For the averaged spectrum the ratio corresponds again to the statistical one. These ratios are the ones derived by Erskine and Stern for ferromagnetic Ni in 1975 [40].

In general, the line shape of an XMCD spectrum varies depending on the P_s^{3d} : the XMCD signal shows dispersive-like peaks for small polarizations and symmetric peaks for high polarizations at the $L_{2,3}$ edges. A mixture of the two extrema illustrated in Figure 1.3 provides a graphical description of the overall XMCD signal

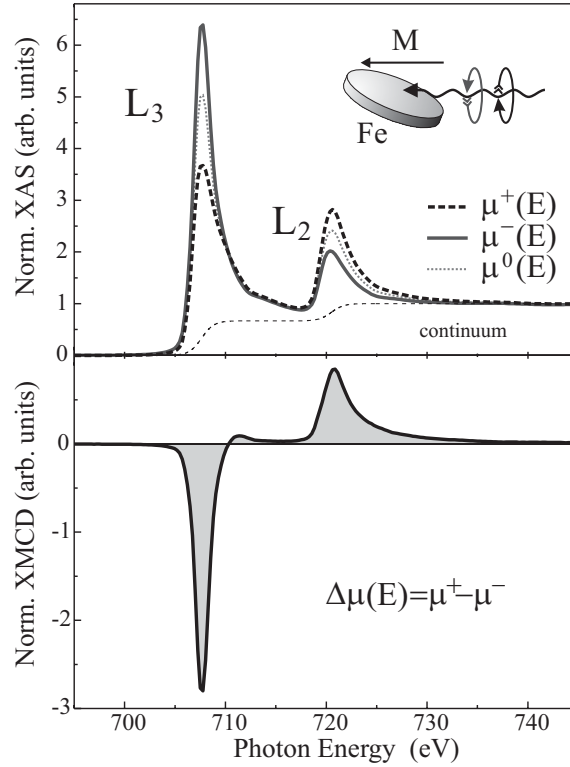


Figure 1.4: Experimental absorption spectra for (solid line) left, (dashed line) right circularly polarized light. The average over both polarizations and the XMCD spectrum is given as a dotted line (top) and solid line (bottom), respectively.

for the $3d$ TM's. However, these ratios obtained by the simplified two-step-model deviate from those observed in experimental XMCD spectra as shown, e.g., for Fe bulk in Figure 1.4. Even for Co and Ni with almost occupied $3d$ valence bands, the L_3/L_2 ratio in the XMCD spectrum deviates in favor of the L_3 contribution being more close to $-2 : 1$ (see chapter 3). This effect is attributed to the spin-orbit coupling in the final states. The stronger the spin-orbit coupling the more different d states are selected from the $2p_{3/2}$ and the $2p_{1/2}$ channels following the dipole selection rules. This is indicated in Figure 1.5 where the dipole-allowed transitions for left circularly polarized light ($+\hbar$) are drawn. Depending on the relative vacancies of the $3d_{3/2}$ and $3d_{5/2}$ sublevels the L_3/L_2 ratio of the polarization-averaged as well as of the XMCD spectrum changes, since the transitions from the L_2 edge are restricted to final states of $3d_{3/2}$ -character. Due to a lower energy of the $3d_{3/2}$ states a filling of the d valence states reduces their vacancies with regard to the $3d_{5/2}$ states and consequently enhances the intensities of the absorption spectra at the L_3 edge

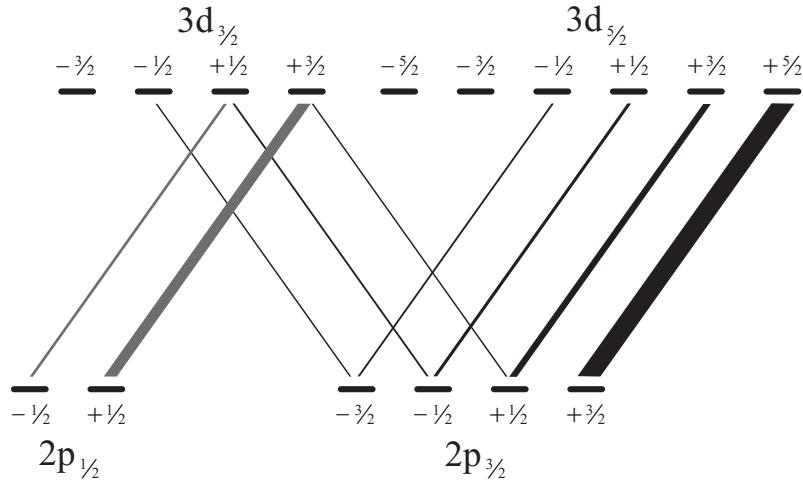


Figure 1.5: Dipole-allowed transitions from the initial $2p_{3/2}$ and $2p_{1/2}$ core states into the spin-orbit splitted $3d_{5/2}$ and $3d_{3/2}$ valence states adapted from [45]. The oscillator strengths are reflected by the thickness of the lines. Note that dipole-allowed transitions into $4s$ valence states are skipped in the sketch.

relative to the L_2 edge. In the limit of atomic Ni ($3d^9$ configuration) all $3d_{3/2}$ states are occupied leading to an absence of the resonance at the L_2 edge as it has been previously demonstrated by Gambardella and coworkers [44].

Magneto-optical sum rules

Magneto-optical sum rules were derived within a localized picture, i.e. single ions in a crystal field with a partly filled valence shell, by Thole and Carra and coworkers in 1992 and 1993 [2, 3]. Later, the sum rules were rederived within an independent particle approximation [46, 47]. These sum rules interrelate, under certain approximations, in a quantitative manner the integrated XMCD of a specific shell to the ground-state orbital and spin magnetic moment. For an excitation of a photoelectron from the core state $j^\pm = c \pm \frac{1}{2}$ into the valence shell $l = c \pm 1$ with n electrons, the transitions between pure initial and final states were taken into account, i.e. between the configurations $c^{4c+2}l^n$ and $c^{4c+1}l^{n+1}$.

The orbital sum rule states that the integral over both spin-orbit-splitted absorption cross sections j^\pm is proportional to the orbital magnetic moment $\mu_l = -\langle L_z \rangle$:

$$\frac{1}{N} \int_{j^+ + j^-} dE (I^+ - I^-) = \frac{1}{2} \frac{l(l+1) + 2 - c(c+1)}{l(l+1)(4l+2-n)} \langle L_z \rangle, \quad (1.16)$$

where

$$N = \int_{j^+ + j^-} dE(I^+ + I^- + I^0) \quad (1.17)$$

is the integral over the unpolarized absorption cross section. Note that $I_{j^\pm}^\pm(E) = \frac{1}{4\pi^2\alpha\hbar\omega}\sigma_{j^\pm}^\pm(E)$ is a normalized cross section, see Eq. (1.7). The normalization factor N ensures cancellation (approximation) of the radial part of the matrix element.

The spin sum rule yields that the spin moment $\mu_s = -2\langle S_z \rangle$ is proportional to the expression

$$\begin{aligned} \frac{1}{N} \left\{ \int_{j^+} dE(I^+ - I^-) - \frac{(c+1)}{c} \int_{j^-} dE(I^+ - I^-) \right\} &= \frac{l(l+1) - 2 - c(c+1)}{3c(4l+2-n)} \langle S_z \rangle \\ &+ \frac{l(l+1)[l(l+1) + 2c(c+1) + 4] - 3(c-1)^2(c+2)^2}{6lc(l+1)(4l+2-n)} \langle T_z \rangle \end{aligned} \quad (1.18)$$

where $\langle T_z \rangle$ is the magnetic dipole operator that corresponds to the asphericity of the charge density of the l valence shell. The operator is defined as

$$\mathbf{T} = \sum_i \mathbf{S}_i - 3 \frac{\mathbf{r}_i(\mathbf{r}_i \cdot \mathbf{S}_i)}{r_i^2}. \quad (1.19)$$

The magnetic properties of $3d$ TM's are probed at the $L_{2,3}$ edges. Using $c = 1$ ($2p$ core state) and considering only transitions into $3d$ final states $l = 2$ with the number of $3d$ holes $n_h = 4l + 2 - n$, the sum rules become readily

$$\langle L_z \rangle = \frac{2n_h}{N} \int_{j^+ + j^-} dE(I^+ - I^-) \quad (1.20)$$

$$2\langle S_z \rangle + 7\langle T_z \rangle = \frac{3n_h}{N} \left\{ \int_{j^+} dE(I^+ - I^-) - 2 \int_{j^-} dE(I^+ - I^-) \right\}. \quad (1.21)$$

Approximations of the sum rules Several approximations have been made deriving the spin and orbital sum rules. So far, the $2p-4s$ dipole-allowed transitions ($l = c - 1$) have been ignored for the $3d$ TM's. A mixture of the two transition channels $l = c \pm 1$ will hinder the application of the sum rules. However, the shallow $4s$ -band has a small density of states. Comparing the radial matrix elements for transitions into $3d$ - and $4s$ -like final states, one finds $\frac{\|\langle 4s|r|2p \rangle\|^2}{\|\langle 3d|r|2p \rangle\|^2} \approx \frac{1}{50}$. Hence, the transitions into the d -like valence states dominate to 98 % the absorption process at the $L_{2,3}$ edges and it allows for applying the sum rules concerning entirely $2p - 3d$ transitions. The sum rules are based on the assumption that transitions between pure configurations $c^{4c+2}l^n$ and $c^{4c+1}l^{n+1}$ occur. Apart from free atoms the initial

and final states cannot in principle be described by pure configurations (no intershell interaction) but one needs to account for configuration interactions. The question whether the sum rules solely apply to rigorous atomic systems or are applicable to itinerant magnets has been given by Guo [10] rederiving the sum rules under similar approximations [2,3] in the framework of *ab initio* spin-polarized relativistic multiple-scattering theory that is appropriate for metallic systems.

It is assumed that normalizing the sum rules with N ensures cancellation of the radial matrix element, i.e. the radial matrix element is taken constant. Indeed the radial matrix element is energy- and spin-dependent as shown for the $L_{2,3}$ edges of the rare earth elements [48] and needs to be considered when applying the sum rules [49]. Calculations by Wu *et al.* [5] have shown for the transition metal Ni that the radial matrix element increases linearly with energy from the bottom to the top of the d band by 30 %. Hereby, the spin-orbit coupling of the photoelectron is found to be proportional to the radial matrix element. Since the orbital moment is proportional to the spin-orbit coupling energy the variation does not affect the orbital sum rule. However, energy-dependent radial matrix elements are in conflict with the validation of the spin sum rule [5].

The calculated absorption spectra of $3d$ transition ions and their related magnetic moments based on multiplet theory have revealed that the sum rules are verified [8]. However, appropriate *ab initio* spin-polarized relativistic band-structure calculations for $3d$ transition metals indicate that the values obtained from the sum rule analysis differ from the related magnetic moments [4–6, 50, 51]. The orbital sum rule was found to be accurate within 10 % [4, 5]. The spin sum rule can deviate between 15 % to 40 % for the bulk ferromagnets Fe and Ni, respectively. The origin of the failure of the sum rules for itinerant magnets is related to the ambiguity in the choice of the integration range and the definition of the number of d holes. Therefore, Wu and coworkers proposed to use another sum rule [5] that avoids these problems by taking the ratio of the orbital and spin sum rules (Eqn. (1.20) and (1.21))

$$\frac{\langle L_z \rangle}{2 \langle S_z \rangle + 7 \langle T_z \rangle} = \frac{2 \int_{j^+ + j^-} dE (I^+ - I^-)}{3 \int_{j^+} dE (I^+ - I^-) - 2 \int_{j^-} dE (I^+ - I^-)}. \quad (1.22)$$

The orbital to spin moment ratio² is found to be accurate within 10 % for the ferromagnets Fe, Co and Ni.

²Note that the magnetic dipole operator must be known. By angular-dependent absorption measurements the magnetic dipole operator can be experimentally disentangled in the spin sum rule [52].

Finally, another important assumption is that the two transition channels j^\pm , i.e. $L_{2,3}$ edges, do not interfere. In other words, the core hole must be denoted by well defined quantum numbers jm . This assumption is satisfied when the spin-orbit coupling in the core hole ξ_c is large compared to other interactions. However, as demonstrated by Teramura *et al.* this is not the case going towards the early 3d TM's where strong core hole interaction [31, 32] redistributes the $L_{2,3}$ transition channels leading to considerable disagreement of the spin values obtained from the sum rule analysis (between 8 % to 30 % for Ni and Mn ions, respectively). This effect has been encountered and systematically analyzed in the present work [53] and is discussed in chapter 3. One finds deviations up to 80 % of the spin moment value (Ti and V) indicating the breakdown of the spin sum rule.

Multipole moment analysis (MMA)

The concept of the Multipole Moment Analysis (MMA), realized recently by van der Laan in Ref. [54], is to describe the spectral shape of the XMCD spectra. Contrary to the magneto-optical sum rules, where one relates areas to certain ground-state moments, one may analyze their influence on the spectral distribution. As shown for the simple two-step model, one can calculate the probability for creating a core hole jm with certain ground-state properties of the 3d valence band. The latter are represented by the multipole moments $\langle \underline{w}^{xyz} \rangle$ where the orbital moment x and spin moment y couple to the total moment z [55, 56]:

$$\begin{aligned} \underline{w}^{000} &= n_h, & \underline{w}^{101} &= L_z/2, & \underline{w}^{011} &= 2S_z, \\ \underline{w}^{110} &= -\sum_i l_i \cdot s_i, & \underline{w}^{202} &= -Q_{zz}/2, & \underline{w}^{211} &= 7T_z/2, \end{aligned}$$

where $\langle \underline{w}^{xyz} \rangle \equiv (-1)^z$ is normalized per hole and Q_{ij} is the quadrupole moment of the charge distribution. The resulting intensities I_{jm}^a for the creation of a core hole jm can be expressed in terms of $\langle \underline{w}^{xyz} \rangle$

$$I_{jm}^a = \sum_{xyz} \langle \underline{w}^{xyz} \rangle \sum_r C_j^{xyzar} u_{jm}^r \quad (1.23)$$

with $a = 0$, and 1 for the isotropic XAS and XMCD, respectively, and

$$u_{jm}^r = (2r+1)(-1)^{j-m} \begin{pmatrix} j & r & j \\ -j & 0 & j \end{pmatrix} \begin{pmatrix} j & r & j \\ -m & 0 & m \end{pmatrix} \quad (1.24)$$

using the Wigner $3-j$ symbols for the coupling of the angular momenta. The coefficients C_j^{xyza} can be derived from the transition matrix element. They are

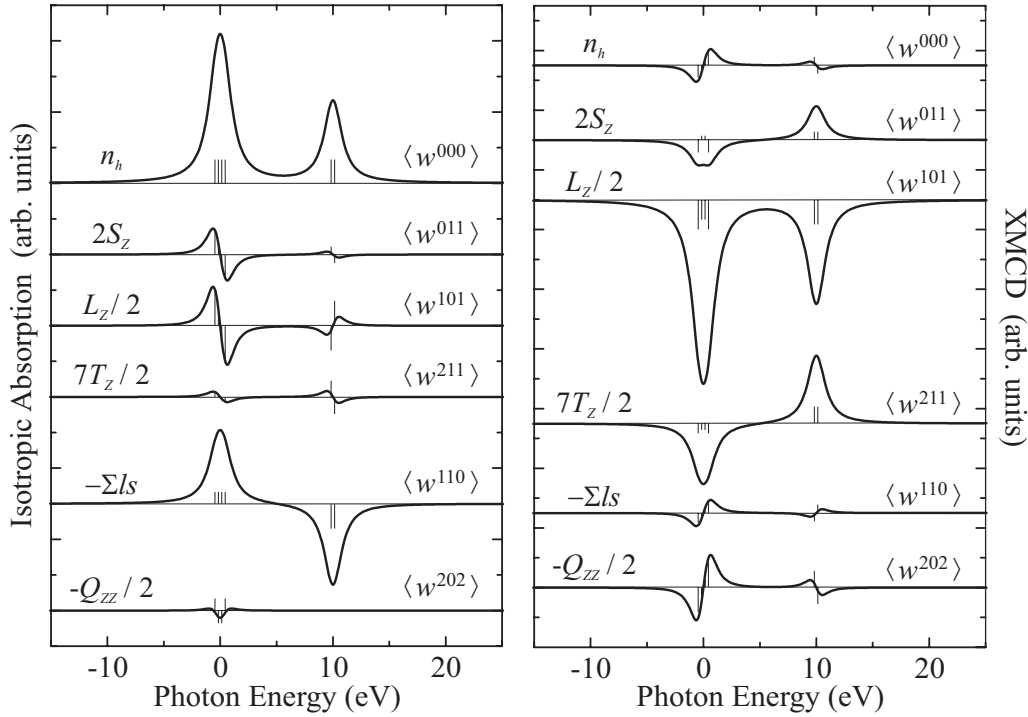


Figure 1.6: (left) The isotropic XAS and (right) XMCD spectra for various ground-state moments adapted from Ref. [54]. The degeneracy of the $2p$ core levels (core splitting: $\frac{3}{2}\xi_c = 10$ eV) is lifted by an effective exchange field H_{ex} . The intensities of the jm sublevels are indicated by the vertical lines.

determined and presented in Ref. [54]. The intensity for each jm level can be calculated from Eqs. (1.23) and (1.24). In appendix C corresponding Tables are provided for the isotropic ($a = 0$) and dichroic ($a = 1$) absorption spectra together with the coefficients C_j^{xyza} of Ref. [54].

In Fig. 1.6 (left) the isotropic XAS and (right) the XMCD spectra for the various ground-state moments are presented. The final XAS and XMCD spectra are obtained by summation over all the contributions of the ground-state moments. For the isotropic XAS of $3d$ TM's, the most important ones are the number of holes $\langle w^{000} \rangle$, the spin moment $\langle w^{011} \rangle$ and the spin-orbit coupling in the $3d$ valence states $\langle w^{110} \rangle$. The spectrum of $\langle w^{000} \rangle$ reflects the statistical branching ratio 2 : 1 of the $L_{2,3}$ edges. One sees from the spectral distribution of $\langle w^{110} \rangle$ that the spin-orbit coupling transfers spectral weight between the $L_{2,3}$ edges, thus, changing the branching ratio. This relation between spin-orbit coupling and the branching ratio is well understood and has been reported and analyzed in detail [57]. The spin moment

changes the peak asymmetry ($\langle \underline{w}^{011} \rangle$) of the XAS spectrum but does not change the relative $L_{2,3}$ weights. For the XMCD of $3d$ TM's, the most important ones are the spin moment $\langle \underline{w}^{011} \rangle$, the orbital moment $\langle \underline{w}^{101} \rangle$, and the number of holes $\langle \underline{w}^{000} \rangle$. In analogy to the discussion of the isotropic XAS, the XMCD spectrum of the spin moment $\langle \underline{w}^{011} \rangle$ reflects the ratio $-1 : 1$ of the $L_{2,3}$ edges in agreement with the simple two-step model. The orbital moment $\langle \underline{w}^{101} \rangle$ transfers spectral weight from the L_2 to the L_3 edge in the XMCD spectrum. Complementary to the role of the spin moment for the XAS line shape, the number of holes $\langle \underline{w}^{000} \rangle$ modifies the peak asymmetry of the XMCD spectrum but does not influence the relative $L_{2,3}$ weights. Hence, according to the definition of the spin-polarization of the $3d$ valence band (Eq. (1.15)), one expects symmetric XMCD peaks for the ferromagnets Fe, Co and Ni (large spin-polarization) and asymmetric XMCD peaks for the early $3d$ TM's (small spin-polarization) in agreement with the experimental observation, see chapter 3.

It is valuable to note that the isotropic XAS and XMCD spectra satisfy the magneto-optical sum rules discussed in the previous section. The integration over both edges of the XAS and the XMCD spectrum gives the number of holes $\langle \underline{w}^{000} \rangle$ (hole count) and the orbital moment $\langle \underline{w}^{101} \rangle$ (orbital sum rule), respectively. This is due to the fact that the other ground-state moments have either an asymmetric distribution or opposite contributions at the L_3 and L_2 edge that cancel each other (see Fig. 1.6). The spin moment (spin sum rule) is obtained by integrating over $L_{2,3}$ weighted differences. Accordingly, the spin and orbital sum rules can be readily rederived using $\int u_{jm}^r = \delta_{r0}$ and C_j^{xyzar} from Table C.2:

$$\begin{aligned}
 N &= \int_{j^++j^-} dE(I_{jm}^0) = 3 \langle \underline{w}^{000} \rangle = 3n_h & (1.25) \\
 \frac{3n_h}{N} \int_{j^++j^-} dE(I_{jm}^1) &= 3 \langle \underline{w}^{101} \rangle = \frac{3}{2} \langle L_z \rangle \\
 \frac{3n_h}{N} \left\{ \int_{j^+} dE(I_{jm}^1) - 2 \int_{j^-} dE(I_{jm}^1) \right\} &= \langle \underline{w}^{011} \rangle + 2 \langle \underline{w}^{211} \rangle = 2 \langle S_z \rangle + 7 \langle T_z \rangle
 \end{aligned}$$

Since the $L_{2,3}$ edges partly overlap in the XMCD spectra of the early $3d$ TM's it has been proposed to analyze the spectral shape with the MMA in order to circumvent the problematic of deconvoluting the $L_{2,3}$ edges [58, 59]. However, as it will be in chapter 3 demonstrated, the XAS and XMCD spectra of early $3d$ TM's suffer from core hole correlation effects resulting in the breakdown of the spin sum rule. Therefore, the results of the MMA analysis appear highly suspect. The validity of this approach is tested in sec. 3.4.

1.3 Analysis of experimental data

Normalization of the absorption spectra

The absorption measurements by means of the total electron yield (TEY) are proportional to the absorption cross section $\sigma_{j\pm}^{\pm}(E)$ times the photon energy. The required energy-range for the XMCD spectra, which is for the $3d$ TM's of the order of the spin-orbit splitting of the $L_{2,3}$ edges, is small compared to the photon energy of the $L_{2,3}$ thresholds. Hence, the direct relation of TEY and $\sigma_{j\pm}^{\pm}(E)$ is well satisfied. In order to rule out artificial magnetic backgrounds in the XMCD spectra, absorption measurements were carried out for the possible orientations $(H, P_{\hbar\omega})$ of the magnetization (or external magnetic field) and the helicity of the x-rays, i.e. $\mu^+(+, +)$, $\mu^-(+, -)$, $\mu^+(-, -)$ and $\mu^-(-, +)$. Each XMCD pair is checked for drop-ins from the detector or the experimental setup and for estimating the statistical error of the measurements before adding up the collected data. Then the absorption spectra μ^+ and μ^- are normalized to unity just below the L_3 threshold. The XMCD spectra, $\Delta\mu$, may reveal an artificial magnetic offset above the L_2 edge due to the detection system or stray fields. Such magnetic offsets were corrected and the spectra were considered for further analysis if the deviation appears linear in energy and is smaller than 1 % of the XMCD signal. In most of the cases the XMCD pairs revealed much smaller magnetic offsets (if any). Note that the XMCD spectrum does not necessarily become zero above the $L_{2,3}$ edges. The XMCD signal in the continuum range is determined by spin-dependent scattering processes of the photoelectron (MEXAFS) [60] and could give large contribution to the $L_{2,3}$ XMCD signal of rare earth's [42, 49]. However, for the transition metals the MEXAFS signal is two orders of magnitude smaller than the XMCD response at the $L_{2,3}$ resonances. The μ^+ and μ^- spectra are renormalized in the continuum region to unity after subtracting a linear background from the absorption spectra. Hence, the experimental absorption spectra in Fig. 1.7 become independent of the edge-jump related to the film thickness and are comparable on a per-atom basis.

Saturation effects and degree of circular polarization

The rigorous proportionality between TEY and the absorption cross section is realized if the attenuation length of the incident photons $1/\mu(E)$ is much larger than the electron escape depth λ_{e^-} . However, the condition $1/\mu(E) \sim \lambda_{e^-}$ arises under

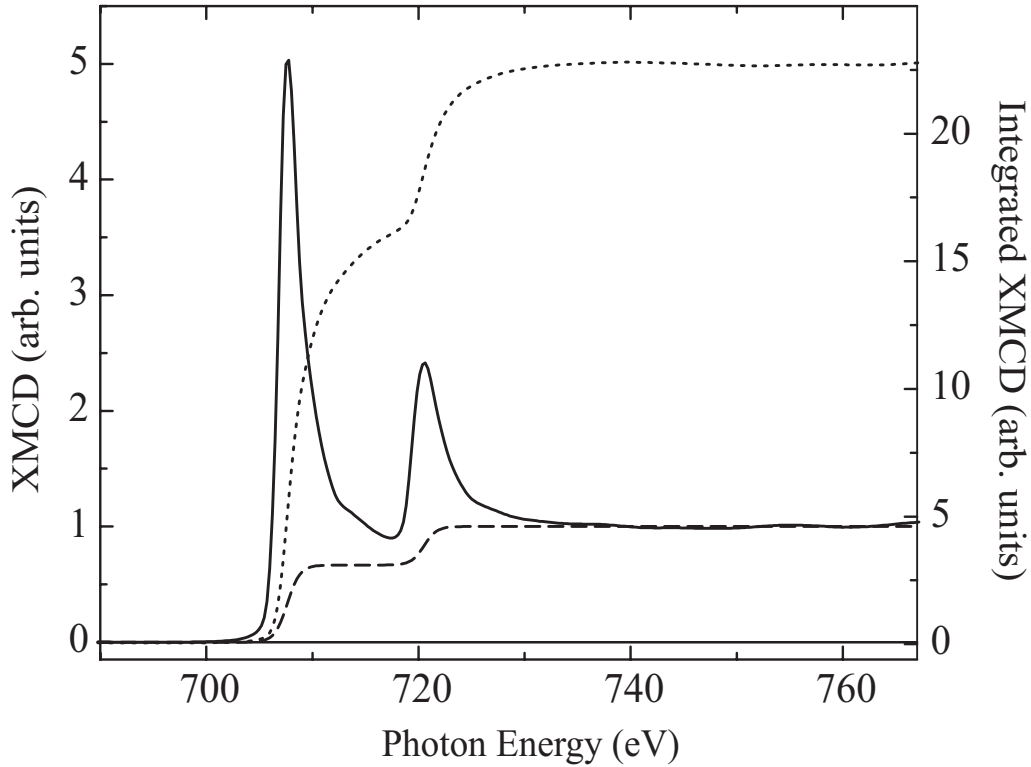


Figure 1.7: The $L_{2,3}$ isotropic spectrum (solid line) of Fe and the simulation of the continuum contribution (dashed line) by the step-function. The dotted curve indicate the integral of the XAS spectrum after removal of the continuum.

glancing angles and the absorption spectra suffer from self-absorption [61–64]. The saturation effects can be corrected as it is shown in appendix B. Moreover, the spectra have to be corrected for the degree of the circular polarization P_c provided by the beamline especially when P_c depends on the photon energy. The angle ϕ between the wave vector \mathbf{k} and the magnetization \mathbf{M} (or external field \mathbf{H}) has to be corrected to parallel alignment ($\phi = 0$). The corrections allow finally to compare absorption spectra with one another in literature. Alternatively, one may account for P_c (constant) and $\cos \phi$ as prefactors in the sum rules.

Removal of the continuum

For the application of the sum rules it is necessary to remove the contribution of photoelectron excitations into continuum states from the absorption cross section. It is common to use an *ad hoc* step function [7] as shown in Fig. 1.7 for the removal of the continuum. The simulation of the continuum remains, however, rather ap-

proximative and consequently, systematic errors are introduced by the removal in particular for Ni which has low $L_{2,3}$ absorption intensities according to the small number of d holes. There is some arbitrariness in the choice of the energy position of the continuum onset. A recent theoretical work provide the underlying continuum spectrum [65] and helps for a better simulation of the continuum with the step function, see e.g. [66].

Integration range and hole count

The integration range should ideally be infinite. In the analysis, the integration range is set from just below the L_3 edge to ~ 40 eV above the L_2 edge where the integrals approach their saturation values in Fig. 1.7 and Fig. 1.8. The integral N , Eq. (1.17), should be performed over the sum of ϵ^0 -, ϵ^+ - and ϵ^- -polarized absorption spectra which is the isotropic absorption spectrum according to Eq. (1.10). Because the effect of x-ray magnetic linear dichroism (XMLD) is orders of magnitude smaller than XMCD in metallic solids, it is justified to approximate the circular-averaged absorption spectrum, $\mu^+ + \mu^-$, with the isotropic one. In this work, it is called the isotropic absorption spectrum for convenience. The number of d holes n_h is taken from theory. While a deconvolution of the $L_{2,3}$ edges (j^\pm) is not required for the orbital sum rule, they need to be separated for the spin sum rule. In case of the late $3d$ TM's the separation of j^\pm can be performed without difficulties because the spin-orbit splitting of the core states is large enough. The deconvolution becomes subsequently problematic going towards the early $3d$ TM's. Here, a deconvolution can be performed with the help of calculated absorption spectra. As an example, a crude energy cut-off at the onset of the L_2 edge introduces a systematic error of about 15 % for the spin moment in case of V (see sec. 3.2) as estimated with the help of theoretical $L_{2,3}$ XMCD spectra.

Magnetic dipole operator

For the determination of the spin moment one needs to know the expectation value of the magnetic dipole operator $\langle T_z \rangle$. The $\langle T_z \rangle$ term is a measure of the anisotropy of the spin density (Eq. (1.19)) and can be written as $T_i = \sum_j Q_{ij} S_j$ where Q reflects the charge and S the spin components. This term appears (even though the spin is isotropic) because the spin couples to the spatial space through the spin-orbit coupling. However, the influence of spin-orbit coupling on $\langle T_z \rangle$ can be neglected

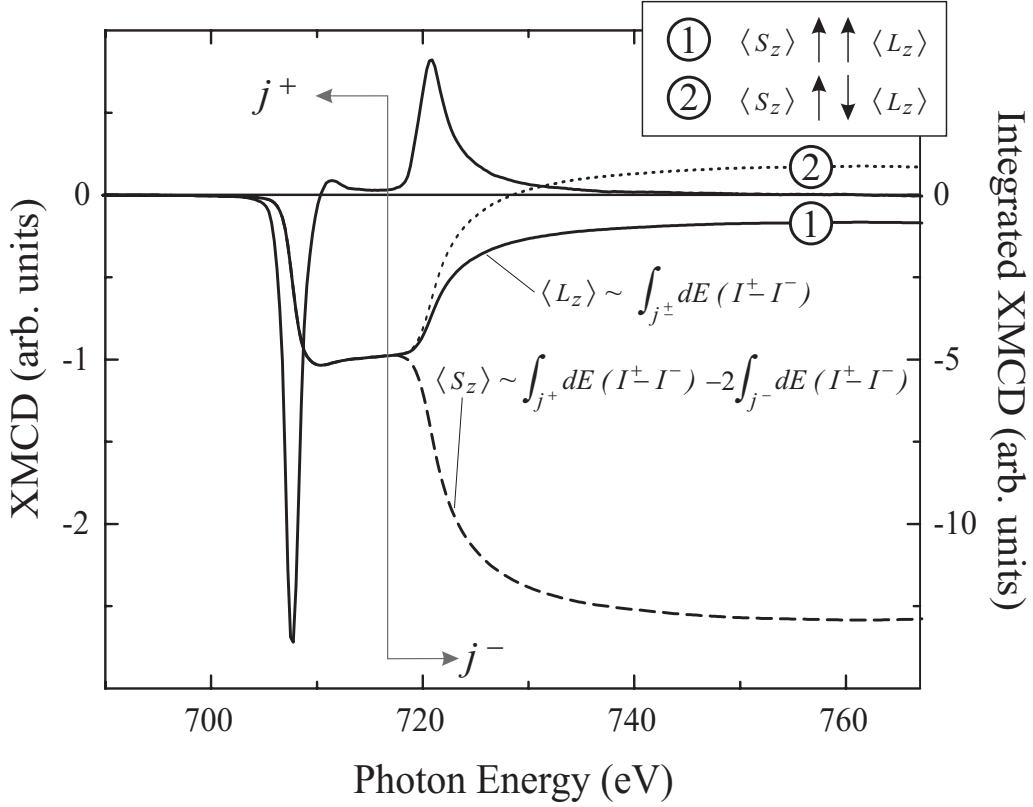


Figure 1.8: The $L_{2,3}$ XMCD spectrum for Fe and the integral of the XMCD according to the orbital (solid line) and spin (dashed line) sum rule. The vertical line shows the separation energy of the L_3 (j^+) and L_2 (j^-) edge for the spin integral. The hypothetical orbital integral (dotted line) for Fe would indicate an antiparallel alignment of the orbital and spin moment, for detail see text.

for the metallic systems (weak spin-orbit coupling). This allows to decouple the spin and the charge [52] and the magnetic dipole operator can be rewritten as $\langle T_i \rangle = \langle S_i \rangle \cdot \langle Q_{ii} \rangle$ for cubic symmetry. As a consequence, the application of the spin sum rule (Eq. (1.21)) to the absorption spectrum measured along the direction i yields

$$\left[2 \langle S_i \rangle \left(1 + \frac{7}{2} \langle Q_{ii} \rangle \right) \right].$$

Since Q_{ii} is a tensor with vanishing trace ($Q_{xx} + Q_{yy} + Q_{zz} = 0$), the spin moment can be determined by averaging the sum rule results for three orthogonal directions or by measuring the XMCD spectrum under a magic angle [52, 67]. Depending on the investigated system, large magnetic field must be supplied in order to ensure magnetic saturation along the directions i of the sample. While for cubic symme-

try the $\langle T_z \rangle$ term can be neglected, its contribution increases subsequently with lowering the symmetry or reducing the dimensionality of the magnetic system e.g., surfaces/interfaces of magnetic nanostructures [68] or magnetic nanowires [69]. On the other hand, the condition $\sum_i \langle T_i \rangle = 0$ is no longer fulfilled when the influence of the spin-orbit coupling increases as theoretically shown for magnetic monatomic chains [70, 71].

Orbital to spin moment ratio

Part of the problems related to integration range and hole count can be tackled by dividing the orbital by the spin sum rule. Here, one does not need to evaluate the integral N that relies on the choice of the integration range and the simulation of the continuum. Furthermore, n_h , P_c and ϕ are not required for determination of the orbital to spin moment ratio μ_l / μ_s . It has been demonstrated theoretically [4] as well as experimentally [7] that the error stays within 10 % for the ferromagnets Fe, Co and Ni. Note that the problem of the magnetic dipole term in the spin sum rule remains. Sometimes an effective ratio μ_l / μ_s^{eff} is introduced indicating that the ratio has to be corrected for $\langle T_z \rangle$. The value of μ_l / μ_s is basically given by the ratio $R = \int_{j-} dE(I^+ - I^-) / \int_{j+} dE(I^+ - I^-)$, i.e. the ratio of the $L_{2,3}$ XMCD areas. If $\langle T_z \rangle$ is negligible then

$$\frac{\mu_l}{\mu_s} = \frac{2}{3} \frac{1+R}{1-2R} \begin{cases} -\infty < R < -1 & \mu_l / \mu_s < 0 & \mu_l, \mu_s \text{ antiparallel} \\ R = -1 & \mu_l / \mu_s = 0 & \mu_l \text{ quenched} \\ -1 < R < 0 & \mu_l / \mu_s > 0 & \mu_l, \mu_s \text{ parallel} . \end{cases} \quad (1.26)$$

Hence, the relative alignment of the orbital and spin moment can be concluded from the ratio R . Another way to visualize the orbital contribution is to look for the integral of the orbital sum rule. According to R , the orbital and spin moments are parallel aligned when the orbital integral does not cross the zero line illustrated in Fig. 1.8 for Fe (*case 1*). The orbital and spin moments of Fe would be antiparallel aligned if the orbital integral has a node (*case 2*). Indeed, the latter is observed for the early 3d TM's (see chapter 3 and 6).

1.4 Electronic and magnetic properties of 3d TM's

The transition metals are characterized by the d states which are successively filled across the series. Typical values for the important interactions are summarized in

Table 1.2: Typical values for the most important interactions for the 3d TM's [67].

Interaction	Energy per atom (eV)
3d bandwidth / d hybridization	5
electrostatic and exchange interaction / multiplet splitting	0–2
magnetic exchange interaction	1
crystal field splitting	0.1
spin-orbit coupling	0.05

Table 1.2. The 3d band of these metals is about 5 eV broad and therefore, small in comparison with the sp bands where the electrons behave as nearly free electrons. Because of the small band width that holds up to 10 electrons per atom, the density of the d states is considerably increased. Since the 3d band encloses the Fermi level E_F , the corresponding Fermi surface is basically formed by the d states and differs from the quasi-spherical one of nearly free electrons.³ Hence, the electronic and magnetic properties of the transition metals are mostly governed by the d states.

One of the striking features of the 3d TM's is the occurrence of collective magnetism. While atoms with partially filled shells develop in general a magnetic moment, magnetism in pure solids is exceptional. The origin of the magnetic moments is the interplay of the Coulomb interaction and the Pauli principle which states that two electrons with parallel spins cannot occupy the same state. The electrons tend to couple their spins in parallel. This results in an antisymmetric spatial wave function for the electrons and therefore, minimizes their Coulomb repulsion.⁴ This argument is also formulated in the first Hund's rule which gives the ground-state spin moment for an incomplete filled shell of a free atom. In solids these electrons become delocalized and the gain of exchange energy must overcome the additional kinetic energy needed for parallel spin orientations. Therefore, the more the system becomes itinerant the smaller the tendency to reveal magnetic order. The presence of band-ferromagnetism for the 3d TM's Fe, Co, and Ni is due to the specific properties of the d band, i.e. the small band-width being ~ 5 eV and the large density of d states $\rho(E)$. A rigorous itinerant description of band-ferromagnetism is the Stoner

³The 3d states exhibit some localized character, i.e. the d electrons are not fully itinerant.

⁴With regard to the exchange interaction between two electrons the entire wave function of the electrons must be antisymmetric. Thus the electrons must form a symmetric spin function when their spatial wave function is antisymmetric, or *vice versa*.

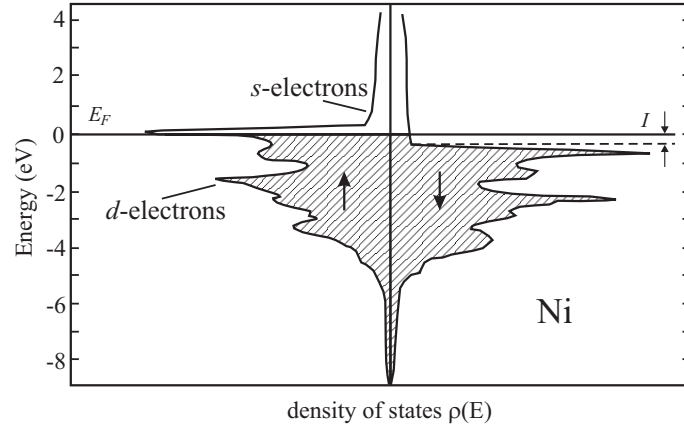


Figure 1.9: Calculated band structure for the 3d and 4s electrons for Ni, taken from Ref. [72].

model. The ferromagnetism is represented by a shift of the spin-up and spin-down d bands against each other. The difference I between the centers of gravity determines the exchange-splitting of the band. The so-called Stoner criterion $I\rho(E_F) \geq 1$ is met only at the end of the 3d series (Fe, Co and Ni) where $\rho(E_F)$ is large enough for ferromagnetic coupling of the spins without increasing the kinetic energy of the d electrons considerably, see Figure 1.9. The resulting spin magnetic moment is directly given by

$$\mu_s = (n_\uparrow - n_\downarrow)\mu_B, \quad (1.27)$$

i.e. as the difference between the occupation numbers for the spin-up (minority) and spin-down (majority) band. However, within this itinerant model the magnetization as well as the magnetic moment vanishes when I goes to zero, and the Stoner criterion overestimates the Curie temperature of the band ferromagnet. To account for the partly atomic character of the d electrons, a possible description of the collective magnetic order is to couple localized spins on the atomic sites i and j through an effective Hamiltonian. The Heisenberg model describes the coupling as $\mathcal{H} = -\frac{1}{2}\sum_{i,j} J_{ij}\mathbf{S}_i\mathbf{S}_j$ with the exchange integral J_{ij} being positive (negative) for ferromagnetic (antiferromagnetic) coupling. Contrary to the Stoner model the magnetic moment does not vanish at the Curie temperature but the ensemble of magnetic moments is disordered with a net magnetization equals zero (without an external field). A compromise for the description of the 3d band-ferromagnets might be finally the Hubbard model that combines localized features with the itinerant ones, see e.g. [73].

The entire magnetization of 3d ferromagnets is composed of several contribution: As revealed by theory [74, 75], the 4sp electrons have no orbital moment contribution, but they have a small contribution to the total spin moment with $\sim 5\%$. Furthermore, the magnetic moment of the d electrons consists to $\sim 90\%$ of the spin magnetic moment due to quenching of the orbital moment in cubic symmetry. Even though the orbital magnetism in bulk is small for the Fe, Co and Ni ferromagnets, it is fundamental for the understanding of the magnetic anisotropy. An exclusive spin system is isotropic, i.e. there exists no preferable quantization axis along a crystallographic direction. It is the shape-anisotropy and magneto-crystalline anisotropy that pins the spins to the spatial lattice. The easy-axis of magnetization is finally a result of the competition between these two contributions. While the origin of the shape-anisotropy is the classical magnetic dipole-dipole interaction determined by the external shape of the sample, the magneto-crystalline anisotropy arises from the relativistic spin-orbit coupling forcing the magnetic moment along a certain crystallographic direction. Concerning the latter, the orbital magnetism is of increasing relevance for the magnetic properties going from cubic symmetry in bulk materials towards low dimensional magnetic system, i.e. thin films, magnetic multilayers and nanostructures, which dominated the research of magnetism in the solid-state community for the last decades. With regard to this, XMCD provides access to both the spin and orbital moments. Moreover, one can study the induced magnetism in artificial layered structures of elements which are non-magnetic in their bulk configuration via the element-specificity of the technique.

Chapter 2

Experimental Details

The UHV-chamber [76] which has been used for the *in situ* sample-preparation and measurements at the synchrotron facility in Berlin (BESSY II) is equipped with turbomolecular-, iongetter- and titansublimation (TSP) pumps. The typical base pressure of the chamber is in the low 1×10^{-10} mbar. The cylinder-like chamber is divided into an upper and a lower part as indicated in the Figure 2.1. In the upper part the characterization and preparation of the samples are performed. A Cu(100) single crystal was used as a substrate for all the measurements carried out in this work. The Cu(100) surface was cleaned with a sputter gun by numerous cycles of Ar^+ bombardment under 45 degrees incidence and annealing the crystal up to 900 K (e^- bombardment at the rear of the sample). This procedure allows to heal the imperfection and roughness of the surface after the sputtering process [77]. The terraces are up to 3000 Å broad (line in Figure 2.2) indicating that the miscut of the crystal is less than 0.2 degrees. The films were prepared by evaporating from high-purity rods using a commercial triple e^- -beam evaporator. A special feature of this watercooled evaporator is that the high voltage can be applied individually for the three sources. This makes it possible to co-evaporate material for the preparation of alloys. The evaporation rate is controlled with a flux-monitor for each source. The pressure in the chamber during evaporation remains $2 - 5 \times 10^{-10}$ mbar depending on the deposited transition metal. The resulting film-deposition rates were of the order 1 Å per minute. The Cu surface and the films were characterized by means of low-energy electron diffraction (LEED) and Auger-electron spectroscopy (AES) using a cylindrical mirror analyzer (CMA). The thickness calibration of the films is done by AES and the $L_{2,3}$ edge jumps of the absorption spectra [64, 78].

The sample holder is mounted at the cooling tip of a lHe, IN_2 -flow cryostat,

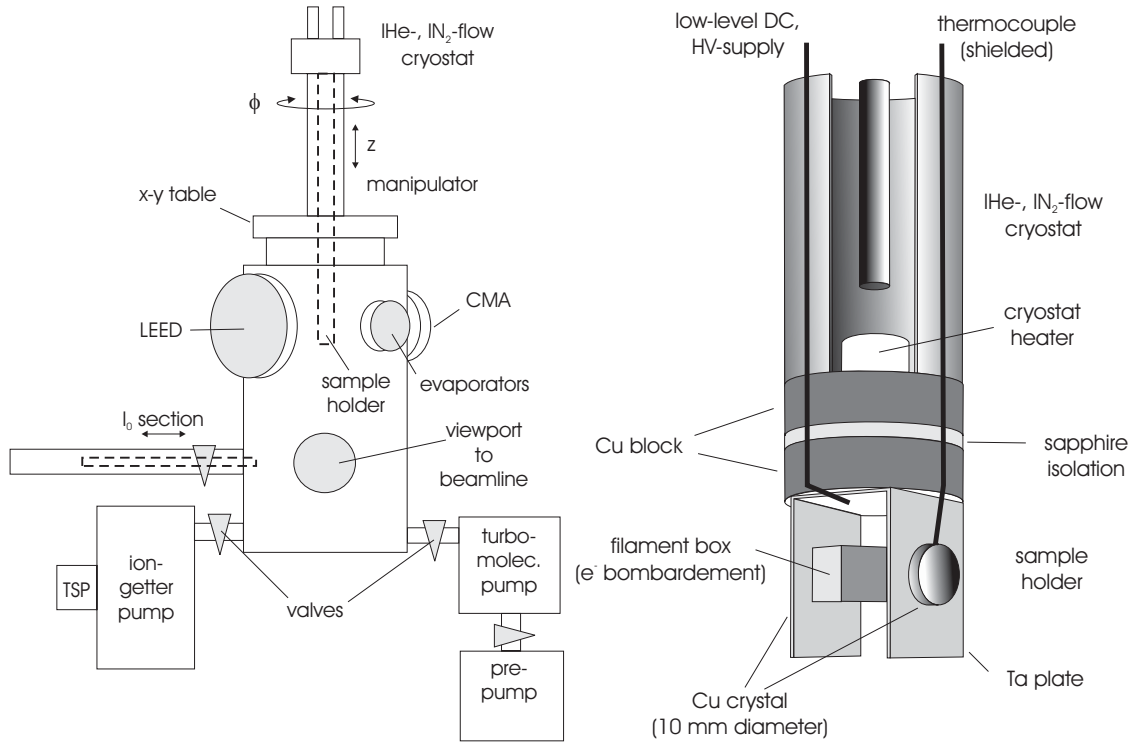


Figure 2.1: (left) Experimental setup of the UHV-chamber [76]. (right) The sample holder for low-level DC measurements.

Figure 2.1 on the right. The sample is electrically isolated ($R_{sample} > 200 \text{ G}\Omega$) required for the low-level DC measurements, see below. A sapphire plate is used for the isolation keeping a good thermal contact between the cryostat and the sample holder and for generating little charges under mechanical stress. In order to reduce vibrations (inducing electronic noise) during the cooling with IHe-flow the samples (max. two samples) are mounted on a robust 1.5 mm thick Ta plate. The temperature of the sample can be chosen between 25 – 300 K during the experiments. A commercial feedback heating system at the tip of the cryostat stabilizes the sample temperature (within 1 K). An alumel/chromel-thermocouple is directly plugged to the side of the crystal. In addition, the thermocouple is shielded against electronic noise with an aluminum foil for the low-level DC measurements of the sample.

The lower part of the chamber is used for the absorption measurements as illustrated in Figure 2.3. For the investigation of the magnetic properties the sample is irradiated with circularly polarized x-rays. The angle ϕ between the surface of the crystal and the wave-vector \mathbf{k} can be varied: $\phi = 90$ degrees is the geometry for measuring the out-of-plane component of sample magnetization \mathbf{M} , while the

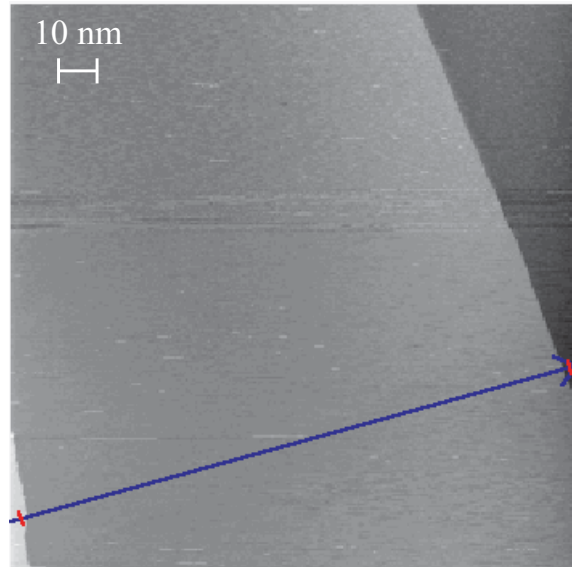


Figure 2.2: STM picture ($300 \times 300 \text{ nm}^2$) of the Cu(100) single crystal after sputtering and annealing up to 900 K.

sample is probed under $\phi = 20$ degrees incidence for in-plane magnetized samples. Therefore, the XMCD spectra investigated under glancing angles are corrected with regard to parallel alignment of \mathbf{k} and \mathbf{M} . In this work the absorption spectra were carried out with the total electron yield (TEY) detection mode by means of the sample photocurrent. It has been quantitatively demonstrated in [79, 80] that the total electron yield¹ is proportional to the absorption coefficient as long as the electron escape depth λ_{e^-} is much smaller than the absorption length $1/\mu(E)$. The equivalence of photocurrent and TEY has been proven in [81] for Ni and confirmed for the $3d$ TM's at the $L_{2,3}$ edges by TEY measurements using a microchannel-plate multiplier² below the sample. However, due to electronic drifts of the collector voltage and the HV-supply for the multiplier, it was preferable to measure the photocurrent, since the circular dichroism of the early $3d$ TM's Ti and V is $\leq 2\%$ of the absorption cross section. Contrary to the fluorescence yield, TEY is highly surface sensitive with respect to the small electron escape depth being $\sim 20 \text{ \AA}$ [63, 83, 84]. The attenuation length ($1/\mu(E)$) of x-rays ranges between 6000 \AA in the pre-edge range and 800 \AA after the $L_{2,3}$ resonant absorption for example for Co. Hence, the proportionality of the TEY and $\mu(E)$ is valid for $\phi = 90$ in excellent approximation. Saturation effects have to be considered when measuring TEY under grazing inci-

¹TEY consists of photoelectrons, Auger electrons and secondary electrons generated from inelastic scattering processes of the primary electrons.

²The channel-plate is located just below the positive bias-grid in Figure 2.3. For details see [82].

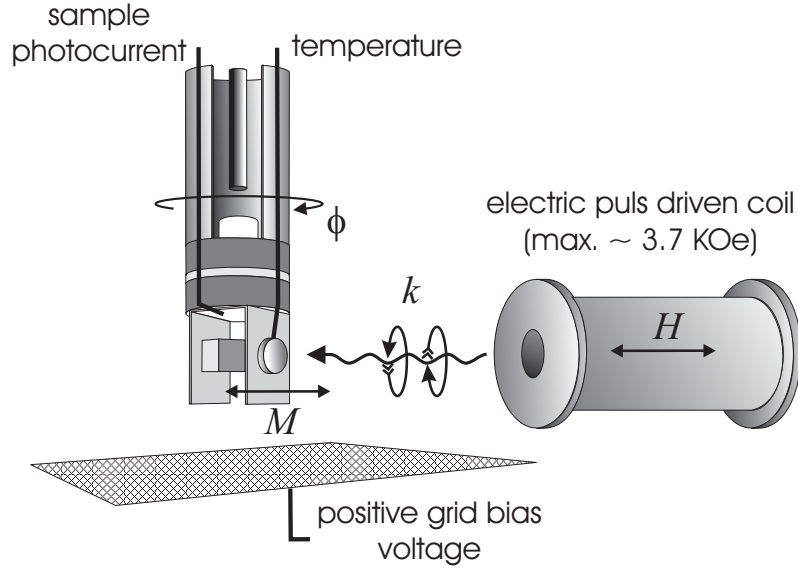


Figure 2.3: Experimental arrangement for the absorption measurements in total-electron-yield detection mode (TEY) probed by the photocurrent.

dence of the soft x-ray [61–64] when the condition $\lambda_e / \sin\phi \sim 1/\mu(E)$ is fulfilled. The saturation effects for single films, trilayers and multilayers were corrected with the SATEFF-code developed in this work, for details see appendix B.

The sample magnetization \mathbf{M} can be reversed by an electric pulse driven coil. The setup and calibration of the *in situ* coil can be found in [78]. At the position of the sample a maximum pulsed field of 3.7 kOe can be applied which was sufficient for the *in situ* samples in this work revealed by the field-independence of the XMCD spectra. In addition, measurements in small static magnetic fields are possible. Therefore, a positive bias grid (*extractor*) below the sample ensures proper operation of the photocurrent.

2.1 Measurements at BESSY II: UE56/1-PGM

The measurements for the *in situ* grown samples have been carried out at the insertion device beamline UE56/1-PGM of BESSY II. In contrast to dipole beamlines, the brilliance of the x-rays given by an undulator is several orders of magnitude higher. While a dipole produces a continuous x-ray spectrum, the undulator provides narrow intense peaks at certain energies, e.g., ~ 10 eV broad at 850 eV (3^{rd} harmonic, see Figure 2.5). The energy position is defined by the vertical gap between

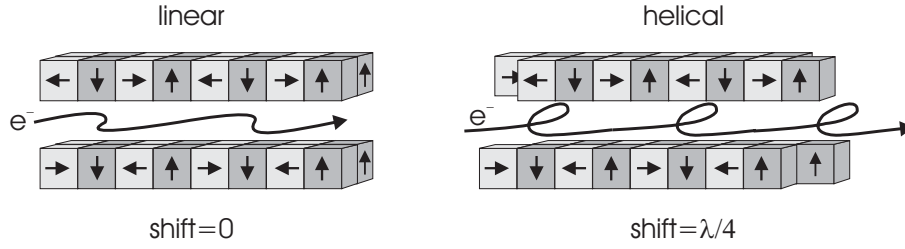


Figure 2.4: The arrangement of the magnet arrays with a period λ on the left hand side leads to oscillating trajectory of the electron bunch in the horizontal plane. Consequently, the emitted x-rays are 100 % linearly polarized in the horizontal plane. Shifting the magnet arrays as indicated on the right hand side by max. $\lambda/4$, forces the electron bunch on an elliptical or max. circular trajectory. The emitted x-rays are accordingly max. 100 % circularly polarized. Finally, the undulator provides vertically polarized x-rays when the shift is $\lambda/2$ (not shown).

the electron beam and the magnet arrays. The UE56/1 undulator of the APPLE-type is an elliptical polarizing insertion device. By shifting horizontally the separated magnet rows as illustrated in Figure 2.4, a helical magnetic field is generated that brings the electron bunch on an elliptical trajectory emitting elliptical ($P_c < 1.0$, 3^{rd} harmonic) polarized x-rays, for details see [85].

The beamline has a plane grating monochromator. The 1200 mm^{-1} grid was used for the measurements providing an energy-resolution ($E/\Delta E$) at 400 eV (900 eV) of about 9000 (7000). The exit slit of the beamline was $100 \mu\text{m}$ for all the experiments presented in this work. The narrow undulator peak at a certain energy limits the usage for absorption measurements even if they require only the near edge energy-range. Moreover, it is experimentally demonstrated in this work that the circular polarization degree P_c is highly energy-dependent (Figure 2.5). The solid squares correspond to the intensity at the L_3 edge energy of magnetic Ni bulk and the open circles show the correlated XMCD intensity. The energy-dependence is obtained by moving the gap relatively to the Ni L_3 edge. The problem can be tackled by driving both the monochromator and the undulator simultaneously for each data point. This so-called *gap-scan* technique can be optimized in two ways: (i) The first option is that the shift is constant and the gap and the monochromator are moving. Hereby, the energy-dependent photon flux can be maximized while consequently, P_c is changing. This option could be preferable for measurements at higher energies, e.g. Ni $L_{2,3}$ edges at $\sim 850 \text{ eV}$, where the photon flux decreases considerably for a large $P_c \sim 0.9$. (ii) The second option is to move both the shift and the gap together

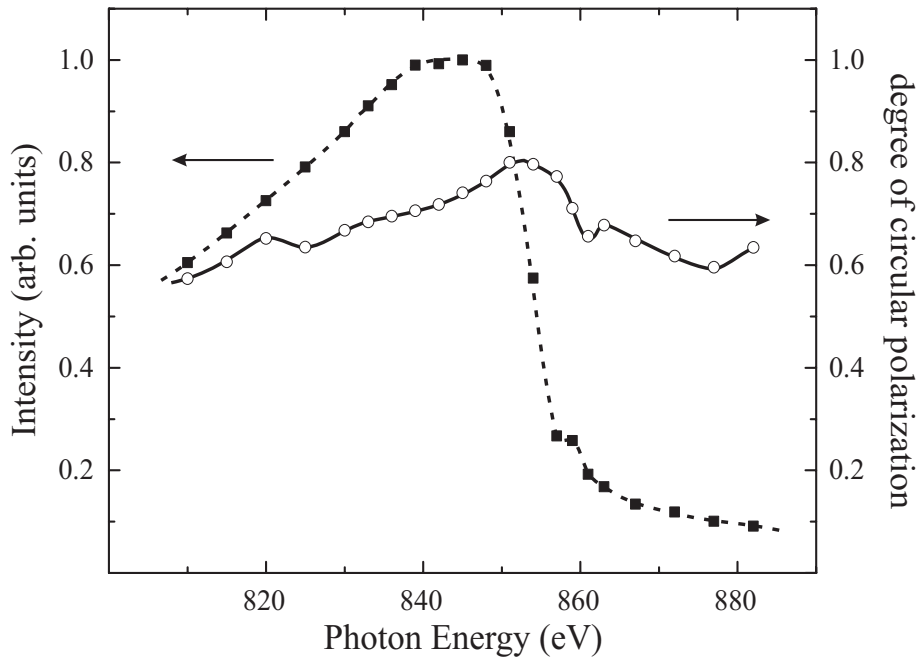


Figure 2.5: Photon flux (solid squares) and degree of circular polarization (open circles) as a function of the photon energy with fixed vertical undulator-gap.

with the monochromator. In this mode the undulator provides a constant $P_c = 0.9$ over the full energy-range.

Finally, the XMCD spectra are obtained both by reversing the magnetic field with the pulse-driven coil and by switching the helicity of the x-rays. Both methods are known to be equivalent due to time-reversal symmetry: The magnetic field direction as well as the polarization vector of the x-rays invert by time-reversal. The absorption spectra were divided by the photocurrent signal of a gold grid in order to remove the superposed background, originating from the transmission function of the beamline and from the photon-flux decay/noise of the storage ring. At least four XMCD pairs at given angle and temperature were measured for a sufficient signal to noise ratio and for exclusion of artificial structures in the absorption spectra.

2.2 Measurements at ESRF: ID8 (Former ID12B)

The measurements of the Fe_n/V_m superlattices (chapter 5) and the dilute $3d$ impurities in noble metal hosts (chapter 6) have been performed on the former ID12B and the ID8 beamline station, respectively, at the European synchrotron radiation

facility (ESRF) in Grenoble. The capabilities of the beamline station are the application of high magnetic fields up to 70 kOe and the adjustable temperature between 4–300 K. The samples are installed in a pre-chamber from which the samples were subsequently transferred to the experimental chamber. In case of the 3*d* impurities in Au and Cu, the samples were softly sputtered with Ar⁺ before the experiments until all traces of oxygen and compound formation were eliminated from the absorption spectra at the oxygen *K* edge and at the *L*_{2,3} edges of the 3*d* elements.

The insertion device is an Apple-type undulator (ID8) producing 100 % circularly polarized x-rays in a energy-range of 400–1500 eV, while the former HELIOS I undulator (500–8000 eV) provided a circular polarization degree of 80–90 % at ~ 800 eV. The monochromator is a Dragon-type spherical grating monochromator. Contrary to the gap-scan-technique at BESSY II, the undulator peak is positioned at an optimized energy (between the *L*_{2,3} edges) during the measurements. The spectra were measured via the TEY (photocurrent of the sample) and were normalized to the photon flux probed by the photocurrent of a gold grid. The absorption spectra for the possible orientations of the magnetic field and the photon helicity (++) , (+-), (- -), and (+ +) can be routinely collected. The field-dependent magnetization curves are measured at a fixed energy where the XMCD signal is maximal (typically at the *L*₃ edge).

Chapter 3

Absorption Fine Structure of Early $3d$ TM's

In this chapter the absorption fine structure of the x-ray magnetic circular dichroism has been studied in a systematic fashion (Fig. 3.1) for the early $3d$ TM's polarized in vicinity to the ferromagnet Fe. To study the magnetic properties of thin films and magnetic nanostructures, the determination of element-specific magnetic moments and the separation into their spin and orbital components (μ_s and μ_l) is one of the striking applications of XMCD. Concerning the spin and orbital magnetic moments of $3d$ TM's the magneto-optical sum rules [2,3] are most commonly applied. These interrelate in a quantitative manner the integrated XMCD of the d valence states to the ground-state orbital and spin magnetic moment (see sec. 1.2). Even though certain approximations limit the validity of the sum-rules ([9], sec. 1.2), it has been demonstrated that they can successfully be applied to the late $3d$ TM's, i.e. Fe and Co bulk metals [7]. In this way orbital and spin magnetism of thin films, multilayers, clusters and one-dimensional chains have been explored by means of XMCD, since most of the magnetic nanostructures are composed of the $3d$ ferromagnets Fe, Co, and Ni. In a similar manner XMCD was applied to the beginning of the $3d$ series, $4d$ and $5d$ elements in magnetic multilayers which usually show induced magnetic moments at an interface to a ferromagnetic layer [25, 89–93].

Contrary to the $4d$ and $5d$ TM's, the spin-orbit splitting of the core levels in $3d$ TM's is much lower ranging from ~ 6 eV to ~ 18 eV between Ti and Ni, respectively. This means accordingly that other interactions such as the electrostatic and exchange interaction between the core hole and the valence electrons may become important for the understanding of $L_{2,3}$ absorption spectra. Indeed, the statistical

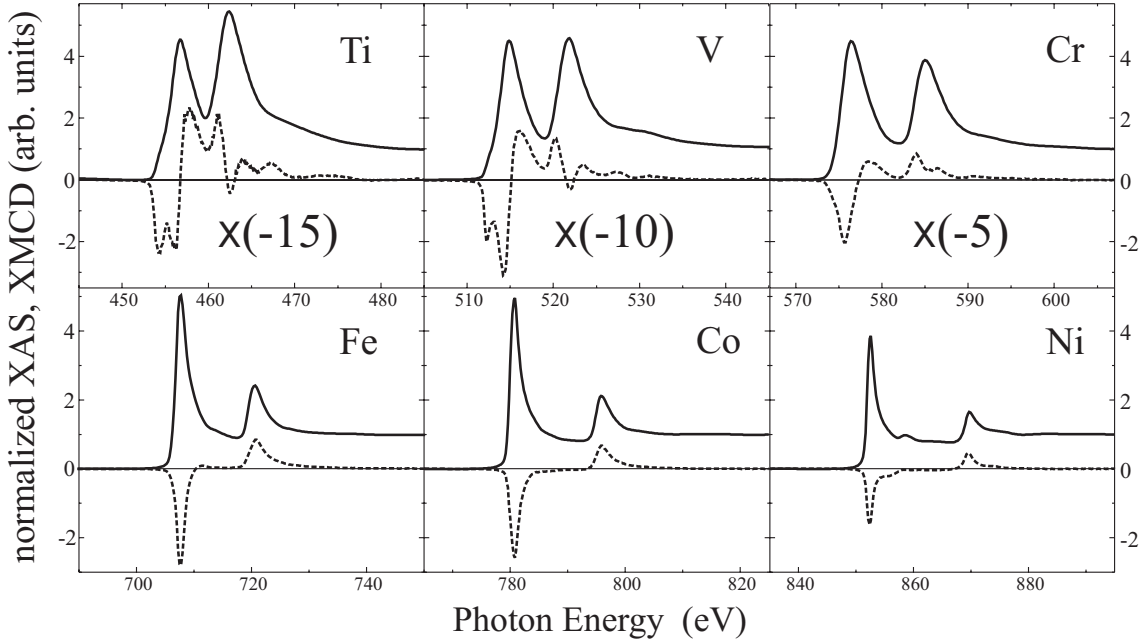


Figure 3.1: Normalized isotropic absorption spectra and corresponding XMCD spectra of the early $3d$ TM's in the upper panel versus the late $3d$ TM's, i.e. the ferromagnetic Fe, Co and Ni, in the lower panel. For clearer presentation of the systematics we have changed the sign of the XMCD spectra (please note the negative enlargement factors for Ti, V and Cr).

weights of the L_3 and the L_2 modifies going towards the early $3d$ TM's in favor of the L_2 edge (Figure 3.1). This effect is attributed to the electron core-hole interaction as revealed by several experimental [31,94–96] and theoretical studies [32–34,57,97] have revealed. However, a comprehensive theory is up to now not established that can describe the variation of the spectral L_3 and L_2 weights across the entire $3d$ metal series. Hereby, the absorption spectra of the early $3d$ TM's (upper row in Figure 3.1) are mostly affected by the presence of the core hole. In this chapter a simple theoretical model is introduced in order to determine the correlation energies of the electron core-hole interaction from experimental spectra. It will be demonstrated that the main effects in the absorption spectra are contained in this model. The deduced values for $3d$ metals were compared with atomic calculations [32] and can be used in the future as an input for theory to decide whether a theoretical model is appropriate or not for the description of the absorption spectra in *solids*. Moreover, a study of its likely influence on the spin-dependent absorption spectra was theoretically as well as experimentally up to now missing. Therefore, the XMCD spectra

particularly of the early $3d$ TM's have been investigated including Ti, which even suffers strongly from core hole effects (Figure 3.1). As a first step, the experimental data have been compared with fully-relativistic spin-polarized KKR calculations of the absorption spectra for the determination of the ground-state spin and orbital moments. By this comparison it was possible to address the observed features in the absorption fine structure of the early $3d$ TM's in Figure 3.1 to the electronic band structure and to correlation effects. The latter indicates the need for calculations of the $3d$ TM's-absorption spectra that take the electrostatic and exchange interactions of the d electrons and the core hole into account. By analyzing the XMCD spectra with the commonly used procedure it turned out that in particular the spin sum rule breaks down for the early $3d$ TM's suffering from the core hole correlation effects [99]. The derived values of the spin sum rule deviate between a factor 5 and a factor 2 for Ti and Cr, respectively, while they hold for Fe and Co within 10 %. As a result, the deviation of the spin sum rule and the variation of the spectral weight at the L_3 and L_2 edge have been correlated in a quantitative manner. Finally, an alternative approach to derive ground state moments from experimental spectra of $3d$ TM's by analyzing their spectral shape [54] has been tested.

3.1 Electron core-hole interaction

Isotropic absorption fine structure

The isotropic absorption spectra for part of the $3d$ series are presented in Figure 3.2. The dashed lines indicate the relative positions of the $L_{2,3}$ along the $3d$ series. The spin-orbit splitting in the core-states increases with the atomic number Z of the element and consequently, the $L_{2,3}$ absorption edges appear well separated for Fe, Co and Ni, while they strongly overlap for the early $3d$ TM's. As discussed in detail in sec. 1.2, the absorption at the L edges maps the density of d valence states above the Fermi level. Thus, one would expect that the resonant absorption intensity at the L_3 edge increase continuously towards the early $3d$ elements the larger the d vacancies. This behavior is found for the late $3d$ TM's, i.e. Ni, Co, and Fe, see Fig. 3.2. For the less-than-half filled d bands, however, the L_3 absorption intensities even slightly decreases. The behavior of the branching ratio for the $3d$ TM's has been discussed in several experimental [31, 94–96] and theoretical studies [32–34, 57, 97]. In a naive picture one expects the statistical ratio of 2:1 (sometimes called “ideal” branching ratio) for the spectral weights of the L_3 and L_2 edges according to the

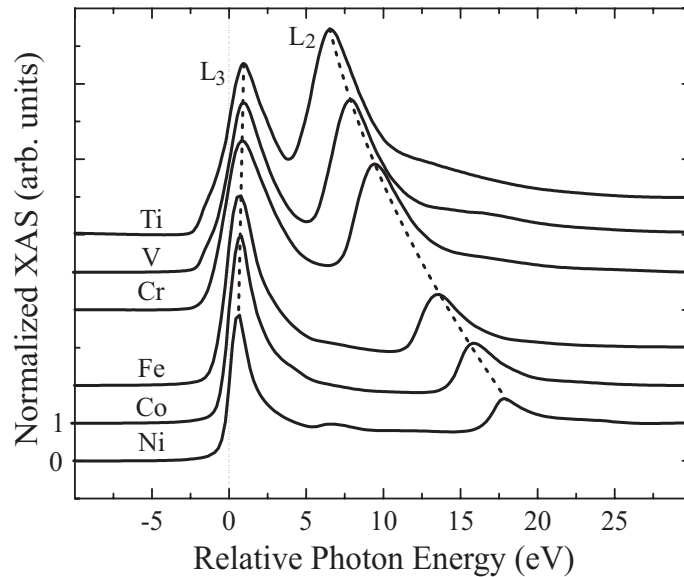


Figure 3.2: The isotropic absorption spectra at the $L_{2,3}$ edges for the 3d TM's. The edge jumps of the spectra are normalized to unity for direct comparison. The dashed lines indicate how the splitting of the $2p_{3/2}$ and $2p_{1/2}$ core levels develops with the atomic number Z across the series

manifold of the $2p_{3/2}$ and $2p_{1/2}$ states, respectively (see sec. 1.2 and [57]). In general, the following effects result in deviations from the statistical ratio: (i) The inclusion of relativistic effects in the 3d valence shell will change the relative peak heights in favor of the L_3 edge [57], see sec. 1.2. (ii) The electron core-hole interaction leads to a transfer of spectral weight between the $L_{2,3}$ absorption edges in favor of the L_2 edge. (iii) The relative $L_{2,3}$ peak heights modify due to differences in the lifetime broadening of the core hole due to Coster-Kronig transitions [100,101]. The experimental core width (FWHM) is shown in Figure 3.3 for the 3d series. While the L_2 core width stays approximately constant, the smaller L_3 core width (longer lifetime) increases towards Ti where the $L_{2,3}$ edges are equally broadened.

For a quantitative analysis of the $L_{2,3}$ spectral ratios, it is helpful to define the branching ratio as

$$D_1 = \frac{A_3}{A_3 + A_2} \quad (3.1)$$

with A_3 and A_2 (see sec. 1.2) being the absorption areas under the corresponding $L_{2,3}$ edges, respectively. Then, the branching ratio becomes independent of the different L_3 and L_2 lifetime broadening of the core hole with regard to (iii) and the experimental broadening. Two more parameters, namely, the relativistic effects in

Figure 3.3: Variation of the full-width-at-half-maximum (FWHM) for the $L_{2,3}$ as a function of the $3d$ TM's. The error-bars increase towards the early $3d$ TM's, because uncertainties are introduced by the overlap of the edges. While the L_2 edge shows almost no change in the peak-broadness, the broadness of the L_3 edge doubles. The lines serve as guide-to-the-eyes.

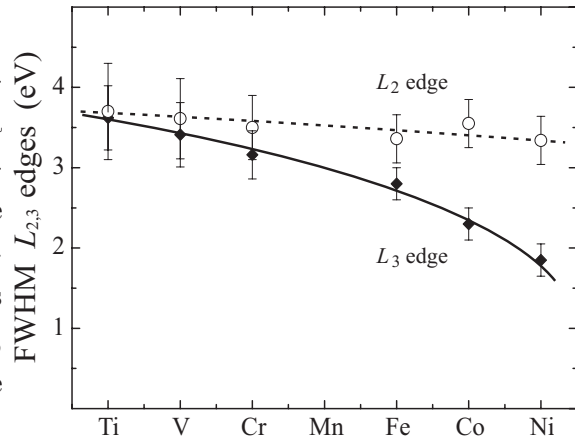


Table 3.1: The isotropic absorption areas for the $L_{2,3}$ edges of the $3d$ TM's investigated in this work. The number of d holes (last row) were taken from SPR-KKR calculations for the respective experimental samples.

(per atom)	Ti	V	Cr	Fe	Co	Ni
A_3	18.7	17.4	17.4	15.9	13.6	9.1
A_2	21.1	16.7	13.7	6.8	5.1	2.6
n_h	7.36	6.44	5.46	3.45	2.4	1.45

the final states and the core-hole interaction remain responsible for the deviations from the statistical branching ratio. Moreover, the determination of absorption areas make it easier to compare the branching ratio with other experiments and theory instead of comparing relative peak heights as it was done in e.g. [31, 32, 94]. For the removal of the continuum contribution, the common procedure (sec. 1.3) of subtracting an *ad hoc* step-function from the absorption spectra has been applied as indicated for Ni in Figure 3.4. The deconvolution of the $L_{2,3}$ edges in case of Ti, V and Cr is more complicated, because of the strong overlap. The areas have been approximated using the the absorption spectrum of Fe as a background simulation underneath the L_2 edge and above. This approximation appears justified, because the L_2 onsets for the early $3d$ TM's follow the energy-dependence of the Fe absorption at the L_3 edge (see the marked area in Figure 3.4).

Finally, the $A_{2,3}$ areas derived by this procedure are given in Table 3.1. The resulting branching ratio is shown as a function of the $3d$ TM's (d count) in Fig-

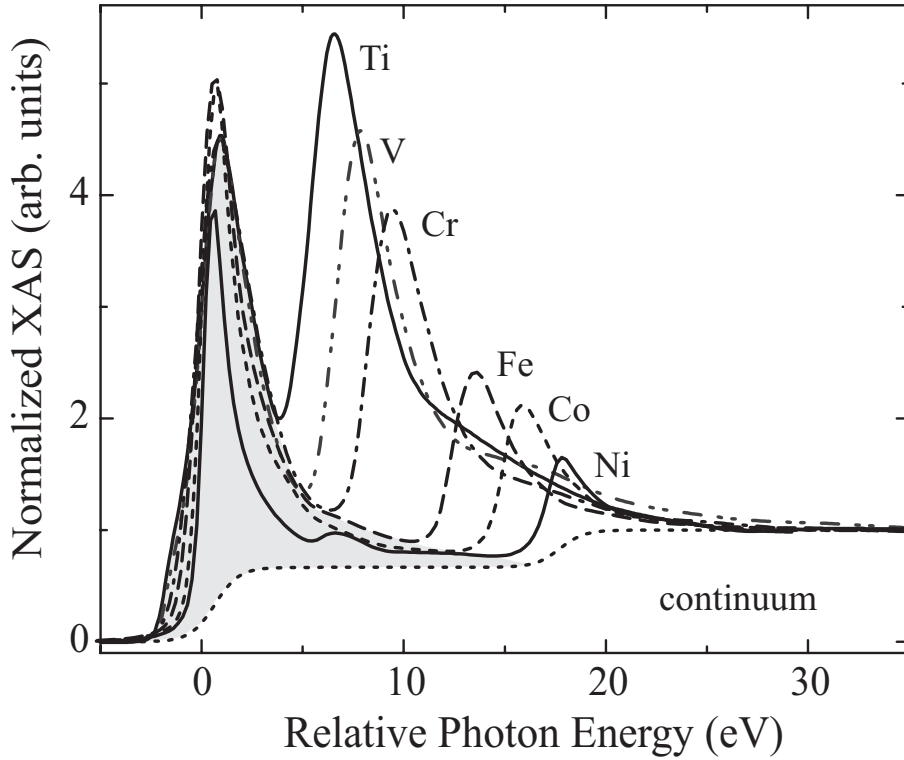


Figure 3.4: Overlay of the $L_{2,3}$ edges for the 3d TM's. The removal of the continuum in the absorption spectra by the common step-function is indicated for Ni. The highlighted area marks the assumed devolution of the L_3 edge underneath the L_2 edge.

Figure 3.5. The error bars increase towards the early 3d TM's due to the uncertainties (e.g. fine structures) related to the overlap of the edges. The experimental values for the 3d TM's increase monotonously from 0.47 for Ti to 0.78 for Ni, which is quite comparable with respect to the branching ratios derived from atomic calculations, i.e. ~ 0.50 for Ti and ~ 0.73 for Ni ions in Ref. [57] accounting for both the core-hole and the relativistic effects. At the end of the 3d TM's the branching ratio differs from the statistical one due to the spin-orbit induced transfer of spectral weight in favor of the L_3 edge as discussed in sec. 1.2, while at the beginning of the 3d series the effect of the electron core-hole interaction (ii) is expected to determine the branching ratio of the early 3d TM's, since the spin-orbit splitting in the core hole is getting compatible small (a few eV, Table 3.2) [32–34]. Although the variation of the branching ratio is elucidated in the presence of the core hole, there is up to now no comprehensive theory available for the description of the branching ratio across the 3d TM's in particular for the spin-dependent 3d absorption cross section.

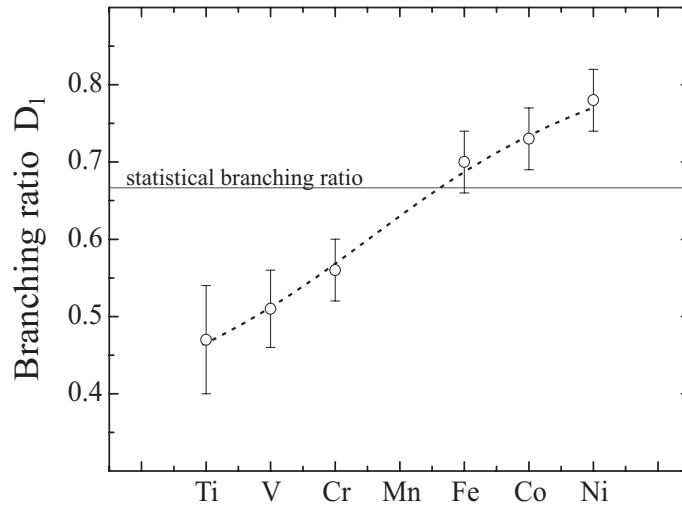


Figure 3.5: Variation of the branching ratio D_1 across the $3d$ TM's. For the determination of the branching ratio the $L_{2,3}$ absorption areas were used. The vertical line represents the statistical branching ratio and the dashed line is a guide-to-the-eye.

Interaction with excited core-hole: double-pole approximation

Time-dependent linear response theory A simple model is established that enables to determine the electrostatic and exchange energies between the core hole and the valence electrons from experimental data in a quantitative manner. It will be demonstrated that the model describes reasonably well the experimental branching ratio for the early $3d$ TM's even though drastic approximations are made. It has been demonstrated that time-dependent density functional theory (TDDFT) can successfully be applied to evaluate excitation energies for molecules, however, depending crucially on the approximations for the exchange correlation functional f_{xc} [102,103]. The scheme of linear response theory on the basis of TDDFT has been used for calculating the x-ray absorption spectra of the $3d$ TM's by Schwitalla and Ebert [33]. Using a local approximation for the exchange-correlation part as it was proposed by Gross and Kohn [104] the trend of the branching ratio across the $3d$ series could qualitatively be reproduced. However, experimental XAS spectra have revealed in particular for the early $3d$ elements that electron core-hole interactions should result in much stronger deviations of the branching ratio than the theory predicts. In order to account better for the systematics in the $3d$ branching ratios A. L. Ankudinov and co-workers have proposed a frequency-dependent exchange-

correlation functional [34]. The purpose, finally, is to provide experimental values that enables theory to improve the models for the exchange-correlation part and to evaluate optical spectra for solids. This is of great importance for the understanding and the interpretation of experimental data.

One assumes [105] that the initial ground-state density n_0 of the electron system with corresponding initial potential ϕ_0 is exposed to an additional frequency-dependent perturbation $\phi_1(\vec{r}, \omega)$. In case of a small perturbation one can expand the frequency-dependent density $n(\vec{r}, \omega)$ to first order and obtains the linear density response of the electrons

$$n_1(\vec{r}, \omega) = n(\vec{r}, \omega) - n_0(\vec{r}) = \int d^3r' \chi(\vec{r}', \vec{r}, \omega) \phi_1(\vec{r}', \omega) \quad (3.2)$$

where $\chi(\vec{r}', \vec{r}, \omega)$ is the frequency-dependent linear response function of the interacting particles having poles at the *true* excitation energies Ω_{fi} . As it is shown in Ref. [105], the response function χ is related to the response function χ_s of non-interacting particles:

$$\chi(\vec{r}, \vec{r}', \omega) = \chi_s(\vec{r}, \vec{r}') + \chi_s(\vec{r}) K(\vec{r}, \vec{r}', \omega) \chi(\vec{r}'). \quad (3.3)$$

The kernel K consists of the Coulomb (electrostatic interaction) and a frequency-dependent exchange interaction represented by the functional f_{xc} :

$$K(\vec{r}, \vec{r}', \omega) = \frac{e^2}{|\vec{r} - \vec{r}'|} + f_{xc}(\vec{r}, \vec{r}', \omega). \quad (3.4)$$

The representation of χ allows for calculating the shift of the single-particle transitions $\omega_{fi} = E_f - E_i$, at which the non-interacting χ_s has poles, towards the true excitation energies Ω_{fi} of the interacting-particle system. Here, the core-hole effects are addressed in *solids* at the $L_{2,3}$ edges of 3d transition metals. This involves excitations from the localized initial states (core levels) to the itinerant ones of the 3d valence band. Hence, in order to succeed one needs precise knowledge of K which must be appropriate for itinerant systems. It is the agreement between the experiment and the theory that validates whether an approximation for the electrostatic interaction and the exchange-correlation functional is suitable or not, see e.g. Ref. [34, 103].

Double-pole approximation (DPA) As it is shown in Ref. [105], a possible way to evaluate Eq. (3.2) is to solve the representation of the eigenvalue problem

without further approximations

$$\sum_{\sigma'} \sum_{q'} [M_{q\sigma q'\sigma'}(\Omega) + \omega_{q\sigma} \delta_{qq'} \delta_{\sigma\sigma'}] \beta_{q'\sigma'} = \Omega \beta_{q\sigma} \quad (3.5)$$

where the sum runs over all possible transitions. The matrix elements are given by

$$M_{q\sigma q'\sigma'}(\omega) = C_{q'\sigma'} \int d^3r \int d^3r' \Phi_{q\sigma}^*(\vec{r}) K(\vec{r}, \vec{r}', \omega) \Phi_{q'\sigma'}(\vec{r}') \quad (3.6)$$

and the following notations for single-particle transitions have been defined:

$$\begin{aligned} \omega_{q\sigma} &\equiv E_{f\sigma} - E_{i\sigma} \\ \Phi_{q\sigma}(\vec{r}) &\equiv \varphi_{i\sigma}^*(\vec{r}) \varphi_{f\sigma}(\vec{r}) \\ C_{q\sigma} &\equiv f_{f\sigma} - f_{i\sigma} ; f_{\text{occ. (unocc.)}} \equiv 1(0) . \end{aligned} \quad (3.7)$$

At this point, the double-pole approximation can be derived from introducing some approximations. For a relativistic treatment of the final d states one needs to solve Eq. (3.5) for $q = 9$ poles depending on the polarization of the light and on the related dipole selection rules, as shown in sec. 1.2. As shown by relativistic spin-polarized *ab initio* calculation (without core hole interaction) [33,34], the branching ratio is very close to the statistical one due to the fact that the spin-orbit coupling is small in the final $3d$ states. Therefore, instead of solving Eq. (3.5) for 9 poles, the relativistic effects are neglected in the following and the statistical ratio 2 : 1 of the L_3 and L_2 edge is fixed for the unperturbed system according to the four-fold and two-fold degeneracy of the $2p_{3/2}$ and $2p_{1/2}$ core levels, respectively. Furthermore, the spin-index σ is skipped assuming a balance of the spin-up and spin-down states in the d valence band (non-magnetic) sec. 1.2. Thus, the system can be reduced to two poles $q = 1, 2$ with their corresponding unperturbed statistical weights C_q :

$$\begin{aligned} q = 1 & \quad (2p_{3/2} \rightarrow 3d) ; \quad C_1 \equiv 2 \\ q = 2 & \quad (2p_{1/2} \rightarrow 3d) ; \quad C_2 \equiv 1 . \end{aligned} \quad (3.8)$$

Finally, one has to solve the eigenvalue problem of a (2×2) matrix

$$\sum_{q'=1,2} [M_{qq'}(\Omega) + \omega_q \delta_{qq'}] \beta_{q'} = \Omega \beta_q \quad (3.9)$$

where the matrix elements are given by

$$M_{qq'}(\omega) = C_{q'} \int d^3r \int d^3r' \Phi_q^*(\vec{r}) K(\vec{r}, \vec{r}', \omega) \Phi_{q'}(\vec{r}') . \quad (3.10)$$

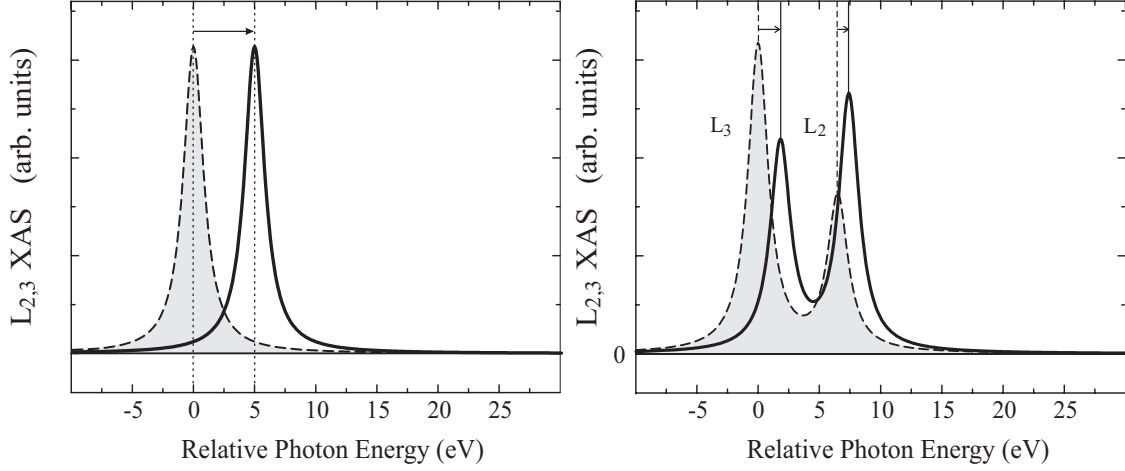


Figure 3.6: (left) In presence of a core hole the single particle transition (dashed line) occurs at a different excitation energy (solid line). (right) Effect of the core hole on the XAS spectra within the double-pole approximation. The calculation (solid line) represents a realistic $L_{2,3}$ spectrum of Ti using an ideal branching ratio for the unperturbed spectrum (dashed line) and the parameters M_{qq} and $\Delta\omega$ from Table 3.2. In both cases (single and double-pole) the matrix elements M_{qq} are positive resulting in a “blue”-shift of the transition energies.

Introducing the *true* transition energy for the single pole q at the unperturbed transition-energy ω_q

$$\Omega_q^s = M_{qq} + \omega_q \quad (3.11)$$

and solving Eq. (3.9) via

$$\begin{vmatrix} \Omega_1^s - \Omega & M_{12} \\ M_{21} & \Omega_2^s - \Omega \end{vmatrix} \stackrel{!}{=} 0, \quad (3.12)$$

one derives

$$\Omega_{1(2)} = \frac{1}{2} (\Omega_1^s + \Omega_2^s) \mp \frac{1}{2} \Delta\Omega \quad (3.13)$$

for the two poles of the perturbed system. The splitting of the transitions is given by

$$\Delta\Omega = \sqrt{(\Omega_2^s - \Omega_1^s)^2 + 4M_{12}M_{21}}. \quad (3.14)$$

In case of $M_{qq'} > 0$ ($M_{qq'} < 0$) the single transitions $\Omega_{q=1,2}^s$ appear at higher (lower) energies. The total shift of both $L_{2,3}$ edges is determined by the center of gravity

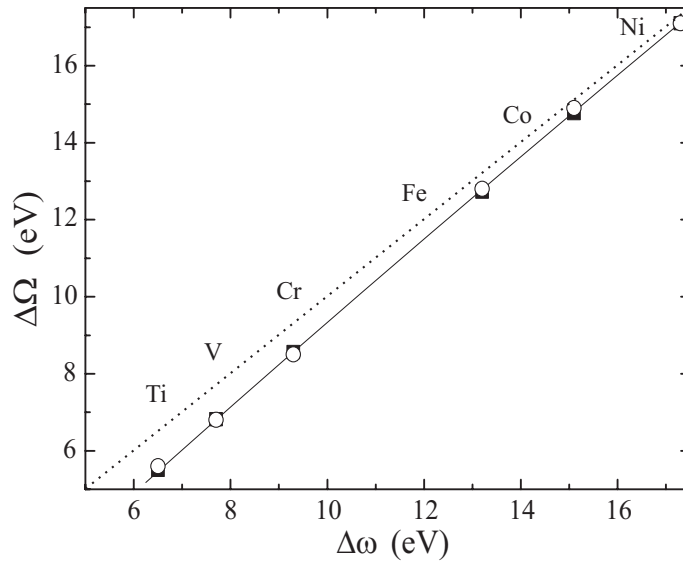


Figure 3.7: The experimentally deduced values (open circle) for $\Delta\Omega$ (this work) are systematically smaller than $\Delta\omega$ obtained from measurements of core-level binding energies listed in Ref. [106]. Note that the error bars are within the point size. The solid line serves as a guide to the eyes. DPA calculation of $\Delta\Omega$ (solid squares) accounts for the core hole, see text.

$\frac{1}{2}(\Omega_1^s + \Omega_2^s)$. Since the energy-shifts for the edges, see Eq. (3.11), are in general different depending on M_{qq} , the splitting of the $L_{2,3}$ edges will change upon the core hole interaction. Hence, an apparent spin-orbit splitting in the experimental absorption spectra can be observed and is analyzed below. The off-diagonal matrix elements in Eq. (3.14) indicate that a minimum energy splitting of the two poles

$$\delta_{min} = \sqrt{4M_{12}M_{21}}$$

exists. In other words, if the initial splitting $\Delta\omega$ of the unperturbed edges is below a *critical* splitting then the $L_{2,3}$ edges repulse effectively each other (see below).

In the next step, an expression for the branching ratio is derived. Therefore, one defines:

$$\chi_s = \frac{C_1}{\omega - \omega_1} + \frac{C_2}{\omega - \omega_2} \quad (\text{unperturbed}) \quad (3.15)$$

$$\chi = \frac{D_1}{\omega - \Omega_1} + \frac{D_2}{\omega - \Omega_2} \quad (\text{perturbed}). \quad (3.16)$$

In general χ_s and χ are complex having a real and imaginary part according to the dispersion and the absorption. Here, only the absorption is considered in order to

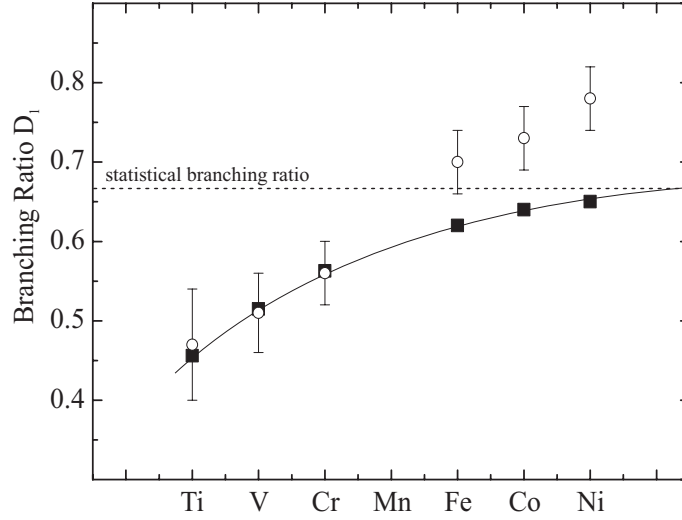


Figure 3.8: The experimental branching ratios versus the DPA branching ratios for the 3d TM's. The vertical line indicates the statistical branching ratio.

reduce the parameters of the model, although the core hole interaction influences the lifetime broadening in particular at the L_3 edge, see Fig. 3.3. Inserting Eq. (3.15) into the relation (3.3) one yields

$$\chi = \frac{C_1(\omega - \omega_2) + C_2(\omega - \omega_1)}{(\omega - \Omega_1)(\omega - \Omega_2)} \quad (3.17)$$

where the kernel K shifts the poles of χ_s towards $\Omega_{1,2}$ (Eq. (3.13)). Comparing the right-hand side of Eq. (3.17) and Eq. (3.16) one finds the identity

$$D_1(\omega - \Omega_2) + D_2(\omega - \Omega_1) = C_1(\omega - \omega_2) + C_2(\omega - \omega_1) . \quad (3.18)$$

For $\omega \rightarrow \Omega_{1,2}$ one obtains finally the spectral weights of the $L_{2,3}$ edges

$$D_{1(2)} = \frac{1}{2}(C_1 + C_2) \mp \left\{ \frac{C_1 M_{22} + C_2 M_{11}}{\Delta\Omega} + \frac{1}{2}(C_2 - C_1) \sqrt{1 - \frac{\delta_{min}^2}{\Delta\Omega^2}} \right\} \quad (3.19)$$

inserting the corresponding transition-energies of Eq. (3.13).

In Fig. 3.6 the effect of the core hole on the $L_{2,3}$ XAS spectra is illustrated for $M_{qq} > 0$. In fact, a “blue” shift of the $L_{2,3}$ absorption spectra with regard to “bremsstrahlung isochromat spectra” has been experimentally observed [31]. Moreover, $M_{qq} > 0$ is found in general for atoms and molecules by TDDFT, i.e. DFT underestimates the transition energies ω_q . It will be shown below that M_{qq} remains positive in case of solids. Two effects of the core hole interaction are prominent in

Fig. 3.6: Firstly, in presence of the core hole both $L_{2,3}$ edges shift towards higher energies. The energy shift is larger at the L_3 edge leading to a smaller separation of the $L_{2,3}$ thresholds. Secondly, the spectral weight of the L_3 edge reduces whereas the spectral weight of the L_2 edge enhances. Hence, the core hole interaction redistributes the initial weights of the $L_{2,3}$, C_1 and C_2 , according to the sum rule

$$D_1 + D_2 = C_1 + C_2 \quad (3.20)$$

which follows from (3.19) reflecting that the total spectral weight of the edges is constant for the perturbed and unperturbed system. Thus, the larger the core hole interaction the stronger the L_3 spectral weight (the branching ratio) decreases and the more the L_2 spectral weight increases. Furthermore, both terms in the parenthesis on the right-hand side of Eq. (3.19) contribute to the decrease of the branching ratio.

Determination of Coulomb and exchange energies via DPA Aside from the branching ratio the DPA model shows that additional information on the influence of the core hole can be obtained by analyzing the energy shifts of the $L_{2,3}$ edges. To tackle the problem of comparing absolute photon energies (uncertainty of several tens of eV) one can analyze the splitting of the $L_{2,3}$ edges in the absorption spectra reducing the error bar to $\sim \pm 0.1$ eV. Then, in order to take use of Eq. (3.14) one needs experimental values of the spin-orbit splitting of the unperturbed core levels $\Delta\omega$. The influence of the core hole can be neglected when exciting the photoelectrons from the $2p_{3/2}$ and $2p_{1/2}$ into the continuum. Therefore, $\Delta\omega$ can be obtained from measurements of core-level binding energies as tabulated in Ref. [106].

In Figure 3.7 the splitting of the $L_{2,3}$ edges in the absorption spectra is plotted versus the difference of the $2p_{3/2}$ and $2p_{1/2}$ binding energies. It reveals that $\Delta\Omega$ is systematically smaller than $\Delta\omega$. Moreover, the difference $\Delta\omega - \Delta\Omega$ reduces with the $3d$ count towards Ni, and one finds that $\Delta\Omega \approx \Delta\omega$ in the limit of Ni with $d_h = 1.45$ holes per atom. This can be qualitatively understood from the fact that a consecutive filling of the $3d$ valence states restricts the amount of phase space available for the excited photoelectron and consequently, limits the influence of Coulomb and exchange interactions in the absorption spectra. Thus, if the initial state is a d^9 configuration (\sim Ni) then there exists no interaction with the core hole, since the d band will be completely filled with the additional photoelectron. Interestingly, this deviation, i.e. $\Delta\omega - \Delta\Omega$ (see Table 3.2), is proportional to the

Table 3.2: The effective correlation energies (M_{qq}) determined by the DPA model for the 3d TM's. The apparent and real spin-orbit splitting (experimental) and the branching ratio (experimental) are also set out.

	Ti	V	Cr	Fe	Co	Ni
experiment						
D_1	0.47(7)	0.51(5)	0.56(4)	0.70(4)	0.73(4)	0.78(4)
$\Delta\omega$ (eV)	6.5(1)	7.7(1)	9.3(1)	13.2(1)	15.1(1)	17.3(1)
$\Delta\Omega$ (eV)	5.6(1)	6.8(1)	8.5(1)	12.8(1)	14.9(1)	17.1(1)
$(\Delta\omega - \Delta\Omega)$	0.9(2)	0.9(2)	0.8(2)	0.4(2)	0.2(2)	0.2(2)
$(\Delta\omega - \Delta\Omega)/n_h$ (eV)	0.122	0.141	0.148	0.118	0.083	0.138
DPA model						
M_{11} (eV)	1.70	1.67	1.44	0.87	0.60	0.36
M_{22} (eV)	0.80	0.77	0.64	0.40	0.28	0.17

number of d holes (Table 3.1). It turns out that the deviation is about 0.125 eV per d hole.

Furthermore, the linear behavior of the apparent spin-orbit splitting in Figure 3.7 suggest that there is no effective repulsion of the edges above ~ 5 eV. Therefore, the off-diagonal matrix elements $M_{12,21}$ are much smaller than $M_{11,22}$ and one can approximate

$$\delta_{min} \ll (\Omega_2^s - \Omega_1^s)^2.$$

Indeed, TDDFT calculations for atoms and molecules indicate that the off-diagonal matrix elements can be neglected [103]. Then the $L_{2,3}$ energy splitting and their spectral weights recast to

$$\Delta\Omega = \Delta\omega + M_{22} - M_{11} \quad (3.21)$$

and

$$D_{1(2)} = C_{1(2)} \mp \frac{C_1 M_{22} + C_2 M_{11}}{\Delta\Omega}. \quad (3.22)$$

Finally, from (3.21) and (3.22) one finds an expression for the matrix elements:

$$M_{11(22)} = \frac{C_1 - D_1}{C_1 + C_2} \Delta\Omega \pm \frac{C_{1(2)}}{C_1 + C_2} (\Delta\omega - \Delta\Omega). \quad (3.23)$$

The final results for the matrix elements M_{11} and M_{22} of Ti, V and Cr are listed in Table 3.2. The positive signs of M_{11} and M_{22} for all the early $3d$ TM's indicate that the correlation energies are generally positive for atoms, molecules and solids. In other words, the transition energies of the unperturbed system will be corrected towards higher energies including the core hole effects by TDDFT. Moreover, one finds that $M_{11}/n_h \approx 0.251$ eV per d hole and $M_{22}/n_h \approx 0.115$ eV per d hole for Ti, V and Cr. Hence, one can extrapolate the matrix elements across the entire $3d$ series in order to calculate the apparent spin-orbit splitting $\Delta\Omega$ and to estimate the branching ratio without relativistic effects. The results of the DPA model are set out in Fig. 3.7 and 3.8. The good agreement of the apparent spin-orbit splitting and the resulting branching ratios with the experiment in Figure 3.7 supports the used extrapolation. The branching ratios for Fe and Co are already close to the statistical branching ratio presented in Figure 3.8 and therefore, suggest that the intermixing of $L_{2,3}$ edges due to the transfer of spectral weight is much smaller compared to the early $3d$ TM's. This is an important information because the core hole interaction causes the breakdown of the spin sum rule as discussed in more detail in sec. 3.3. However, the discrepancies for the branching ratios of the late $3d$ TM's can be attributed to the relativistic effects in the valence states which have been neglected in the simple DPA model.

Finally, the derived values for the correlation energies can be compared to atomic Hartree-Fock calculations [32]. The atomic-like exchange interaction for Ti and V is about 3.37 eV and 3.80 eV, respectively. The values have been estimated to be reduced by 30 % in the metal [32], i.e. $G_1 = 2.36$ eV(Ti) and 2.66 eV(V). This information can be used to disentangle the Coulomb and the exchange interaction in the matrix elements, see Eqn. (3.4) and (3.10). Hence, the Coulomb interaction is about $F_0 = 0.81$ eV(Ti) and 1.2 eV(V), which is consistent with values reported by Zaanen *et al.*, indicating that the core hole interaction is strongly screened in the $3d$ TM's [32]. This has been implemented in recent *ab initio* calculations using a model for a non-local, dynamically screened Coulomb interaction [34]. In this work, the determined correlation energies M_{qq} from experimental spectra can be in the future used for a appropriate TDDFT model to treat core hole effects in the solid state.

3.2 Relation between XMCD and the magnetic ground-state for V

To study the magnetic properties of thin films and magnetic nanostructures the determination of element-specific magnetic moments and the separation into their spin and orbital components (μ_s and μ_l) is one of the striking applications of XMCD. Concerning the spin and orbital magnetic moments of 3d TM's the magneto-optical sum rules [2, 3] were most commonly applied. These interrelate, under certain approximations in a quantitative manner the integrated XMCD of the d valence states to the ground-state orbital and spin magnetic moment (see sec. 1.2). Even though certain approximations limit the validity of the sum-rules ([9], sec. 1.2), it has been demonstrated that they can successfully be applied to the late 3d TM's, i.e. Fe and Co bulk metals [7]. In this way orbital and spin magnetism of thin films [107], multilayers [23, 24, 68, 108], clusters [109] and one-dimensional chains [69] have been explored by means of XMCD, since most of the magnetic nanostructures are composed of the 3d ferromagnets Fe, Co, and Ni. In a similar manner XMCD was applied to the beginning of the 3d series, 4d and 5d elements in magnetic multilayers which usually show induced magnetic moments at an interface to ferromagnetic layers [25, 89–93]. Investigations of the induced magnetic moments in the non-ferromagnetic constituent of magnetic multilayers, e.g. Fe/TM with TM=V, and Cr [12, 23, 25], has also attracted considerable interest. The observation of circular dichroism at the $L_{2,3}$ edges of the early 3d TM's can evidence the existence of a net magnetic moment. However, the application of the sum-rules to the early 3d TM's in order to determine quantitatively the spin and orbital moments has several drawbacks:

- (i) $L_{2,3}$ edges partially overlap which makes a deconvolution of the individual contributions of the L_3 and L_2 edge difficult. The deconvolution is necessary for application of the spin sum rule.
- (ii) The branching ratio strongly deviates from the statistical 2:1 due to the $2p-3d$ core hole interaction.
- (iii) According to (i) and (ii) the core hole interaction may become competitive to the small spin-orbit coupling in the core shell (few eV) resulting in a remixing of the 2p transition channels [99]. Then, the core hole cannot be characterized

in terms of the quantum numbers jm which is required for the applicability of the spin sum rule.

- (iv) Early $3d$ TM's are either non-magnetic (Ti, V) or antiferromagnetic (Cr) in their bulk configurations revealing *per se* no magnetic circular dichroism. Contrary to Fe, Co and Ni, this makes an independent validation of the sum rule results difficult.

In order to tackle and circumvent the problems (i)-(iv) for the early $3d$ TM's, another concept is proposed in this work. The key question is how information contained in the XMCD spectra can safely be transferred to spin and orbital magnetic moments. Contrary to the idea of integral sum rules which neglect the absorption fine structure completely, one analyzes the spectral line shape of the circular dichroism in more detail. This approach deals with deriving magnetic moments from the absorption fine structure of the circular dichroism which reflects the spin-dependent band structure as a function of energy [10]. For the interpretation of the experimental data *ab initio* calculations are applied based on the fully relativistic spin-polarized Korringa-Kohn-Rostoker Green's function method (SPR-KKR). The SPR-KKR calculations are within the independent particle approximation appropriate for itinerant magnetic systems. The theory provides both the spin-dependent absorption cross sections and the correlated spin and orbital magnetic moments. Furthermore, the theory may help to disentangle the contributions of the $L_{2,3}$ edges in the experimental data according to (i). The comparison of the experiment to theory enables to test the validity of the spin and orbital sum rules in view of the core hole interaction, (ii) and (iii), in a direct way. Considering (iv), an $\text{Fe}_{0.9}\text{V}_{0.1}$ disordered alloy has been chosen as a reference sample for which the induced V magnetic moments are known from literature ($\sim -1.0 \mu_B$) [12, 110, 111]. In order to study the possible influence of the electronic and magnetic state on the absorption fine structure, an Fe/V(110) trilayer has additionally been investigated. The presented SPR-KKR calculations in this work are carried out in collaboration with J. Minár and H. Ebert. In the theoretical calculation the Fe/V₃/Fe(110) trilayer is treated as an Fe₇/V₃(110) multilayer for convenience. As a first step, the potentials were created self-consistently for the disordered alloy and the layered system. In case of the alloy the calculations were performed within the coherent potential approximation (CPA). For the calculation of the corresponding absorption coefficient both involved core states were taken into account. The itinerant final states above the Fermi level are represented by the electronic Green's function obtained within

the multiple scattering theory. The calculated spectra of V were broadened, i.e. a Lorentzian broadening of 0.5 eV and 0.3 eV for the L_2 and L_3 edge, respectively, was applied to account for the lifetime of the core hole and a Gaussian broadening of 0.4 eV was used to model the experimental resolution [9]. All details on the SPR-KKR Green's function method and the used expression for the absorption coefficient can be found in [9, 35, 112] and references therein. As discussed in the previous sec. 3.1, the theoretical description of the electron core-hole interaction in the spin-dependent absorption process is an issue of current interest. The SPR-KKR code cannot reproduce so far the observed deviation of the branching ratio in the experimental $L_{2,3}$ -XAS spectra [33, 113].

XAS and XMCD: experiment versus theory

Figure 3.9 presents the experimental XAS spectra (top panel) and the calculated ones (bottom panel) of V for the $\text{Fe}_{0.9}\text{V}_{0.1}$ alloy and the Fe/ V_3 /Fe trilayer. The edge jumps for the experimental and calculated spectra were normalized to unity for better comparison. As discussed in sec. 3.1, the $L_{2,3}$ edges of V partially overlap due to the small spin-orbit splitting (6.8 eV) of the core states. Because the electron core-hole interaction is not taken into account in theory, the calculated spectra reveal the statistical branching ratio, whereas the experimental branching ratio is 0.51. One might expect changes between the experimental XAS spectrum for the alloy (solid line) and the trilayer (dashed line), since the electronic structure of V should be different in an alloy and in a layered structure. However, the slight variations of the experimental XAS spectra suggest that modifications of the electronic structure have a weak influence on the absorption spectrum. The peaks of the $L_{2,3}$ edges for the trilayer appear to be shifted by 0.15 eV only with respect to the alloy case and secondly, exhibit lower intensities.

Two features can be discriminated in the experimental absorption spectra that could not be resolved in previous investigations of the V absorption fine structure [23, 59, 89]: (i) A small feature at the L_3 threshold, labeled A, is revealed in the experimental XAS of the alloy and trilayer. The feature A is enlarged in the inset in the top panel of Figure 3.9 for the alloy and trilayers with different V thicknesses as indicated. Obviously, A depends on the V thickness such that it gets more pronounced the larger the thickness of the V layer while for the alloy the feature A almost vanishes. This means accordingly that hybridization effects between the V and Fe diminish the formation of the feature A. (ii) A broad satellite S, which

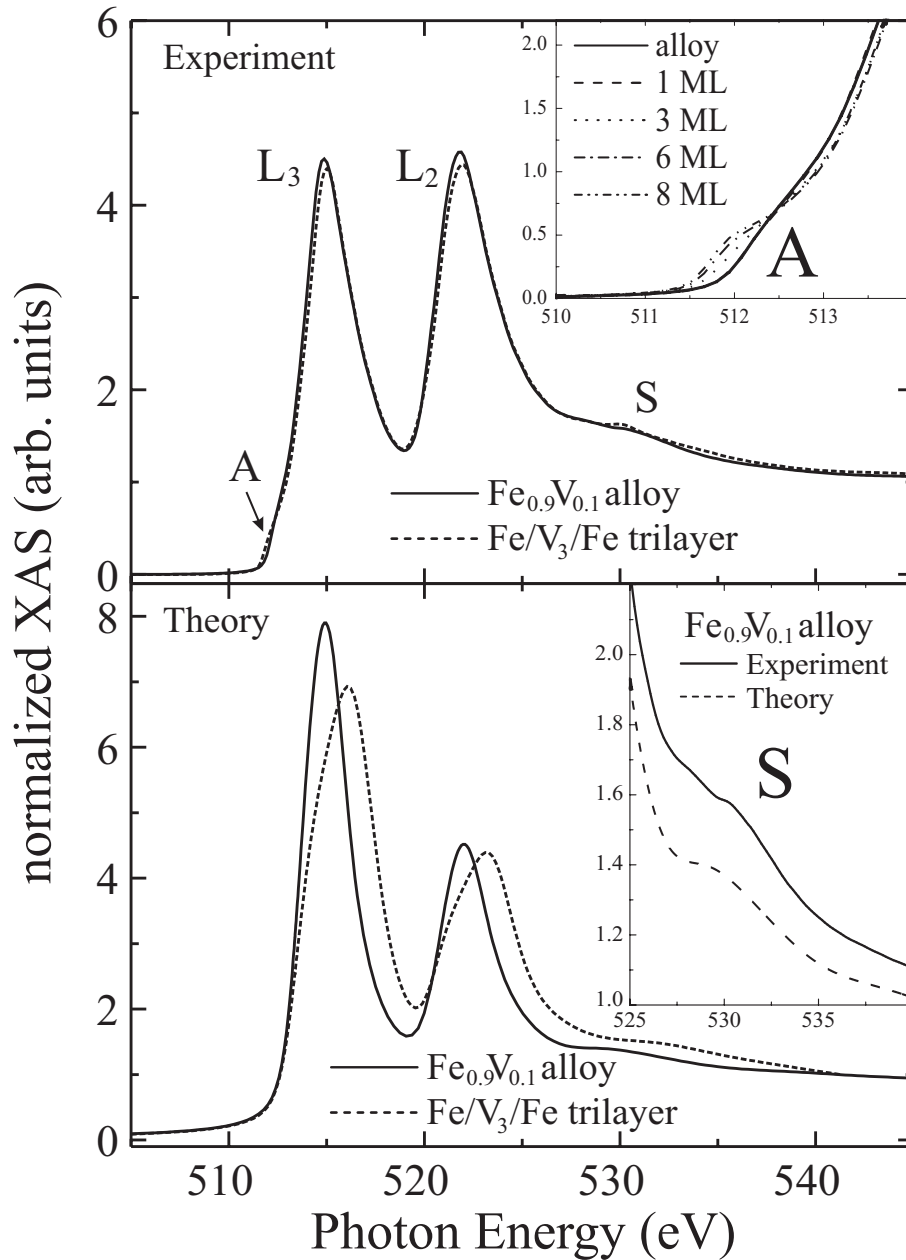


Figure 3.9: Normalized XAS spectra at the vanadium $L_{2,3}$ edges for an $\text{Fe}_{0.9}\text{V}_{0.1}$ alloy (solid line) and a $\text{Fe}/\text{V}_3/\text{Fe}$ trilayer (dashed line). The experiments and the calculations are shown in the top and bottom panel, respectively. The inset of the top panel shows a series of experimental spectra for the alloy and for trilayers with various thicknesses of V in the pre-edge energy range. The inset of the bottom panel is a magnification of the satellite S for the $\text{Fe}_{0.9}\text{V}_{0.1}$ alloy which is perceived by experiment and theory.

is located ~ 8 eV above the L_2 edge, is shown as an inset of the bottom panel in Figure 3.9. The satellite is not observable in the absorption spectra of *ex situ* samples (oxygen contamination) and samples containing oxygen (for instance V compounds), since the energy position coincides with the oxygen K edge at ~ 532 eV. Therefore, in literature the V XAS spectra are usually truncated just below the oxygen K edge [23, 89]. By investigating *in situ* samples, we are able to present and analyze the V spectra in the full required energy-range.

The origin of the two features can be found out by comparing the experimental data with the calculated XAS spectra in the bottom panel. While the shoulder A at the L_3 threshold is absent for the FeV alloy and the Fe/V(110) trilayer, the satellite S is reproduced in the calculations (see the inset in the bottom panel) which in turn proves the high quality of an oxygen-free sample. In addition, the theoretical XAS spectrum for the trilayer exhibits a broad shoulder at the $L_{2,3}$ thresholds and a larger energy shift (~ 2 eV) of the maximum intensities of the absorption edges with reference to the alloy similar to the experiment. As evidenced for the V-XMCD spectra below, the calculated shoulder at the $L_{2,3}$ edges and the feature A

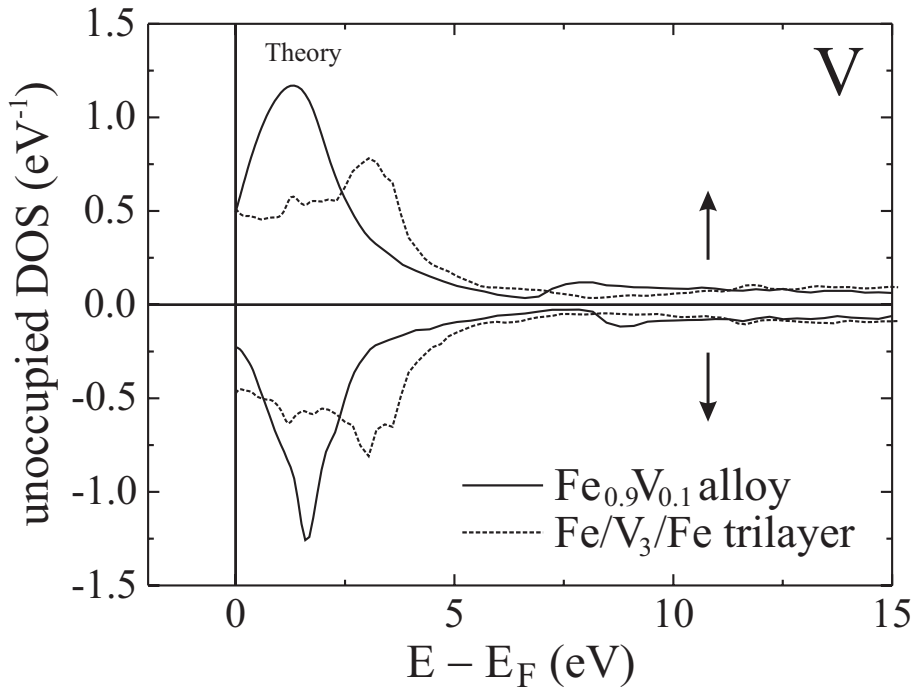


Figure 3.10: Spin-dependent density of unoccupied d states of V for the $\text{Fe}_{0.9}\text{V}_{0.1}$ alloy (solid line) and the Fe/V₃/Fe trilayer (dotted line). The zero energy corresponds to the Fermi level.

have different origins. In Figure 3.10 the spin-resolved density of unoccupied d states is shown as a function of energy relatively to the Fermi level. By comparing the theoretical absorption spectrum with the density of states (DOS) of V (Figure 3.10) one can relate the satellite S to the structure in the DOS (at 7 – 9 eV above the Fermi level) which originates from a van Hove singularity at the N point of the bcc-Brillouin zone. From the energy position in the DOS, one can conclude that the satellite S in the experimental and calculated XAS spectra refers to transitions from the L_2 channel, whereas the corresponding feature at the L_3 edge is covered by the L_2 threshold due to the $L_{2,3}$ overlap.

Furthermore, one can assign the energy shift and the reduced intensities observed in the V-XAS spectra to modifications in the V band structure. For the alloy with only 10 % V the DOS curve is very similar to that of V impurities dissolved in an Fe host [114]. In particular the peak in the majority band has the shape typical for a virtual band state showing only minor hybridization with the host. For the layered structure on the other hand, the V atoms in the inner layers and at the Fe/V interface have 8 and 4 V atoms as next nearest neighbors, respectively. Accordingly the DOS is quite different and much more structured than for the disordered FeV alloy. Moreover, the maximum of the DOS for the Fe/V trilayer is broadened and appears at higher energy. This explains the shoulder at the calculated L_3 absorption edge as well as the energy-shifts and reduced intensities in the XAS for the trilayers in Figure 3.9. However, the less pronounced changes in the overall line-shape of the experimental XAS, even saturating with increasing V thickness up to 8 ML, suggest that other effects, such as the electron core-hole interaction, smear out the details in the experimental absorption spectra. The observed discrepancies can also arise from the fact that the theory assumed perfect Fe/V interfaces while the experimental trilayers suffer from intermixing at the Fe/V interface of the Fe/V trilayers. The interdiffusion effects in Fe/V multilayers are investigated in this work (chapter 4) and have been directly probed, for the first time to our knowledge, in an experiment. Here, the relation between the absorption fine structure of the XMCD spectra and imperfections at the Fe/V interface is addressed in more detail.

The experimental and theoretical XMCD spectra, i.e. the difference between the absorption coefficients for right- (μ^+) and left-circularly (μ^-) polarized light, are presented in Figure 3.11. Contrary to the XAS spectrum, the XMCD reveals more fine structures which are discussed in the following. The main contributions of the L_3 and the L_2 edges in the V dichroism are the signals B and C (highlighted),

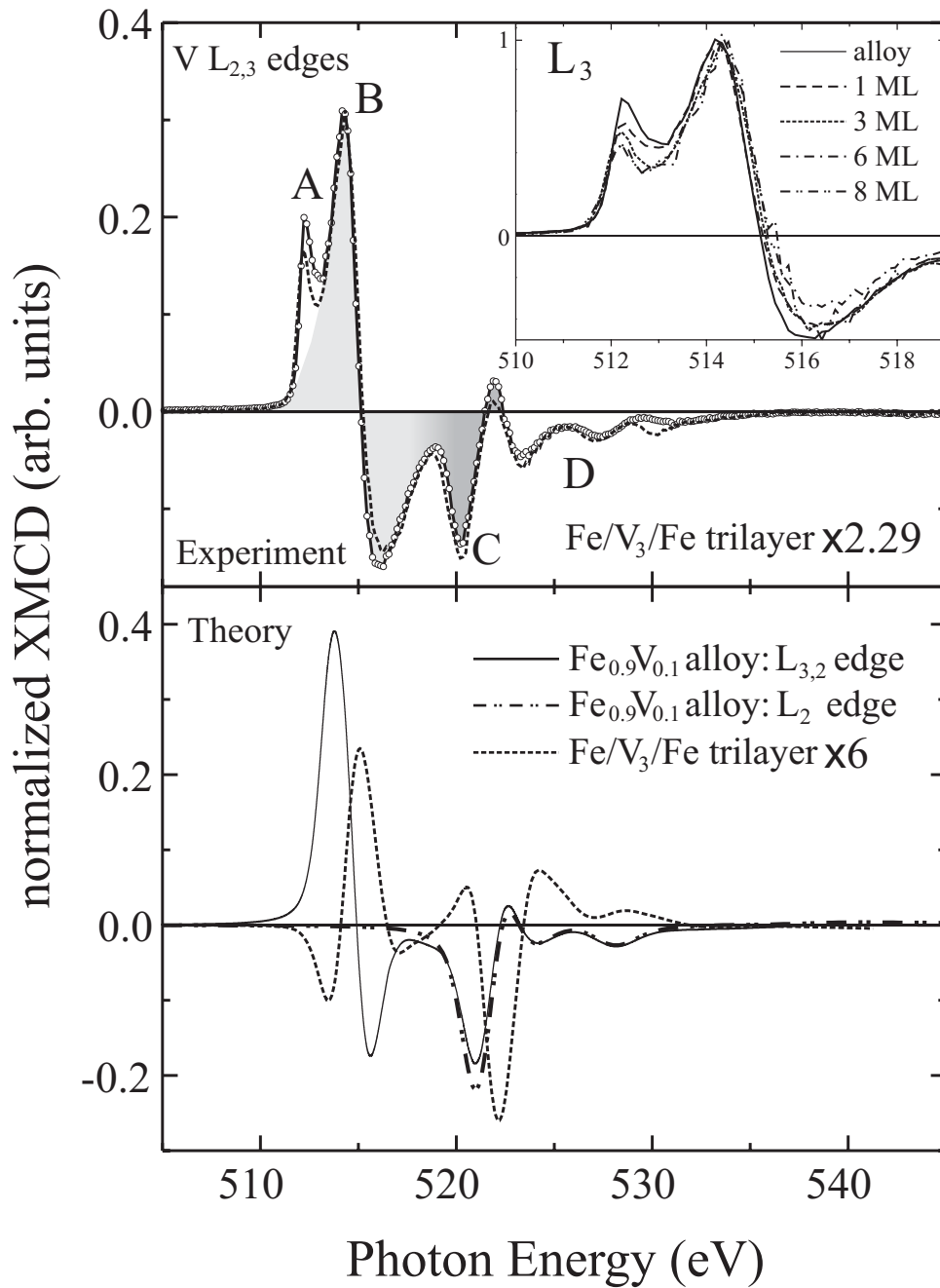


Figure 3.11: Normalized V-XMCD spectra for the $\text{Fe}_{0.9}\text{V}_{0.1}$ alloy (solid line) and the $\text{Fe}/\text{V}_3/\text{Fe}$ trilayer (dashed line). The top panel and bottom panel shows the experimental and the calculated results, respectively. For better comparison the XMCD spectra of the trilayer system have been rescaled as indicated. In the bottom panel the calculated XMCD spectrum of the L_2 edge (dash-dotted line) is added.

respectively. Here, μ^+ and μ^- are defined in reference to the Fe magnetization in our samples, see the corresponding Fe-XMCD spectrum of the Fe/V alloy in Figure 3.13.¹ Oppositely to Fe, the circular dichroism of V reveals a positive onset at the L_3 edge. Hence, this positive onset of B clarifies the antiparallel alignment of the induced V magnetization to Fe in agreement to theoretical predictions and previous experiments [12, 23, 24, 110, 115]. The obvious differences of the V-XMCD with respect to Fe, Co, and Ni are the asymmetries of its main $L_{2,3}$ contributions, i.e. positive and negative intensities at each L edge. While B exhibits a dispersive line shape, the asymmetry of C is less pronounced. The XMCD spectrum of the Fe/V₃/Fe trilayer has been rescaled by $\times 2.29$ to match the XMCD for the Fe_{0.9}V_{0.1} alloy. This indicates, similar to the isotropic XAS spectra, that the XMCD spectrum of V appears at first glance independent of the investigated Fe/V structures. Therefore, the major difference is that the intensity of the V-XMCD spectrum changes corresponding to the induced V magnetic moment.

Furthermore, the prominent feature A in the XAS spectrum in Figure 3.9 has a magnetic counterpart A in the corresponding XMCD spectrum in Figure 3.11. Due to the partial overlap of the $L_{2,3}$ edges, one can only focus on the modifications at the L_3 edge which are shown in the inset of Figure 3.11 for the alloy and the series of trilayers. The peak maximum of B is relatively shifted to the L_3 peak of the XAS spectrum by about 0.15 eV. Although the line-shape is in principle maintained, we can differentiate three systematics in the series with increasing V thickness: (i) The asymmetry of B decreases. (ii) The peak maximum moves slightly to higher energies corresponding to the energy shift in the XAS spectra. (iii) The maximum intensity of A gradually decreases and moves slightly to lower energies.

The calculations for the alloy and the trilayer show in principle similar features. The calculated XMCD spectrum for the alloy (solid line, bottom panel) shows good agreement with the overall experimental line-shape excluding the feature A which is missed by the calculations. Also the absolute intensities of B and C are well reproduced by theory. This suggests that the core-hole correlation effects as discussed in previous section have a minor influence on the spectral distribution except that they broaden the XMCD signal at the L_3 edge. The clear absence of A in the calculations suggests that this feature most likely arises from a splitting (~ 2 eV) of the main contribution B and therefore, stems from correlation effects which are not described by the SPR-KKR calculations. Comparable atomic calculations including the elec-

¹The Fe-XMCD spectra for the trilayers are discussed in chapter 4.

tron core-hole interaction for the d^3 and d^4 configurations of 3d ions in a crystal field indeed reveal a sharp feature at the onset of the L_3 edge [116]. On the other hand, the XMCD spectrum reveals above ~ 520 eV an oscillatory fine structure D that is completely reproduced by the calculations demonstrating band-structure effects. In accordance with the broad satellite S in the isotropic XAS spectrum the oscillations stem from spin-dependent van Hove singularities. Moreover, this part of the XMCD spectrum is almost completely governed by the L_2 contribution as the dash-dotted line in the bottom panel evidences. This is important to know if one needs, however, to separate their contribution in an experiment.

The theory predicts a pronounced change of the XMCD spectrum for the tri-

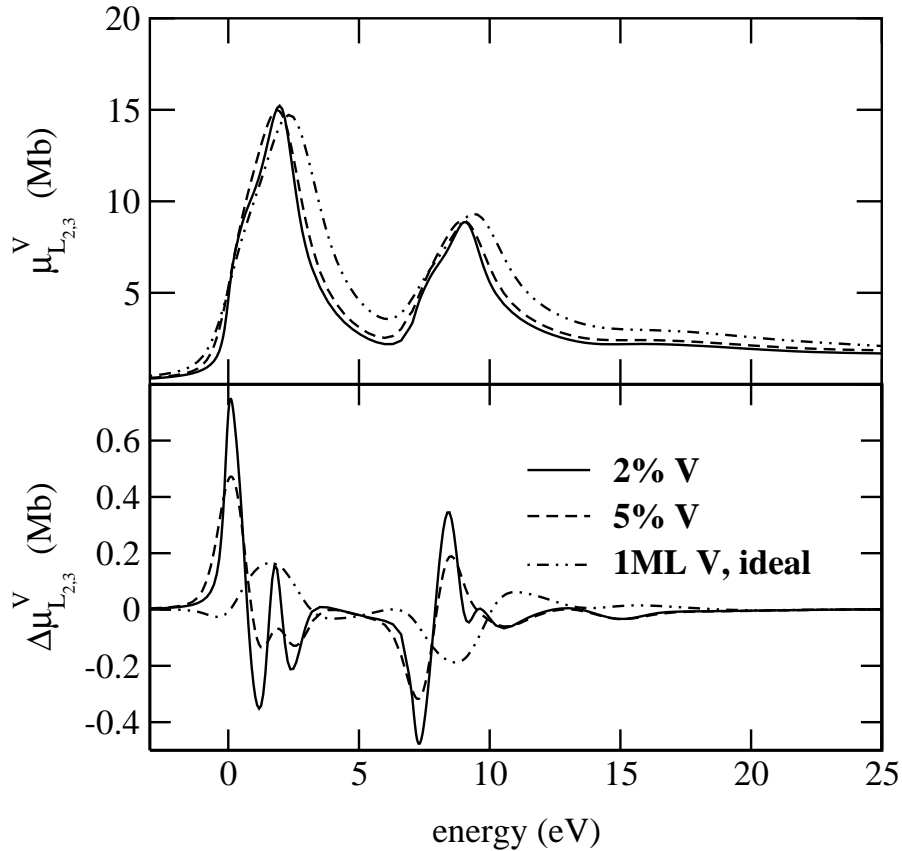


Figure 3.12: Influence of interdiffusion effects at the Fe/V interface on the V absorption fine structure, as calculated by J. Minár *et al.* [35]. The calculations were performed for three concentrations as indicated, i.e. $x = 0, 0.02$ and 0.05 , in a $(\text{Fe}_3/\text{Fe}_{1-x}\text{V}_x/\text{V}_{1-2x}\text{Fe}_{2x}/\text{Fe}_{1-x}\text{V}_x)$ multilayer, where $x = 0$ corresponds to perfect Fe/V interfaces.

layer (dashed line in the bottom panel). Moreover, the calculated XMCD signal was rescaled by a factor 6 because of the smallness of the calculated induced moment for the trilayer system. While the modifications in the XMCD spectrum highlight the sensitivity of the absorption fine structure to the electronic and magnetic structure, it also demonstrates that the magnetic moments of V and the related structural properties are different in the *ab initio* theory and the experiment. For that reason the influence of imperfect Fe/V interfaces on the line shape of the XMCD spectrum was studied by J. Minár [35]. The calculation were performed for three concentrations, i.e. $x = 0, 0.02$ and 0.05 , in a $(\text{Fe}_3/\text{Fe}_{1-x}\text{V}_x/\text{V}_{1-2x}\text{Fe}_{2x}/\text{Fe}_{1-x}\text{V}_x)$ multilayer. The results are shown in Figure 3.12. Contrary to the isotropic XAS spectra in the top panel, the XMCD spectra is modified dramatically. This is remarkable, because low interdiffusion levels of a few percent are considered. The theoretical XMCD spectra of the Fe/V_n layered structures with $n=1$ and 3 in Figures 3.11 and 3.12, respectively, are basically the same except their magnitude. Going from the perfect interface, $x = 0$, to the imperfect ones $x > 0$, the XMCD line-shape systematically transfers into the one known from the experiment and the theory of the disordered Fe/V alloy. Moreover, one sees an increase of the XMCD intensities due to an increase of the induced magnetic moments at the interface. Hence, already a small interdiffusion level at the Fe/V interfaces explains the observed experimental XMCD spectra and the discrepancy of the XMCD intensities for the Fe/V trilayer in Figure 3.11 between theory and experiment.

Determination of magnetic moments

As demonstrated for induced magnetism of V in an FeV alloy and an Fe/V trilayer, the XMCD spectra strongly depend on the structural properties (e.g. the Fe/V interface) and the induced magnetic moments. Even though a large variety of absorption fine-structure is revealed in the XAS and XMCD spectra, often the integral sum rules are used for the determination of spin and orbital magnetic moments via certain areas in the absorption spectra, see sec. 1.2. Here, the theory provides both the entire XMCD spectrum and the correlated spin and orbital moments. The good agreement between theory and experiment for the reference sample $\text{Fe}_{0.9}\text{V}_{0.1}$ alloy allows to estimate the total magnetic moment of V to be $\sim 1.0 \mu_B$ as determined from theory and supported independently from a polarized neutron study (PNS) [110], see Table 3.3. Moreover, in the dilute limit of FeV alloys the induced magnetic moment at V only slightly depends on the V concentration [110]. Therefore, we

can test the validity of the sum rules [2, 3] for V in view of the $2p - 3d$ core hole interaction and the small spin-orbit coupling in the V core shell [99].

The orbital and spin moment can be determined by the Eqn. (1.20) and (1.21). In a pioneering work Harp *et al.* [89] applied the sum rules to the V dichroism for an Fe/V multilayer. They found that the ratio of the orbital to spin moment is close to 1. Moreover, the orbital sum rule appears to break down since the ratio was found to be positive whereas the theory predicts a negative one (see Table 3.3). As discussed in Ref. [89], the presence of strong absorption at the oxygen K edge introduces artificial magnetic background signals in the XMCD spectra that reduces the reliability of the integrated intensities and consequently, results in the question-

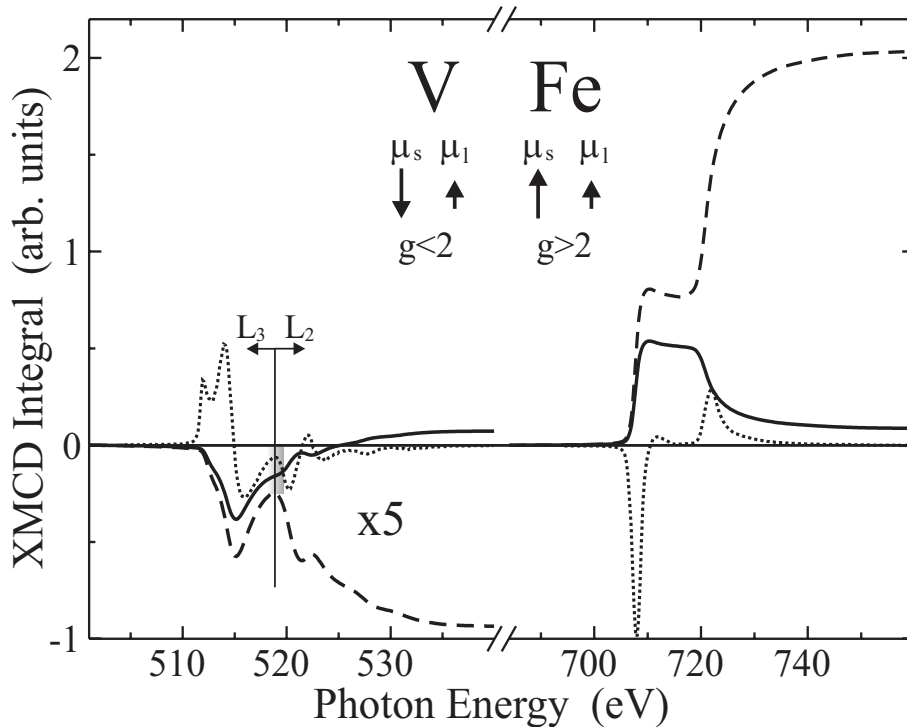


Figure 3.13: The integrals over the XMCD spectra (dotted lines) for V and Fe in the $\text{Fe}_{0.9}\text{V}_{0.1}$ alloy. Both the XMCD and the corresponding integrals of V have been rescaled for better illustration. The solid integral is proportional to the V and Fe orbital moments whereas the dashed integral corresponds to the V and Fe spin moments. The gray area illustrates the overlap of the V $L_{2,3}$ edges indicating the problem of the separation of their contributions for the spin sum rule. The arrows indicate the directions of the spin and orbital moments for Fe and V predicted by the orbital sum rule and the sign of L_3 onsets for Fe and V.

able outcome of the sum rules. Moreover, the normalization of the XMCD spectra to the number of relevant $3d$ atoms becomes highly problematic when part of the V atoms form compounds with oxygen and contribute to the XMCD signal or not. As already discussed in the previous sections, those uncertainties do not exist in the present work. Therefore, the test of the sum rules can be performed in a quantitative manner and it will be shown that background problems as well as uncertainties of the $L_{2,3}$ deconvolution are not responsible for the questionable results of the sum rules.

The integral over both edges of the XMCD spectrum (Figure 3.13) is directly proportional to the orbital moment μ_l following Equation (1.20). Therefore, a deconvolution of the $L_{2,3}$ edges is not necessary. In contrast to Fe the integral for V (solid line) has a node before saturating above the $L_{2,3}$ edges in Figure 3.13. The crossing of the orbital integral implies, as long as the orbital sum rule holds, that μ_l must be antiparallel aligned to the spin moment μ_s , because the integral of the spin sum rule cannot change its sign. In other words, the directions of μ_l and μ_s are given by the sign at the onset and at the end of the orbital integral, respectively. This means accordingly that the orbital moments of V and Fe are parallel aligned while the spin moments of Fe and V are antiparallel aligned in Figure 3.13. This finding is in agreement with the *ab initio* calculations (SPR-KKR code) listed in Table 3.3. Hence, the $3d$ TM's V (Fe) orbital and spin moment are antiparallel (parallel) aligned and obey Hund's third rule (dedicated for atoms) for a less (more) than half-filled d shell.²

For applying the spin sum rule the $L_{2,3}$ contributions should be deconvoluted. This can be readily performed for Fe where the edges appear well separated with respect to the spin-orbit splitting. Instead of deconvoluting the V $L_{2,3}$ edges, the two contributions were separated in the simplest way by an energy cut-off at the onset of the L_2 edge as it is illustrated in Figure 3.13. For removing the $L_{2,3}$ edge jumps we used a two-step-function [7, 123] in order to determine N which is the absorption area of the isotropic spectrum. The number of $3d$ holes $n_h = 6.44$ was taken from theory.³ As revealed by the calculations (see Table 3.4), the magnetic dipole-term $\langle T_z \rangle$ [5, 124] in Equation 1.21 can be ignored for the FeV alloy but is enhanced at the Fe/V interface in layered structures. The final results for the spin

²Note that an apparent breakdown of the Hund's third rule was found in theoretical and experimental studies of uranium and $5d$ metals [93, 119–122].

³Note that the degree of circular polarization and the angle of incidence of the x-rays were already taken into account in the experimental spectra.

Table 3.3: Apparent spin and orbital moments of V and Fe for the $\text{Fe}_{0.9}\text{V}_{0.1}$ alloy obtained by XMCD via the sum rules and calculated by theory. The total magnetic moments are presented together with the ones obtained by PNS [110]. The V-XMCD results (brackets) strongly deviate from theory and PNS and cannot be taken as final results (see text).

$\text{Fe}_{0.9}\text{V}_{0.1}$ (μ_B/atom)	V			Fe		
	XMCD	PNS	Theory	XMCD	PNS	Theory
μ_s^{3d}	(-0.20)	-	-1.01	2.09	-	2.22
μ_l^{3d}	(0.016)	-	0.020	0.093	-	0.053
μ_{tot}^{3d}	(-0.18)	-1.07	-0.99	2.18	2.23	2.27

and orbital moment for the reference sample are given in Table 3.3.

The comparison of the absolute values for μ_s with theory evidences clearly that the spin sum rule deviates by $\sim 80\%$. The main errors introduced exclusively by the commonly applied procedure are the following: Firstly, the theory can separately evaluate the contributions of the L_3 and the L_2 edge. This allows for a rough deconvolution of the edges in the experimental spectra and gives an estimate for the systematic error indicating that the spin moments are at most 15 % smaller due to the simple energy cut-off. Secondly, another systematic error is introduced by the removal of the $L_{2,3}$ edge jumps with the *ad hoc* step-function (see sec. 1.2) which enters in both the orbital and spin moment values. However, the error bar is rather small (estimated: $< 10\%$) due to the large absorption intensities at the $L_{2,3}$ edges in case of V. On the other hand, sizable absorption at the oxygen K edge [89] (*ex situ* samples) could dramatically increase the error bar. Thus, the applied procedure cannot account for the strong deviation of the spin sum rule and indicates their invalidity for the early 3d TM's. Interestingly, in addition to the correct prediction of the direction, the value of μ_l derived by the orbital sum rule appears to be valid within $\sim 20\%$ in reference to the theoretical value. This deviation is similar to the ones obtained for the ferromagnets Fe, Co and Ni ($\sim 10\%$) by theory [5].

The failure of the spin sum rule, however, exists not only in x-ray absorption experiments but also for the x-ray resonant magnetic scattering technique [91]. There are two ways to overcome this difficulty: The combination of XMCD experiments with conventional magnetometry enables to determine absolutely the induced mag-

Table 3.4: Corrected spin-, orbital-, and total-moment for vanadium of the FeV alloy and Fe/V/Fe(110) trilayer as well as a $(\text{Fe}_4/\text{V}_2)_{60}$ superlattice (see chapter 5): as obtained from the sum rules (in brackets) and deduced by scaling to the reference sample. The T_z term (see Eq. 1.21) is obtained from calculation for the $\text{Fe}_{0.9}\text{V}_{0.1}$ alloy and the Fe/V₃/Fe(110) trilayer. The relative error for the total moment is $\sim 15\%$.

Vanadium (μ_B/atom)	$\text{Fe}_{0.9}\text{V}_{0.1}$ reference	Fe/V ₃ /Fe(110) scaled	$(\text{Fe}_4/\text{V}_2)_{60}$ scaled
$\mu_s^{3d} - 7 \langle T_z \rangle$	(-0.20) - 1.01	(-0.092) - 0.46	(0.19) - 0.97
$7 \langle T_z \rangle$	-0.0014	0.0401	-
μ_s^{3d}	-1.01	-0.42	-0.93
μ_l^{3d}	(0.016) 0.020	(0.009) 0.011	(0.012) 0.015
μ_{tot}^{3d}	-0.99	-0.41	-0.91

netic moment for V [24] and is demonstrated in this work in chapter 5. Alternatively, the V-XMCD spectra from FeV alloys with known concentration and magnetic moments can be used as an experimental reference sample [23, 45, 51, 125]. Since the line shape of the overall V dichroism is in principle maintained for the trilayers and the alloy, the only change is the amplitude of the dichroism which is in good approximation proportional to the magnetic moment. Then, the results of the sum rules can be corrected with respect to the reference, i.e. the $\text{Fe}_{0.9}\text{V}_{0.1}$ alloy. The advantage of using this method is that the systematic errors mentioned above partially cancel out. However, the $\langle T_z \rangle$ term obtained from calculation contributes to the spin sum rule with 10 % for the layered structures and has to be taken into account. The obtained realistic V moments are summarized in Table 3.4. In order to confirm the consistency of the “scaling procedure”, it was applied to the $(\text{Fe}_4/\text{V}_2)_{60}$ superlattice yielding $\mu_{tot} = -0.91 \mu_B$ which is in fair agreement with the independently deduced value of $\mu_{tot} = -1.06 \mu_B$ [24].⁴ This provides a possibility to correct the outcome of the sum rules and to estimate the magnetic moments which are related to the measured XMCD spectra.

⁴The sample is analyzed and discussed in chapter 5 and Ref. [24].

3.3 Limitations of magneto-optical sum rules for 3d TM's

In the previous section the absorption fine structures and the correlated magnetic moments for V have been analyzed in detail. Here and in the following section, the discussion of the XMCD line shape and the related ground-state spin and orbital moments is extended throughout the 3d TM's in a systematic fashion with regard to the isotropic XAS and the corresponding XMCD spectra of the 3d series in Fig. 3.1. The concept of analysis presented for V was assigned to the absorption spectra of Fe/TM/Fe(110) trilayers with TM=Ti and Cr.⁵ In the Figures 3.14, 3.15 and 3.16 the experimental XAS and XMCD spectra (solid lines) are presented for Ti, V and Cr at the $L_{2,3}$ edges, respectively, together with the *ab initio* calculations (dashed lines). The positive onset of the dichroism at the L_3 edge reveals antiparallel orientations of the net magnetization of Ti, V, and Cr with respect to Fe in agreement with theory. As abovementioned, the core-hole correlation effects were not considered in the calculations and therefore, the branching ratios in the XAS spectra for the experiment and the theory are different.

Contrary to V and Cr, the Fe/Ti/Fe(110) trilayers measured in this work have revealed that the Ti-XMCD signal is independent of the deposited Ti-thickness (< 1.5 nm). This suggests that in average all Ti atoms become equally polarized through Fe. This result can be understood from considering the formation of a TiFe_2 structure in the trilayers as it was reported for Fe/Ti multilayers [126–128]. Therefore, the SPR-KKR calculation for the Ti spectra were performed for the TiFe_2 structure in Figure 3.14. The reasonable agreement between theory and experiment supports the structural properties of the experimental trilayers with respect to Refs. [126–129]. The Cr-XMCD in Figure 3.16 evolves from uncompensated spins in the 3 monolayers of Cr sandwiched between the two Fe layers, which are coupled in parallel by the interlayer exchange coupling for a 3 ML Cr-spacer [25,130]. Similar to V, the calculations of the XMCD spectrum assuming perfect interfaces for the Fe/Cr₃/Fe(110) sample differs strongly from the experiment. However, the agreement with the experiment improves considering partly interdiffused interfaces. Hence, the theoretical spectra for an $\text{Fe}_{0.90}\text{Cr}_{0.10}$ alloy is included in Figure 3.16 serving as a reference. There are broad satellites in all spectra slightly above the L_2 edge that stem from van Hove singularities in the bcc-Brillouin zone. For the

⁵For details concerning the structural properties see sec. 4.1.

investigated samples, the XMCD to XAS peak height ratio at the L_3 edge is $\sim 3\%$, $\sim 7\%$, and $\sim 9\%$ for Ti, V, and Cr, respectively. Similar to V, the Ti- and Cr-XMCD spectra are well reproduced by the SPR-KKR calculations excluding the splitting at the L_3 edge of Ti. In correspondence to the XAS spectrum the circular dichroism for Ti, V, and Cr reveals an oscillatory fine structure above the L_2 edge that originates from the spin-dependent band structure and is perfectly reproduced by the calculations. Furthermore, the theory calculates correctly the dispersive-like

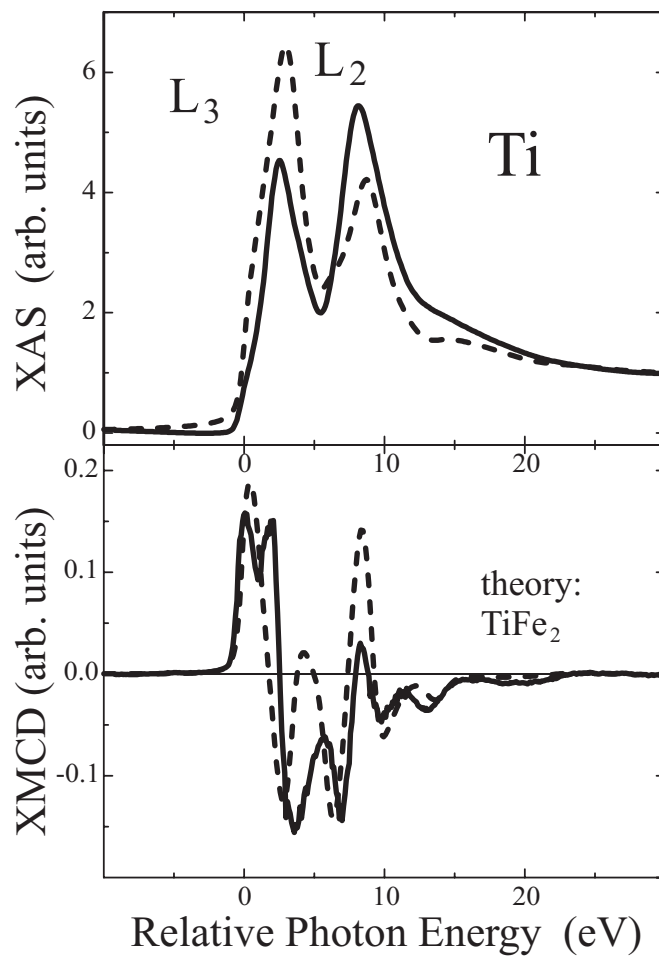


Figure 3.14: Normalized (above) XAS and (below) XMCD spectra for the early TM Ti at the $L_{2,3}$ edges: (solid line) experimental data versus (dashed lines) *ab initio* calculations. The experimental data have been corrected corresponding to measurements with 100 % circularly polarized x-rays with the k vector parallel to the magnetization. Note that *no* scaling factors between theory and experiment as well as between the XAS and XMCD intensities are needed.

line shape across the early 3d TM's, i.e. the lower the filling of the d valence band the more the $L_{2,3}$ peaks become asymmetric.

The theory provides both the XMCD to XAS peak ratios and the correlated spin and orbital magnetic moments which are listed in Table 3.5. In order to test the validity of the integral sum-rules we compared those values with the ones derived from the application of the commonly used procedure (sec. 1.2 and sec. 3.2). The numbers of d holes were taken from theory being 7.36, 6.44, and 5.46 per atom for Ti, V, and Cr, respectively. Instead of separating the $L_{2,3}$ contributions we used a simple energy cut-off determined by the local minimum between the edges. Ti acquires an induced spin moment of $-0.7 \mu_B$ predicted by theory for the Fe_2Ti structure.

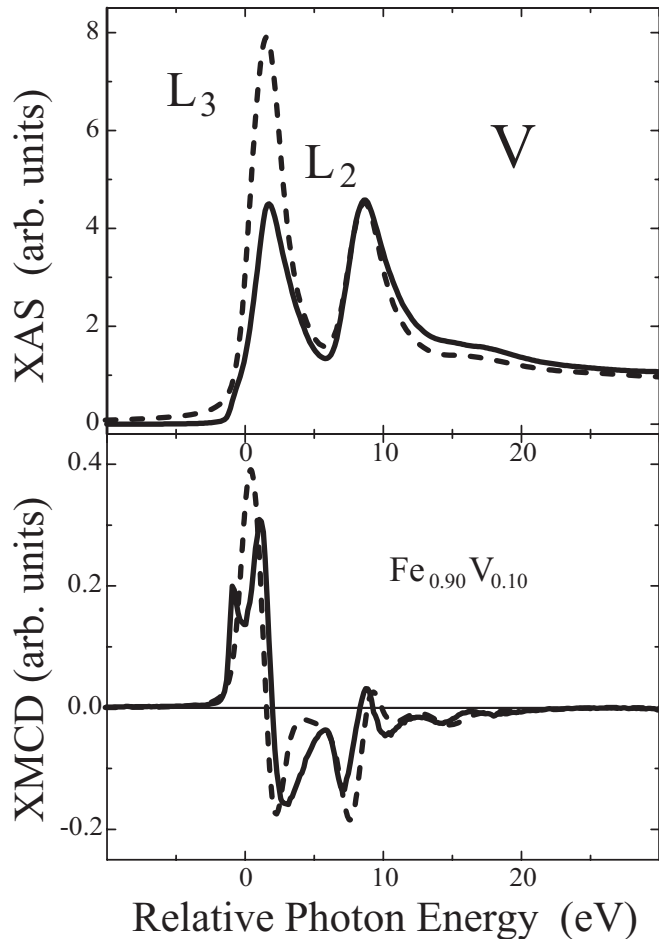


Figure 3.15: Normalized (above) XAS and (below) XMCD spectra for the early TM V at the $L_{2,3}$ edges: (solid line) experimental data versus (dashed lines) *ab initio* calculations. (*no* scaling factors, see Fig. 3.14)

Even though the XMCD to XAS peak ratios are in reasonable agreement between experiment and theory the spin sum rule fails similar to V. The experimental Cr data indicate a magnetic moment of about $-0.6 \mu_B$ in comparison with the $\text{Fe}_{0.90}\text{Cr}_{0.10}$ reference and with measurements on Fe/Cr trilayers reported by Idzerda *et al.* [25], while the application of the spin sum rule yields $-0.28 \mu_B$, i.e. the spin magnetic moment deviates by a factor of 2. Furthermore, we applied the sum rule analysis to the ferromagnetic bulk-like films of Fe (~ 50 ML), Co (~ 50 ML) and Ni (~ 20 ML) on Cu(100). The results are added in Table 3.5 together with theoretical calculations [74, 75, 131]. The spin and orbital moments for Fe and Co are in agreement with those values obtained in transmission detection mode by Chen and co-workers [7],

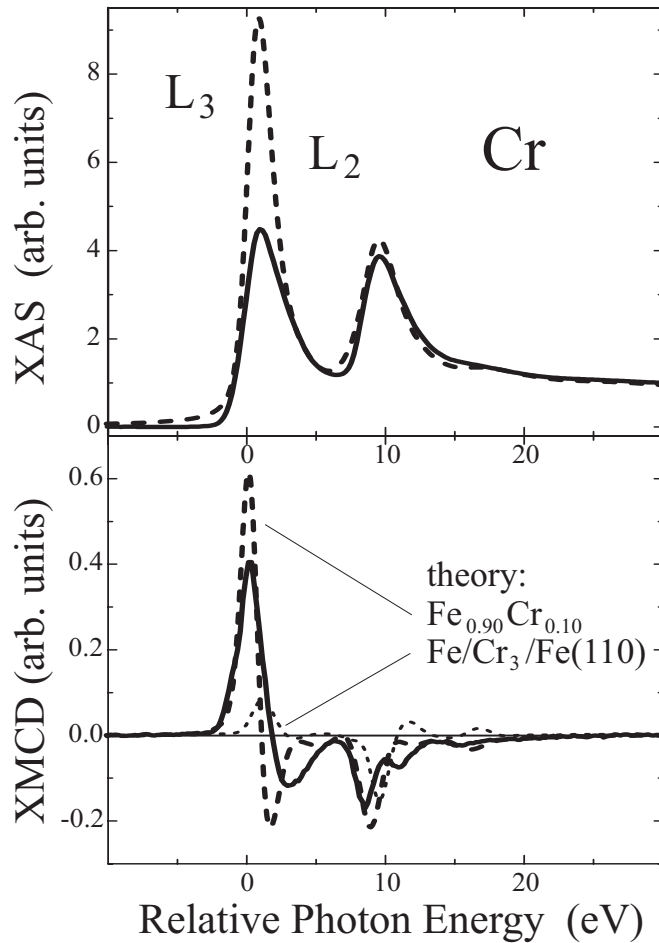


Figure 3.16: Normalized (above) XAS and (below) XMCD spectra for the early TM Cr at the $L_{2,3}$ edges: (solid line) experimental data versus (dashed lines) *ab initio* calculations. (*no* scaling factors, see Fig. 3.14)

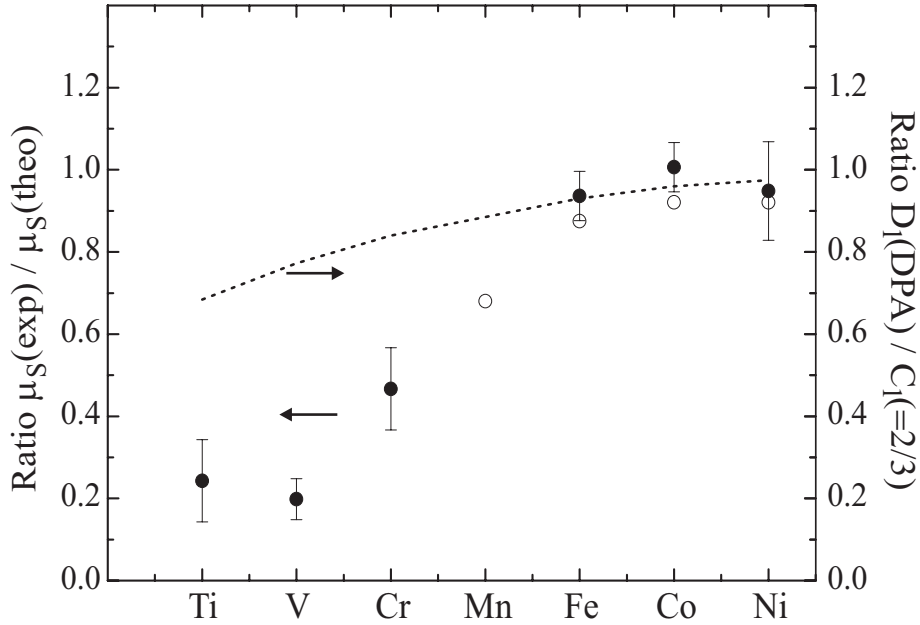


Figure 3.17: The apparent (sum rule) to theoretical spin moment ratio (closed circles) is shown for the 3d TM's. The ratios (open circles) obtained by atomic multiplet calculations for the late 3d TM's including core hole effects are also presented from Ref. [99]. The influence of the core hole on the $L_{2,3}$ absorption spectra is reflected by the ratio of the perturbed to statistical branching ratio (dotted line) obtained from the DPA model.

while the spin and orbital moment for Ni is in reasonable agreement with results of Ni bulk-like films [66, 107, 132, 133].

It turns out that going towards the late 3d elements the systematic error of the spin sum-rule reduces and explains why they hold for Fe and Co. The direct relation between the deviation of the spin sum rule and the branching ratio across the 3d TM's series is shown in Figure 3.17. Hereby, the apparent (sum rule) to theoretical spin moment ratio is plotted (closed circles). The deviation increases, when the core hole interaction increases depicted by the deviation of branching ratio from the statistical one. The origin of this effect is that the core hole is no longer well characterized by the quantum numbers jm when the core hole interacts with the valence electrons. However, this is a demand for the applicability of the spin sum rule. This has been theoretically verified in calculation of late 3d ions (open circles) on the basis of an atomic model including the full multiplets and crystal field effects by Teramura et al. [99]. In this work, the first experimental determination of the sum rule deviations across the 3d series has been performed. This allows

Table 3.5: The spin and orbital magnetic moments as calculated by *ab initio* theory corresponding to the theoretical XAS and XMCD spectra in Figure 3.1. The apparent magnetic moments derived by application of the sum rules to the experimental data reveal a considerable underestimation of their ‘real’ values, see text.

3d TM	theory			sum rules		
	μ_s (μ_B)	μ_l (μ_B)	μ_l / μ_s	μ_s (μ_B)	μ_l (μ_B)	μ_l / μ_s
Ti (TiFe ₂)	-0.70	0.014	-0.02	-0.17(8)	0.069(20)	-0.41(28)
V (Fe _{0.9} V _{0.1})	-1.01	0.020	-0.02	-0.20(5)	0.016(7)	-0.08(6)
Cr (Fe _{0.9} Cr _{0.1})	-0.95	0.014	-0.015	-	-	-
Cr (Fe/Cr ₃ /Fe)	-	-	-	-0.28(6)	0.011(5)	-0.04(3)
Fe bulk †	2.19	0.091	0.042	2.05(15)	0.087(8)	0.043(6)
Co bulk †	1.57	0.140	0.089	1.58(10)	0.22(2)	0.14(2)
Ni bulk ††	0.58	0.058	0.100	0.55(8)	0.10(3)	0.18(8)

† theoretical values taken from Reference [74, 75].

†† theoretical values taken from Reference [131, 133].

for corrections or estimations of the spin moments deduced in other experimental XMCD studies. It is valuable to note that the orbital sum-rule provides the correct sign. This means accordingly that the spin and orbital moments are antiparallel aligned for Ti, V and Cr and aligned in parallel for Fe and Co in agreement with the theoretical expectations in Table 3.5.

3.4 Multipole moment analysis versus SPR-KKR

The decrease of the XMCD to XAS peak area ratios towards lower d counts can be explained by the lower spin-polarization $P_S^{3d} = (n_h(\uparrow) - n_h(\downarrow))/(n_h(\uparrow) + n_h(\downarrow))$ in the d valence band [54]. Hence, according to the proportionality of the XMCD and XAS to the densities of spin-up and spin-down states the XMCD to XAS peak area ratio is $\propto P_S^{3d}$. This results in reduced XMCD intensities with respect to the XAS intensities albeit the magnetic moments of Ti, V and Cr ranges between 0.6 – 1.0 μ_B (see Table 3.5). The ferromagnets Fe, Co and Ni, which have the majority spin-band (\downarrow) almost or completely filled due to a large exchange-splitting, show typically

symmetric peaks at the $L_{2,3}$ edges in the XMCD spectra. Looking at the opposite limit Ti and V with a less-than-half filled d band, one observes asymmetric line shapes. Thus the asymmetry increases the lower the occupation of the d band. The appearance of an asymmetric XMCD in particular at the L_3 edge has been related to the initial state splitting [45, 54]. Hereby, the degeneracy of the core states is lifted by an effective exchange field H_{ex} depicting the interaction of the core hole with the exchange-split $3d$ valence states [45]. More recently, this effect on the XMCD line shape across the 3d TM's has been modeled in terms of multipole moments of the ground state within an independent particle model [54–56].⁶

For the transition metals the most dominant ones are the spin moment, $\mu_s = (n_h(\uparrow) - n_h(\downarrow)) \mu_B$, and the number of d holes, $n_h = (n_h(\uparrow) + n_h(\downarrow))$, representing symmetric and asymmetric line-shapes (sec. 1.2), respectively. Thus, the overall line-shape depends on the competition of their contributions throughout the 3d series. A large spin-polarization P_s^{3d} results in symmetric XMCD peaks (Ni, Co, Fe) whereas a small spin-polarization leads to asymmetric peaks (Cr, V, Ti). It is demonstrated in this work that the XMCD signal of Ti even turns completely asymmetric. Hence, the tendency across the 3d series can in principle be modeled and in addition to the sum rules, further information on the ground-state properties might be obtained by analyzing the spectral distribution of the XMCD spectra.

In a similar way, the multipole-moment analysis has been used in order to separate contributions of different valence states of Cr and V in complicated XMCD spectra of compounds and to determine the magnetic moments [58, 59]. However, the multipole-moment analysis is only correct within the independent-particle model and $2p - 3d$ core-hole interaction has to be taken into account, while the spectra calculated from the MMA model obey rigorously the sum rule analysis, i.e. the spin and orbital moments, used as input parameters for the calculations, can be rederived by applying the sum rules. The latter makes the MMA approach highly suspect, since the spin sum rule breaks down for the early 3d TM's as demonstrated in the previous section. While a proof of the MMA analysis is still lacking, it has been used for detailed analysis of experimental XMCD spectra [58, 59] giving magnetic moments with an accuracy of a few percent. Therefore, it is worthwhile to test the MMA model here.

For the application of the MMA model it is necessary to know the effective exchange field H_{ex} and the lifetime broadening. For this reason the MMA approach

⁶This concept of the multipole moment analysis is explained in sec. 1.2.

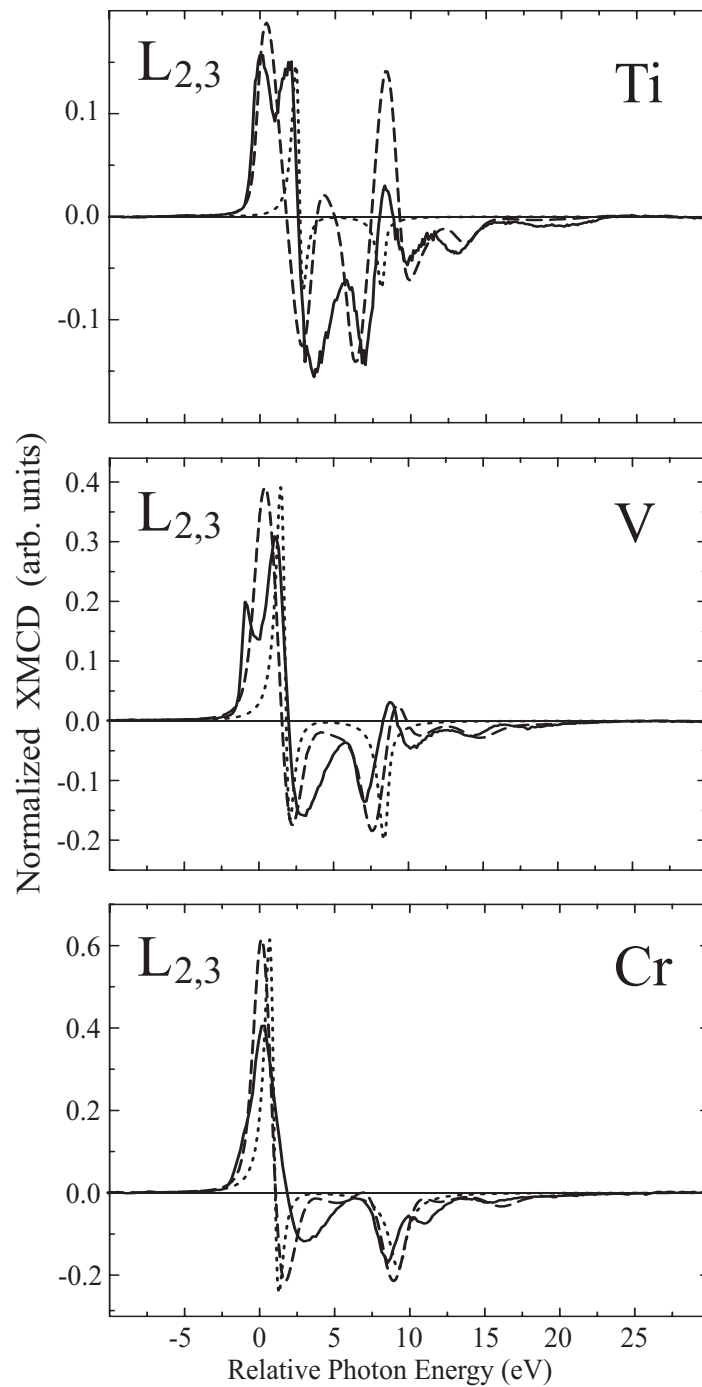


Figure 3.18: Theoretical XMCD spectra for the early 3d TM's: SPR-KKR calculations (dashed lines) versus MMA calculations (dotted lines). Both models are based on an independent particle model. However, the experimental data (solid lines) are described in detail by the SPR-KKR calculations including the spin-dependent band structure.

is tested using the parameters of the SPR-KKR Green's function method. These are: the spin and orbital moments (Table 3.5), the number of d holes (Table 3.1), $H_{ex} = 0.14, 0.25$ and 0.26 eV for Ti, V and Cr, respectively, and a Lorentzian broadening to account for the lifetime of the core hole, i.e. 0.3 eV for the L_3 edge and 0.3 (Ti), 0.5 (V) and 0.8 eV (Cr) for the L_2 edge. The comparison of the two theoretical models (band-structure calculations and multipole-moment analysis) is given in Figure 3.18. The results of the MMA had to be rescaled to match the experimental and theoretical data. Interestingly, the approach qualitatively describes the asymmetric peaks at the L_3 edge and the more symmetric ones at the L_2 edge indicating that the peak asymmetry at the L_3 edge is mostly determined by the spectral distribution of the core hole. However, the energy-dependency of the L_2 XMCD cannot be reproduced. The main difference between the two theoretical models shown for Ti, V and Cr in Figure 3.18 originates from the difference in the spin-dependent DOS, which is only included in the *ab initio* SPR-KKR calculations. One has to note that the line-shape of the L_3 and L_2 edge can be considerably improved upon variation of H_{ex} and the lifetime broadening. Assuming H_{ex} for V is known within 30 % (i.e. ± 0.07 eV) and keeping all other parameters fixed, the uncertainty of the fitted V spin-moment (asymmetry at the L_3 edge) is already of the order of 70 %. The value for spin moment of V is $-1.3 \pm 0.9 \mu_B$ per atom. In turn this result shows that various values for the spin moment can be fitted from the identical XMCD spectrum depending on the strongly correlated parameters of the lifetime broadening and H_{ex} . This demonstrates that the determination of the magnetic moments using a multipole-moment analysis for the early transition metals is questionable. Therefore, the fit to the experiment is not performed but the two calculations are compared to each other in Figure 3.18. The experimental spectra clearly demonstrate that the description of the XMCD is most accurately described by including the band structure. This explains why most of the absorption fine structures, e.g. the oscillatory part slightly above the L_2 edge, are missed by this model.

Chapter 4

Fe/V/Fe(110) Trilayers

$\text{Fe}_n/\text{V}_m(001)$ multilayers grown on $\text{MgO}(001)$ substrates have attracted considerable interest. These single-crystalline epitaxial metallic superlattices (SL's) are a characteristic example for the progress in film-preparation methods. The exceptional structural and magnetic homogeneity have been demonstrated in various works [16, 17, 20, 21, 23, 134, 135]. The Fe_n/V_m SL's thus serve as prototype systems to investigate the rich variety of multilayer magnetism such as the spin-dependent transport properties [17], interlayer exchange coupling [18], the magnetic anisotropies and orbital magnetism [20, 21, 24], the reversible tuning of the magnetic exchange coupling and magnetic moments using hydrogen [19, 136], and the optical constants of Fe probed by x-ray resonant magnetic scattering (XRMS) [137]. Often, the non-magnetic spacer layers in multilayers are assumed to be non-polarized by the ferromagnetic layers. Vanadium, which is at the border to reveal magnetic ordering (next to Cr), is, however, an easy-polarizable element. Therefore, the knowledge of the magnetic and structural properties at the Fe/V interface are of particular interest since the spin-dependent scattering at the interface contributes to the properties of oscillatory interlayer exchange, giant magnetoresistance and spin injection, see e.g. [11–15].

Recent experimental [22, 23] and theoretical [12, 29] studies have shown that the V layers in Fe/V superlattices exhibit induced magnetic moments coupled antiferromagnetically to Fe. However, disagreement exists between experiment and theory concerning the magnitude and the layer-dependent distribution of the V magnetic moment. While theory predicts the V moment to be mainly located at the interface (see Fig. 4.1, Ref. [12]), it is observed from thickness-dependent measurements on Fe/V superlattices that sizable V magnetic moments are induced more than 4 ML

beyond the Fe/V interface [22]. The observation of a long-range polarization of V is explained by a ‘transient ferromagnetic’ state of V [23] and appears controversial with regard to theoretical expectations [29]. Furthermore, *ab initio* calculations found consistently much smaller induced V moments [12, 29, 125, 138]. They are reduced by a factor of 2 – 4, depending on the superlattice orientation, contrary to experiments [22–24]. In Fig. 4.1 the calculated magnetic moment profiles of Fe_n/V_m SL’s are presented for different crystallographic orientations [12]. The hybridization between adjacent Fe and V leads to a reduction of the Fe moment and to a polarization of V at the Fe/V interface. The changes in the Fe and V magnetic moments are thus limited to the interfacial layers and the Fe and V atomic layers approach rapidly their bulk properties beyond the interface. From the top to the bottom in Fig. 4.1, the layer distance of the moment profiles decreases successively according to the SL orientation. The calculations indicate that larger hybridization effects at the Fe/V interface (smaller layer-distance) result in a stronger reduction of the Fe moment

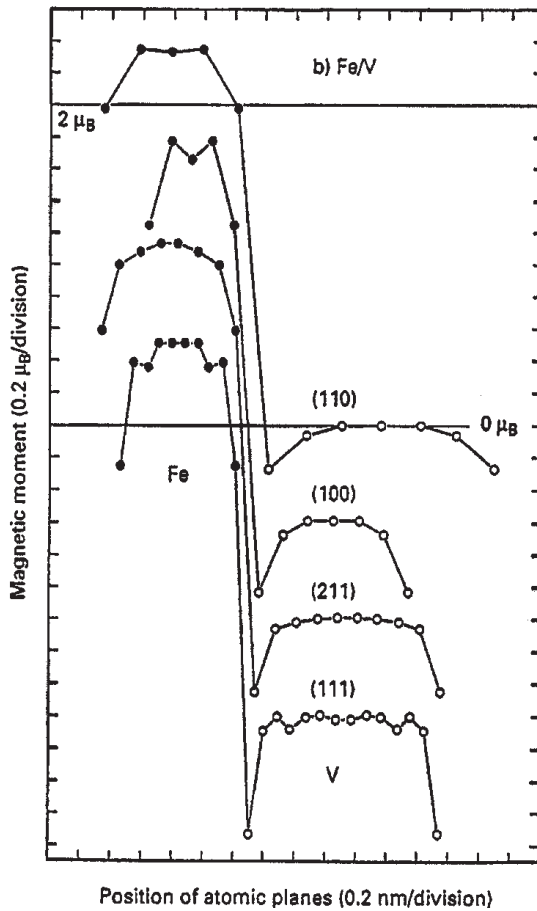


Figure 4.1: Layer-resolved magnetic moment profiles in Fe/V superlattices for various crystallographic directions as indicated, taken from [12]. Each profile has been shifted by $-0.6 \mu_B$ for better readability.

and larger induced V moment. Hence, the observed discrepancies were considered to occur due to intermixing at the first 1–2 interfacial atomic layers [24, 27, 29, 92, 139]. However, no direct probe of the effects of atomic intermixing on the interface magnetic moments exists and the theoretical considerations [12, 27, 30, 139] remain still hypothetical.

In this work Fe/V/Fe(110) trilayers were selected as a prototype unit-cell of the $(\text{Fe}_n/\text{V}_m)_k$ SL's to study the layer-dependent distribution of the V magnetic moment, see the illustration in Fig. 4.2. This selection offers the possibility to *control and modify in situ* the growth and interface quality step-by-step, whereas the growth parameters for SL's such as the deposition rate and temperature cannot be varied *in statu nascendi* in order to improve or modify the interfacial properties. Moreover, the structural and magnetic characterization of the Fe/V/Fe(110) trilayers can be performed *in situ* without protective overlayers which reduce the signal for x-ray absorption measurements. In contrast to *ex situ* samples, the absence of oxygen-contamination allows for measurements of the V-XAS in the full required energy range.

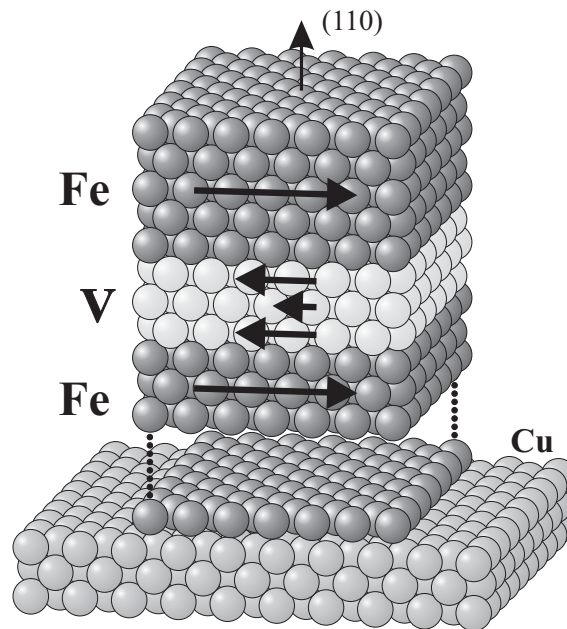


Figure 4.2: Schematic illustration of the Fe/V/Fe(110) trilayers grown on a Cu(100) single crystal.

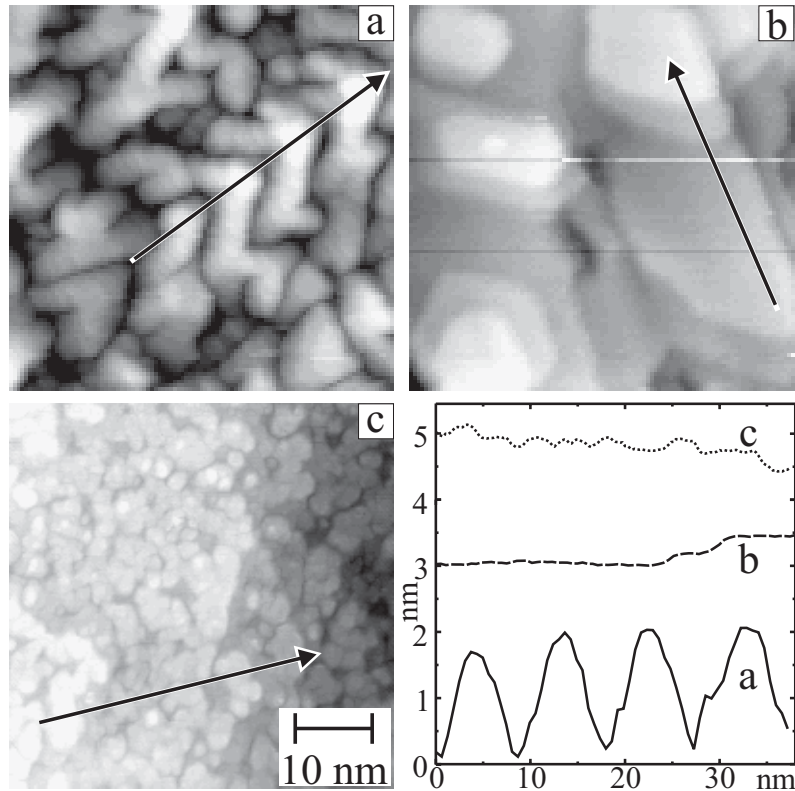


Figure 4.3: STM images illustrate the step-by-step preparation of the trilayers grown at 300 K: (a) 50 ML Fe(110) as grown on Cu(100) and (b) after annealing softly to 450 K. (c) Deposition of 3.0 ML V on the Fe(110)-buffer. (d) Topographic view for (a), (b), and (c) via representative line scans. In (c) the steps are 1 ML high, as expected for layer-by-layer growth.

4.1 Structural properties

$\text{Fe}_5/\text{V}_n/\text{Fe}(110)$ trilayers with n in the range of 1–8 ML were grown on a Cu(100) single crystal by evaporation from high purity rods *in situ* under UHV conditions ($P_{\text{base}} \sim 2 \times 10^{-10}$ mbar). The Cu surface was prepared by several cycles of Ar^+ bombardment and annealing to 900 K. First, a thick Fe buffer-layer (thickness $d \sim 50$ ML) was deposited and then annealed softly to 450 K. Low energy electron diffraction spots showed a bcc(110) structure in agreement with structural investigations of Fe films on Cu(100) [140–142]. In order to investigate the structural properties of the trilayers a Scanning Tunneling Microscopy (STM) study [143] has monitored step-by-step the growth recipe. The STM images for the (a) as-deposited and (b) annealed Fe buffer-layer in Fig. 4.3 confirm that by soft annealing at 450 K the

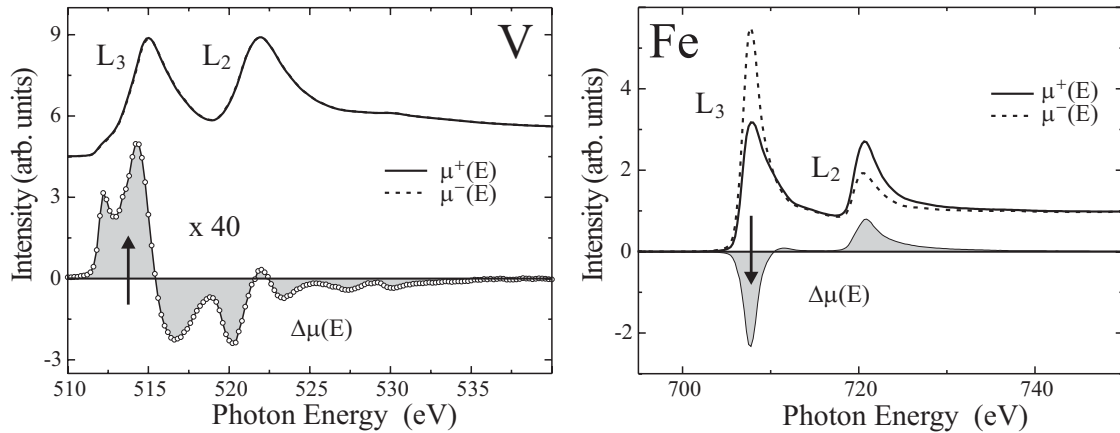


Figure 4.4: Normalized XAS of left (dashed line) and right (solid line) circularly polarized light and the XMCD (highlighted) at the $L_{2,3}$ edges of V (left panel) and Fe (right panel) for a Fe/ V_2 /Fe(110) trilayer. For better illustration the V XMCD has been multiplied by 40, as indicated. Note that the spectra are not corrected for the glancing angle and the circular polarization degree (thus as measured).

surface roughness reduces dramatically as clearly exhibited by the corresponding line-scans. On the annealed surface one can see atomically flat terraces with a broadness of about 15 nm. The possibility to decrease the surface roughness is important for distinguishing between the influence of roughness and interdiffusion on the interfacial magnetic properties.

In order to study the influence of interface quality on the induced V moments two series of trilayers were prepared with variable thickness of the V spacer layers between 1 – 8 ML. For achieving the best interface quality with minute amount of interface atomic exchange, the V spacer was evaporated at 300 K after reducing the roughness of the Fe buffer-layer by soft annealing. It is obvious that this type of growth, i.e. variation of temperature to reduce both atomic exchange processes and roughness, is practically impossible to be employed in conventional multilayers. The low deposition rates for V and Fe were 1 Å per minute promoting a quasi layer-by-layer growth at lower temperatures. In the fabrication process of SL's much higher deposition rates (~ 0.5 Å per second [17, 23]) are typically used and consequently, SL's are grown at higher temperatures (~ 570 K) to achieve the best structural and magnetic homogeneity supported by x-ray diffraction (XRD) data [134] (see chapter 5). Hence, for the first series the V spacer and the top Fe ($d_{Fe} = 5$ ML) films were successively deposited at room temperature (300 K) without further annealing. The STM-image (c) indicates that the growth of V on top of the annealed Fe-buffer

enhances slightly the surface roughness. However, the arithmetic mean roughness for 3 ML V on Fe(110) is 0.09 nm and thus, comparable to the one of 5 ML Ni/Cu(100) for which a layer-by-layer growth up to 5 ML is well established [144, 145]. Since interfaces in these trilayers are atomically flat, any effect of roughness on the interface moments may be neglected. By eliminating the roughness, interdiffusion remains as the only free parameter concerning interface quality. This enables to *switch on* interdiffusion effects by raising the deposition temperature from 300 K to 600 K for the second series of trilayers. The thickness calibration was done via Auger electron spectroscopy and the Fe/V $L_{2,3}$ edge jumps of the x-ray absorption spectra (XAS) and cross-checked with the STM-study. The easy axis of magnetization of the Fe/V-trilayers is in-plane along the [001] Cu direction. Therefore, the samples were measured under 20° grazing incidence of the light and consequently, the Fe and V-XAS spectra were corrected for self absorption effects. The Fe layers for all samples exhibited a magnetization equal to the bulk value (see below) ensuring that the remanent magnetization can be safely translated into magnetic moment per atom units.

4.2 Evidence of short-range spin-polarization

Representative XAS and XMCD spectra at the V and Fe $L_{2,3}$ edges are given in Fig. 4.4. The difference between the absorption spectra of left (dashed line) and right (solid line) circularly polarized x-rays is hardly seen by eye in case of V. The XMCD to XAS intensity ratio of V in the trilayers ranges between 1–7 %. Note the enlargement factor 40 in Fig. 4.4. The reproducibility of the absorption spectra in the ultrathin V films was excellent with a very low signal-to-noise ratio taking benefit of the high brilliance and high degree of circular polarization of an undulator beamline in conjunction with the gap-scan technique (see sec. 2.1). Moreover, working thoroughly *in situ* the absorption signals are not damped by protective capping layers. The high purity of the trilayers is reflected in the absence of the O K edge (~ 530 eV) and allows to carry out the measurements in the required V near-edge energy range. The opposite L_3 onsets of the V and Fe dichroism indicate an antiferromagnetic coupling of the Fe and the induced V magnetic moments in agreement with theory and previous experiments [12, 23, 28, 29]. This interfacial effect can be understood by comparing the Fe and V d bands as illustrated by the scheme in Fig. 4.5. The dip in the density of d states at the Fermi energy stabilizes the Fe

spin-down band. Therefore, the gain of exchange energy lowers the V spin-down band by a transfer of a small amount of spin-up electrons into the spin-down band on the V site forming a common spin-down band with Fe [28]. Thus the $3d$ band of V is spin-split in the opposite direction to Fe, and the induced magnetic moment at the V site is antiparallel aligned to Fe. Through hybridization with the V d band, spin-up electrons are moved to the spin-down band at the Fe site reducing the Fe moment [28].

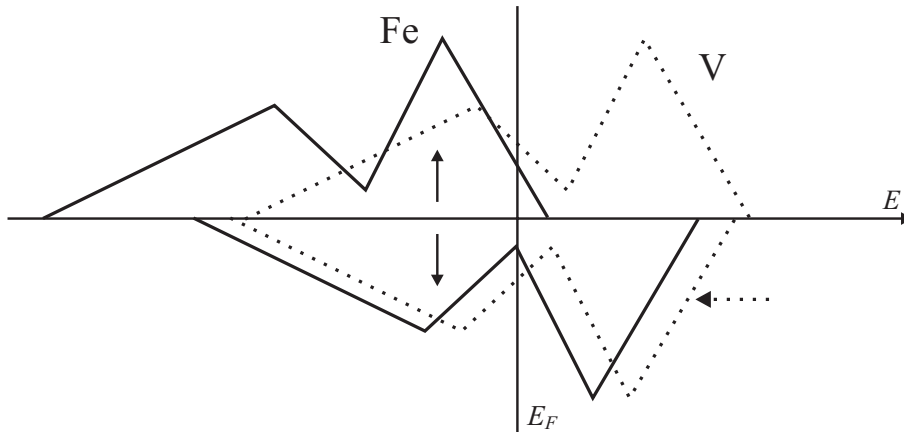


Figure 4.5: Schematic illustration of the Fe and V bulk-like spin-split bands.

However, the reduction of the Fe moment at the interface cannot be probed in this type of trilayers because of the use of thick Fe buffer-layers that limit the sensibility to the interfacial Fe layers. Indeed, the comparison with the Fe bulk spectrum and the conventional analysis using the magneto-optical sum rules [2, 3] (see chapter 3) yielded for all investigated trilayers an Fe magnetic moment which equals within 8% the bulk value of $2.22 \mu_B$ per atom [146]. Moreover, this indicates that the Curie temperature of the samples is bulk-like as one expects for thick Fe layers and the remanent XMCD signals can be safely translated into magnetic moment per atom units. The first direct evidence of reduced Fe moments at the Fe/V interface is given in this work (chapter 5) investigating Fe_n/V_m SL's in the ultrathin Fe film limit [24, 147].

As discussed in chapter 3 the conventional analysis using the sum rules yields erroneous spin magnetic moments for the early $3d$ TM's due to the small spin-orbit splitting of the initial $2p$ core levels that leads to a remixing of spin components of the $2p_{3/2}$ and $2p_{1/2}$ states. Here, the measured amplitudes and areas of the V-XMCD are used for the determination of the induced V moments in the Fe/V/Fe(110) trilayers

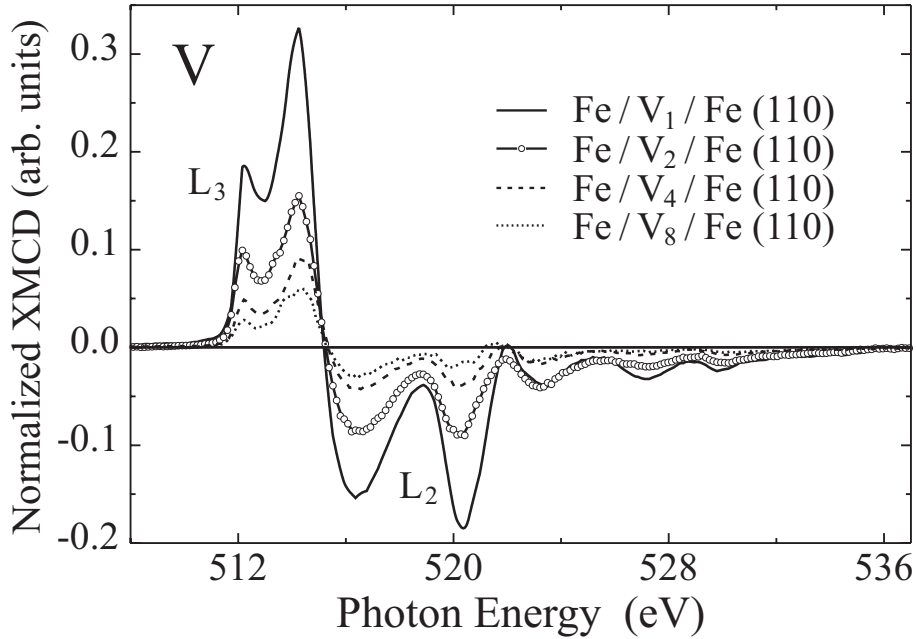


Figure 4.6: Series of normalized XMCD spectra at the V $L_{2,3}$ edges for Fe/ V_n /Fe(110) with $n = 1, 2, 4, 8$ ML as indicated. The amplitude of the XMCD signal decays monotonically with increasing n .

by scaling to the Fe_{0.9}/V_{0.1} reference sample analyzed in chapter 3.

The thickness dependence of the V-XMCD spectra ranging between $n = 1 - 8$ atomic layers is shown in Fig. 4.6. Note that the $L_{2,3}$ edge jumps are normalized to unity. Since XMCD is not a layer-resolved technique the observed XMCD amplitudes reflect the induced V magnetization and the average induced V magnetic moment per atom $\bar{\mu}_V$, respectively. Clearly, the XMCD signal and in correspondence $\bar{\mu}_V$ decays rapidly with the V thickness indicating a short range spin-polarization in V. With regard to the theoretical prediction that the induced V moment is mainly located at the Fe/V interface, the XMCD signal of $n = 8$ ML should be half of the XMCD signal of $n = 4$ ML and the XMCD signal of $n = 4$ ML should be half of the XMCD signal of $n = 2$ ML. This expectation is close to the experimental observation in Fig. 4.6. The slight deviation arises from small contributions of the internal V layers to $\bar{\mu}_V$. Hence, the average induced moment can be expressed in terms of the moments of the individual layers μ_i as

$$\bar{\mu}_V n = \sum_{i=1}^n \mu_i = 2\mu_{Int} + \sum_{i=2}^{n-1} \mu_i = 2\mu_{Int} + (n-2)\bar{\mu}_{Vol}(n) \quad (4.1)$$

where μ_{Int} is the interface V magnetic moment and $\bar{\mu}_{Vol}$ is the average volume

contribution for given thickness n . Hereby, the Fe/V_{*n*}/Fe(110) trilayer with $n = 1$ is a specific case where the single V layer is adjacent to two Fe interfaces and consequently, each V atom has double Fe nearest neighbors compared to the trilayer with $n = 2$. Moreover, it has a two times larger induced V moment as Fig. 4.6 reveals. This means accordingly that the induced V moment depends linearly on the number of Fe neighbors and confirms *ab initio* calculations for Fe/V interfaces [12, 29].

The layer-resolved magnetic moment profile of V in the trilayers in Fig. 4.7 has been deduced under two approximations: both Fe/V interfaces in the trilayers exhibit the same structural and magnetic properties and the induced V moments depend only on the distance of the layer to the Fe/V interface. Both approximations are justified for perfect Fe/V interfaces with regard to theoretical calculations [29]. Hence, according to Eq. (4.1) the profile can be subsequently constructed, starting with $n = 2$ where the interface moment is equal to $\bar{\mu}_V = -0.54(5) \mu_B/\text{atom}$. One finds that already the first layer away from the interface is strongly reduced. Con-

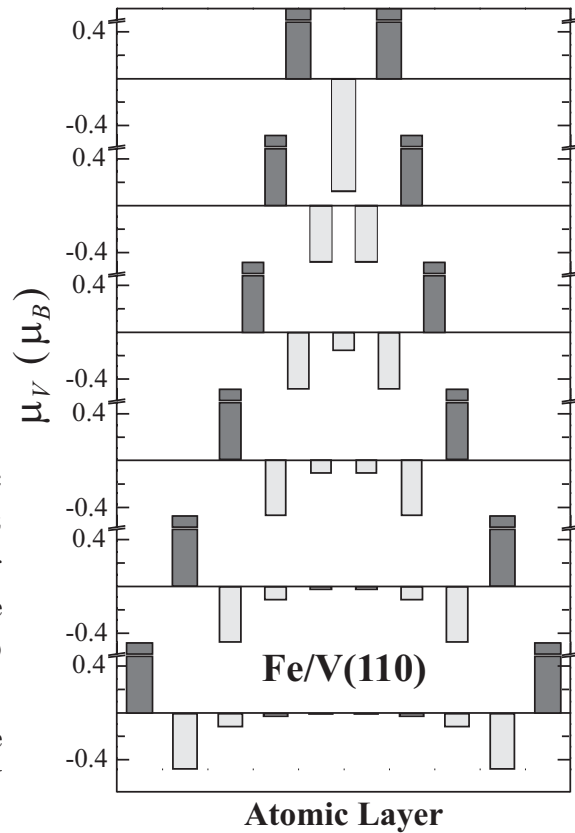


Figure 4.7: Layer-resolved magnetic moment profiles of vanadium (light grey) in Fe/V_{*n*}/Fe(110) trilayers for $n = 1, 2, \dots, 8$ as determined from the thickness-dependence of the V XMCD spectra. The Fe moment (dark grey) at the interface illustrates only the antiparallel alignment of the Fe and V moments.

tributions originating from the second and third layer beyond the Fe/V interface are already small with respect to the interface moment. Hence, the strong thickness-dependence of V-XMCD spectra and the V magnetic moment profile is the first support of the theoretical predictions. The exponential-like decay of the induced V moments is finally quite similar to the calculation from Coehoorn [12] in Fig. 4.1. On the other hand, the existence of a ‘transient ferromagnetic state’ of V in Fe/V superlattices can be excluded in the present work. It is more likely that interdiffusion and/or roughness at the interface accounts for the apparent ‘long range polarization’ in SL’s since the preparation of the Fe/V/Fe(110) trilayers was optimized in terms of reduced interfacial roughness and interdiffusion. This is supported by the interface V moment being $\sim -0.5 \mu_B/\text{atom}$ found in the Fe/V/Fe(110) trilayers. It is closer to the theoretical V moment of $-(0.3 - 0.4) \mu_B/\text{atom}$ (Fe_n/V_m(110) and (100) SL’s, respectively) with perfect interfaces [12, 29] than the experimental one $\sim -1.0 \mu_B/\text{atom}$ (independent of Fe_n/V_m SL orientation) [22, 24].

4.3 Influence of interdiffusion effects on V spin polarization

Several studies during the last decade have determined induced magnetic moments [148, 149] and have revealed extraordinary effects such as the apparent breakdown of the third Hund’s rule [93, 122]. Thickness-dependent XMCD studies [22, 26, 115, 150] and layer-resolved techniques [151] such as the x-ray resonant magnetic scattering (XRMS) have exposed the magnetic moment profiles in magnetic multilayers in an element-specific manner. On the other hand, the role of interdiffusion and roughness in magnetic multilayers and their influence on interface magnetic moments remains from theoretical as well as from experimental point of view hypothetical. However, this is a key point in order to resolve the quite frequently reported discrepancies of the layer-dependent induced magnetic moments. Two characteristic examples are the Ni moments at the Ni/Pt(111) interface, where the experiment revealed by a factor of two reduced Ni moments as compared to theory [26] and, as discussed in the previous section, the V moments at the Fe/V(100) and Fe/V(110) interface, where the experimentally deduced V moments are at least a factor of two larger than the ones that theory predicts [22, 23]. These differences were attributed to interdiffusion effects while a clear evidence of these effects on the interfacial magnetic properties of multilayers is still lacking. In this work the first direct probe of the influence

of interdiffusion on the induced V spin-polarization at Fe/V interfaces in terms of polarization range and magnitude of magnetic moments is presented. This was made possible by eliminating roughness at the Fe/V interfaces and staying with one more free parameter, namely interdiffusion.

In Fig. 4.8(a) the Vanadium XMCD spectra of the trilayers grown at 300 K are plotted against (b) the XMCD spectra of trilayers deposited at 600 K. For

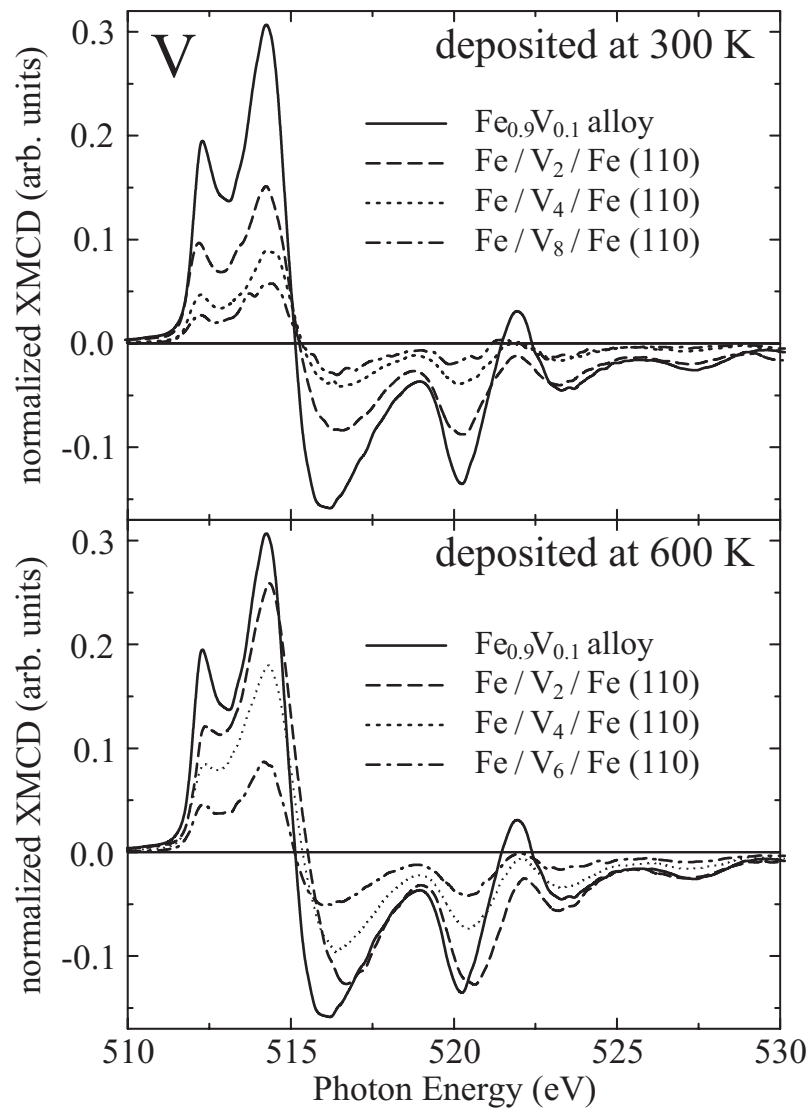


Figure 4.8: Vanadium XMCD spectra in Fe/V/Fe(110) trilayers grown at (a) 300 K and (b) 600 K. The thickness of the V spacer layers is indicated by an index. A spectrum for V in a $\text{Fe}_{0.9}\text{V}_{0.1}$ alloy with an induced V moment $\sim 1\mu_B/\text{atom}$ is included as a reference in both data sets.

visualizing the magnitude of the induced magnetic moments, the XMCD reference spectrum of an $\text{Fe}_{0.9}\text{V}_{0.1}$ alloy for which the V moment is equal to $0.99\mu_B/\text{atom}$ (see chapter 3) has been added to both series. By raising the deposition temperature, the V-XMCD signal for $n = 2$ almost doubles with regard to the V spectrum for $\text{Fe}/\text{V}_2/\text{Fe}$ trilayer at 300 K which corresponds to $\sim -0.5 \mu_B/\text{atom}$. Interestingly, *ab initio* calculations for the $\text{Fe}/\text{V}(110)$ interfaces expect such an increase of the interfacial V moment as one moves from the ideal (non mixed) to the diffused Fe/V interface [29, 110]. Hereby, the value of the induced V moment at the Fe/V interface approaches the magnitude of V in the alloy and thus, is of the order of the induced V moments reported in Fe_n/V_m SL's [23, 24]. Moreover, the XMCD intensities of trilayers at 600 K are systematically enhanced with respect to the series at 300 K. This suggests that internal V layers are polarized and contribute to the XMCD signal.

In Fig. 4.9 thickness-dependent integrated V magnetic moments in $\text{Fe}/\text{V}(110)$ trilayers deposited at 300 K (closed circles) and at 600 K (open squares) are plotted. This type of plot has the advantage of revealing whether the internal atomic layers of V are magnetized or not. If the integrated-moment curve does not saturate then also the internal layers are magnetized. According to Eq. (4.1), the contributions of the interface and the internal layers are schematically shown in Fig. 4.9 for the trilayers grown at 300 K. The strong effect of the deposition temperature on the XMCD intensities as seen in Fig. 4.8 (a) and (b) is also reflected in the integrated V moments of Fig. 4.9. The curve for the trilayers deposited at 300 K approaches very fast the saturation (~ 3 ML). This is basically the observation of the ‘short-range’ V polarization as discussed in the previous section. Moreover, the slight deviation of the monotonous increase of the integral might be due to small variation of the V moments of the interface and the inner layers with the total V thickness. Indeed, theoretical calculations found such variations with the thickness in the layer-resolved moment profiles of V [23, 29]. However, these variations are small with respect to the magnitude of the induced V moments. Hence, the theoretical curve for the ideally sharp interfaces (solid-line) is practically constant with small oscillations as a function of the V thickness. The main behavior of the integral curve, i.e. the short-range polarization of V, does not change upon interdiffusion at the Fe/V interface in the theory. The dotted curve corresponds to calculations where the Fe and V interface layers are modeled as a single intermixed interface layer and termed as ‘diffused’ interfaces [12]. The direct comparison with the trilayer datasets

manifests that the current deposition on atomically flat Fe(110) terraces at 300 K leads to integrated V magnetic moment curves similar to the ones expected for almost ideal interfaces. However, the integrated-moment curve for trilayers grown at 600 K (open squares) shows a considerable increase. This result is consistent with the experimentally deduced dashed-line curve [23] which does not saturate and corresponds to the so-called ‘long-range’ order polarization of V in Fe/V superlattices on MgO(001). This term was used to characterize the polarization of the internal V for at least 3 – 4 atomic layers beyond the Fe/V interface and suggested a ‘transient ferromagnetic state’. Here, it is demonstrated on the basis of the trilayer datasets that deposition at 600 K results in the formation of more than one interdiffused layer at the Fe/V interface. Interestingly, the considerable decrease of the integrated moment for $n = 6$ ML of the 600 K deposited trilayers reveals a reduction of the V

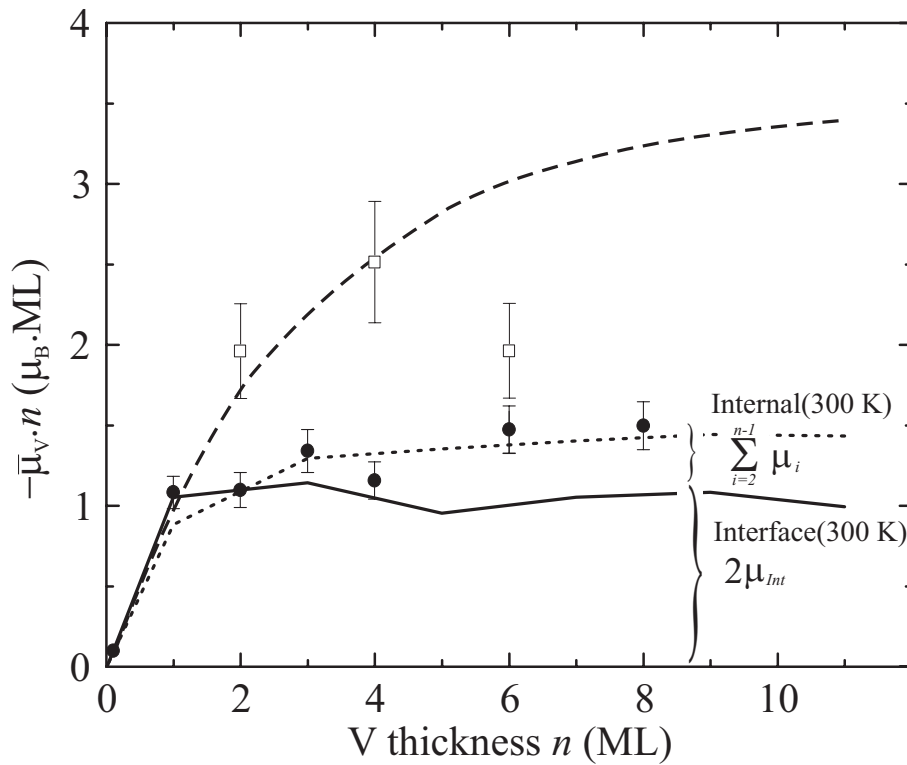


Figure 4.9: Thickness dependence of the integrated V magnetic moments in Fe/V(110) trilayers grown at 300 K (closed circles) and grown at 600 K (open circles). A ‘long-range’ spin-polarization of V in Fe/V(100) superlattices was reported in Ref. [23] (dashed line). Theoretical calculation of the integrated V moments assuming perfect (solid line) and ‘diffused’ interfaces (dotted line) indicating a ‘short-range’ spin-polarization [12, 23].

spin-polarization in the intermixed layers. The Fe atoms positioned at the interface and within the interdiffused layers carry reduced magnetic moments relative to Fe bulk depending very strongly on the number of V neighbors [12, 24, 29]. Therefore, they influence the spin-polarization in the intermixed layers. This could explain why the polarizability of the intermixed-layers for $n = 6$ ML reduces, even when the V-thickness is sufficient to separate the Fe buffer-layer from the top Fe layers.

The V magnetic moments at the interface (I) and at the second inner V layer (I-1) presented in Fig. 4.10 are deduced under two approximations as already above-mentioned: both Fe/V interfaces in the trilayers exhibit the same structural and magnetic properties and the induced V moments depend only on the distance of the layer to the Fe/V interface. The values of the V moments for the series deposited at 300 K are similar to the theoretical ones of Refs. [12, 29] deduced for the ‘short-range’ V polarization. Since the approximations for the layer-resolved moments become *invalid* for the interdiffused samples, the ‘long-range’ polarization of

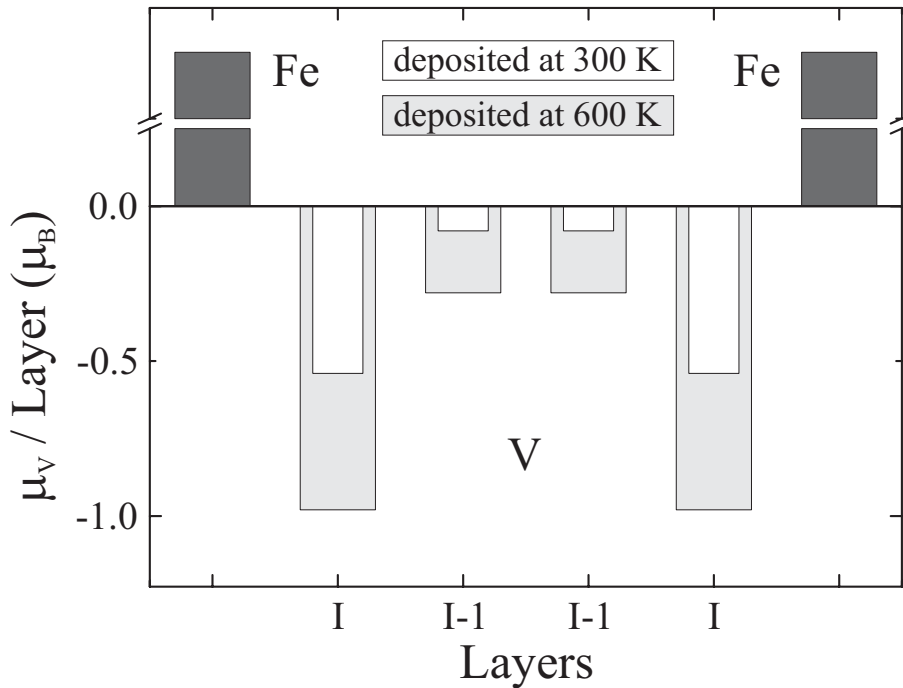


Figure 4.10: Influence of the interdiffusion by raising the deposition temperature from 300 K to 600 K on the layer-resolved induced V moment profiles in the Fe/V(110) trilayers. The errors of the absolute values $\bar{\mu}_V$ are 10 % and 15 % for the 300 K and 600 K series, respectively. The Fe interface moment has been plotted for better illustration only. The negative V moments indicate antiparallel alignment between Fe and V.

V is an apparent one. The large V moments for the interdiffused trilayers are close to the experimental ones shown for Fe/V superlattices grown on MgO(001) [22–24] (see chapter 5).

Finally, the results allow for discussing another two observations in Fe_n/V_m SL's: (i) The enhanced interface V moments and the 'long-range' polarization of V were probed in SL's grown at lower temperatures of 370 K [22] and higher temperatures of 570 K [23]. (ii) The induced V magnetic moments as a function of the V-layer thickness for the (001) and the (110) growth orientations were found to be indistinguishable [22]. Measurements of XRD spectra of Fe_n/V_m SL's deposited at temperatures slightly above room temperature indicate that those SL's suffer from roughness [134]. Therefore, it turns out that roughness also results in the formation of large interface V moments and 'long-range' polarization profiles. In prototype trilayers, even though deposited at room temperature, roughness was avoided (Fig. 4.3) because the trilayers are ultrathin (2 nm or thinner) while superlattices are typically more than one order of magnitude thicker. Since roughness increases with the total film thickness mainly due to kinetics, the superlattices are deposited at higher temperatures leading to atomically flat layers and improving considerably the XRD patterns [134], see also Fig. 5.2 for the Fe_n/V_m superlattices investigated in this work. However, this promotes atomic exchange processes and results in interdiffused interfaces and, subsequently, to the formation of large V moments at the Fe/V interfaces [23, 24]. The *in situ* control of interfaces by tuning the deposition temperature helped in bridging experiment and theory and shed light on the effects of interdiffusion on the induced spin polarization at spacers in magnetic multilayers.

Chapter 5

Interfacial Magnetic Properties of Fe/V(100) Superlattices

In the previous chapter 4 the induced magnetic moment profiles and the role of interdiffusion has been discussed in detail. Here, the magnetic properties of the ferromagnetic Fe layers in $\text{Fe}_n/\text{V}_m(100)$ on $\text{MgO}(100)$ SL's are investigated (see schematic illustration 5.1). In previous investigations the Fe moments in the SL's were found to be bulk-like [22, 23]. However, the results remain doubtful, since theoretical investigations report unanimously a sizable reduction of the Fe moments at the Fe/V interface [12, 28–30] leading to a controversial discussion in literature. In this work Fe_n/V_m SL's were selected with very thin $n = 1, 2, 4$ and $m = 2, 4, 5$ Fe and V layers in order to be sensitive to the interface magnetism and to quantify the Fe and V moments at the common interface. Investigations by SQUID [152] and VSM show strongly reduced magnetizations of the SL's with regard to Fe bulk. There might be two origins for the decrease: (i) The Fe moments are reduced at the Fe/V interfaces and (ii) the Fe moments are *not* reduced but the induced, negative V moments lower the entire sample magnetization. By combining conventional magnetometry with the element-specific XMCD technique one can disentangle the two contributions. It turns out that both effects (i) and (ii) account for the reduced magnetizations in these SL's in agreement with theory resolving the controversial discussion. Moreover, measurements of the spectroscopic splitting g -tensor in Fe_n/V_m SL's by Ferromagnetic Resonance (FMR) revealed a large orbital magnetism [21] which was attributed solely to the ferromagnetic Fe layers. By comparing the orbital to spin moment ratios for Fe via XMCD with the g -factors of FMR, it is demonstrated that the unquenching of the Fe orbital moment and the antiparallel

induced V magnetic moments contribute -within the FMR measurements- to the (apparent) enhancement of the orbital magnetism in these SL's. Finally, superparamagnetic behavior is observed in the ultrathin Fe film limit $n = 1.6$ which is a novel effect in superlattices.

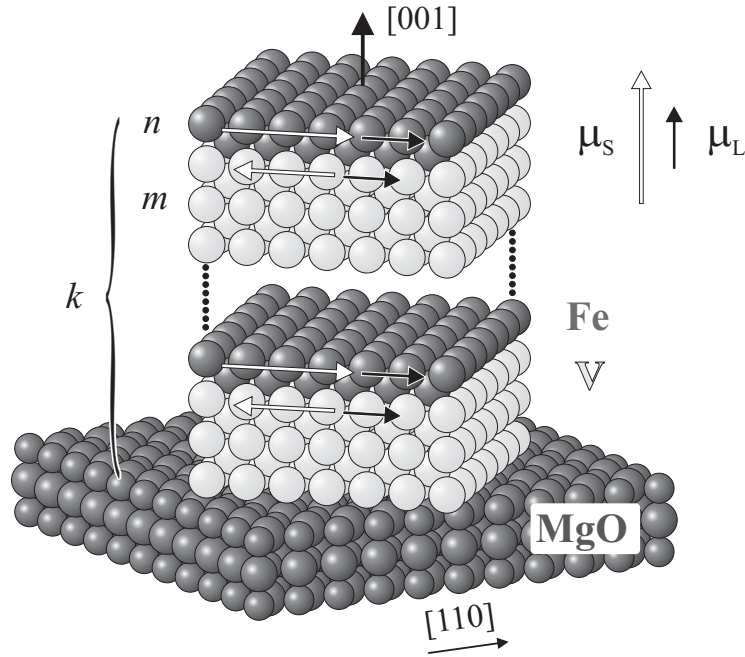


Figure 5.1: Schematic illustration of the $(\text{Fe}_n/\text{V}_m)_k$ SL's.

5.1 Structural properties

The $(\text{Fe}_n/\text{V}_m)_k$ superlattices with n, m being the individual thicknesses in atomic layers and k being the number of repetitions of the unit cells were prepared by P. Blomquist at the University in Uppsala-Sweden. These single-crystalline SL's of Fe/V(001) were grown on MgO(001) wafers using a three-source ultra-high-vacuum-based sputtering equipment. Typical deposition rates were 0.5 \AA per second and the deposition temperature of 600 K was optimized to achieve the highest crystal coherence [134]. The latter is proven by conventional $\theta - 2\theta$ x-ray diffraction (XRD) measurements (Cu $K\alpha$ radiation) by P. Blomquist and are presented in Fig. 5.2 for the investigated samples $(\text{Fe}_2/\text{V}_5)_{50}$, $(\text{Fe}_4/\text{V}_4)_{45}$ and $(\text{Fe}_4/\text{V}_2)_{60}$. In the low-angle XRD (glancing incidence of the x-rays) one observes the so-called Kiessig fringes that stem from interference of reflected beams between the multilayer/substrate-

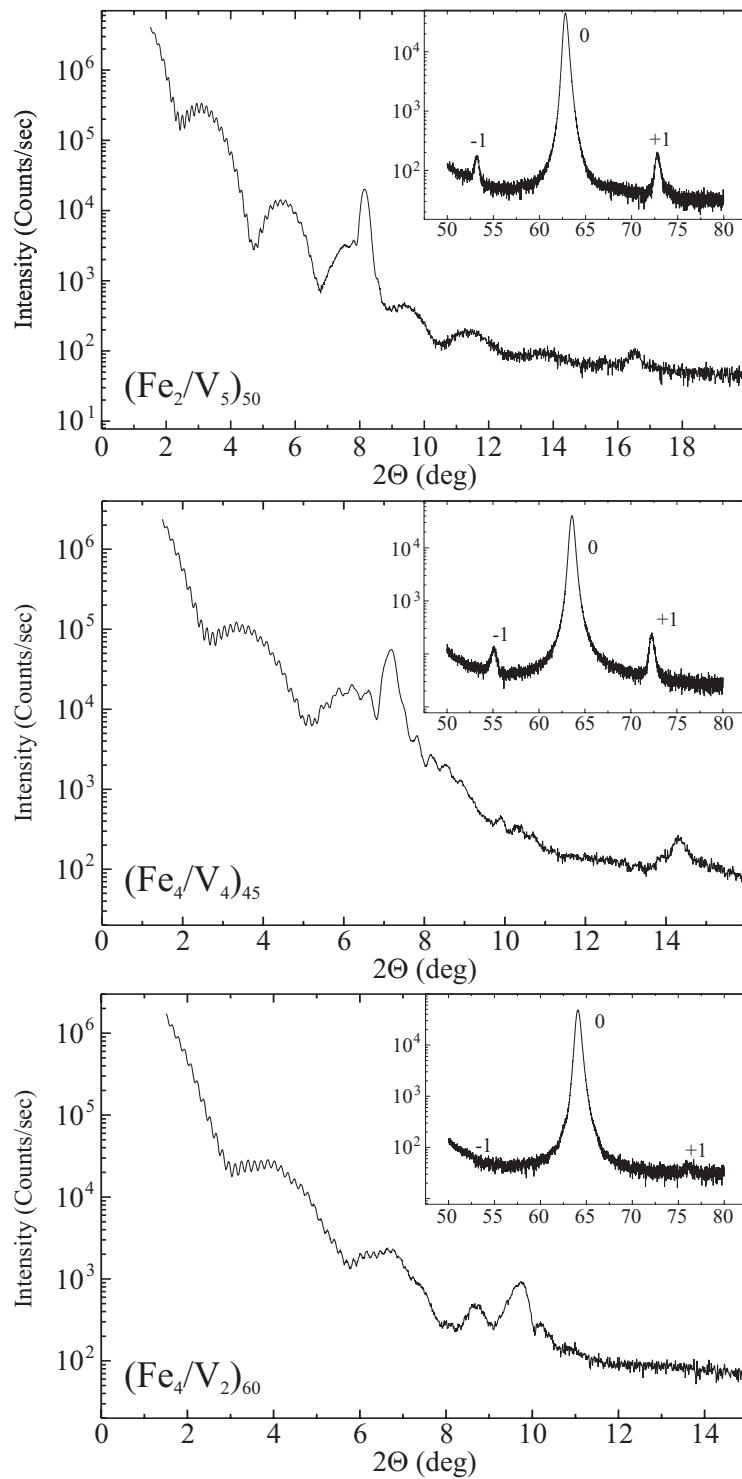


Figure 5.2: The small-angle and the high-angle XRD spectrum (inset) are shown for the investigated $(\text{Fe}_n/\text{V}_m)_k$ SL's as indicated.

interface and multilayer-surface (small period). The longer period originates from the protective Pd-layer on top of the samples. Hereby, the more the features become prominent the smaller is the thickness-variation throughout the multilayer stack. Moreover, distinct Bragg peaks appear through variation of the reflectivity according to the multilayer period. The appearance of higher order peaks indicate sharp Fe/V interfaces. However, there is only a single prominent peak in case of the $(\text{Fe}_4/\text{V}_2)_{60}$ SL suggesting that the Fe/V interfaces are less sharp due to roughness or interdiffusion. It is valuable to note that XRD measurements cannot accurately discriminate between roughness and interdiffusion [155]. A disentanglement of the two effects at interfaces in multilayers and their role in view of the magnitude and polarization-range of the induced magnetism has been presented in chapter 4 for prototype Fe/V trilayers. The individual layer thicknesses d_{Fe} and d_{V} can be determined from simulations of the low-angle reflectivity data and the modulation period $\Lambda = d_{\text{Fe}} + d_{\text{V}}$ can be deduced from the position of the multilayer peaks. The high SL quality of the $(\text{Fe}_2/\text{V}_5)_{50}$ and $(\text{Fe}_4/\text{V}_4)_{45}$ SL is also supported by the presence of satellite diffractions $(+1, -1)$, except for the $(\text{Fe}_4/\text{V}_2)_{60}$ sample, around the average interplanar spacing diffraction (0) in the high-angle XRD spectra (insets in Fig. 5.2) which is a signature of a well-defined multilayered structure. The interfacial roughness is in correspondence $\pm 1 \text{ \AA}$ for these samples [153]. From the average interplanar spacing diffraction the average lattice parameter $c_{\text{Fe,V}}$ was determined to 2.93 \AA , 2.90 \AA and 2.89 \AA for the $(\text{Fe}_2/\text{V}_5)_{50}$, $(\text{Fe}_4/\text{V}_4)_{45}$ and $(\text{Fe}_4/\text{V}_2)_{60}$, respectively. In comparison to the bulk values $a_{\text{Fe}} = 2.87 \text{ \AA}$ and $a_{\text{V}} = 3.03 \text{ \AA}$ the average interplanar spacing is closer to the V bulk value when the multilayer composition incorporates more V than Fe layers and vice versa. According to this, one expects strain induced effects on the Fe side for V-rich multilayers. More details on the structural analysis can be found in Refs. [16–18, 134].

5.2 XMCD versus VSM: Interfacial Fe and induced V moments

For the determination of the saturation magnetization hysteresis loops were recorded along the easy axis of the magnetization in the film-plane at 10 K by VSM, i.e. along the $[100]$ -direction for the $(\text{Fe}_4/\text{V}_2)_{60}$ and $(\text{Fe}_4/\text{V}_4)_{45}$ SL's and along the $[110]$ -direction for the $(\text{Fe}_2/\text{V}_5)_{50}$ SL. The XMCD experiments have been performed at the ESRF on the ID12B beamline [86–88]. Element-specific $L_{2,3}$ XMCD spectra

of Fe and V were carried out at 10 K according to the VSM measurements. The Fe_n/V_m SL's were probed along the normal of the surface plane (the hard axis of the magnetization). In this geometry one circumvents the drawback of saturation effects in the TEY ([61,62,64], see appendix B). Large magnetic fields up to 60 kOe were found to be sufficient for the complete magnetic saturation of the samples. The XMCD spectra were obtained both by reversing the direction of the magnetic field and by inverting the helicity of the x-rays. This procedure allows to rule-out artificial magnetic backgrounds in the XMCD spectra in applied fields using the TEY. The circular polarization degree was 85 % (72 %) for Fe (V) $L_{2,3}$ energy range [88] with the wave vector k parallel to the magnetization direction.

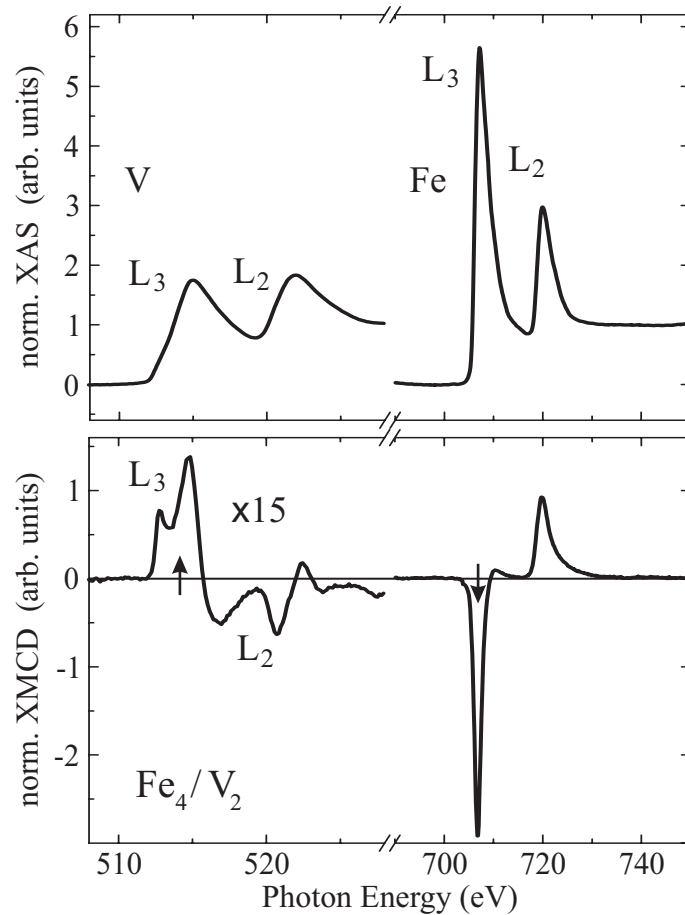


Figure 5.3: Normalized (top) XAS and (bottom) XMCD spectra at the $L_{2,3}$ edges of V and Fe for the Fe_4/V_2 superlattice. The V dichroism has been enlarged by factor 15 for better illustration. The directions of the Fe and V magnetization reflected by signs of the dichroic onsets are indicated by the arrows.

Normalized XAS and XMCD spectra at the Fe and V $L_{2,3}$ edges of the Fe_4/V_2 SL are displayed in Fig. 5.3. Since the Fe_n/V_m SL's are removed from UHV after capping them with a protective Pd layer and exposed to air, they reveal traces of oxygen. As a consequence, the V XAS spectra are truncated just below the energy of the O K edge (~ 530 eV) due to the oxygen edge jump, and the V $L_{2,3}$ edge jump cannot be normalized to unity. Therefore, the $L_{2,3}$ XAS intensities of V appear smaller with regard to Fe. However, the V and Fe XAS spectra exhibit a clear metallic signature, i.e. there is no indication of compound formation (see Fig. 5.3). The presence of an XMCD in vanadium shows an induced magnetic moment. As found in Fe/V/Fe(110) trilayers in chapter 4, the dichroism of V and Fe reveal opposite signs of the L_3 onsets marked by the arrows in Fig. 5.3 and manifests the antiparallel alignment between Fe and V moments in agreement with theory and previous experiments [12, 23, 29]. As discussed in chapter 3, the V dichroism is small compared to the isotropic XAS spectrum. Therefore, the XMCD spectrum has been enlarged by factor 15. About twenty XMCD pairs were needed in order to resolve the dichroism with a high signal-to-noise ratio. This is mainly due to (i) the damping of the absorption signal from the protective capping layers and (ii) the lower flux and circular polarization degree in the V $L_{2,3}$ energy range. Direct comparison of the XMCD to XAS peak ratios with the $\text{Fe}_{0.9}\text{V}_{0.1}$ reference sample (chapter 3) indicate an induced V moment of the order of $-1 \mu_B$ per atom for the Fe_4/V_2 SL. In the following the induced V moments are obtained without invoking the problematic sum rule analysis for the early 3d TM's (chapter 3).

Unlike previous works, the V magnetization and the related average V moment μ^V were determined in an absolute manner by subtracting the Fe magnetization deduced from the XMCD measurements from the total magnetization probed by the conventional magnetometry VSM. In Fig. 5.4 the XMCD spectra of Fe in Fe_n/V_m with $n/m = 4/2, 4/4$ and $2/5$ are shown in comparison with a 40 nm Fe/MgO(001) sample serving as a bulk reference. Since the XMCD intensity is approximately proportional to the magnetic moment, the Fe magnetic moment μ^{Fe} in the Fe_4/V_2 SL is almost bulk-like. On the other hand, one sees a clear reduction of μ^{Fe} when increasing the number of V layers or decreasing the number of Fe layers in the unit cell of the multilayer stack. The results show that the magnetic moment per Fe atom μ_{Fe} (see Table 5.1) is strongly influenced by the numbers n and m in the Fe_n/V_m SL's. The average Fe magnetic moments were determined by application of the sum rules. Hereby, the common procedure for the transition elements discussed

in chapter 3 has been used. The sum rules give a total moment for the 40 nm Fe/MgO(001) sample using a value of $n_h = 3.4 d$ holes per atom [7] which is within 6 % the literature value being $2.22 \mu_B$ for bulk Fe [146]. This proves the applicability to the measured spectra. The results for the Fe magnetic moments in the Fe_n/V_m SL's are summarized in Table 5.1. In case of the Fe bulk-sample the magnetic dipole term $\langle T_z \rangle$ can be neglected in the spin sum rule, while it may be enhanced at the Fe/V interface. Therefore, the deduced values of the spin moment μ_S are effective values.

On the same samples, measurements of the entire magnetization at 10 K were performed. In Ref. [21] the assumption was that the sample magnetization is rigorously determined by the ferromagnetic Fe layers. The magnetic moment μ^{tot} is thus normalized to the Fe atoms only and set out in Table 5.1. For all Fe_n/V_m SL's it is evident from the deviation of μ^{tot} from μ^{Fe} that there exists an additional negative

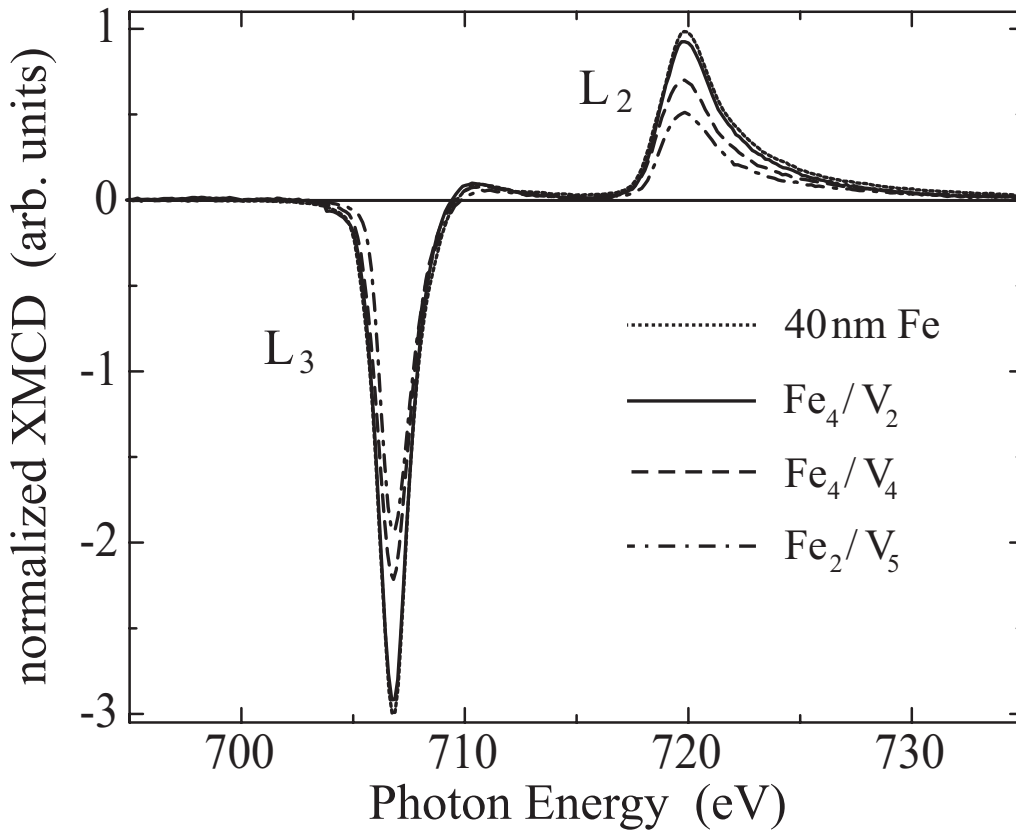


Figure 5.4: Normalized XMCD spectra at the $L_{2,3}$ edges of Fe for the Fe_n/V_m SL's and a 40 nm Fe/MgO(001) reference sample as indicated at $T = 10$ K and $H = 60$ kOe.

Table 5.1: Total magnetic moment μ^{tot} measured by VSM and normalized to the number of Fe atoms only, Fe moment μ^{Fe} by XMCD and V moment μ^V obtained as it is explained in the text. Typical error bars by the VSM and XMCD technique are in the range of 5–10 %.

sample	μ_{tot} (μ_B/atom)	μ^{Fe} (μ_B/atom)	μ^V (μ_B/atom)
40 nm Fe	–	2.22	–
$(Fe_4/V_2)_{60}$	1.59	2.12	-1.06
$(Fe_4/V_4)_{45}$	1.28	1.70	-0.42
$(Fe_2/V_5)_{50}$	0.67	1.34	-0.27

contribution arising from the polarization of the V spacer layers. Moreover, the contribution of V to the sample magnetization is sizable (deviations of 20–50 %) when comparing the values for μ^{tot} and μ^{Fe} . It demonstrates that the contribution of polarized spacers in multilayers have to be taken explicitly into consideration for the interpretation of non-element-specific data such as the sample magnetizations by conventional magnetometry (e.g. SQUID [152], VSM) and spectroscopic splitting g -tensors by FMR [21, 154].

The induced V moments μ^V in Table 5.1 are the difference between μ^{Fe} and $\mu^{tot} = \mu^{Fe} + \mu^V$ normalized per Fe and V atoms. The negative sign of μ^V is consistent with the antiparallel coupling of the Fe and V moments deduced from the signs of the Fe-XMCD and V-XMCD spectra in Fig. 5.3. As abovementioned for Fe, the V moments also seem to depend on the SL composition. The maximum induced V moment $\mu_V = -1.06 \mu_B/\text{atom}$ is obtained by intercalating only $m = 2$ atomic layers of V between Fe in the Fe_4/V_2 SL. Such large induced V moments cannot account for perfectly sharp interfaces as *ab initio* calculations [12, 29] suggest. This is supported by the single multilayer peak in the low-angle and the absence of satellite diffractions in the high-angle XRD spectrum of the Fe_4/V_2 sample indicating imperfect Fe/V interfaces. As it was demonstrated with the help of prototype Fe/V/Fe(110) trilayers in chapter 4, both roughness and interdiffusion lead to the considerable enhancement of the V spin-polarization. Moreover, one can assume that the ferromagnetic Fe layers are not completely separated by very thin V spacer ($m = 2$) through roughness and interdiffusion and could explain why the observed Fe moment μ^{Fe} in the SL approaches the bulk value, see Table 5.1. By increasing

the spacer m both the induced V moment and the Fe moment decreases considerably. Note that the latter samples revealed a well-defined multilayered structure by means of the XRD measurements. The reduction of the Fe moment supports the theoretical predictions [12, 28, 29] (see also explanation of Fig. 4.5) and a previous experiment for Fe₁₀/V _{m} SL with $m = 5 - 10$ ML [156]. In addition, by keeping m almost constant, one observes a decrease of μ^V when the Fe thickness n is decreasing. Hereby, the induced V magnetic moment seems to scale with the one of Fe (see the last two rows of Table 5.1). Hence, the Fe moments are reduced at the Fe/V interface and the strength of the V spin-polarization depends on the Fe moment.

The influence of the Fe _{n} /V _{m} SL composition on the Fe and V moments can be summarized as follows: (i) By decreasing n and keeping m constant, the Fe moment decreases due to the reduction of the Fe moments at the interface. (ii) By increasing m and keeping n constant, a sizable reduction larger than 20 % of the Fe moment is deduced. This suggests that the Fe moment at the interface depends on the quality of the Fe/V interface with regard to the results from XRD data. The induced V moment reduces since inner V layers are less polarized in agreement with the results found in prototype Fe/V/Fe(110) trilayers.

5.3 XMCD versus FMR: Orbital magnetism in layered structures

In this section the orbital to spin moment ratio μ_L^{Fe}/μ_S^{Fe} of the Fe _{n} /V _{m} SL's is analyzed. The ratio is deduced from the sum rule analysis as illustrated in section 1.3. The circular polarization degree P_c , the number of d holes n_h and the normalization factor N (integrated isotropic absorption spectrum) do not enter into the determination of the orbital to spin moment ratio via the sum rules. A first indication of enhanced orbital contributions for the thin Fe layers in the Fe _{n} /V _{m} SL's can be seen Fig. 5.4 where the series of Fe XMCD spectra are presented. Going towards the thin Fe layers, $n = 2$, the XMCD signal reduces differently by ca. 35 % at the L_3 edge and ca. 45 % at the L_2 edge with respect to the Fe bulk reference sample. Hence, the ratio R with $-1 < R < 0$ (defined as the L_2 over the L_3 dichroic area with regard to Eq. (1.26)) becomes smaller and $\mu_L^{Fe}/\mu_S^{Fe} = 2(1 + R)/3(1 - 2R)$ increases.

The complete results for Fe determined by the use of the sum rules are denoted by full circles in Fig. 5.5. The orbital to spin moment ratio for the Fe bulk reference sample is in very good agreement with the literature value [7] given by the dotted

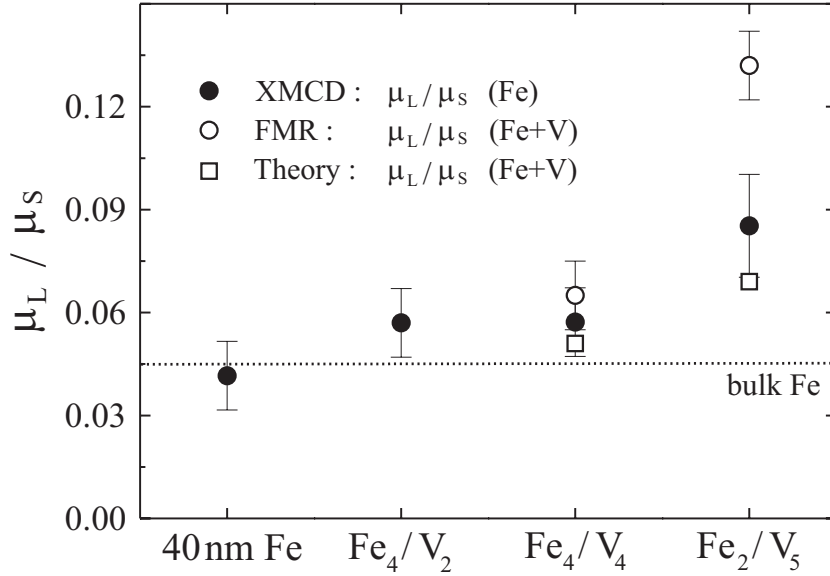


Figure 5.5: The ratio μ_L^{Fe}/μ_S^{Fe} for Fe (full circles) in three superlattices and the bulk reference sample as indicated. The ratios $\mu_L^{Fe+V}/\mu_S^{Fe+V}$ for those samples (open circles) are deduced by FMR [21,154]. Theoretical calculations are given as open squares [30].

line. A systematic enhancement of μ_L^{Fe}/μ_S^{Fe} is found by going from the bulk towards the thinner Fe layers. For the Fe₂/V₅ sample this enhancement is about 100 %. In the same figure values for μ_L/μ_S (open circles) determined by g -tensor measurements via FMR [21, 154] are included according to the relation [157]

$$\frac{\mu_L}{\mu_S} = \frac{g - 2}{2}. \quad (5.1)$$

Since the entire magnetization (Fe and V) precesses resonantly to the microwave field in an applied external magnetic field (for details see [158]) FMR is not element-specific. Therefore, the method provides an averaged $\mu_L^{Fe+V}/\mu_S^{Fe+V}$ value for the Fe_{*n*}/V_{*m*} SL's and one needs to account for the contribution from the induced V moments which cannot be neglected for the Fe_{*n*}/V_{*m*} SL's investigated in this work. The 3*d* shell of the early 3*d* element V is less-than-half filled and the orbital and spin moment are antiparallel aligned in the atomic configuration predicted by the third Hund's rule, i.e. $\mu_L^V/\mu_S^V < 0$ and $g < 2$. As shown in chapter 3 in the Fe/V/Fe(110) trilayers and Fe_{*n*}/V_{*m*} SL's, relative alignment of the orbital and spin moment of V obeys the third Hund's rule also in the solid state. This, however, has the following consequence: Due to the antiferromagnetic coupling between Fe and V, the spin moments of Fe and V are antiparallel oriented but the orbital moments are aligned

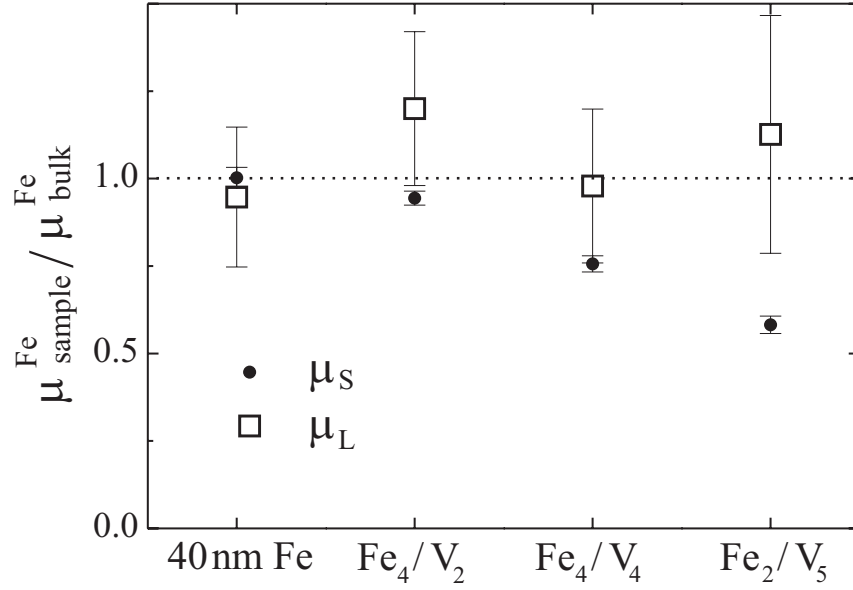


Figure 5.6: The orbital and the spin moment for three superlattices and the bulk reference sample as indicated.

in parallel. This means that in FMR measurements the spin moments partially cancel out and the orbital moments add up. Hence, the ratio probed by FMR is apparently larger than the one of Fe probed by XMCD as Fig. 5.5 reveals. The same trend for the enhancement of the total ratio is determined by *first principles* theoretical calculations (open squares) [30]. This demonstrates that the enhanced orbital over spin magnetism measured by FMR has two origins: (i) unquenching of the orbital moment in the ultrathin Fe limit (see below) and (ii) the contribution of the induced magnetism in the V spacer layers.

In Fig. 5.6 the orbital moment μ_L is separated from the spin moment μ_S for Fe. Both contributions are normalized to their corresponding bulk values $\mu_S^{\text{bulk}} = 2.12 \mu_B$ and $\mu_L^{\text{bulk}} = 0.095 \mu_B$. It turns out that within the error bar μ_S reduces by 40 % at the ultrathin limit, while μ_L stays constant. The trend of the spin moment is in agreement with theory that predicts a reduction of the Fe moment at the Fe/V interface caused by hybridization effects. On the other hand, there is a significant unquenching of the orbital moment, see e.g. [68, 159], due to the lowering of the symmetry at the Fe/V interface. Moreover, in the ultrathin Fe limit the structure deviates from Fe bulk, i.e. the specific lattice parameter of Fe and V normal to the surface plane depends on the composition n, m of the SL as indicated by the XRD data for the Fe_{*n*}/V_{*m*} SL's [16, 17]. Therefore, the constant orbital moment can be

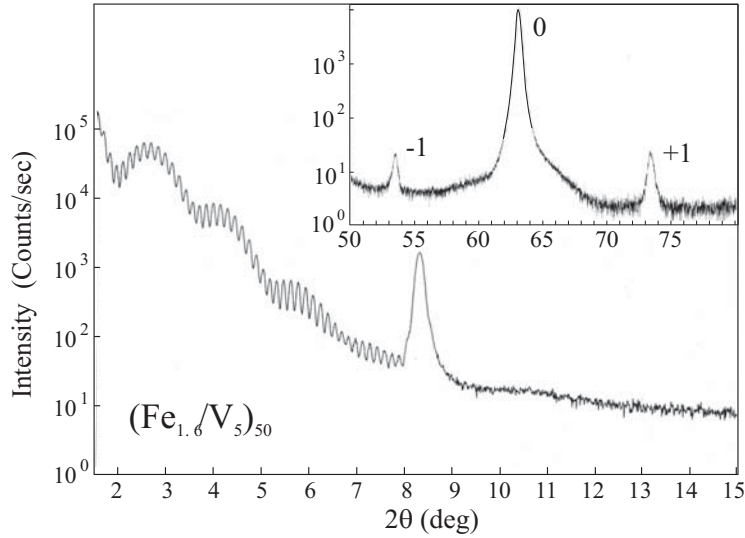


Figure 5.7: The small-angle XRD spectrum and the high-angle XRD spectrum (inset) is shown for the investigated $(\text{Fe}_{1.6}/\text{V}_5)_{50}$ SL indicating layered structure.

interpreted as the outcome of a competition between a negative (hybridization) and a positive (unquenching of μ_L) contribution.

5.4 Superparamagnetic behavior in ultrathin ferromagnetic layers

In this section the magnetic behavior of ultrathin ferromagnetic Fe layers in an $(\text{Fe}_{1.6}/\text{V}_5)_{50}$ SL is discussed. The ferromagnetic layers consist of 1 and 2 atomic layers with an averaged thickness of 1.6 ML. The XRD spectrum of the SL confirms a well-defined multilayer structure in Fig. 5.7. Similar to the $(\text{Fe}_4/\text{V}_4)_{45}$ and $(\text{Fe}_2/\text{V}_5)_{60}$, the $(\text{Fe}_{1.6}/\text{V}_5)_{50}$ reveals Kiessig fringes in the low-angle reflectivity data indicating homogeneous thicknesses across the multilayer stack. The multilayer Bragg peak in the low-angle and the sharp interplanar spacing diffraction (0) as well as the distinct satellite diffractions (± 1) are a signature of an excellent layering.

Contrary to the results for the Fe_n/V_m SL's with $n \geq 2$ ML [20], temperature-dependent FMR measurements (10 – 300 K) observe *two* resonances with small linewidth typical for Fe/V SL's [147,158]. The two signals, denoted as A and B in the following, show a quite different behavior as a function of temperature. In Fig. 5.8

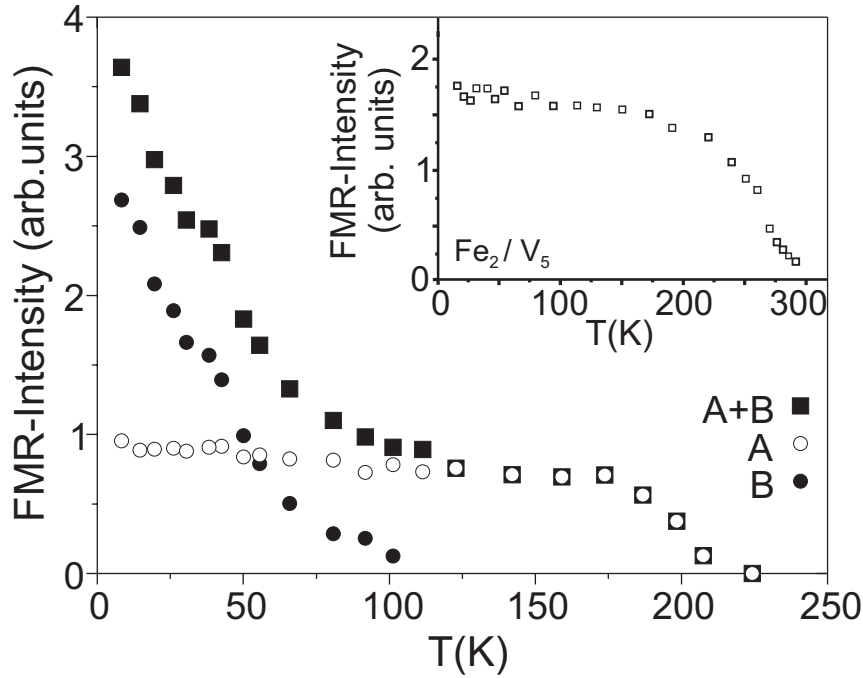


Figure 5.8: Intensity of the FMR signal for the two resonances denoted A and B found in the $\text{Fe}_{1.6}/\text{V}_5$ as indicated. The inset shows the intensity of the FMR signal measured in a Fe_2/V_5 SL, for details see [147, 158].

the normalized FMR intensity is given being proportional to the magnetization. The signal A shows a magnetization curve arising from regular ferromagnetic layers in comparison with the one of the Fe_2/V_5 presented in the inset of Fig. 5.8. The signal A vanishes at about $T_C = 200$ K. The Curie temperature T_C is lower with regard to Fe_2/V_5 SL (~ 300 K) because the interlayer exchange coupling, suppressing spin-fluctuations and thus stabilizing ferromagnetic order at higher temperature, is smaller for the $\text{Fe}_{1.6}/\text{V}_5$ SL [158, 160]. On the other hand, signal B dominates the magnetization at low temperatures and diminishes rapidly at about 100 K. The temperature-dependence of the magnetization reminds of superparamagnetic behavior. Note that the applied external field varies according to the resonance condition of the FMR signal for a given microwave frequency.

Recently, a similar behavior was found in Co/Pd SL's originating from the spin-polarization of the Pd spacer layers [161]. To clarify the origin of the unusual magnetic behavior at low temperatures, temperature- and field-dependent XMCD measurements were carried out. In Fig. 5.9 element-specific hysteresis loops at 10 K are presented for the Fe_2/V_5 and $\text{Fe}_{1.6}/\text{V}_5$ superlattices. The hysteresis loop

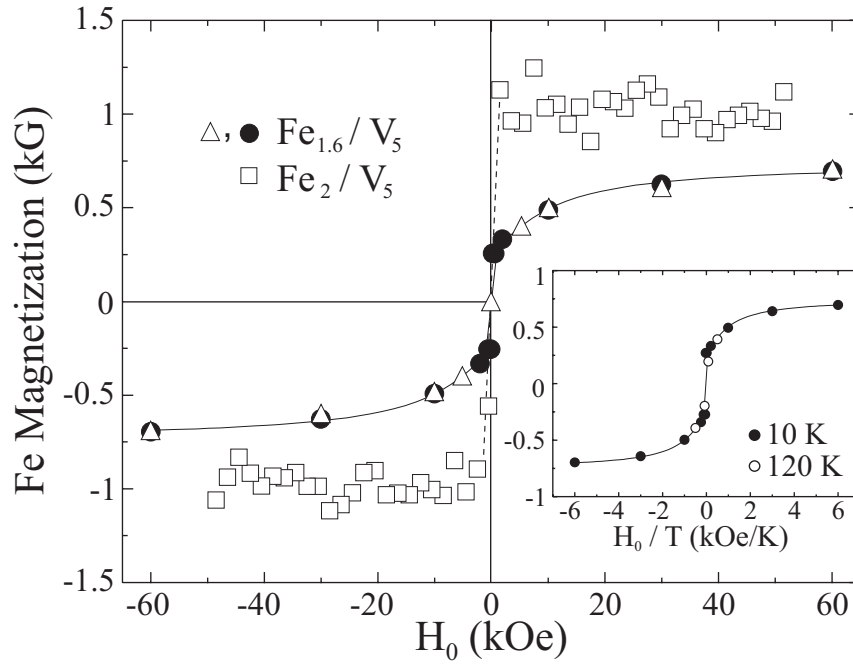


Figure 5.9: Field dependence of the Fe magnetization in $(\text{Fe}_{1.6}/\text{V}_5)_{50}$ along the in-plane (solid circles) and out-of-plane (open triangles) direction measured by XMCD. The corresponding in-plane Fe magnetization curve (open squares) in $(\text{Fe}_2/\text{V}_5)_{50}$ is included for comparison. The solid line is a fit, see text.

in case of the Fe_2/V_5 SL is measured at constant photon energy of the L_3 edge where the XMCD response is maximized. The absorption signal is divided by the absorption signal in the pre edge region (absence of XMCD signal) determined for each magnetic field up to 60 kOe. The magnetic signal is finally normalized to the XMCD signal of the 40 nm Fe/MgO(100) bulk reference sample. The hysteresis of the Fe_2/V_5 SL (open squares) is measured in-plane along [110]-direction (easy axis of magnetization) under 15 degrees grazing incidence of x-rays to the surface normal indicating clearly ferromagnetic layers. Note that the step-width of the magnetic field is much larger than the coercive field ~ 50 Oe of the sample [158] so that the coercivity cannot be resolved. Moreover, the magnetic response of the Fe layers remains constant up to 60 kOe. The magnetization as well as the magnetic response at the L_3 edge is strongly reduced for the $\text{Fe}_{1.6}/\text{V}_5$ SL as can be seen in Fig. 5.9. Therefore, full XMCD spectra had to be measured at each field strength explaining the lower density of points. The error bars, however, are within the point size for the $\text{Fe}_{1.6}/\text{V}_5$ SL. The field-dependent Fe magnetization was measured along the easy axis

[110] (solid circles) and along the surface normal (open triangles). Along the easy axis a remanent magnetization of ~ 260 G is observed while the magnetic remanence vanishes along the hard axis (out-of-plane). The occurrence of a remanence signal can be related to the ferromagnetic signal A obtained in the FMR measurements. In comparison with the Fe_2/V_5 SL ($\mu^{\text{Fe}} = 1.34 \mu_B/\text{atom}$), the magnetization of Fe and thus the average magnetic moment ($\sim 0.33 \mu_B/\text{atom}$) appear strongly reduced exhibiting that most likely not all Fe atoms contribute to the ferromagnetic signal. Furthermore, magnetic saturation of the sample was not reached even for the largest available magnetic fields. Despite the remanent signal, the high-field dependency of the curve supports the idea of superparamagnetic regions and is related to the signal B. Hereby, the magnetization at high fields does not change whether probed along the easy-axis or the hard-axis. The measurements were redone at $T = 120$ K, below the onset of the superparamagnetic behavior, under 10 and 60 kOe applied fields. The coincidence of the data points for 10 and 120 K as a function of H_0/T proves superparamagnetic behavior (inset of Fig. 5.9). Finally, it is evident from the element-specific measurements at the Fe edges that the observed FMR signals stem from the ultrathin Fe layers. These magnetic properties are thus quite unusual in superlattices while superparamagnetic behavior is frequently reported in granular multilayers, see e.g. [162].

As discussed in the previous section, the Fe_n/V_m SL's show enhanced orbital magnetism in the ultrathin Fe limit $n = 2$ atomic layers. While in the limit of small fields the ferromagnetic contribution A is dominant, the magnetic response at higher fields is successively determined by the superparamagnetic layered regions B. In order to reveal the orbital magnetism of the two contributions, field-dependent measurements of the orbital to spin moment ratio μ_L/μ_S were performed. They are shown in Fig. 5.10. The ratio μ_L/μ_S at 5 kOe is close to the one determined in the Fe_2/V_5 SL. Hence, the orbital magnetism of the ferromagnetic signal A is comparable to the one of $n = 2$ atomic Fe layers in the SL's. Then, μ_L/μ_S increases gradually with the external field. This is correlated with an increasing contribution of the superparamagnetic regions B to the total magnetic response. The considerable increase of about 10 % demonstrates that the superparamagnetic regions possess larger orbital moments μ_L due to less effective quenching by the crystal field compared to the ferromagnetic layers. The ratio μ_L/μ_S at a 60 kOe is almost three times larger than the Fe bulk value. A similar enhancement of the orbital to spin moment ratio were recently reported for Fe clusters [163].

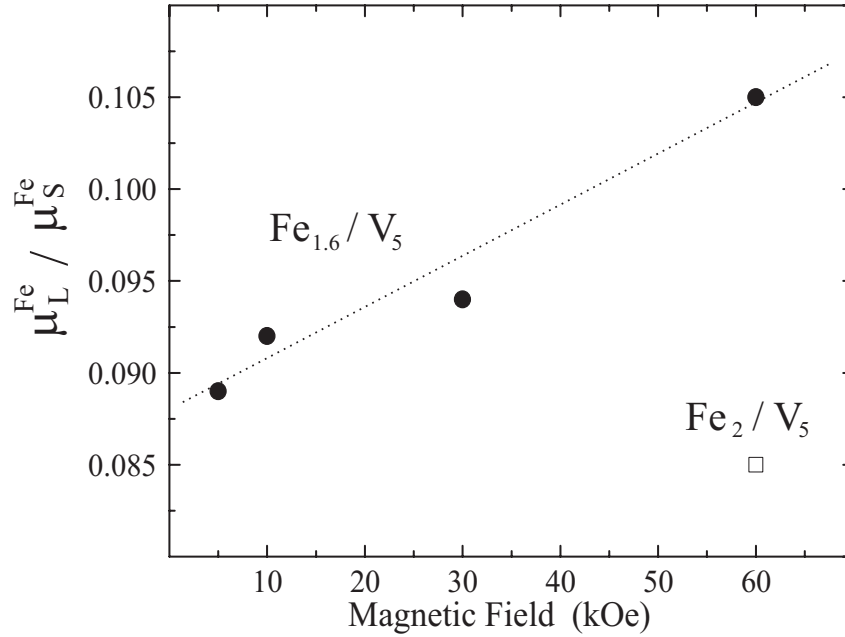


Figure 5.10: The orbital to spin moment ratio (solid circles) is shown as a function of the magnetic field for the $(\text{Fe}_{1.6}/\text{V}_5)_{50}$ SL. Corresponding value (open square) at 60 kOe for the $(\text{Fe}_2/\text{V}_5)_{50}$ SL is added for comparison. The error bar is about 10 %. The dashed line is a guide to the eye.

In Fig. 5.9 a fit of the superparamagnetism (solid line) is presented based on a simple model derived in Ref. [147]. It reveals that the superparamagnetic regions possess only small magnetic moments ranging between $3(2)$ and $54(2) \mu_B$ (for details see [147]). This suggests that the size of the superparamagnetic regions are rather small and the magnetic dipole-dipole interaction may be neglected with regard to the direct exchange. The limited size distribution with a small variation of the blocking temperatures T_B (temperature where the superparamagnetic regions become blocked and show a spontaneous magnetization) as well as the magnetic moments is finally consistent with the observation of sharp FMR resonance lines of the related signal B. In summary, the results shed light on the magnetic properties of ferromagnetic layers in SL's in the limit of ultrathin films. At this limit from $n = 1$ atomic layer to $n = 2$ ferromagnetic layers of Fe in Fe_n/V_m SL's, the system undergoes a transition where small regions exhibit superparamagnetic behavior.

Chapter 6

$3d$ Impurities in Au-Host

In this chapter the first XMCD experiments on dilute $3d$ impurities in Au are presented. The focal point of the investigation is the systematic observation of the orbital magnetism of the $3d$ impurities in Au by means of XMCD. The appearance and suppression of orbital magnetism in impurities has been intensely and controversially discussed in literature [164–171]. While in the free $3d$ atom a large orbital moment is formed according to the Hund’s rules, it is strongly reduced (quenched) due to crystal field and hybridization effects in the solid state. However, in case of dilute Fe and Ni impurities in alkali metal hosts indirect evidence was given that these impurities have localized $3d$ shell configurations with giant magnetic moments due to the orbital contribution [164, 165]. Theoretical investigations have shown that the large orbital moments are a result of the weak interaction of the $3d$ impurities with the alkali metal hosts [170, 171]. The discussion was recently revitalized by corresponding experiments using the XMCD technique confirming directly the localization of the $3d$ impurity states [44].

The XMCD technique is particularly suited because it (i) probes element-selectively the electronic and magnetic properties of the impurity $3d$ shell, (ii) provides access to the spin and orbital moments and (iii) is submonolayer-sensitive which is necessary for the investigation of the dilute systems. Here, the XMCD capabilities are employed for revealing the hybridization effects and the degree of localization of the $3d$ states in the Au host and for determining the orbital contribution of the $3d$ impurities via the orbital to spin moment ratio. The results were discussed with respect to recent *ab initio* calculations [172].

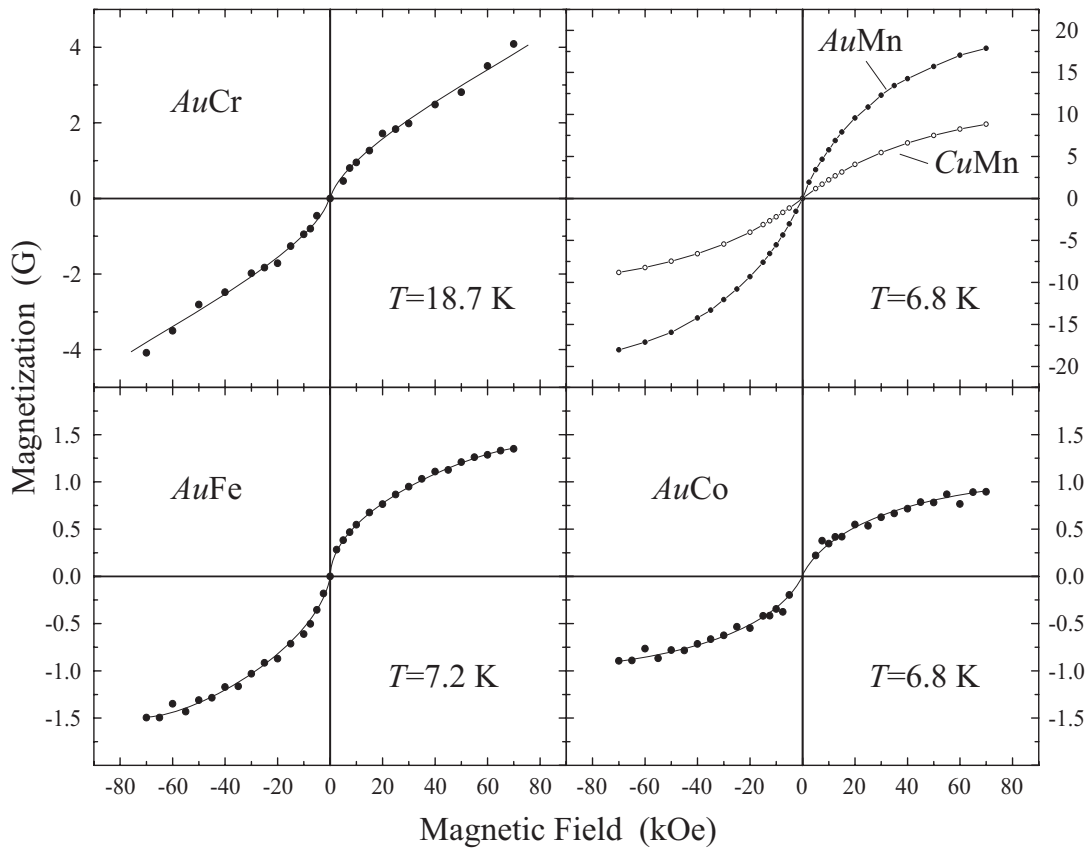


Figure 6.1: Field-dependent magnetization curves of the 3d impurities in Au and Cu measured at the corresponding L_3 absorption edge. The curves are normalized to SQUID measurements of the sample magnetization at given temperature. The lines serve as guides to the eye.

6.1 Structural and magnetic properties

The $Au_{1-x}TM_x$ and $Cu_{1-x}Mn_x$ with TM= Cr, Mn, Fe, and Co were prepared by the group of W.D Brewer [173,174]. As a first step, master alloys were produced by induction-levitation melting or by electron-beam melting of high-purity materials in an inert gas or under ultrahigh vacuum conditions. The homogeneous master alloy with higher concentrations is used to prevent the formation of clusters of ordered phases that are more difficult to dissolve in the fabrication process [173]. Then, the master alloy is successively diluted to the desired concentration. The alloys with the final impurity concentrations were pressed and rolled to plates (~ 1 mm thickness and ~ 6 mm diameter). In order to remove strain induced effects, the plates were annealed for 48 hours near the melting point. The alloys were then

quenched rapidly to room temperature. The following samples are investigated in this work: $AuCr$ ($x = 1.0\%$), $AuMn$ ($x = 1.0\%$), $CuMn$ ($x = 1.0\%$), $AuFe$ ($x = 0.8\%$), and $AuCo$ ($x = 1.5\%$). They were characterized by X-ray diffraction and SQUID magnetometry. All of the magnetic characteristics (glass temperature T_G , magnetic moment per atom) were consistent with literature values for similar alloys [173, 174].

The TM's dissolved in noble metals with impurity concentrations about $x = 1.0\%$ are known to be spin glasses, e.g., $AuFe$.¹ Furthermore, for impurity concentrations of $x = 1.0\%$, the probability of a cluster consisting of two impurities is about 10% while the probability of larger clusters is negligible. For the smallest cluster the magnetic moment changes only slightly with regard to the single impurity as recent calculations have shown [175].

6.2 Absorption fine structure

The measurements were carried out on the ID8 beamline (former ID12B) at the ESRF (sec. 2.2). The *ex situ* samples were softly sputtered with Ar^+ for several hours and all traces of oxidation were removed. This was monitored at the oxygen K edge and $L_{2,3}$ edges of the $3d$ TM's. The absorption spectra were probed with the k -vector normal to the surface. The measuring temperature was above the glass temperature of the corresponding sample. Magnetic fields up to 70 kOe were applied along k . Magnetization curves of the paramagnetic impurities were recorded as a function of the magnetic field and constant temperature at the L_3 edge of the corresponding $3d$ TM's. They were calibrated with values of the magnetization obtained from SQUID of the identical sample at same temperatures and a magnetic field of 50 kOe. The results presented in Fig. 6.1 exhibit that the magnetic saturation (full alignment of the paramagnetic moments) could not be attained in these Kondo systems.

The XMCD spectra were obtained both by reversing the direction of the magnetic field and by switching the helicity of the x-rays. No artificial magnetic backgrounds were found using the TEY by this cross-check. Instabilities of the beam

¹The spins of the impurities interact according to the RKKY-model, i.e. the exchange is mediated by the polarized sp conduction band of the host. The oscillatory RKKY-interaction couples the spins parallel or antiparallel depending on their distance. Since distances between the spins are statistical distributed in a random alloy, the magnetic state below the glass temperature is not homogeneous.

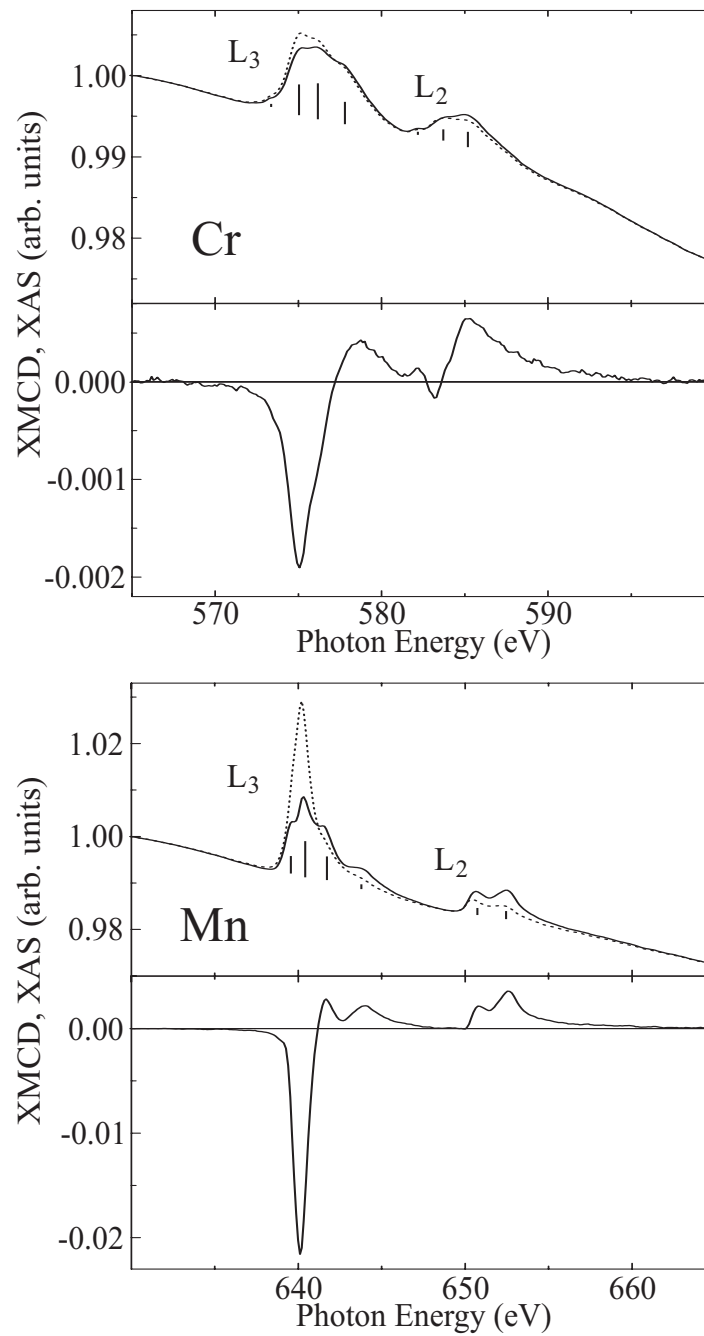


Figure 6.2: Absorption fine structure for left (dotted line) and right (solid line) circularly polarized light and the XMCD spectrum for Cr (top) and Mn (bottom) impurities in Au. The applied field was 70 kOe and the temperature was 18.7 K and 6.8 K for Cr and Mn, respectively. Due to the small edge jumps of impurities the spectra are normalized at the pre-edge only.

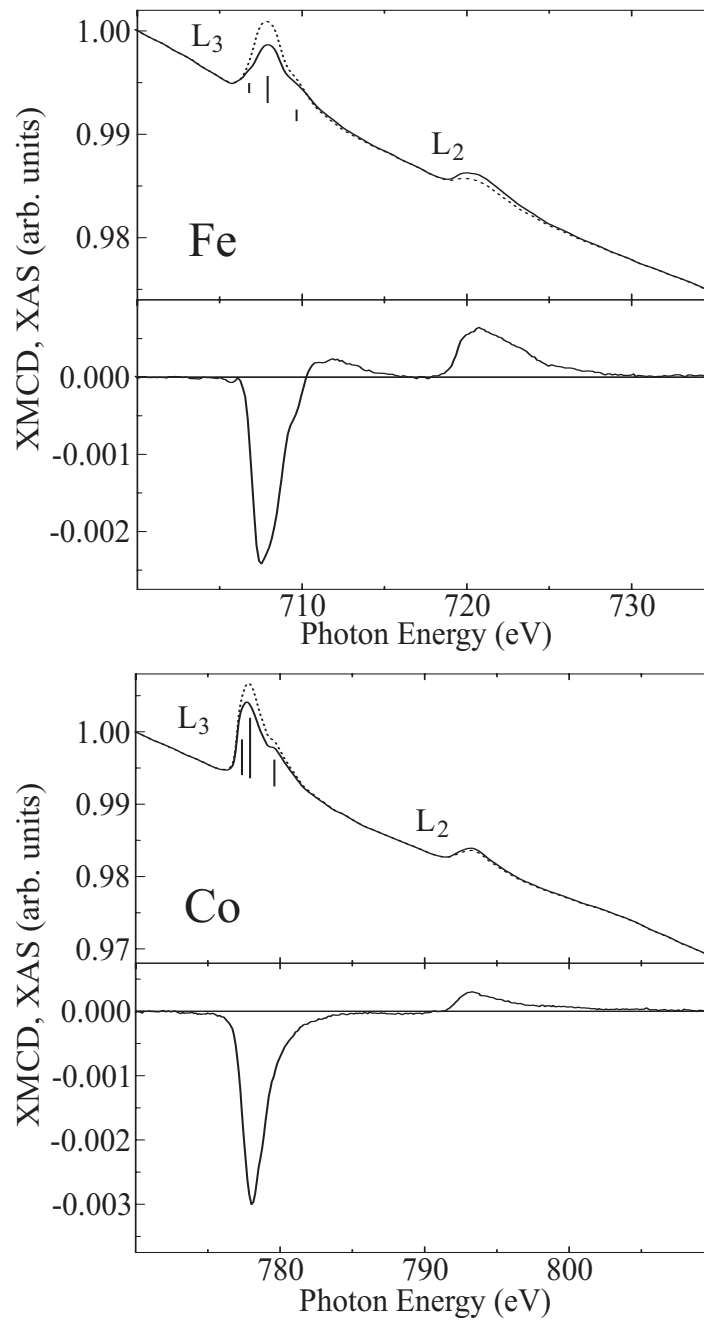


Figure 6.3: Absorption fine structure for left (dotted line) and right (solid line) circularly polarized light and the XMCD spectrum for Fe (top) and Co (bottom) impurities in Au. The applied field was 70 kOe and the temperature was 7.2 K and 6.8 K for Fe and Co, respectively. Due to the small edge jumps of impurities the spectra are normalized at the pre-edge only.

intensity I_0 and the transmission function of the beamline were normalized with the I_0 photocurrent-signal of a gold grid. Though normalization with I_0 , the spectra revealed a strong non-linear background. This is because the $L_{2,3}$ edge jumps of the 3d impurities are in the range of 0.1 % with respect to the background signal. Therefore, all the XAS spectra have been normalized to the absorption of a clean gold sample which was measured at corresponding external field and temperature in order to remove the superposed background originating from the host material and the transmission function of the beamline. Despite of the XAS background, excellent XMCD spectra were obtained on subtraction. Figs. 6.2 and 6.3 show the XAS spectra normalized to unity at the pre-edge and the corresponding XMCD curves obtained from them.

Recent investigation of Fe, Co and Ni adatoms (submonolayer coverages) on alkali films using the XMCD technique have demonstrated that those transition metals form highly localized atomic configurations [44]. In the atomic limit the $L_{2,3}$ XAS reveal sharp multiplet structures which are a sensitive fingerprint for the atomic configuration [116]. Those prominent features, however, diminish in the shallow d bands of the solid state and are consequently expected to be absent in bulk XAS. In Figs. 6.2 and 6.3 the absorption fine structure (XAS and XMCD) of 3d impurities in a Au matrix reveal an overall line shape that reminds of the 3d TM's absorption spectra in the solid state. However, there are distinct features marked by vertical lines in the absorption spectra. This can be attributed to some localized character of the 3d states. Hence, the current measurements of impurities bridge the gap of absorption spectra between the atomic [44] and the solid state (see e.g. chapter 3). Hereby, the absorption fine structure is an indicator for the hybridization-degree of the d orbitals with the Au host.

The role of crystal field effects and hybridization can be assessed from the branching ratio [57].² The maximum branching ratio is obtained for the ground-state according to Hund's rule and decreases successively with the crystal field and hybridization effects lowering the spin-polarization of the 3d states. The measured branching ratios of the impurities are determined from the averaged absorption spectra and presented in Table 6.1. All branching ratios of the impurities are considerably enhanced relative to the corresponding bulk values except for Co. Since the branching ratio reaches a maximum in the free atom with regard to the Hund's rule ground state [57] the larger branching ratios of the impurities suggests that

²The branching ratio is the fraction of the $2p_{3/2}$ transition channel (chapter 1 and 3).

Table 6.1: Branching ratios for the $3d$ impurities in a Au matrix and for the $3d$ TM's of thin films and bulk absorption spectra (chapter 3).

Configuration	Cr	Mn	Fe	Co
impurity in Au host	0.67	0.79	0.79	0.82
bulk-like	0.56	0.67 [†]	0.70	0.79

[†] Ref. [176]

they form higher spin moments as it is expected by theory [172] in Fig. 6.5. Unfortunately, the samples could not be magnetically saturated under the given experimental conditions. Thus, a quantitative prove of the conclusions drawn from the branching ratios, e.g., by applying the spin sum rule to the XMCD spectra, cannot be provided.

6.3 Orbital magnetism

The influence of the crystal field and the hybridization with the Au host on the orbital moment for the $3d$ impurity can be deduced from the orbital to spin moment ratio μ_l/μ_s measured via the XMCD technique. As demonstrated in chapter 3 for the series of the $3d$ transition metals, the orbital contribution μ_L to the total moment and its relative orientation to the spin moment μ_S can be determined from the XMCD spectra by evaluating the ratio R from the L_2 and L_3 peak areas. The orbital moment is quenched if the $L_{2,3}$ peak areas are equal ($R = -1$).³ The inspection of the XMCD spectra in Figs. 6.2 and 6.3 shows clearly that the integration of the L_3 and L_2 XMCD signals give similar areas, i.e. R is close to -1 , with the exception of Co where the L_3 area is strongly enhanced relative to the L_2 area. This indicates without invoking the sum rule analysis that a large orbital moment with respect to the spin moment is formed in case of Co.

The $L_{2,3}$ -peak areas were extracted from the XMCD spectra and the orbital to spin moment ratio is quantitatively evaluated according to Eq. (1.26). The results (solid circles) are shown in Fig. 6.4, where μ_l / μ_s is plotted versus the d count of the $3d$ impurities in Au. As shown in this work (chapter 3), the spin sum rule un-

³In the following it is assumed that the magnetic dipole operator $\langle T_Z \rangle$ is negligible with respect to the spin moment of the $3d$ impurity.

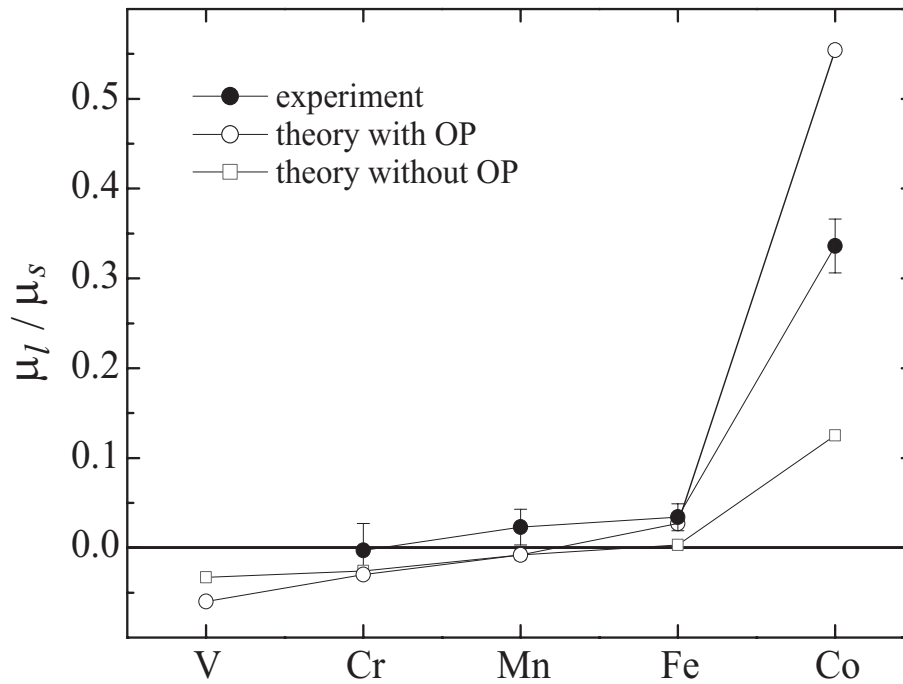


Figure 6.4: The orbital to spin moment ratio according to the sum rules (solid circles) is shown for the 3d impurities in Au as a function of d -count. Calculations with OP-scheme (open circles) and without OP-scheme (open squares) are given for comparison, see text.

derestimates the spin moments for the early 3d elements and the values of μ_l / μ_s for Cr and Mn are thus most likely overestimated. Nevertheless, the orbital to spin moment ratio of Cr, Mn and Fe impurities in Au ranges only from 0–3 % (see also Table 6.2). This indicates that the magnetic moment is mainly determined by the spin moment. The orbital moment is quenched with regard to the formed orbital moments in the corresponding free atoms. From Cr to Fe the orbital contribution slightly increases with the 3d occupation number within the experimental uncertainties. Moreover, the sign of the experimental ratio μ_l / μ_s changes between Cr and Mn indicating a negative orbital moment for Cr and a positive orbital moment for Mn. The third Hund's rule predicts for free atoms negative (positive) orbital to spin moment ratios for less(more)-than-half-filled 3d shells. Hence, the general trend of the experimental ratios can be understood in terms of the third Hund's rule. In case of Co, which is adjacent to Fe, the ratio reveals a sudden increase by factor 10. Relative to the ratio of Co bulk metal ($\mu_l / \mu_s = 0.089$ [7,75]) the orbital contribution is almost four times larger.

Table 6.2: The derived orbital to spin moment ratios for the $3d$ impurities in noble metals at given temperature. The applied field was 70 kOe.

sample	<i>AuCr</i> (1.0 %)	<i>AuMn</i> (1.0 %)	<i>CuMn</i> (1.0 %)	<i>AuFe</i> (0.8 %)	<i>AuCo</i> (1.5 %)
T (K)	18.7	6.8	6.8	7.2	6.8
μ_l / μ_s calc.+OP [†]	-0.003(30)	+0.023(20)	+0.013(20)	+0.034(15)	+0.336(30)
μ_l / μ_s	-0.030	-0.008	+0.002	+0.027	+0.554

[†] Ref. [172]

In Fig. 6.4 theoretical values of μ_l / μ_s [172] for the $3d$ impurities in Au are included for direct comparison. The corresponding spin and orbital moments are given in Fig. 6.5. The calculations are based on *first principles* real-space linear muffin-tin formalism in the atomic sphere approximation. The calculations were performed with orbital polarization (OP) (open circles) and without OP (open squares). It has been shown that the OP scheme improves the agreement of μ_L between theory and experiment and reproduces better the trends of μ_L across the series [75]. The theory confirms very nicely the experimental findings: (i) A systematic increase of μ_l / μ_s is predicted being negative at the beginning and positive at the second half of the $3d$ series. (ii) The remarkable jump of the ratio at Co is also found in theory. In principle both calculations with and without the OP scheme contain the observation (i) and (ii). The main difference is the prediction of the magnitude of the enhanced Co orbital contribution. The inclusion of the OP scheme does not strongly affect the orbital moments between Cr–Fe (middle of the series) but it considerably changes the orbital polarization of V and Co which are at the borders of the series. The present experiments on $3d$ impurities in Au are thus a suitable test of the consistency of the OP scheme. The comparison with experiment clearly demonstrates that the current OP scheme improves the size of the orbital contribution for Co even though the orbital moments are overestimated whereas exclusion of OP leads to an underestimation.

The orbital magnetism across the $3d$ series can be understood when decomposing the orbital polarization $L_z(\uparrow, \downarrow)$ for the majority (\uparrow) and minority (\downarrow) band in Fig. 6.6 [75]. The d states are consecutively filled starting in the majority band with the spin-

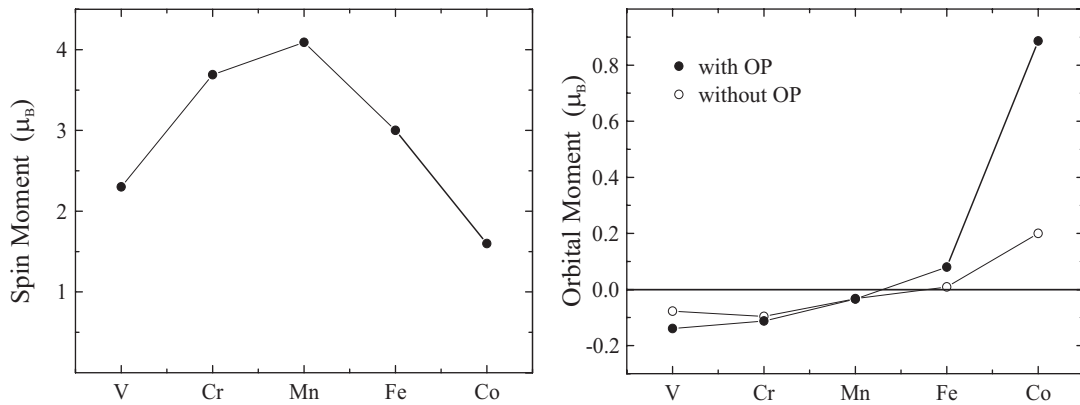


Figure 6.5: Calculations of (left) spin moments and (right) orbital moments with (solid circles) and without OP-scheme (open circles) for the 3d impurities in Au taken from Ref. [172]

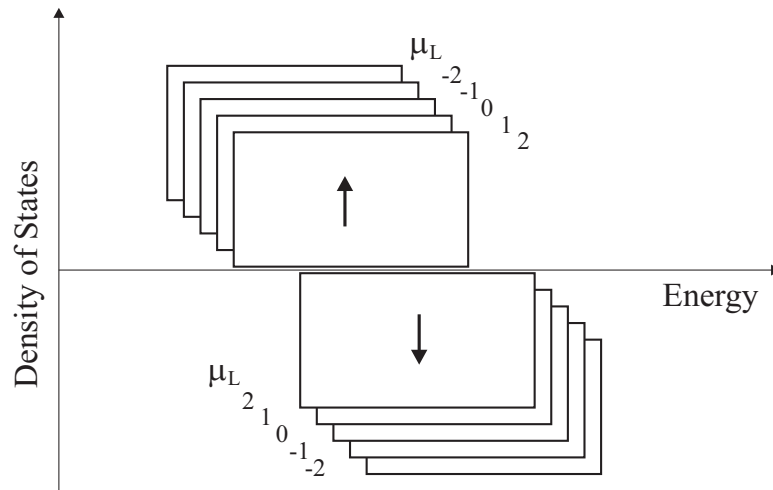


Figure 6.6: Schematic representation of the m_L -splitted (spin-orbit coupling) d states broadened by hybridization effects, adapted from [75].

orbit-splitted sublevels $m_L = -2, -1, 0, \dots$. The orbital moment is thus negative at the beginning of the series. With increasing d count also the minority band becomes filled in reversed sequence $m_L = 2, 1, 0, \dots$. At a certain point of the d occupation both the negative (majority band) and the positive (minority) orbital polarization compensate each other resulting in a node of the orbital moment curve in Fig. 6.5. The orbital polarization of the majority band is zero if the majority band is completely populated and the positive orbital polarization of the minority band determines the positive orbital moments at the second half of the 3d series.

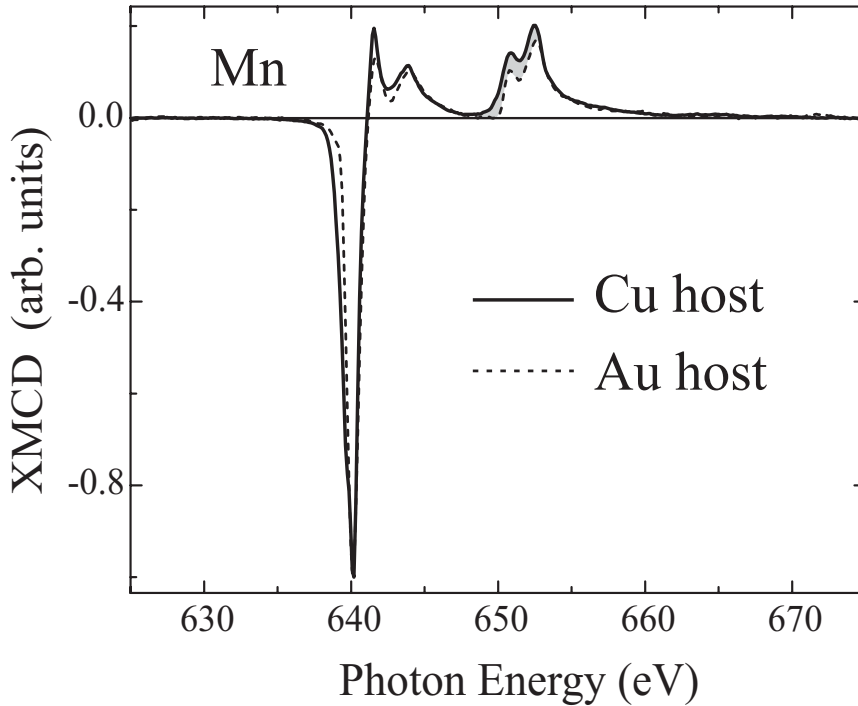


Figure 6.7: XMCD spectra for Mn dissolved in Cu and Au host. The area indicate some relative enhancement of the L_2 area in case of the Mn in Cu.

Ebert *et al.* have approximated the systematics of $3d$ orbital moments to first order (spin-orbit coupling treated as a weak perturbation) by the difference of the spin-splitted local density of states at the Fermi level $n^{\uparrow,\downarrow}(E_F)$ [177]. For Mn, Fe and Co impurities the virtual bound state in the minority band is consecutively filled, while the majority band is filled [172]. Since the virtual bound state is more narrow at the end of the $3d$ series, $n^{\downarrow}(E_F)$ is larger and the orbital moment considerably increases for the late $3d$ impurities. The width and the energy position (occupation) of the virtual bound state, i.e. the hybridization with the host ($3d-d$ and $3d-sp$), determine sensitively the formation of large orbital moments as it is found for Co in Au. Interestingly, in the experiment as well as in the calculation the orbital moment of Fe in Au is ten times smaller, while the theory predicts huge orbital moments for both Fe and Co in Ag [172]. This suggests that the large value of $n^{\downarrow}(E_F)$ and the related large orbital polarization is less affected for Co whether dissolved in Au or Ag. However, the stronger hybridization of Fe in Au with regard to Fe in Ag leads to a broadening and a decrease of $n^{\downarrow}(E_F)$ at the Fermi level [172]. This explains

why the Fe orbital moment is considerable smaller in the Au matrix revealing an orbital to spin moment ratio that is 10 times smaller than the one of Co, which is adjacent to Fe in the 3d series.

The influence of hybridization effects on the 3d impurities can be studied by comparing different hosts. Measurements were performed on dilute Mn impurities in a Cu matrix. This is unfortunately a more difficult case because the orbital moment curve of the 3d series has a node close to Mn and the effects of hybridization on the orbital contribution is expected to be rather small. Nevertheless, in Fig. 6.7 corresponding XMCD spectra are shown for Mn dissolved in a Cu and Au matrix. Since the magnetization of Mn was different in Au and Cu at 70 kOe, both spectra have been normalized to unity at the L_3 edge to emphasize the modifications arising from the host. The overall line shape of the XMCD (and XAS) signal remains. However, the structural details are sharpened for Mn in a Au matrix. This can be understood by considering the stronger hybridization of the impurity with Cu, favored by the smaller lattice constant compared to Au. Moreover, one sees clearly for Mn in the Cu host an enhancement of the L_2 peak area relative to the L_3 peak area, where the positive and negative contributions of the XMCD intensities almost cancel each other. The increase of the L_2 peak area thus indicates a lowering of the orbital to spin moment ratio of Mn in Cu. The ratio μ_l / μ_s for Mn is +0.013 in Cu and +0.023 in Au. This suggests that the stronger hybridization with Cu leads to a more effective quenching of the Mn orbital moment.

Summarizing, the first XMCD experiments on dilute 3d impurities in Au are presented in the present work. The absorption fine structures at the $L_{2,3}$ edges of the 3d impurities bridge the gap between the pure atomic and the solid state. The enhanced branching ratios indicate the tendency of the 3d impurities to form high-spin states. Sizable orbital moments were deduced by evaluating the orbital to spin moment ratio in agreement with *ab initio* theory including orbital polarization. It is experimentally shown that hybridization effects with the Au host play an important role for the appearance of orbital magnetism in Co impurities (four time larger relative to the bulk) and the quenching of the orbital moments in Fe.

Conclusion

In this work we investigated the magnetic and structural properties at the interfaces in layered magnetic structures consisting of alternating ferromagnetic and non-magnetic layers. The measurements are carried out on Fe_n/V_m superlattices and prototype $\text{Fe}/\text{V}/\text{Fe}$ trilayers. The present results shed light on the magnetic properties of both the spin-polarized V spacers and the ferromagnetic Fe layers at the thin film limit, $n, m = 2 - 5$ atomic layers, in Fe_n/V_m superlattices. Exploiting the element-specificity of the XMCD technique, it is demonstrated that the origin of reduced sample magnetizations measured by conventional magnetometry is also due to the antiparallel induced magnetization on the V site. Hereby, the samples with the thinnest Fe or V layers reveal the strongest reduction of the Fe moment ($1.34 \mu_B$ per atom) and the largest induced V moment ($-1.1 \mu_B$ per atom), respectively, indicating that the interfacial magnetic properties depend on the superlattice composition. The observation of large g -factors by ferromagnetic resonance in thin Fe layers of the superlattices is explained in this thesis by two effects: (i) the unquenching of the Fe orbital moment in very thin Fe layers and (ii) the antiparallel induced V magnetic moments at the Fe/V interface. Furthermore, at the ultrathin film limit from non-magnetic to ferromagnetic Fe layers between 1 and 2 atomic layers, we demonstrated that the system consists of ferromagnetic as well as of superparamagnetic regions.

Even though the XRD measurements confirm a high structural homogeneity for the Fe/V superlattices, the results are, however, in conflict with theoretical predictions assuming perfect interfaces in particular of the magnitude of both the reduced Fe and the induced V magnetic moments. Therefore, we studied the role of interdiffusion and roughness at the interfaces in prototype $\text{Fe}/\text{V}/\text{Fe}$ trilayers in order to resolve the quite frequently reported discrepancies of the interfacial magnetic properties as a key point. This was experimentally realized by working thoroughly *in situ* and tuning the deposition temperature. The deposition temperature was found

to play a dramatic role in the modification of the induced magnetism in terms of the polarization range and the magnitude of the magnetic moments. The deposition on atomically flat Fe layers at low temperatures results in smaller V moments ($-0.5 \mu_B$ per atom) in agreement with the theoretical prediction for sharp Fe/V interfaces while depositing at higher temperatures leads to a doubling of induced V moments ($-1.0 \mu_B$ per atom) at the interface consistent with the observations in Fe/V superlattices. Moreover, the non-magnetic V spacer reveal a short-range spin-polarization, i.e. the induced magnetic moments are mainly located at the Fe/V interface, for ideal-like interfaces while interdiffusion and roughness lead to an apparent long-range spin-polarization as observed in Fe/V superlattices. By studying this model system, we present the first direct probe of interdiffusion effects on the induced spin-polarization at interfaces with easily polarizable elements. These results clarify the inconsistencies between earlier experimental and theoretical works.

For the determination of the spin and orbital moments of V, the corresponding XMCD spectra needed to be analyzed. Two main points were addressed in the analysis: (i) the influence of the core hole on the absorption spectra and (ii) the relation between the magnetic ground state and the spectral distribution of the XMCD for the early $3d$ TM's. Thus, in the framework of this thesis a systematic study of the $L_{2,3}$ absorption fine structure along the $3d$ TM's is performed. Resolving the complex and detailed spin-dependent absorption fine structure of unique XMCD spectra using the gap-scan technique of an insertion device beamline, a more detailed picture of the spectral distribution $\Delta\mu(E)$ is given for the early $3d$ TM's Ti, V and Cr. The results can be summarized as follows:

- The first experimental determination of the sum rule deviations across the $3d$ series has been performed. The results of the magneto-optical sum rules applied to the early $3d$ TM's were tested for their validity and it is demonstrated that in particular the spin sum rule breaks down. The apparent spin moments of Ti–Cr were found to be underestimated between a factor $\times 5$ and $\times 2$, respectively. This effect is related to the core hole interaction which becomes competitive to the reduced spin-orbit coupling for the early $3d$ TM's. In light of the reduced core hole effects for the late $3d$ TM's Fe, Co, and Ni the application of the spin sum rule appears to be justified and explains why reasonable values are deduced from the corresponding XMCD spectra. In general, the present results help to estimate the magnetic moments from XMCD spectra of $3d$ TM's in future investigations.
- Due to the sum rule limitations for the early $3d$ TM's, an alternative concept

is proposed by analyzing the spectral line shape of the circular dichroism in conjunction with theory. This approach deals with deriving magnetic moments from the absorption fine structure of the XMCD which depends on the magnetic ground state properties of the $3d$ states. For the interpretation of the XMCD spectra, the experimental data are compared with calculation based on the SPR-KKR Green's function method which is appropriate for magnetic solids. It turned out that the overall line shape of the XMCD can be adequately described by theory, even though the $2p - 3d$ core hole correlation effects are not included in the calculations. An exception is the observed splitting of the XMCD signal at the L_3 edge leading to a distinct feature at the L_3 threshold which can be explained by comparative atomic-multiplet calculations including the core hole. It is shown that the XMCD yields valuable information for the spin-dependent band-structure such as the oscillatory fine structure observed at the L_2 edge of the early $3d$ TM's arising from van Hove singularities in the Brillouin-zone.

- In this thesis, we elaborated a simple model derived from TDDFT that allows to determine the $2p - 3d$ correlation energies of the electron core-hole interaction from experimental spectra. The analysis of the systematic variation of the branching ratios D_1 and the apparent $L_{2,3}$ spin-orbit splitting $\Delta\Omega$ in the isotropic absorption spectra give $2p - 3d$ correlation energies of 0.251 eV (L_3) and 0.121 eV (L_2) per d hole per atom, respectively. It is experimentally deduced that the correlation energies scale linearly with the d count for Ti, V and Cr. Extrapolating the correlation energies to the late $3d$ elements indicates that the influence of the core hole may be neglected for the latter. The determined $2p - 3d$ correlation energies can be used in the future for establishing of a comprehensive theory to treat core hole effects in absorption spectra of magnetic solids.

The first XMCD experiments on dilute $3d$ impurities in Au are presented in this work. The absorption fine structures at the $L_{2,3}$ edges of the $3d$ impurities reveal their intermediate character between a pure atomic configuration and the solid state. The enhanced branching ratios indicate the tendency of the $3d$ impurities to form high-spin states. Sizable orbital moments were deduced by evaluating the orbital to spin moment ratio in agreement with *ab initio* theory including orbital polarization. The hybridization effects with the Au host, as it is experimentally shown, play an important role for the appearance of orbital magnetism in Co (four time larger relative to the bulk) and the quenching of the orbital moments in Fe impurities.

Appendix A

XMCD Filemanager

For the normalization and analysis of the absorption spectra, the XMCD-filemanager program has been developed in this work.¹ The software provides the automatic loading of large numbers of experimental data, their normalization and their analysis. The latter are discussed in sec. 1.3. The concept of the program is specially design for the analysis of XMCD spectra. The normalization of the absorption spectra for left and right circularly polarized light can be performed on a graphical display.

The main features for analysis can be summarized as follows:

- flexible loading options for different file formats of the experimental data and optional auto-normalization of the absorption spectra to the incoming photon intensity
- the adding and the grouping of XAS and XMCD spectra
- the correction of saturation effects in conjunction with the SATEFF code, see appendix B
- the simulation and removal of the continuum
- the application of the magneto-optical sum rules to the experimental data

¹The XMCD filemanager is written in the *Interactive Data Language* (IDL) which is a trademark of Research Systems.

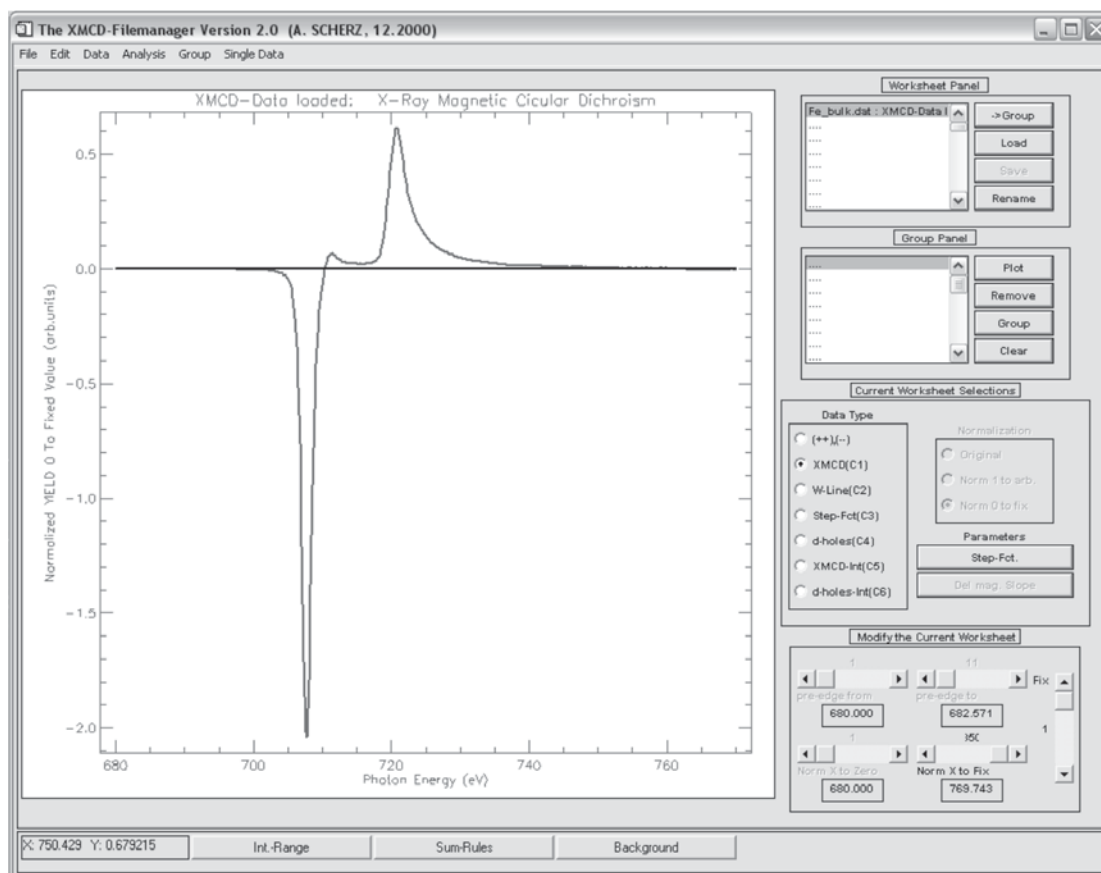


Figure A.1: Screen-shot of the XMCD filemanager developed in this work using IDL.

Appendix B

SATEFF: Saturation Effects in XAS using TEY

The proportionality between the TEY and the absorption coefficient is violated if the attenuation length $1/\mu(E)$ of the x-rays in matter is comparable to the electron escape depth λ_{e^-} . The TEY becomes then increasingly proportional to the intensity of the incoming light $I_0(E)$ (independent of the absorption coefficient) in direction of the ultimate case where $I_0(E)$ is entirely absorbed in the probing depth of the TEY detection mode. This effect is well known as the saturation effect [61–63]. The attenuation length is some tens of a micron ($\sim 1000 \text{ \AA}$) in the $L_{2,3}$ energy range for the $3d$ TM's (see Fig. B.1) while the electron escape depth is about 20 \AA highlighting the surface sensitivity of the TEY detection mode and indicating that the proportionality between TEY and $\mu(E)$ is satisfied at normal incidence of the x-rays. At glancing angles ($\theta > 0$, see Fig. B.2) the attenuation length normal to the surface plane decreases according to $\frac{1}{\mu_{eff}(E)} = \frac{\cos \theta}{\mu(E)}$. Hence, for the latter case the TEY measurements need to be corrected for the saturation effect when the condition $\frac{1}{\mu_{eff}(E)} \sim \lambda_{e^-}$ is satisfied.

The saturation effect can be removed from experimental absorption spectra. Therefore, the code SATEFF (Fig. B.3) has been developed in this work. It takes into account this effect in various types of layered structures, e.g., bulk samples, single thin films, bilayers, trilayers and multilayers including the substrate and protective capping layers.¹ The sample investigated at given angle θ has the schematic structure as shown in Fig B.2. The contribution $dY(E, d)$ at depth d to the TEY is

¹The SATEFF code is written in the *Interactive Data Language* (IDL) which is a trademark of Research Systems.

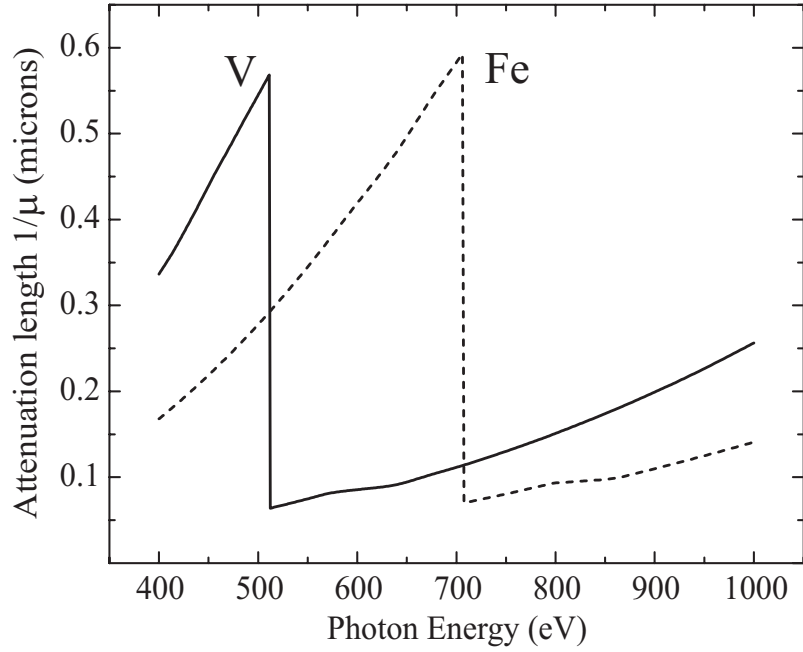


Figure B.1: The attenuation length $1/\mu(E)$ of V and Fe in the $L_{2,3}$ energy range [178].

limited by λ_{e^-} and can be written as

$$dY(E, d) = dY_d(E) \exp[-d/\lambda_{e^-}] . \quad (\text{B.1})$$

The quantity $dY_d(E)$ is the electron yield of the absorption from incoming light at depth d , i.e.

$$dY_d(E) \propto \left\{ I_0(E) \exp\left[-\frac{\mu}{\cos\theta} d\right] \right\} \frac{\mu}{\cos\theta} dd . \quad (\text{B.2})$$

The TEY is derived by integrating the electron yield over the sampling depth. From Eqs. (B.1) and (B.2) one obtains

$$Y(E) \propto \int_0^\infty dd \frac{\mu_X}{\cos\theta} \exp[-\gamma_X d] , \quad (\text{B.3})$$

where the effective self-absorption γ_X of matter X is introduced by

$$\gamma_X = \frac{\mu_X}{\cos\theta} + \frac{1}{\lambda_X} . \quad (\text{B.4})$$

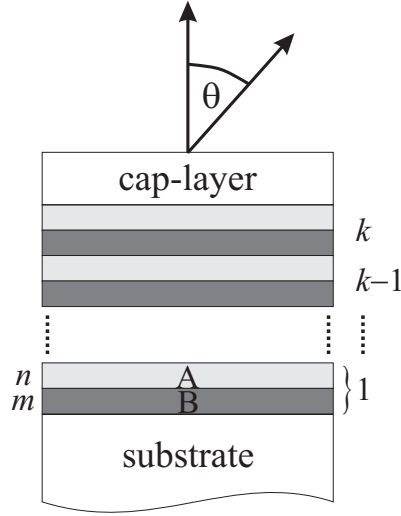


Figure B.2: Schematic representation of a multilayer stack. Other samples such as single crystals, thin films, bilayers and trilayers with protective capping layers and substrates can be adjusted in the SATEFF code by omitting corresponding layers.

Resolving atomic layers, the integral is substituted by the sum over the discrete layers. Finally, for the sample $\{\text{cap}/(A_n B_m)_k/\text{substrate}\}$ with $d_A = na$ and $d_B = mb$ (a, b : the interplanar spacing of layers A and B) the TEY at given angle θ is

$$\begin{aligned}
 Y(E) &\propto \frac{\mu_{cap}}{\cos \theta} \frac{1 - \exp[-\gamma_{cap} d_{cap}]}{\gamma_{cap}} \\
 &+ \left\{ \frac{\mu_A}{\cos \theta} \frac{1 - \exp[-\gamma_A d_A]}{\gamma_A} + \exp[-\gamma_A d_A] \frac{\mu_B}{\cos \theta} \frac{1 - \exp[-\gamma_B d_B]}{\gamma_B} \right\} \\
 &\times \frac{1 - \exp[-k(\gamma_A d_A + \gamma_B d_B)]}{\gamma_A d_A + \gamma_B d_B} \exp[-\gamma_{cap} d_{cap}] \\
 &+ \frac{\mu_{sub}}{\gamma_{sub} \cos \theta} \exp[-\gamma_{cap} d_{cap} - k(\gamma_A d_A + \gamma_B d_B)]. \quad (B.5)
 \end{aligned}$$

The code SATEFF evaluates numerically the relative absorption coefficient $\frac{\mu_x(E)}{\cos \theta}$ from Eq. (B.5) for the required energy range. The absorption coefficient of the entire sample at the pre-edge and after the corresponding edge is determined from literature values [178] as e.g. presented in Fig. B.1 for V and Fe in the soft x-ray energy-range. The saturation effect is removed from the absorption spectra by setting $\theta = 0$ before the TEY is recalculated. In general, it is possible to simulate the absorption spectra at various angles with the code. Additionally, the SATEFF code also provides a cross-check of the measured edge jumps in the absorption spectra.

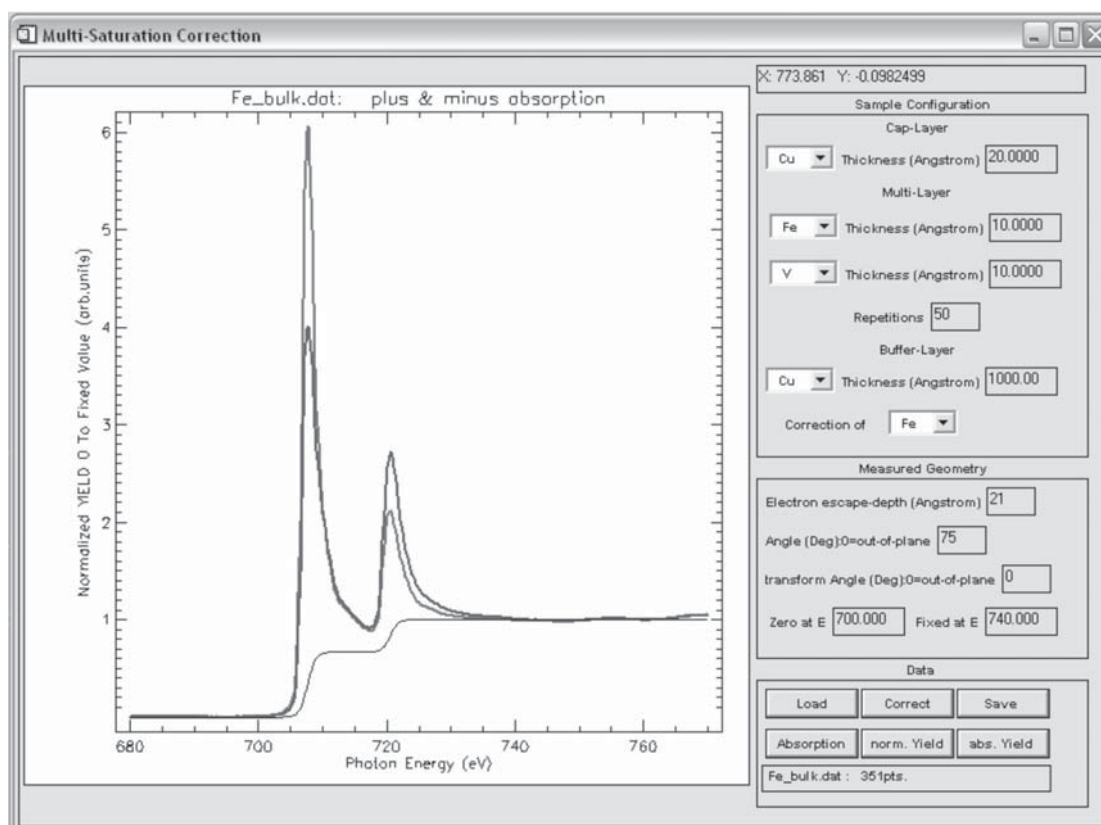


Figure B.3: Screen-shot of the SATEFF program developed in this work using IDL.

Appendix C

Multipole Moment Analysis

According to Eq. (1.24), u_{jm}^r is obtained (Table C.1) using the following Wigner $3 - j$ identities:

$$\begin{aligned}
 (-1)^{j-m} \begin{pmatrix} j & 0 & j \\ -m & 0 & m \end{pmatrix} &= \frac{1}{\sqrt{2j+1}} \\
 (-1)^{j-m} \begin{pmatrix} j & 1 & j \\ -m & 0 & m \end{pmatrix} &= \frac{m}{\sqrt{(2j+1)(j+1)j}} \\
 (-1)^{j-m} \begin{pmatrix} j & 2 & j \\ -m & 0 & m \end{pmatrix} &= \frac{2(3m^2 - j(j+1))}{\sqrt{(2j+3)(2j+2)(2j+1)(2j)(2j-1)}}
 \end{aligned} \tag{C.1}$$

Table C.1: u_{jm}^r according to Eq. (1.24).

u_{jm}^r	$\frac{3}{2}, +\frac{3}{2}$	$\frac{3}{2}, +\frac{1}{2}$	$\frac{3}{2}, -\frac{1}{2}$	$\frac{3}{2}, -\frac{3}{2}$	$\frac{1}{2}, +\frac{1}{2}$	$\frac{1}{2}, -\frac{1}{2}$
u^0	$\frac{1}{4}$	$\frac{1}{4}$	$\frac{1}{4}$	$\frac{1}{4}$	$\frac{1}{2}$	$\frac{1}{2}$
u^1	$\frac{9}{20}$	$\frac{3}{20}$	$-\frac{3}{20}$	$-\frac{9}{20}$	$\frac{1}{2}$	$-\frac{1}{2}$
u^2	$\frac{1}{4}$	$-\frac{1}{4}$	$-\frac{1}{4}$	$\frac{1}{4}$	0	0

Table C.2: The coefficients C_j^{xyzar} of the core hole j in the isotropic and dichroic absorption, Ref. [54].

$\sum_r C_j^{xyzar} u_j^r$	$\langle \underline{w}^{000} \rangle$	$\langle \underline{w}^{110} \rangle$	$\langle \underline{w}^{101} \rangle$	$\langle \underline{w}^{011} \rangle$	$\langle \underline{w}^{211} \rangle$	$\langle \underline{w}^{202} \rangle$
isotropic: $a = 0$						
$j = \frac{3}{2}$	$2u^0$	u^0	$\frac{5}{3}u^1$	$\frac{10}{9}u^1$	$\frac{2}{9}u^1$	u^2
$j = \frac{1}{2}$	u^0	$-u^0$	u^1	$-\frac{1}{3}u^1$	$-\frac{2}{3}u^1$	--
dichroic: $a = 1$						
$j = \frac{3}{2}$	$\frac{5}{9}u^1$	$\frac{4}{9}u^1$	$2u^0 + \frac{2}{5}u^2$	$\frac{1}{3}u^0 + \frac{2}{3}u^2$	$\frac{2}{3}u^0 + \frac{2}{15}u^2$	$\frac{10}{9}u^1$
$j = \frac{1}{2}$	$\frac{1}{3}u^1$	$-\frac{1}{3}u^1$	u^0	$-\frac{1}{3}u^0$	$-\frac{2}{3}u^0$	$\frac{2}{3}u^1$

Table C.3: The isotropic intensities of the jm sublevels I_{jm}^0 .

I_{jm}	$\langle \underline{w}^{000} \rangle$	$\langle \underline{w}^{110} \rangle$	$\langle \underline{w}^{101} \rangle$	$\langle \underline{w}^{011} \rangle$	$\langle \underline{w}^{211} \rangle$	$\langle \underline{w}^{202} \rangle$
$\frac{3}{2}, +\frac{3}{2}$	$\frac{1}{2}$	$\frac{1}{4}$	$\frac{3}{4}$	$\frac{1}{2}$	$\frac{1}{10}$	$\frac{1}{4}$
$\frac{3}{2}, +\frac{1}{2}$	$\frac{1}{2}$	$\frac{1}{4}$	$\frac{1}{4}$	$\frac{1}{6}$	$\frac{1}{30}$	$-\frac{1}{4}$
$\frac{3}{2}, -\frac{1}{2}$	$\frac{1}{2}$	$\frac{1}{4}$	$-\frac{1}{4}$	$-\frac{1}{6}$	$-\frac{1}{30}$	$-\frac{1}{4}$
$\frac{3}{2}, -\frac{3}{2}$	$\frac{1}{2}$	$\frac{1}{4}$	$-\frac{3}{4}$	$-\frac{1}{2}$	$-\frac{1}{10}$	$\frac{1}{4}$
$\frac{1}{2}, +\frac{1}{2}$	$\frac{1}{2}$	$-\frac{1}{2}$	$\frac{1}{2}$	$-\frac{1}{6}$	$-\frac{1}{3}$	0
$\frac{1}{2}, -\frac{1}{2}$	$\frac{1}{2}$	$-\frac{1}{2}$	$-\frac{1}{2}$	$\frac{1}{6}$	$\frac{1}{3}$	0

Table C.4: The dichroic intensities of the jm sublevels I_{jm}^1 .

I_{jm}	$\langle \underline{w}^{000} \rangle$	$\langle \underline{w}^{110} \rangle$	$\langle \underline{w}^{101} \rangle$	$\langle \underline{w}^{011} \rangle$	$\langle \underline{w}^{211} \rangle$	$\langle \underline{w}^{202} \rangle$
$\frac{3}{2}, +\frac{3}{2}$	$\frac{1}{4}$	$\frac{1}{5}$	$\frac{3}{5}$	$\frac{1}{4}$	$\frac{1}{5}$	$\frac{1}{2}$
$\frac{3}{2}, +\frac{1}{2}$	$\frac{1}{12}$	$\frac{1}{15}$	$\frac{2}{5}$	$-\frac{1}{12}$	$\frac{2}{15}$	$\frac{1}{6}$
$\frac{3}{2}, -\frac{1}{2}$	$-\frac{1}{12}$	$-\frac{1}{15}$	$\frac{2}{5}$	$-\frac{1}{12}$	$\frac{2}{15}$	$-\frac{1}{6}$
$\frac{3}{2}, -\frac{3}{2}$	$-\frac{1}{4}$	$-\frac{1}{5}$	$\frac{3}{5}$	$\frac{1}{4}$	$\frac{1}{5}$	$-\frac{1}{2}$
$\frac{1}{2}, +\frac{1}{2}$	$\frac{1}{6}$	$-\frac{1}{6}$	$\frac{1}{2}$	$-\frac{1}{6}$	$-\frac{1}{3}$	$\frac{1}{3}$
$\frac{1}{2}, -\frac{1}{2}$	$-\frac{1}{6}$	$\frac{1}{6}$	$\frac{1}{2}$	$-\frac{1}{6}$	$-\frac{1}{3}$	$-\frac{1}{3}$

Bibliography

- [1] G. Schütz, W. Wagner, W. Wilhelm, P. Kienle, R. Zeller, R. Frahm, and G. Materlik, “*Absorption of circularly polarized x-rays in iron*”, Phys. Rev. Lett. **58**, 737 (1987).
- [2] B.T. Thole, P. Carra, F. Sette, and G. van der Laan, “*X-ray circular dichroism as a probe of orbital magnetization*”, Phys. Rev. Lett. **68**, 1943 (1992).
- [3] P. Carra, B.T. Thole, M. Altarelli, and X. Wang, “*x-ray circular dichroism and local magnetic fields*”, Phys. Rev. Lett. **70**, 694 (1993).
- [4] R. Wu, D. Wang, and A.J. Freeman, “*First principles investigation of the validity and range of applicability of the x-ray magnetic circular dichroism sum rule*”, Phys. Rev. Lett **71**, 3581 (1993).
- [5] R. Wu and A.J. Freeman, “*Limitation of the Magnetic-Circular-Dichroism Spin Sum Rule for Transition Metals and Importance of the Magnetic Dipole Term*”, Phys. Rev. Lett **73**, 1994 (1994)
- [6] G.Y. Guo, H. Ebert, W.M. Temmerman, and P.J. Durham, “*First-principles calculation of magnetic x-ray dichroism in Fe and Co multilayers*”, Phys. Rev. B **50**, 3861 (1994).
- [7] C. T. Chen, Y. U. Idzerda, H.-J. Lin, N. V. Smith, G. Meigs, E. Chaban, G. H. Ho, E. Pellegrin, and F. Sette, “*Experimental Confirmation of the X-Ray Magnetic Circular Dichroism Sum Rules for Iron and Cobalt*”, Phys. Rev. Lett. **75**, 152 (1995).
- [8] P. Sainctavit, M.-A. Arrio and C. Brouder, “*Analytic calculation of the spin sum rule at the $L_{2,3}$ edges of Cu^{2+}* ”, Phys. Rev. B **52**, 12766 (1995).
- [9] H. Ebert, “*Magneto-optical effects in transition metal systems*”, Rep. Prog. Phys. **59**, 1665–1735 (1996).
- [10] G.Y. Guo, “*Interpretation of x-ray circular dichroism: Multiple-scattering theory approach*”, Phys. Rev. B **57**, 10295 (1998).
- [11] R. Wu, C. Li, A.J. Freeman, “*Structural, electronic and magnetic properties of Co/Pd(111) and Co/Pt(111)*”, J. Magn. Magn. Mater. **99**, 71 (1991).

- [12] R. Coehoorn, “*Relation between interfacial magnetism and spin-dependent scattering at non-ideal Fe/Cr and Fe/V interfaces*”, J. Magn. Magn. Mater. **151**, 341 (1995).
- [13] N. Nakajima, T. Koide, T. Shidara, H. Miyauchi, H. Fukutani, A. Fujimori, K. Ito, T. Katayama, M. Nvl, and Y. Suzuki, “*Perpendicular Magnetic Anisotropy Caused by Interfacial Hybridization via Enhanced Orbital Moment in Co/Pt Multilayers: Magnetic Circular X-Ray Dichroism Study*”, Phys. Rev. Lett. **81**, 5229 (1998).
- [14] S. S. P. Parkin, “*Origin of Enhanced Magnetoresistance of Magnetic Multilayers: Spin-Dependent Scattering from Magnetic Interface States*”, Phys. Rev. Lett. **71**, 1641 (1993).
- [15] M. N. Baibich, J. M. Broto, A. Fert, F. Nguyen Van Dau, F. Petroff, P. Eitenne, G. Creuzet, A. Friederich, and J. Chazelas, “*Giant Magnetoresistance of (001)Fe/(001)Cr Magnetic Superlattices*”, Phys. Rev. Lett. **61**, 2472 (1988).
- [16] P. Isberg, P. Granberg, E.B. Svedberg, B. Hjörvarsson, R. Wäppling, P. Nordblad, “*Structure and magnetic properties of Fe/V(110) superlattices*”, Phys. Rev. B **57**, 3531 (1998).
- [17] P. Granberg, P. Nordblad, P. Isberg, B. Hjörvarsson, and R. Wäppling, “*Magnetic and transport properties of epitaxial Fe/V(001) superlattice films*”, Phys. Rev. B **54**, 1199 (1996).
- [18] A. Broddefalk, R. Mathieu, P. Nordblad, P. Blomqvist, R. Wäppling, J. Lu, and E. Olsson, “*Interlayer exchange coupling and giant magnetoresistance in Fe/V (001) superlattices*”, Phys. Rev. B **65**, 214430 (2002).
- [19] D. Laberge, K. Westerholt, H. Zabel, B. Hjörvarsson, “*Hydrogen induced change of the atomic magnetic moments in Fe/V-superlattices*”, J. Magn. Magn. Mater. **225**, 373–380 (2001).
- [20] A. N. Anisimov, W. Platow, P. Pouloupoulos, W. Wisny, M. Farle, K. Baberschke, P. Isberg, B. Hjörvarsson, and R. Wäppling, “*The temperature-dependent in- and out-of-plane magnetic anisotropies in $Fe_n/V_m(001)$ superlattices*”, J. Phys.: Condens. Matter **9**, 10581 (1997).
- [21] A. N. Anisimov, M. Farle, P. Pouloupoulos, W. Platow, K. Baberschke, P. Isberg, R. Wäppling, A. M. N. Niklasson, and O. Eriksson, “*Orbital Magnetism and Magnetic Anisotropy Probed with Ferromagnetic Resonance*”, Phys. Rev. Lett. **82**, 2390 (1999).
- [22] M. A. Tomaz, W. J. Antel Jr, W. L. O’Brien, and G. R. Harp, “*Induced V moments in Fe/V(100), (211), and (110) superlattices studied using x-ray magnetic circular dichroism*”, J. Phys.: Condens. Matter **9**, L179 (1997).
- [23] M. M. Schwickert, R. Coehoorn, M. A. Tomaz, E. Mayo, D. Lederman, W. L. O’Brien, Tao Lin, and G. R. Harp, “*Magnetic moments, coupling, and interface interdiffusion in Fe/V(001) superlattices*”, Phys. Rev. B **57**, 13681 (1998).

- [24] A. Scherz, H. Wende, P. Pouloupoulos, J. Lindner, K. Baberschke, P. Blomquist, R. Wäppling, F. Wilhelm and N.B. Brookes, “*Induced V and reduced Fe moments at the interface of Fe/V(001) superlattices*”, Phys. Rev. B **64**, 180407(R) (2001).
- [25] Y.U. Idzerda, L.H. Tjeng, H.-J. Lin, C.J. Gutierrez, G. Meigs, and C.T. Chen, “*Magnetic structure of Fe/Cr/Fe trilayers*”, Phys. Rev. B **48**, 4144 (1993).
- [26] F. Wilhelm, P. Pouloupoulos, G. Ceballos, H. Wende, K. Baberschke, P. Srivastava, D. Benea, H. Ebert, M. Angelakeris, N.K. Flevaris, D. Niarchos, A. Rogalev and N.B. Brookes, “*Layer-Resolved Magnetic Moments in Ni/Pt Multilayers*”, Phys. Rev. Lett. **85**, 413 (2000).
- [27] S. Frota-Pessôa, A. B. Klautau, and S. B. Legoas, “*Influence of interface mixing on the magnetic properties of Ni/Pt multilayers*” Phys. Rev. B **66**, 132416 (2002).
- [28] N. Hamada, K. Terakura, and A. Yanase, “*Distribution of magnetic moments near the Fe-V interface: band-structure calculation and local environment effect*”, J. Phys. F: Met. Phys. **14**, 2371 (1984).
- [29] J. Izquierdo, A. Vega, O. Elmouhssine, H. Dreyssé, and C. Demangeat, “*Induced spin polarization in V: Fe_nV_m superlattices and thin V films on Fe substrates*”, Phys. Rev. B **59**, 14510 (1999).
- [30] O. Eriksson, L. Bergqvist, E. Holmström, A. Bergman, O. LeBacq, S. Frota-Pessoa, B. Hjörvarsson, and L. Nordström, “*Magnetism of Fe/V and Fe/Co multilayers*”, J. Phys.: Condens. Matter **15**, S599–S615 (2003).
- [31] J. Fink, Th. Müller-Heinzerling, B. Scheerer, W. Speier, F. U. Hillebrecht, J. C. Fuggle, J. Zaanen, G. A. Sawatzky, “*2p absorption spectra of the 3d elements*”, Phys. Rev. B **32**, 4899 (1985).
- [32] J. Zaanen, G.A. Sawatzky, J. Fink, W. Speier, and J.C. Fuggle, “*L_{2,3} absorption spectra of the lighter 3d transition metals*”, Phys. Rev. B **32**, 4905 (1985).
- [33] J. Schwitalla and H. Ebert, “*Electron Core-Hole Interaction in the X-ray Absorption Spectroscopy of 3d Transition Metals*”, Phys. Rev. Lett. **80**, 4586 (1998).
- [34] A.L. Ankudinov, A.I. Nesvizhskii, and J.J. Rehr, “*Dynamic screening effects in x-ray absorption spectra*”, Phys. Rev. B **67**, 115120 (2003).
- [35] Jan Minár and H. Ebert, “*Magnetic circular dichroism in x-ray absorption - Theoretical description and applications*”, to appear in DPG proceedings, Appl. Phys. A (2003).
- [36] M. Faraday, “*Experimental research in electricity: On the magnetization of light and the illumination of magnetic lines of force*”, Philosoph. Trans. Royal Soc. London **136**, 1 (1846).
- [37] J. Kerr, “*On rotation of the plane of polarization by reflection from the pole of a magnet*”, London, Edinburgh, and Dublin Philosoph. Magazine and Journal of Science **3**, 321 (1877).

- [38] J.C. Chapman “*Some experiments on polarized Röntgen radiation*”, London, Edinburgh, and Dublin Philosop. Magazine and Journal of Science **25**, 792 (1913).
- [39] A.H. Forman “*The effect of magnetization on the opacity of iron to Röntgen rays*”, Phys. Rev. **7**, 119 (1916).
- [40] J.L. Erskine and E.A. Stern, “*Calculation of the $M_{2,3}$ magneto-optical absorption spectrum of ferromagnetic nickel*”, Phys. Rev. B **12**, 5016 (1975).
- [41] J.H. Hubbel, J. Phys. C4 **32**, 4 (1971).
- [42] H. Wende, Z. Li, A. Scherz, G. Ceballos, K. Baberschke, A. Ankudinov, J.J. Rehr, F. Wilhelm, A. Rogalev, D.L. Schlagel and T.A. Lograsso, “*Quadrupolar and Dipolar Contributions to XMCD at the Tb $L_{3,2}$ -edges: Experiment versus Theory*”, J. Appl. Phys. **91**, 7361 (2002).
- [43] J.J. Rehr and R.C. Albers, “*Theoretical approaches to x-ray absorption fine structure*”, Review of Modern Physics **72**, 621–654 (2000).
- [44] P. Gambardella, S. S. Dhesi, S. Gardonio, C. Grazioli, P. Ohresser, and C. Carbone, “*Localized Magnetic States of Fe, Co, and Ni Impurities on Alkali Metal Films*”, Phys. Rev. Lett. **88**, 047202 (2002).
- [45] H. Ebert, in “*Spin–Orbit-Influenced Spectroscopies of Magnetic Solids*”, edited by H. Ebert and G. Schütz (Springer, Berlin, 1996), vol. 466 of *Lecture Notes in Physics*, p. 159.
- [46] M. Altarelli, “*Orbital-magnetization sum rule for x-ray circular dichroism: A simple proof*”, Phys. Rev. B **47**, 597 (1993).
- [47] A. Ankudinov and J.J. Rehr, “*Sum rules for polarization-dependent x-ray absorption*”, Phys. Rev. B **51**, 1282 (1995).
- [48] X. Wang, T.C. Leung, B.N. Harmon and P. Carra, “*Circular magnetic x-ray dichroism in the heavy rare-earth metals*”, Phys. Rev. B **47**, 9087 (1993).
- [49] A.L. Ankudinov, J.J. Rehr, H. Wende, A. Scherz, K. Baberschke, “*Spin-dependent sum rules for x-ray absorption spectra*”, submitted to Europhys. Lett.
- [50] P. Strange, “*Magnetic absorption dichroism and sum rules in itinerant magnets*”, J. Phys.: Condens. Matter **6**, L491 (1994).
- [51] G.Y. Guo, H. Ebert, W.M. Temmerman, and P.J. Durham, “*Band theoretical investigation of circular magnetic X-ray dichroism in Fe and Co multilayers*”, J. Magn. Magn. Mater. **148**, 66 (1995).
- [52] J. Stöhr and H. König, “*Determination of Spin- and Orbital-Moment Anisotropies in Transition Metals by Angle-Dependent X-ray Magnetic Circular Dichroism*”, Phys. Rev. Lett. **75**, 3748 (1995).

- [53] A. Scherz, H. Wende, C. Sorg, K. Baberschke, J. Minár, D. Benea, H. Ebert, “*Limitations of integral sum rules for the early 3d elements*”, submitted to Physica scripta.
- [54] G. van der Laan, “*Line shape of 2p magnetic-x-ray-dichroism spectra in 3d metallic systems*”, Phys. Rev. B **55**, 8086 (1997).
- [55] G. van der Laan, “*The role of the spin polarization in x-ray magnetic circular dichroism spectra of itinerant magnets*”, J. Phys.: Condens. Matter **9**, L259 (1997).
- [56] G. van der Laan, “*Sum rules and beyond*”, J. Electr. Spectrosc. Relat. Phenom. **101**, 859 (1999).
- [57] B.T. Thole and G. van der Laan, “*Branching ratio in x-ray absorption spectroscopy*”, Phys. Rev. B **38**, 3158 (1988).
- [58] E. Goering, A. Bayer, S. Gold, and G. Schütz, M. Rabe, U. Rüdiger, and G. Güntherodt, “*Strong Anisotropy of Projected 3d Moments in Epitaxial CrO₂ Films*”, Phys. Rev. Lett. **88**, 207203 (2002).
- [59] E. Goering, D. Ahlers, K. Attenkofer, G. Obermeier, S. Horn, G. Schütz, “*XMCD and magnetism of the ferrimagnetic system NaV₆O₁₁*”, J. Synchrotron Rad. **6**, 537-539 (1999).
- [60] H. Wende, “*Extended X-ray Absorption Fine Structure Spectroscopy of Surfaces and Thin Films: Local Structure, Dynamic and Magnetic Properties*”, Ph.D. thesis, Freie Universität Berlin (1999), Verlag Dr. Köster, ISBN 3-89574-341-0.
- [61] J. Hunter Dunn, D. Arvanitis, N. Mårtensson, M. Tischer, F. May, M. Russo, and K. Baberschke, “*An angle-dependent magnetic circular X-ray dichroism study of Co/Cu(100): experiment versus theory*”, J. Phys.: Condens. Matter **7**, 1111 (1995).
- [62] M. Tischer, “*Temperaturabhängige Untersuchungen der magnetischen Eigenschaften ultradünner Filme der 3d-Übergangsmetalle mit Magnetischen Röntgendiffraktion*”, PhD thesis, unpublished, Freie Universität Berlin (1995).
- [63] R. Nakajima, J. Stöhr, and Y. U. Idzerda, “*Electron-yield saturation effects in L-edge x-ray magnetic circular dichroism spectra of Fe, Co, and Ni*”, Phys. Rev. B **59**, 6421 (1999).
- [64] F. Wilhelm, “*Magnetic Properties of Ultrathin Films, Coupled Trilayers and 3d/5d Multilayers studied by X-ray Magnetic Circular Dichroism*”, PhD thesis, Freie Universität Berlin (2000), dissertation.de, ISBN 3-89825-177-2.
- [65] A.L. Ankudinov, A.I. Nesvizhskii and J.J. Rehr, “*Hole counts from x-ray absorption spectra*”, J. Synchrotron Rad. **8**, 92 (2001).
- [66] T. Gleitsmann, “*Einfluss des Surfactants Sauerstoff auf die elektronischen und magnetischen Eigenschaften ultradünner Nickelfilme*”, Diplomarbeit, unpublished, Freie Universität Berlin (2002).

- [67] J. Stöhr, “*X-ray magnetic circular dichroism spectroscopy of transition metal thin films*”, J. Electron Spectrosc. and Relat. Phenom. **75**, 253–272 (1995).
- [68] D. Weller, J. Stöhr, R. Nakajima, A. Carl, M. G. Samant, C. Chappert, R. Mégy, P. Beauvillain, P. Veillet, and G. A. Held, “*Microscopic Origin of Magnetic Anisotropy in Au/Co/Au Probed with X-Ray Magnetic Circular Dichroism*”, Phys. Rev. Lett. **75**, 3752 (1995).
- [69] P. Gambardella, A. Dallmeyer, K. Maiti, M.C. Malagoli, W. Eberhardt, K. Kern and C. Carbone, “*Ferromagnetism in one-dimensional monatomic metal chains*”, Nature **416**, 302 (2002).
- [70] C. Ederer, M. Komelj, J.W. Davenport and M. Fähnle, “*Comment on the analysis of angle-dependent X-ray magnetic circular dichroism in systems with reduced dimensionality*”, J. Electron Spectrosc. Relat. Phenom. **130**, 97 (2003).
- [71] C. Ederer, M. Komelj and M. Fähnle, “*Magnetism in systems with various dimensionalities: A comparison between Fe and Co*”, Phys. Rev. B **68**, 052402 (2003).
- [72] J. Callaway and C.S. Wang, “*Self-Consistent Calculation of Energy Bands in Ferromagnetic Nickel*”, Phys. Rev. B **7**, 1096 (1973).
- [73] W. Nolting, “*Quantentheorie des Magnetismus*”, Vol. **2**, Teubner Studienbücher Physik, Teubner Stuttgart 1986.
- [74] P. Söderlind, O. Eriksson, B. Johansson, R.C. Albers, A.M. Boring, “*Spin and orbital magnetism in Fe-Co and Co-Ni alloys*”, Phys. Rev. B **45**, 12911 (1992).
- [75] O. Eriksson, B. Johansson, R.C. Albers, and A.M. Boring, “*Orbital magnetism in Fe, Co, and Ni*”, Phys. Rev. B **42**, 2707 (1990).
- [76] N. Haack, “*NEXAFS-Untersuchungen an adsorbierten Molekülen und dünnen Nickel-Filmen*”, Ph.D. thesis, unpublished, Freie Universität Berlin (1999).
- [77] M. Ritter, M. Stindtman, M. Farle, and K. Baberschke, “*Nanostructuring of the Cu(001) surface by ion bombardment: a STM study*”, Surf. Sci. **348**, 243 (1996).
- [78] A. Scherz, “*Magnetischer Röntgenzirkulardichroismus an ultradünnen magnetischen Filmen der 3d Übergangsmetalle Kobalt und Nickel: Temperaturabhängige Messungen an Ein- und Dreischichtsystemen*”, Diplomarbeit, unpublished, Freie Universität Berlin (2000).
- [79] W. Gudat, and C. Kunz, “*Close similarity between photoelectric yield and photoabsorption spectra in the soft-x-ray range*”, Phys. Rev. Lett. **29**, 169 (1972).
- [80] J. Stöhr, “*NEXAFS Spectroscopy*”, in “*Springer Series in Surface Science*”, Vol. **25**, Springer-Verlag Berlin Heidelberg 1996.

- [81] J. Vogel and M. Sacchi, “Polarization and angular dependence of the $L_{2,3}$ absorption edges in $Ni(110)$ ”, Phys. Rev. B **49**, 3230 (1994).
- [82] T. Lederer, “Leichte Adsorbate auf Metalloberflächen: Lokale Adsorptionsgeometrie, Bindungsart und Ladungstransfer, Oberflächenspannung und Rekonstruktion. Eine temperaturabhängige Untersuchung der Röntgenabsorption an K -Kanten.”, Ph.D. thesis, unpublished, Freie Universität Berlin (1993).
- [83] W.L. O’Brien and B.P. Tonner, “Orbital and spin sum rules in x -ray magnetic circular dichroism”, Phys. Rev. B **50**, 12672 (1994).
- [84] J. Vogel, M. Sacchi, F. Sirotti, and G. Rossi, “ X -ray dichroism of Dy overlayers on a magnetic substrate”, Appl. Surf. Sci. **66**, 170 (1993).
- [85] URL: http://www.bessy.de/users.info/01.insertion_devices/more/ue56.html
- [86] URL: http://www.esrf.fr/exp_facilities/bl26/handbook/intro.html; http://www.esrf.fr/exp_facilities/ID8/spec.html.
- [87] J. Goulon, N. B. Brookes, C. Gauthier, J. B. Goedkoop, C. Goulon-Ginet, M. Hagelstein, and A. Rogalev, “Instrumentation development for ESRF beamlines.”, Physica B **208&209**, 199 (1995).
- [88] N. Drescher, G. Snell, U. Kleineberg, H.-J. Stock, N. Müller, U. Heinzmann, and N. B. Brookes, “Characterization of the helical undulator HELIOS I in the 520 to 930 eV range using a multilayer polarimeter.”, Rev. Sci. Instr. **68**, 1939 (1997).
- [89] G. R. Harp, S. S. Parkin, W. L. O’Brien and B. P. Tonner, “ X -ray magnetic-circular-dichroism study of Fe/V multilayers”, Phys. Rev. B **51**, 3293 (1995).
- [90] J. Vogel, A. Fontaine, V. Cros, F. Petroff, J. P. Kappler, G. Krill, A. Rogalev, J. Goulon, “Structure and magnetism of Pd in Pd/Fe multilayers studied by x -ray magnetic circular dichroism at the $Pd L_{2,3}$ edges”, Phys. Rev. B **55**, 3663 (1997).
- [91] M. Sacchi, A. Mirone, C. F. Hague, J.-M. Mariot, L. Pasquali, P. Isberg, E. M. Gullikson, and J. H. Underwood, “Soft- x -ray resonant scattering from V/Fe (001) magnetic superlattices”, Phys. Rev. B **60**, R12569 (1999).
- [92] P. Pouloupoulos, F. Wilhelm, H. Wende, G. Ceballos, K. Baberschke, D. Benea, H. Ebert, M. Angelakeris, N.K. Flevaris, A. Rogalev and N.B. Brookes, “ X -ray magnetic circular dichroic magnetometry on Ni/Pt multilayers”, J. Appl. Phys. **89**, 3874 (2001).
- [93] F. Wilhelm, P. Pouloupoulos, H. Wende, A. Scherz, K. Baberschke, M. Angelakeris, N.K. Flevaris, and A. Rogalev, “Systematics of the Induced Magnetic Moments in 5d Layers and the Violation of the Third Hund’s Rule”, Phys. Rev. Lett. **87**, 207202 (2001).
- [94] R.D. Leapman and L.A. Grunes, “Anomalous L_3/L_2 White-Line Ratios in the 3d Transition Metals”, Phys. Rev. Lett. **45**, 397 (1980).

- [95] R.D. Leapman, L.A. Grunes, and P.L. Fejes, “*Study of the $L_{2,3}$ edges in the 3d transition metals and their oxides by electron-energy-loss spectroscopy with comparisons to theory*”, Phys. Rev. B **26**, 614 (1982).
- [96] J. Barth, F. Gerken, and C. Kunz, “*Atomic nature of the $L_{II,III}$ white lines in Ca, Sc, and Ti metals as revealed by resonant photoemission*”, Phys. Rev. B **28**, 3608 (1983).
- [97] W.G. Waddington, P. Rez, I.P. Grant, and C.J. Humphreys, “*White lines in the $L_{2,3}$ electron-energy-loss and x-ray absorption spectra of 3d transition metals*”, Phys. Rev. B **34**, 1467 (1986).
- [98] F.M.F. de Groot, “*X-ray absorption and dichroism of transition metals and their compounds*”, J. Electron Spectrosc. Relat. Phenom. **67**, 529 (1994).
- [99] Y. Teramura, A. Tanaka, T. Jo, “*Effect of Coulomb Interaction on the X-Ray Magnetic Circular Dichroism Spin Sum Rule in 3d Transition Elements*”, J. of Phys. Soc. of Japan **65**, 1053 (1996).
- [100] E.J. McGuire, “*Atomic M-Shell Coster-Kronig, Auger, and Radiative Rates, and Fluorescence Yields for Ca-Th*”, Phys. Rev. A **5**, 1043 (1972).
- [101] J.C. Fuggle, and S.F. Alvarado, “*Core-level lifetimes as determined by x-ray photoelectron spectroscopy measurements*”, Phys. Rev. A **22**, 1615 (1980).
- [102] M. Petersilka, U.J. Gossmann, and E.K.U. Gross, “*Excitation Energies from Time-Dependent Density-Functional Theory*”, Phys. Rev. Lett. **76**, 1212 (1996).
- [103] T. Grabo, M. Petersilka, and E.K.U. Gross, “*Molecular excitation energies from time-dependent density functional theory*”, J. Molecular Struct. (Theochem) **501–502**, 353–367 (2000).
- [104] E.K.U. Gross and W. Kohn, Adv. Quantum Chem. **21**, 255 (1990).
- [105] E.K.U. Gross, J.F. Dobson, and M. Petersilka, “*Density functional theory of time-dependent phenomena*”, in “Density Functional Theory”, edited by R.F. Nalewajski, Topics in Current Chemistry, Vol. **181**, p. 81, Springer-Verlag Berlin Heidelberg 1996.
- [106] J.C. Fuggle and N. Mårtensson, “*Core-level binding energies in metals*”, J. Electron Spectrosc. and related Phenom. **21**, 275–281 (1980).
- [107] P. Srivastava, F. Wilhelm, A. Ney, M. Farle, H. Wende, N. Haack, G. Ceballos, and K. Baberschke, “*Magnetic moments and Curie temperatures of Ni and Co thin films and coupled trilayers*”, Phys. Rev. B **58**, 5701 (1998).
- [108] F. Wilhelm, P. Pouloupoulos, P. Srivastava, H. Wende, M. Farle, K. Baberschke, M. Angelakeris and N.K. Flevaris, W. Grange, J-P. Kappler, G. Ghiringhelli, and N.B. Brookes, “*Magnetic anisotropy energy and the anisotropy of the orbital moment of Ni in Ni/Pt multilayers*”, Phys. Rev. B **61**, 8647 (2000).

- [109] J. T. Lau, A. Föhlisch, R. Nietubyc, M. Reif, and W. Wurth, “*Size-Dependent Magnetism of Deposited Small Iron Clusters Studied by X-Ray Magnetic Circular Dichroism*”, Phys. Rev. Lett. **89**, 057201 (2002).
- [110] I. Mirebeau, G. Parette, and J.W. Cable, “*Polarised neutron study of iron-vanadium alloys*”, J. Phys. F: Met. Phys. **17**, 191 (1987).
- [111] J.C. Krause, J. Schaf, M.I. da Costa, Jr., and C. Paduani, “*Effect of composition and short-range order on the magnetic moments of Fe in $Fe_{1-x}V_x$ alloys*”, Phys. Rev. B **61**, 6196 (2000).
- [112] J. Minár, “*Spin-orbit coupling influenced x-ray spectroscopies and resonant x-ray magneto-optical properties of transition metal systems*”, Ph.D. thesis, Logos Verlag Berlin, ISBN **3-8325-0232-7** (2003).
- [113] J. Minár and H. Ebert, private communication.
- [114] B. Drittler, N. Stefanou, S. Blügel, R. Zeller and P. H. Dederichs, “*Electronic structure and magnetic properties of dilute Fe alloys with transition-metal impurities*”, Phys. Rev. B **40**, 8203 (1989).
- [115] A. Scherz, P. Pouloupoulos, H. Wende, G. Ceballos, and K. Baberschke and F. Wilhelm, “*Thickness dependence of the V induced magnetic moment in Fe/V/Fe(110) trilayers*”, J. Appl. Phys. **91**, 8760 (2002).
- [116] G. van der Laan, and B.T. Thole, “*Strong magnetic x-ray dichroism in 2p absorption spectra of 3d transition-metal ions*”, Phys. Rev. B **43**, 13401 (1991).
- [117] T. Jo, and G. A. Sawatzky, “*Ground state of ferromagnetic nickel and magnetic circular dichroism in Ni 2p core x-ray-absorption spectroscopy*”, Phys. Rev. B **43**, 8771 (1991).
- [118] A. I. Nesvizhskii, A. L. Ankudinov, J. J. Rehr, and K. Baberschke, “*Interpretation of x-ray magnetic circular dichroism and x-ray absorption near-edge structure in Ni*”, Phys. Rev. B **62**, 15295 (2000), and references therein.
- [119] A. Hjelm, O. Eriksson, and B. Johansson, “*Break-down of Hund’s third rule for induced magnetism in U metal*”, Phys. Rev. Lett. **71**, 1459 (1993).
- [120] I. Galanakis, P.M. Oppeneer, P. Ravindran, L. Nordström, P. James, M. Alouani, H. Dreysse, and O. Eriksson, “*Sign reversal of the orbital moment via ligand states*”, Phys. Rev. B **63**, 172405 (2001).
- [121] R. Tyer, G. van der Laan, W. M. Temmerman, and Z. Szotek, “*Comment on Systematics of the Induced Magnetic Moments in 5d Layers and the Violation of the Third Hund’s Rule*”, Phys. Rev. Lett. **90**, 129701 (2003).
- [122] F. Wilhelm, P. Pouloupoulos, H. Wende, A. Scherz, K. Baberschke, M. Angelakeris, N.K. Flevaris and A. Rogalev, “*Wilhelm et al. Reply*”, Phys. Rev. Lett. **90**, 129702 (2003).

- [123] D. Arvanitis, in *Spin-Orbit-Influenced Spectroscopies of Magnetic Solids*, edited by H. Ebert and G. Schütz (Springer, Berlin, 1996), vol. 466 of *Lecture Notes in Physics*, p. 145.
- [124] C. Ederer, M. Komelj, and M. Fähnle, “*Magnetism in systems with various dimensionalities: A comparison between Fe and Co*”, *Phys. Rev. B* **68**, 052402 (2003).
- [125] A. Scherz, H. Wende, K. Baberschke, J. Minár, D. Benea and H. Ebert, “*Relation between $L_{2,3}$ XMCD and the magnetic ground-state properties for the early 3d element V*”, *Phys. Rev. B* **66**, 184401 (2002).
- [126] A. Fnidiki, J. Jusaszek, J. Teillet, N.H. Duc, T.M. Danh, M. Kaabouchi, and C. Sella, “*Structural and magnetic properties of the Ti/Fe multilayers*”, *J. Appl. Phys.* **84**, 3311 (1998).
- [127] M. Kopcewicz, T. Stobiecki, M. Czapkiewicz, and A. Grabias, “*Microstructure and magnetic properties of Fe/Ti multilayers*”, *J. Phys.: Condens. Matter* **9**, 103 (1997).
- [128] B. Rodmacq, J. Hillairet, J. Laugier, and A Chamberod, “*Structural and transport properties of Fe/Ti multilayers*”, *J. Phys.: Condens. Matter* **2**, 95 (1990).
- [129] E.F. Wassermann, B. Rellinghaus, Th. Roessel and W. Pepperhoff, “*Relation between structure and magnetism of Ti_xFe_{100-x} alloys within the C14 Laves-phase stability range*”, *J. Magn. Magn. Mater.* **190**, 289 (1998).
- [130] D. Stoeffler, and F. Gautier, “*Interface roughness, magnetic moments, and couplings in $(A)_m/(Cr)_n$ (001) superlattices ($A=Fe, Co, Ni$)*”, *Phys. Rev. B* **44**, R10389 (1991).
- [131] O. Hjortstam, J. Trygg, J.M. Wills, B. Johansson, O. Eriksson, “*Calculated spin and orbital moments in the surfaces of the 3d metals Fe, Co, and Ni and their overlayers on Cu(001)*”, *Phys. Rev. B* **53**, 9204 (1996).
- [132] S.S. Dhesi, H.A. Dürr, G. van der Laan, E. Dudzik and N.B. Brookes, “*Electronic and magnetic structure of thin Ni films on Co/Cu(001)*”, *Phys. Rev. B* **60**, 12852 (1999).
- [133] A. Ney, A. Scherz, P. Pouloupoulos, K. Lenz, H. Wende, K. Baberschke, F. Wilhelm and N.B. Brookes, “*Clarification of contesting results for the total magnetic moment of Ni/Cu(001)*”, *Phys. Rev. B* **65**, 024411 (2002).
- [134] P. Isberg, B. Hjörvarsson, R. Wäppling, E. B. Svedberg, and L. Hultman, “*Growth of epitaxial Fe/V(001) superlattice films*”, *Vacuum* **48**, 483 (1997).
- [135] P. Granberg, P. Isberg, E.B. Svedberg, B. Hjörvarsson, P. Nordblad, R. Wäppling, “*Antiferromagnetic coupling and giant magnetoresistance in Fe/V(001) superlattices*”, *J. Magn. Magn. Mater.* **186**, 154–160 (1998).
- [136] B. Hjörvarsson, J. A. Dura, P. Isberg, T. Watanabe, T. J. Udovic, G. Andersson, and C. F. Majkrzak, “*Reversible Tuning of the Magnetic Exchange Coupling in Fe/V(001) Superlattices Using Hydrogen*”, *Phys. Rev. Lett.* **79**, 901 (1997).

- [137] M. Sacchi, C. F. Hague, L. Pasquali, A. Mirone, J.-M. Mariot, P. Isberg, E. M. Gullikson, and J. H. Underwood, “*Optical Constants of Ferromagnetic Iron via 2p Resonant Magnetic Scattering*”, Phys. Rev. Lett. **81**, 1521 (1998).
- [138] A.M.N. Niklasson, B. Johansson, and H.L. Skriver, “*Interface magnetism of 3d transition metals*”, Phys. Rev. B **59**, 6373 (1999).
- [139] S. Lounis, M. Benakki, S. Bouarab and C. Demangeat, “*Ab initio study of the origin of the dead magnetic Ni layers at the Ni/Pt(1 1 1) interface*”, Surf. Sci. **518**, 57 (2002).
- [140] K. Heinz, S. Müller, and L. Hammer, “*Crystallography of ultrathin iron, cobalt and nickel films grown epitaxially on copper*”, J. Phys.: Condens. Matter **11**, 9437 (1999).
- [141] P. Schmailzl, K. Schmidt, P. Bayer, R. Döll, K. Heinz, “*The structure of thin epitaxial Fe films on Cu(100) in the transition range fcc→bcc*”, Surf. Science **312**, 73–81 (1994).
- [142] L. Lemke, H. Wende P. Srivastava,, R. Chauvistré, N. Haack, K. Baberschke, J. Hunter-Dunn, D. Arvanitis, N. Mårtensson, A. Ankudinov, and J.J. Rehr, “*Magnetic extended x-ray absorption fine structure at the $L_{2,3}$ edges of 3d elements*”, J. Phys. Condens. Matter **10**, 1917 (1998).
- [143] R. Nünthel, “Wachstum und Magnetismus dünner 3d Metalle auf Cu Substrate: Einfluss von O als Surfactant”, Ph.D. thesis, Freie Universität Berlin (2003), to be published.
- [144] J. Shen, J. Giergiel, and J. Kirschner, “*Growth and morphology of Ni/Cu(100) ultrathin films: An in situ study using scanning tunneling microscopy*”, Phys. Rev. B **52**, 8454 (1995).
- [145] R. Nünthel, T. Gleitsmann, P. Pouloupoulos, A. Scherz, J. Lindner, E. Kosubek, Ch. Litwinski, Z. Li, H. Wende, K. Baberschke, S. Stolbov, T.S. Rahman, “*Epitaxial growth of Ni on Cu(001) with the assistance of O-surfactant and its magnetism compared to Ni/Cu(001)*”, Surf. Science **531**, 53–67 (2003).
- [146] C. Kittel, “Introduction to Solid State Physics”, Wiley & Sons, New York, 1976.
- [147] J. Lindner, A. Scherz, P. Pouloupoulos, C. Rüdtt, A.N. Anisimov, H. Wende, K. Baberschke, P. Blomquist, R. Wäppling, F. Wilhelm, N.B. Brookes, “*Ultrathin Fe-limit in Fe/V(001) superlattices*”, J. Magn. Magn. Mater. **256**, 404–411 (2003).
- [148] G. Schütz, S. Stähler, M. Knülle, P. Fischer, S. Parkin and H. Ebert, “*Distribution of magnetic moments in Co/Pt and Co/Pt/Ir/Pt multilayers detected by magnetic x-ray absorption*”, J. Appl. Phys. **73**, 6430 (1993).
- [149] W. Grange, M. Maret, J.-P. Kappler, J. Vogel, A. Fontaine, F. Petroff, G. Krill, A. Rogalev, J. Goulon, M. Finazzi and N.B. Brookes, “*Magnetocrystalline anisotropy in (111) $CoPt_3$ thin films probed by x-ray magnetic circular dichroism*”, Phys. Rev. B **58**, 6298 (1998).

- [150] J. Vogel, A. Fontaine, V. Cross, F. Petroff, J.-P. Kappler, G. Krill and J. Goulon, “*Structure and magnetism of Pd in Pd/Fe multilayers studied by x-ray magnetic circular dichroism at the Pd $L_{2,3}$ edges*”, Phys. Rev. B **55**, 3663 (1997).
- [151] L. Séve, N. Jaouen, J. M. Tonnerre, D. Raoux, F. Bartolomé, M. Arend, W. Felsch, A. Rogalev, J. Goulon, C. Gautier, and J. F. Bézar, “*Profile of the induced 5d magnetic moments in Ce/Fe and La/Fe multilayers probed by x-ray magnetic-resonant scattering*”, Phys. Rev. B **60**, 9662 (1999).
- [152] K. Lenz, “*Messung der absoluten Magnetisierung von ultradünnen metallischen Filmen mittels UHV-SQUID-Magnetometrie*”, Diplomarbeit, unpublished, Freie Universität Berlin (2002).
- [153] P. Blomquist, private communication.
- [154] M. Farle, A. N. Anisimov, K. Baberschke, J. Langer, and H. Maletta, “*Gyromagnetic ratio and magnetization in Fe/V superlattices*”, Europhys. Lett. **49**, 658 (2000).
- [155] Eric E. Fullerton, Ivan K. Schuller, H. Vanderstraeten, and Y. Bruynseraede, “*Structural refinement of superlattices from x-ray diffraction*”, Phys. Rev. B **45**, 9292 (1992).
- [156] B. Kalska, L. Häggström, P. Blomquist, and R. Wäppling, “*Conversion electron Mössbauer spectroscopy studies of the magnetic moment distribution in Fe/V multilayers*”, J. Phys. Condens. Matter **12**, 539 (2000).
- [157] C. Kittel, “*On the Gyromagnetic Ratio and Spectroscopic Splitting Factor of Ferromagnetic Substances*”, Phys. Rev. **76**, 743 (1949).
- [158] J. Lindner, “*Ferromagnetische Resonanz an ultradünnen magnetischen Einfach- und Mehrfachlagen der 3d-Übergangsmetalle - Statik und Dynamik*”, PhD thesis, FU Berlin (2002), dissertation.de, ISBN 3-89825-606-5.
- [159] M. Tischer, O. Hjortstam, D. Arvanitis, J. Hunter Dunn, F. May, K. Baberschke, J. Trygg, J. M. Wills, B. Johansson, and O. Eriksson, “*Enhancement of Orbital Magnetism at Surfaces: Co on Cu(100)*”, Phys. Rev. Lett. **75**, 1602 (1995).
- [160] C. Rüdte, P. Pouloupoulos, J. Lindner, A. Scherz, K. Baberschke, P. Blomquist and R. Wäppling, “*Absence of dimensional crossover in metallic ferromagnetic superlattices*”, Phys. Rev. B **65**, 220404(R) (2002).
- [161] P. Pouloupoulos, M. Angelakeris, Th. Kehagias, D. Niarchos, N.K. Flevaris, “*Improved growth and perpendicular anisotropy in PdCo multilayers with intentionally alloyed layers*”, Thin Solid Films **371**, 225 (2001).
- [162] E.A.M. van Alphen, W.J.M. de Jonge, “*Granular Co/Ag multilayers: Relation between nanostructure, and magnetic and transport properties*”, Phys. Rev. B **51**, 8182 (1995).

- [163] K.W. Edmonds, C. Binns, S.H. Baker, S.C. Thornton, C. Norris, J.B. Goedkoop, M. Finazzi, and N.B. Brookes, “*Doubling of the orbital magnetic moment in nanoscale Fe clusters*”, Phys. Rev. B **60**, 472 (1999).
- [164] D. Riegel, H.J. Barth, L. Büermann, H. Haas, and Ch. Stenzel, “*Fully Localized 3d-Shell Behavior of Fe Ions in Alkali-Metal Hosts*”, Phys. Rev. Lett. **57**, 388 (1986).
- [165] R. Kowallik, H.H. Bertschat, K. Biedermann, H. Haas, W. Müller, B. Spellmeyer, and W.-D. Zeitz, “*Observation of a Fully Localized 3d⁹ Configuration for Nickel Ions in Alkali Metals*”, Phys. Rev. Lett. **63**, 434 (1989).
- [166] H. Beckmann and G. Bergmann, “*Mystery of the Alkali Metals: Giant Moments of Fe and Co on and in Cs films*”, Phys. Rev. Lett. **83**, 2417 (1999).
- [167] M. Gruyters and D. Riegel, “*Comment on Mystery of the Alkali Metals: Giant Moments of Fe and Co on and in Cs Films*”, Phys. Rev. Lett. **85**, 1582 (2000).
- [168] P. Mohn, P. Weinberger, B. Ujfalussy, O. Eriksson, G. Gutierrez, R. Ahuja, and B. Johansson, “*Comment on Mystery of the Alkali Metals: Giant Moments of Fe and Co on and in Cs Films*”, Phys. Rev. Lett. **85**, 1583 (2000).
- [169] H. Beckmann and G. Bergmann, “*Reply: Beckmann and Bergmann*”, Phys. Rev. Lett. **85**, 1584 (2000).
- [170] S.K. Kwon and B.I. Min, “*Origin of the Giant Magnetic Moments of Fe Impurities on and in Cs Films*”, Phys. Rev. Lett. **84**, 3970 (2000).
- [171] G.Y. Guo, “*Giant orbital moments of Fe and Co in alkali metals Cs, Rb, and K*”, Phys. Rev. B **62**, R14609 (2000).
- [172] S. Frota-Pessôa, “*Magnetic Behavior of 3d Impurities in Cu, Ag, and Au*”, Phys. Rev. B, submitted (2003).
- [173] O. Beutler, “*Lokale Umgebungseffekte auf den Magnetismus von Fe in nichtmagnetischen binären Legierungen und Spingläsern*”, Ph.D. thesis, unpublished, Freie Universität Berlin (1998).
- [174] R. Kirsch, “*Magnetische und strukturelle Eigenschaften von Fe-Ionen in metallischen Systemen*”, Ph.D. thesis, unpublished, Freie Universität Berlin (2001).
- [175] S. Frota-Pessôa, “*Pairs of 3d impurities in Au: local moments and exchange coupling from first-principles*”, J. Magn. Magn. Mater. **226–230**, 1021 (2001).
- [176] H.A. Dürr, G. van der Laan, D. Spanke, F.U. Hillebrecht, N.B. Brookes, “*Electron-correlation-induced magnetic order of ultrathin Mn films*”, Phys. Rev. B **56**, 8156 (1997).
- [177] H. Ebert, R. Zeller, B. Drittler, and P.H. Dederichs, “*Fully relativistic calculation of the hyperfine fields of 5d-impurity atoms in ferromagnetic Fe*”, J. Appl. Phys. **67**, 4576 (1990).

[178] URL: http://www-cxro.lbl.gov/optical_constants/

List of Publications / Contributions to Conferences

I. Refereed Publications

1. F. Wilhelm, U. Bovensiepen, A. Scherz, P. Pouloupoulos, A. Ney, H. Wende, G. Ceballos, and K. Baberschke
Manipulation of the Curie temperature and the magnetic moments of ultrathin Ni and Co films by Cu-capping
J. Magn. Magn. Mater. **222**, 163 (2000).
2. A. Ney, P. Pouloupoulos, F. Wilhelm, A. Scherz, M. Farle, and K. Baberschke
Absolute determination of the magnetic moments of Co monolayers: A combination of UHV magnetometries
J. Magn. Magn. Mater. **226**, 1570 (2001).
3. A. Scherz, F. Wilhelm, U. Bovensiepen, P. Pouloupoulos, H. Wende, and K. Baberschke
Separate Curie temperatures in magnetic trilayers and the effect of spin fluctuations
J. Magn. Magn. Mater. **236**, 1 (2001).
4. A. Scherz, F. Wilhelm, P. Pouloupoulos, H. Wende, and K. Baberschke
Element-specific Magnetization Curves and Crossover in Co/Cu/Ni/Cu(001) Trilayers Studied by XMCD
J. Synchrotron Rad. **8**, 472 (2001).
5. F. Wilhelm, P. Pouloupoulos, H. Wende, A. Scherz, K. Baberschke, M. Angelakeris, N.K. Flevaris, and A. Rogalev
Systematics of the Induced Magnetic Moments in 5d Layers and the Violation of the Third Hund's Rule
Phys. Rev. Lett. **87**, 207202 (2001).

6. A. Scherz, H. Wende, P. Pouloupoulos, J. Lindner, K. Baberschke, P. Blomquist, R. Wäppling, F. Wilhelm, and N.B. Brookes
Induced V and reduced Fe moments at the interface of Fe/V(001) superlattices
Phys. Rev. B **64**, R 180407 (2001).
7. P. Pouloupoulos, A. Scherz, F. Wilhelm, H. Wende, and K. Baberschke
Direct probe of induced magnetic moments at interfaces via x-ray magnetic circular dichroism
Physica Status Solidi (a)**189**, 293 (2002).
8. A. Ney, A. Scherz, P. Pouloupoulos, K. Lenz, H. Wende, K. Baberschke, F. Wilhelm, and N.B. Brookes
Clarification of contesting results for the total magnetic moment of Ni/Cu(001)
Phys. Rev. B **65**, 024411 (2002).
9. C. Rüdtt, P. Pouloupoulos, J. Lindner, A. Scherz, K. Baberschke, P. Blomquist, and R. Wäppling
Absence of dimensional crossover in metallic ferromagnetic superlattices
Phys. Rev. B **65**, 220404(R) (2002).
10. A. Scherz, P. Pouloupoulos, H. Wende, G. Ceballos, K. Baberschke, and F. Wilhelm
Thickness dependence of the V induced magnetic moment in Fe/V/Fe(110) trilayers
J. Appl. Phys. **91**, 8760 (2002).
11. H. Wende, Z. Li, A. Scherz, G. Ceballos, K. Baberschke, A. Ankudinov, J.J. Rehr, F. Wilhelm, A. Rogalev, D.L. Schlagel, and T.A. Lograsso
Quadrupolar and Dipolar Contributions to XMCD at the Tb L_{3,2}-edges: Experiment versus Theory
J. Appl. Phys. **91**, 7361 (2002).
12. A. Scherz, H. Wende, K. Baberschke, J. Minár, D. Benea, and H. Ebert
Relation between L_{2,3} XMCD and the magnetic ground-state properties for the early 3d element V
Phys. Rev. B **66**, 184401 (2002).
13. J. Lindner, A. Scherz, P. Pouloupoulos, C. Rüdtt, A.N. Anisimov, H. Wende, K. Baberschke, P. Blomquist, R. Wäppling, F. Wilhelm, and N.B. Brookes
Ultrathin Fe-limit in Fe/V(001) superlattices
J. Magn. Magn. Mat. **256**, 404 (2003).
14. R. Nünthel, T. Gleitsmann, P. Pouloupoulos, A. Scherz, J. Lindner, E. Kosubek, Ch. Litwinski, Z. Li, H. Wende, K. Baberschke, S. Stolbov, and T. S. Rahman

- Epitaxial growth of Ni on Cu(001) with the assistance of O-surfactant and its magnetism compared to Ni/Cu(001)*
Surf. Sci. **531**, 53 (2003).
15. F. Wilhelm, P. Pouloupoulos, H. Wende, A. Scherz, K. Baberschke, M. Angelakeris, N.K. Flevaris, and A. Rogalev
Wilhelm et al. Reply
Phys. Rev. Lett. **90**, 129702 (2003).
16. H. Wende, A. Scherz, F. Wilhelm, and K. Baberschke
Induced magnetism at thin-film interfaces probed by means of x-ray magnetic circular dichroism
J. Phys.: Condens. Matter **15**, S547 (2003).
17. F. Wilhelm, P. Pouloupoulos, A. Scherz, H. Wende, K. Baberschke, M. Angelakeris, N. K. Flevaris, J. Goulon, and A. Rogalev
Interface magnetism in 3d/5d multilayers probed by x-ray magnetic circular dichroism
Physica Status Solidi (a) **196**, 33 (2003).
18. H. Wende, Ch. Litwinski, A. Scherz, T. Gleitsmann, Z. Li, C. Sorg, K. Baberschke, A. Ankudinov, J.J. Rehr, and Ch. Jung
A systematic study of embedded atom EXAFS: The (2×1)O/Cu(110) reconstruction as an ideal prototype system
J. Phys.: Condens. Matter **15**, 5197 (2003).
19. A. Scherz, H. Wende, and K. Baberschke
Absorption fine structure of the 3d transition metals
Appl. Phys. A, in press (2003).
20. A. Scherz, P. Pouloupoulos, R. Nünthel, J. Lindner, H. Wende, and K. Baberschke
Direct probe of interdiffusion effects on the V spin polarization at Fe/V interfaces
Phys. Rev. B **68**, 140401(R) (2003).
21. A. Scherz, H. Wende, C. Sorg, K. Baberschke, J. Minár, D. Benea, and H. Ebert
Limitations of integral sum rules for the early 3d elements
Conference proceedings XAFS XII, submitted to Physica Scripta (2003).
22. C. Sorg, A. Scherz, H. Wende, T. Gleitsmann, Ch. Litwinski, Z. Li, S. Rüttinger, and K. Baberschke
Co/Cu/Ni trilayers near their Curie temperature studied by XMCD
Conference proceedings XAFS XII, submitted to Physica Scripta (2003).

23. H. Wende, A. Scherz, C. Sorg, Z. Li, P. Pouloupoulos, K. Baberschke, A. Ankudinov, J. J. Rehr, F. Wilhelm, N. Jaouen, A. Rogalev, D. L. Schlagel, and T. A. Lograsso
Temperature dependence of the magnetic EXAFS for rare earth elements
Conference proceedings XAFS XII, submitted to Physica Scripta (2003).
24. C. Rüdte, A. Scherz, P. Pouloupoulos, K. Baberschke, P. Blomquist, and R. Wäppling
Higher harmonics of the ac susceptibility in ultrathin film multilayers
Conference proceedings ICM, Roma-Italy, accepted J. Magn. Magn. Mater. (2003).
25. P. Pouloupoulos, F. Wilhelm, Z. Li, A. Scherz, H. Wende, K. Baberschke, M. Angelakeris, N. K. Flevaris, A. Rogalev, and N. B. Brookes
Element-specific hysteresis loops and the anisotropy of the orbital moment of Pt in Ni/Pt multilayers
Conference proceedings ICM, Roma-Italy, accepted J. Magn. Magn. Mater. (2003).
26. W.D. Brewer, A. Scherz, C. Sorg, H. Wende, K. Baberschke, P. Bencok, and S. Frota-Pessôa
Direct Observation of Orbital Magnetism in Dilute 3d Impurities
submitted to Phys. Rev. Lett.
27. C. Rüdte, P.J. Jensen, A. Scherz, J. Lindner, P. Pouloupoulos, and K. Baberschke
Higher harmonics of the ac susceptibility: a new type of analysis to study hysteresis effects in ultrathin ferromagnets
submitted to Phys. Rev. B.
28. A. Ankudinov, J. J. Rehr, H. Wende, A. Scherz, and K. Baberschke
Spin-dependent sum rules for x-ray absorption spectra
submitted to Europhys. Lett.
29. A. Scherz, H. Wende, C. Sorg, K. Baberschke, and E.K.U. Gross
Spectral Distribution of the $L_{2,3}$ x-ray absorption from time-dependent density-functional theory
to be published
presentation on the International Workshop on X-ray Spectroscopies of Magnetic Solids 2003, Dec. 6.-7. (2003).

II. Annual reports of synchrotron radiation facilities

1. F. Wilhelm, P. Pouloupoulos, H. Wende, A. Scherz, K. Baberschke, M. Angelakeris, N.K. Flevaris, and A. Rogalev
Systematics of the Induced Magnetic Moments in 5d Layers and the Violation of

Hund's Third Rule

ESRF Highlights page 65 (2001).

2. A. Scherz, H. Wende, C. Sorg, K. Baberschke, J. Minár, D. Benea, and H. Ebert
New concept to study magnetic behavior of early 3d elements
BESSY Highlights page 8 (2002).
3. A. Scherz, F. Wilhelm, P. Poulopoulos, H. Wende, G. Ceballos, and K. Baberschke
Direct observation of temperature-dependent switching of the magnetization in Co/Cu/Ni/Cu(001) trilayers by XMCD
Annual report BESSY (2000).
4. A. Scherz, F. Wilhelm, P. Poulopoulos, H. Wende, G. Ceballos, and K. Baberschke
Induced Magnetization of Vanadium in Fe/V/Fe Trilayers studied by XMCD
Annual report BESSY (2000).
5. A. Scherz, P. Poulopoulos, H. Wende, F. Wilhelm, G. Ceballos, and K. Baberschke
Short-range V spin-polarization in Fe/V/Fe(110) trilayers
Annual report BESSY (2001).
6. T. Gleitsmann, A. Scherz, Ch. Litwinski, C. Sorg, Z. Li, H. Wende, and K. Baberschke
NEXAFS investigation of ultrathin Ni films grown on oxygen induced reconstructed $(\sqrt{2} \times 2\sqrt{2})R45^\circ$ O/Cu(001)
Annual report BESSY (2002).

III. Invited Talks

- BESSY Annual User's Meeting,
Analysis of XMCD for the early 3d elements
December 2002 (Berlin-Adlershof, Germany).
- Symposium on Magnetism at surfaces and interfaces, Frühjahrstagung der Deutschen Physikalischen Gesellschaft,
Zusammenhang des $L_{2,3}$ XMCD mit den magnetischen Grundzustandseigenschaften leichter 3d Elemente - Fe/V
March 2003 (Dresden, Germany).

IV. Contributions to Conferences

- Talk, Frühjahrstagung der Deutschen Physikalischen Gesellschaft,
XMCD an Co/Cu/Ni/Cu(001)-Dreilagern: elementspezifische Magnetisierungs-Kurven und -Überkreuzung
March 2001 (Hamburg, Germany).

- Poster, 6th Patras University Euroconference on Properties of condensed matter probed with x-ray scattering,
Interfacial magnetism and magnetic moments of Fe/V(100) superlattices studied by XMCD
September 2001 (Patras, Greece).
- Talk, 46th International Conference on Magnetism and Magnetic Materials,
Thickness dependence of the V induced magnetic moment in Fe/V/Fe(110) trilayers
November 2001 (Seattle, USA).
- Poster, International Workshop on X-ray Spectroscopies of Magnetic Solids,
Interfacial Magnetism and magnetic moments of Fe/V(100) superlattices studied by XMCD
December 2001 (Halle, Germany).
- Poster, 281. WE-Heraeus Seminar,
Vanadium XMCD and the magnetic ground-state in Fe/V
June 2002 (Wandlitz, Germany).
- Talk, International Conference XAFS XII,
Limitations of integral XMCD sum-rules for the early 3d elements
June 2003 (Malmo, Sweden).

Curriculum Vitae

I. Personal Data

Name: Andreas Scherz

Nationality: German

Place and Date of Birth: Berlin-Wilmersdorf, May 15th, 1973

Permanent Address: Freie Universität Berlin
Institut für Experimentalphysik
Arnimallee 14
D-14195 Berlin
Germany
Tel.: +49-30-838 56144
Fax.: +49-30-838 53646
email: scherz@physik.fu-berlin.de

II. Educational Qualifications / Research Experience

summer 1979 to summer 1985 Elementary school “Kronach-Grundschule” in Berlin-Steglitz

summer 1985 to summer 1992 Gymnasium “Lilienthal-Oberschule” in Berlin-Steglitz

May 27th, 1992 Abitur

November 2nd, 1992 to March 30th, 1994 “Zivildienst” (civil service) in Alba-Langenskiöld-Heim in Berlin-Lichterfelde

Since April 1994	Studies of physics at the Freie Universität Berlin
April 16 th , 1996	“Diplom-Vorprüfung” (pre-diploma) in physics
July 1998 to January 2000	Diploma thesis “ <i>Magnetischer Röntgenzirkulardichroismus an ultradünnen magnetischen Filmen der 3d Übergangsmetalle Kobalt und Nickel: Temperaturabhängige Messungen an Ein- und Dreischichtsystemen</i> ” at the Institut für Experimentalphysik, Freie Universität Berlin (2000); advisor: Prof. Dr. K. Baberschke
Since October 1998	Tutor in the laboratory course in physics for medicine students
April 17 th , 2000	“Diplom” in physics
from April 2000	Started Ph. D. work in Prof. Dr. K. Baberschke’s group

Zusammenfassung

In der vorliegenden Arbeit wurden die magnetischen und strukturellen Eigenschaften der Grenzflächen in magnetischen Vielfachschichten bestehend aus abwechselnd ferromagnetischen und unmagnetischen Lagen untersucht. Die Messungen wurden an Fe_n/V_m -Vielfachschichten und $\text{Fe}/\text{V}/\text{Fe}$ -Dreifachschichten durchgeführt. Im Bereich von wenigen atomaren Lagen ($n, m = 2 - 5$) beleuchten die erzielten Ergebnisse die magnetischen Eigenschaften sowohl der spinpolarisierten V-Schicht als auch der ferromagnetischen Fe-Schicht. Unter Ausnutzung der elementselektiven Eigenschaft der XMCD-Methode konnte gezeigt werden, dass der Ursprung von reduzierten Probenmagnetisierungen, die man mit konventioneller Magnetometrie wie SQUID oder VSM misst, nicht alleine auf eine reduzierte Fe-Magnetisierung, sondern auch auf die antiparallel induzierte V-Magnetisierung zurückzuführen ist. Hierbei hängen die magnetischen Momente V und Fe an der gemeinsamen Grenzschicht von der Schichtdickenzusammensetzung der Multilage ab. Die Proben mit jeweils den dünnsten Fe- bzw. V-Schichten weisen dabei die stärkste Reduktion des Fe-Moments ($1.34 \mu_B$ pro Atom) bzw. das größte induzierte V-Moment ($-1.1 \mu_B$ pro Atom) auf. Die Beobachtung von großen g -Faktoren in Vielfachschichten mit dünnen Fe-Schichten durch die FMR kann durch folgende Ursachen begründet werden: Eine Erhöhung des Bahnmoments ergibt sich (i) aus der Aufhebung des "Quenchings" vom Bahnmoment in den dünnen Fe-Schichten und (ii) aus den relativen Ausrichtungen des induzierten Spin- und Bahnmoments von V an der Grenzschicht zu Fe. Des Weiteren wurde für ultradünne Schichtdicken von 1–2 atomaren Fe-Lagen dargelegt, dass Bereiche des Systems neben ferromagnetischen auch superparamagnetisches Verhalten aufweisen können.

Obwohl die XRD-Messungen an den Fe/V -Vielfachschichten eine hohe strukturelle Homogenität bestätigen, widersprechen die Ergebnisse den theoretischen Voraussagen, die von perfekten Grenzflächen ausgehen, über die Größe der magnetischen Momente von Fe und V. Um die recht häufig in der Literatur diskutierten

Diskrepanzen über die magnetischen Grenzflächeneigenschaften zwischen Theorie und Experiment zu erklären, wurde der Einfluss von Interdiffusion und Rauheit an der Grenzfläche an einem Prototyp Fe/V/Fe-Dreischichtsystem untersucht. Dies wurde experimentell realisiert, indem ausschliesslich unter UHV-Bedingungen gearbeitet und die Aufdampftemperatur für die Grenzflächeneigenschaften angepasst wurde. Es konnte gezeigt werden, dass die Aufdampftemperatur bei der Modifikation des induzierten Magnetismus hinsichtlich der Größenordnung und der Reichweite der induzierten magnetischen Momente in der nicht-magnetischen Zwischenschicht eine entscheidende Rolle spielt. Das Aufdampfen auf atomar flache Fe-Schichten bei Raumtemperatur ergibt kleinere V-Momente ($-0.5 \mu_B$ pro Atom), die in Übereinstimmung mit der Theorie unter der Annahme von scharfen Grenzflächen stehen. Im Gegensatz dazu führt das Aufdampfen bei höheren Temperaturen zu einer Verdopplung der induzierten Momente ($-1.0 \mu_B$ pro Atom), wie es in den Fe/V-Vielwandschichten beobachtet wurde. Darüber hinaus zeigt die nicht-magnetische V-Zwischenschicht eine kurzreichweitige Polarisation, das heißt das induzierte magnetische Moment ist an der Grenzfläche lokalisiert. Die Interdiffusion und Rauheit an der Grenzfläche hingegen führen zu einer scheinbar langreichweitigen Polarisation, wie sie in den Fe/V-Vielwandschichten zu beobachten ist. Anhand dieses Modellsystems ist es erstmalig gelungen, den Effekt von Interdiffusion und Rauheit auf den induzierten Magnetismus an Grenzflächen zu untersuchen. Die Ergebnisse erklären die fehlende Übereinstimmung von bisherigen Arbeiten zwischen Theorie und Experiment.

Für die Bestimmung der Spin- und Bahnmomente von V wurden die entsprechenden XMCD-Spektren analysiert. Dies geschah unter Berücksichtigung von zwei Hauptpunkten: (i) Der Einfluss des angeregten Rumpflochs auf die Absorptionsspektren und (ii) die Beziehung zwischen dem magnetischen Grundzustand und der spektralen Verteilung des XMCD-Signals leichter $3d$ TM's. Es wurde daher eine systematische Untersuchung der $L_{2,3}$ Absorptionsfeinstruktur entlang der $3d$ -Reihe vorgenommen. Mit Hilfe der "gap-scan"-Technik am Undulatorstrahlrohr gelang es, die spinabhängige komplexe Absorptionsfeinstruktur aufzulösen und ein genaues Bild der spektralen Verteilung $\Delta\mu(E)$ für die leichten $3d$ TM's zu gewinnen. Die Ergebnisse können im einzelnen wie folgt zusammengefasst werden:

- Die Abweichung der Summenregeln entlang der $3d$ -Serie wurde erstmals experimentell bestimmt. Angewandt auf die leichten $3d$ TM's wurden die Ergebnisse der magneto-optischen Summenregeln im Hinblick auf ihre Gültigkeit geprüft. Es kann-

te gezeigt werden, dass insbesondere die Spinsummenregel zusammenbricht. Die scheinbaren Spinmomente von Ti–Cr weichen um den Faktor 5 bis Faktor 2 vom realen Wert ab. Zurückzuführen ist dieser Effekt auf die Wechselwirkung mit dem $2p$ Rumpfloch, welche konkurrierend zur reduzierten $2p$ Spin-Bahn-Kopplung der leichten $3d$ TM's auftritt. Angesichts der kleineren Rumpflocheffekte bei den schweren $3d$ TM's Fe, Co und Ni erscheint die Anwendung der Spinsummenregel gerechtfertigt und erklärt, warum realistische Werte von den entsprechenden XMCD-Spektren abgeleitet werden können. Im allgemeinen helfen die aktuellen Resultate, die magnetischen Momente aus den XMCD-Spektren für $3d$ TM's in zukünftigen Arbeiten abzuschätzen.

- Aufgrund der begrenzten Anwendungsmöglichkeit der Summenregeln für die leichten $3d$ TM's wurde ein alternatives Konzept vorgeschlagen, in dem die spektrale Linienform des Zirkulardichroismus in Verbindung mit der Theorie analysiert wird. Diese Herangehensweise beinhaltet die Ableitung der magnetischen Momente aus der Absorptionsfeinstruktur des XMCDs, welches von dem magnetischen Grundzustand der $3d$ -Zustände abhängt. Für die Interpretation der XMCD-Spektren wurden die experimentellen Daten mit der Rechnung verglichen, welche auf der SPR-KKR-Methode basiert und für den magnetischen Festkörper geeignet ist. Es stellte sich heraus, dass die Linienform des XMCDs insgesamt adequat durch die Theorie beschrieben werden kann und das obwohl $2p-3d$ Korrelationseffekte des Rumpflochs in der Rechnung nicht enthalten sind. Eine Ausnahme ist die beobachtete Aufspaltung des XMCD-Signals, die zu einer deutlichen Struktur an der L_3 Kante führt. Diese kann über vergleichbare atomare Multiplett-Rechnungen unter Berücksichtigung des Rumpflochs erklärt werden. Darüber hinaus liefert das XMCD wertvolle Informationen über die spinabhängige Bandstruktur, wie z.B. durch die oszillatorische Feinstruktur an der L_2 Kante der leichten $3d$ TM's, die von van-Hove-Singularitäten in der Brillouinzone herrühren.

- Innerhalb der vorliegenden Arbeit wurde ein einfaches theoretisches Modell erarbeitet, das es ermöglicht, die Korrelationsenergien der $2p-3d$ Elektron-Rumpflochwechselwirkung aus den experimentellen Spektren heraus zu bestimmen. Die Analyse der systematischen Variation des "Branching Ratios" D_1 und die Aufspaltung der $L_{2,3}$ Kanten in den isotropen Absorptionsspektren $\Delta\Omega$ ergibt Korrelationsenergien von 0.251 eV (L_3) und 0.121 eV (L_2) pro d Loch pro Atom. Experimentell wurde abgeleitet, dass die Korrelationsenergien linear mit der Anzahl der d Elektronen für Ti, V und Cr skalieren. Die Extrapolation der Korrelationsenergien zu

den schwereren $3d$ Elementen weist darauf hin, dass der Einfluss des Rumpflochs für diese vernachlässigt werden kann. Die ermittelten $2p - 3d$ Korrelationsenergien können in Zukunft genutzt werden, um eine umfassende Theorie aufzustellen, die die Rumpflocheffekte in Absorptionsspektren von magnetischen Festkörpern beschreibt.

Darüber hinaus wurden in dieser Arbeit erstmals XMCD-Experimente an verdünnten Legierungen von $3d$ -Atomen in Au vorgestellt. Die Absorptionsfeinstruktur der $3d$ -Atome in Au an den $L_{2,3}$ Kanten zeigt den Übergang von einer rein atomaren Konfiguration hin zum Festkörper. Die erhöhten "Branching Ratios" weisen auf die Tendenz zur Formung von großen Spinmomenten in den $3d$ -Momenten hin. Bei der Auswertung des Verhältnisses von Bahn- zu Spinmoment wurden bemerkenswerte Bahnmomente in Übereinstimmung mit der *ab initio* Theorie gefunden. Hybridisierungseffekte mit dem Au-Wirt spielen eine wichtige Rolle für das Auftreten von Bahnmagnetismus in Co-Atomen in Au (viermal so groß wie im Kristallvolumen) und das Auslöschung des Bahnmomentes in Fe-Atomen in Au.

Danksagung

“Last but not least” möchte ich allen, die zum Gelingen dieser Arbeit beigetragen haben, meinen Dank aussprechen.

Allen voran *Prof. Dr. Klaus Baberschke* für seine großartige Unterstützung in allen Phasen dieser Arbeit sowie für seinen stetigen Einsatz und sein Interesse an den Resultaten.

Des weiteren möchte ich *Prof. Dr. Frank Forstmann* für die Zweitbetreuung und die vielen fruchtbaren Diskussionen über Inhalte der Arbeit danken.

Für die zahlreichen Diskussionen über XMCD, Magnetismus und darüber hinaus... in den unendlich langen Tagen und Nächten während der Messzeiten danke ich *Dr. Heiko Wende, Claudia Sorg, Dr. Panagiotis Pouloupoulos, Dr. Fabrice Wilhelm, Dr. Gustavo Ceballos, Tobias Gleitsmann* und *Christian Litwinski*.
Danke, *ευχαριστω*, *Merci*, *Gracias*, *Thanks*.

Für die bestmögliche Umsetzung meiner zahlreichen Wünsche in Rechnungen danke ich *Dr. Jan Minar*.

Prof. Dr. E.K.U. Gross und *Dr. A. Ankudinov* gilt mein Dank für die Hilfe und die langen Diskussionen zu den Rumpflocheffekten in den Absorptionsspektren.

Bei *Prof. W.D Brewer* bedanke ich mich für die hervorragende Zusammenarbeit zu verdünnten Legierungen und die gemeinsame Messzeit an der ESRF.

Für die vielen, vielen gemeinsamen Diskussionen und Ergebnisse zwischen Tür und Angel über Fe/V, FMR und STM möchte ich mich bei *Dr. J. Lindner* und *R.*

Nünthel bedanken.

Christoph Rüdts danke ich neben den vielen Diskussionen über Harmonische, Lock-Ins und fehlgeleitete Computerprogramme für die entspannenden Zigarettenpausen.

Für das exzellente Arbeitsklima und Unterstützung danke ich *Kilian Lenz, Boris Michaelis, Ela Kosubek, Dr. Tomasz Tolinski, Dr. Ponpandian Nagamony, Matthias Bernien, Dr. Andreas Ney* und *Uwe Lipowski*.

Meinen Eltern danke ich für ihre Unterstützung in allen Lebenslagen.

Sabrina - Danke für das schönste Leben weit weg von der Physik...